UC Davis
UC Davis Electronic Theses and Dissertations

Title
Correlating Processing to Structure-Function Relationships of Organic Semiconductors

Permalink
https://escholarship.org/uc/item/57d0h1xq

Author
Murrey, Tucker Lewis

Publication Date
2021

Peer reviewed|Thesis/dissertation

eScholarship.org Powered by the California Digital Library
University of California

Correlating Processing to Structure-Function Relationships of Organic Semiconductors

By

TUCKER LEWIS MURREY

DISSERTATION

Submitted in partial satisfaction of the requirements for the degree of

DOCTOR OF PHILOSOPHY

in

Material Science and Engineering

in the

OFFICE OF GRADUATE STUDIES

of the

UNIVERSITY OF CALIFORNIA

DAVIS

Approved:

Adam Moulé, Chair

Tonya Kuhl

Roland Faller

Committee in Charge

2021

Copyright © 2021 by
Tucker Lewis Murrey
All rights reserved.

CONTENTS

List of Figures vi
List of Tables xvi
Abstract xviii
Acknowledgments xix

1 Introduction **1**
1.1 Preamble 2
1.2 Introduction 2

2 Additive Solution Deposition of Multi-Layered Semiconducting Polymer Films for Design of Sophisticated Device Architectures **9**
2.1 Preface 10
2.2 Introduction 10
2.3 Experimental 14
2.3.1 Materials 14
2.3.2 Thin Film Fabrication, Profilometer, and UV-Vis Measurements 14
2.3.3 Neutron Reflectometry 15
2.3.4 Grazing Incidence Wide-Angle X-ray Scattering 16
2.3.5 Conductivity Measurements 16
2.4 Results and Discussion 16
2.5 Conclusion 24
2.6 Conficts of Interest 24
2.7 Acknowledgments 24

3 Investigation of Hierarchical Structure Formation in Merocyanine Photovoltaics **31**
3.1 Preface 32
3.2 Introduction 32

3.3 Methods . . . 34
3.3.1 Sample Processing: . . . 34
3.3.2 UV-Vis: . . . 34
3.3.3 Single Crystal XRD: . . . 34
3.3.4 GIXRD: . . . 35
3.3.5 SANS: . . . 35
3.3.6 AFM: . . . 35
3.4 Results . . . 35
3.5 Discussion . . . 49
3.6 Conclusions . . . 52
3.7 Supporting Information . . . 52
3.8 Acknowledgments . . . 53
3.9 Conflicts of Interest . . . 53

4 Anion Exchange Doping: Tuning Equilibrium to Increase Doping Efficiency in Semiconducting Polymers 59
4.1 Preface . . . 60
4.2 Introduction . . . 60
4.3 Results and Discussion . . . 61
4.4 Acknowledgments . . . 69
4.5 Supporting Information . . . 69

A Supporting information for "Additive Solution Deposition of Multi-Layered Semiconducting Polymer Films for Design of Sophisticated Device Architectures" 74
A.1 SLD Volume Balance . . . 75
A.2 Grazing Incidence Wide Angle X-ray Scattering . . . 77

B Supporting information for "Investigation of Hierarchical Structure Formation in Merocyanine Photovoltaics" 86
B.1 Synthesis . . . 87

B.1.1 I7TBT . . . 87
B.1.2 I9TBT . . . 88
B.2 Ultraviolet Photoelectron Spectroscopy . . . 90
B.3 UV-Vis . . . 91
B.4 Crystal Stacking . . . 93
B.5 Grazing Incidence X-ray Diffraction . . . 93
B.6 Small-Angle Neutron Scattering . . . 119
B.6.1 Volume Balance . . . 119
B.7 Atomic Force Microscopy . . . 126

C Supporting information for "Anion Exchange Doping: Tuning Equilibrium to Increase Doping Efficiency in Semiconducting Polymers" 129
C.1 Molecular Structure of Materials . . . 130
C.2 Experimental Methods . . . 130
C.3 PDPP-2T Synthesis . . . 132
C.3.1 Materials and Methods . . . 132
C.3.2 PDPP-2T . . . 132
C.4 UV-Vis-NIR Full Gaussian Fits . . . 133
C.5 PDPP-2T $FeCl_3$ Absorption Discussion . . . 143
C.6 Fractional Doping Level (Θ) and Isotherm Fitting . . . 143
C.6.1 PDPP-2T Θ and Isotherm Fitting . . . 144
C.6.2 Anion Exchange Doping Isotherm Derivation . . . 145
C.6.3 % TFSI Calculation . . . 148
C.7 Discussion of ΔG° . . . 149
C.8 P3HT Anion Exchange (Assuming one monomer site) . . . 149
C.9 Anion Exchange Isotherm Site Size Comparison . . . 152
C.10 Discussion of Θ: Is $\Theta \propto P1$ or $\propto \sum(P1, P2, P3)$? . . . 153
C.11 Anion Exchange Simulations . . . 157
C.12 Extra UV-Vis-NIR Tests . . . 158
C.13 Sheet Resistance IV Curves and Discussion of Conductivity Enhancements . . . 161

C.14 Discussion of Carrier Density 164
C.15 X-ray Photoelectron Spectroscopy 165

D Unfinished Work **172**

D.1 Preamble 173
D.2 Small Angle Neutron Scattering of P3HT Nanofiber Dispersions 173
D.2.1 Conclusions 173
D.3 Grazing Incidence Small Angle Neutron Scattering 179
D.4 Small Angle Neutron Scattering of P3HT:PEO Melts 181
D.5 Fabrication of Blade Coater 186
D.6 Upscaling Photothermal Lithography 186
D.6.1 Fabrication of Projection Photothermal Lithography Microscope 188
D.6.2 Effects of Binary Solvent Quality on Photothermal Patterning 191
D.6.3 Photomask Designs 194
D.6.4 Smallest Obtained Feature Size from Projection Photothermal Patterning 202
D.7 Patterning P3HT/ITIC Bulk Heterojunction 203

LIST OF FIGURES

2.1 **Multilayer DISC patterning:** This schematic displays the additive solution deposition of multiple SP layers. (1) shows an initial stack of three alternating layers of doped polymer on a substrate. In (2) a fourth undoped polymer layer is deposited from solution and (3) the solvent is removed. In (4) the top polymer layer is sequentially doped from solution and (5) the solvent is removed. Step (6) demonstrates the chemical process to dedope the polymer film and (7) depicts the final stack of neutral polymer layers. 13

2.2 (a) Processing steps for the single P3HT film sequentially swollen with saturated d-AN vapor and d-CB vapor, then doped with F4TCNQ and sequentially swollen with d-AN vapor and d-CB vapor. (b) Neutron reflectivity data and best fit (c) vertical scattering length density profiles from NR fits. 17

2.3 (a) Neutron Reflectivity from a four layered doped P3HT film with alternating deuterated and protonated layers before and after soaking in CB bath for 4 hours, (b) vertical scattering length density profiles from NR fits. 20

2.4 Two-point vertical conductivity measurements of doped and dedoped single, double, and quadruple P3HT layer devices. 23

3.1 Chemical structures of compounds used in this study: a) a series of MC featuring an indoline donor with varying hydrocarbon side chain length (R) and a tert-butyl-thiazole acceptor, labeled I*n*TBT. b) $PC_{61}BM$. 36

3.2 UV-vis absorption spectra of I*n*TBT:PCBM films normalized to the common peak at 594 nm. 37

3.3 (a) JV curves and (b) extracted power conversion efficiencies from 3:2 by wt. I*n*TBT:PCBM devices. 39

3.4 GIXRD: Ratio of prominent I*n*TBT peak over prominent PCBM peak (peak heights and peak integrations) in mixed 3:2 by wt. I*n*TBT:PCBM films. 42

3.5 a) Small Angle Neutron Scattering data (offset for clarity) of I*n*TBT:PCBM films. I*n*TBTs with linear side chain were fit to an ellipsoidal form factor. IHDTBT was fit with a fuzzy sphere form factor at low Q and a spherical form factor at high Q, the combined fit is plotted. b)(Left axis) Scattering length density (SLD) contrast (black squares) between the form factor and surrounding matrix. (Right axis) Mean short (R_S)(blue squares) and long (R_L)(red dots) ellipsoidal radii from linear I*n*TBT fits. For IHDTBT, the mean fuzzy sphere radii is plotted as (R_L), and the spherical radii is plotted as (R_S). 45

3.6 Atomic Force Microscope (a) height images with mean square roughness (R_{MS}) and (b) phase images of I*n*TBT:PCBM films. 46

3.7 (Left) Mean grain size from AFM phase images of I*n*TBT:PCBM films. Grains are defined by a cutoff phase shift; red (I*n*TBT-rich) grains have greater than 4° phase shift and blue (PCBM-rich) grains have less than -4° phase shift. (Right) Root mean square roughness (R_{MS}) from corresponding AFM height images. . 47

3.8 Illustration representing the bulk morphological differences observed between I8TBT:PCBM, I9TBT:PCBM, and I11TBT:PCBM films. L_C is coherence length from GIXRD, R_S and R_L are the short and long ellipsoidal radii from SANS. . 49

4.1 a) Illustration of $FeCl_3$ doping P3HT sites with equilibrium constant K_I. b) and c) illustrates $FeCl_3$ doping P3HT sites, where $FeCl_3^-$ is subsequently exchanged by $TFSI^-$ with equilibrium constant K_{II}. UV-Vis-NIR absorption spectra for P3HT films doped with various $FeCl_3$ solution concentrations and d) 0 mM, e) 50 mM, and f) 100 mM LiTFSI solutions, respectively. 62

4.2 a) 3D and b) 2D scatter plots of Θ extracted from UV-Vis-NIR and corresponding anion exchange isotherm fit, c) shows the Θ fit contour with respect to the prepared $FeCl_3$ and LiTFSI concentrations, and d) depicts the percentage of doped P3HT sites with $TFSI^-$ anions. The gray region in d) corresponds to the range in which no P3HT sites are doped. 64

4.3 UV-Vis-NIR absorption spectra of PDPP-2T films sequentially doped with varying $FeCl_3$ concentrations and either 0 mM a) or 100 mM b) of LiTFSI. All spectra are fit with with cumulative Gaussian fits (dashed lines) to determine state populations. c) Depicts energy transitions for p-doped alternating D/A copolymers. d) Depicts a 2D scatter plot of Θ extracted from the absorption data and the corresponding Anion Exchange Isotherm fit. e) Shows fit Θ for PDPP-2T as a function of the $FeCl_3$ and LiTFSI concentrations, and f) depicts the percentage of doped polymer sites with $TFSI^-$ anions. The gray region in f) corresponds to the range in which no polymer sites are doped. 65

4.4 a) Four-point probe conductivity of P3HT films with respect to $FeCl_3$ solution concentration at various LiTFSI concentrations, and one conductivity series of PDPP-2T films with respect to $FeCl_3$ solution concentrations with 100 mM LiTFSI. b) Conductivity (filled symbols) and mobility (empty symbols) as a function of charge density. 67

A.1 Normalized UV-Vis absorption profile of neat and doped P3HT films under saturated AN and CB vapor environments 76

A.2 (a) In-plane (Q_{xy}) and (b) out-of-plane (Q_z) GIWAXS of neat and dedoped P3HT film. 77

A.3 2D GIWAXS patterns of (a) neat P3HT and (b) chemically dedoped P3HT. (Note: Q_z is approximate) 78

A.4 Device architecture for two-point conductivity test 78

A.5 IV Data of doped single layer P3HT film from several substrates, 6 electrodes per substrate. Omitted data from electrodes where good electrical connection could not be obtained. 79

A.6 IV Data of doped double layer P3HT film from several substrates, 6 electrodes per substrate. Omitted data from electrodes where good electrical connection could not be obtained. 80

A.7 IV Data of doped quadruple layer P3HT film from several substrates, 6 electrodes per substrate. Omitted data from electrodes where good electrical connection could not be obtained. 81
A.8 IV Data of dedoped single layer P3HT film from several substrates, 6 electrodes per substrate. Omitted data from electrodes where good electrical connection could not be obtained. 82
A.9 IV Data of dedoped double layer P3HT film from several substrates, 6 electrodes per substrate. Omitted data from electrodes where good electrical connection could not be obtained. 83
A.10 IV Data of dedoped quadruple layer P3HT film from several substrates, 6 electrodes per substrate. Omitted data from electrodes where good electrical connection could not be obtained. 84

B.1 I7TBT: (E)-2-(1-heptyl-3,3-dimethylindolin-2-ylidene)acetaldehyde (1) 87
B.2 I7TBT: 2-((Z)-4-tert-butyl-5-((E)-2-(1-heptyl-3,3-dimethylindolin-2-ylidene)ethylidene)thiazol-2(5H)-ylidene)malononitrile 88
B.3 I9TBT: (E)-2-(3,3-dimethyl-1-nonylindolin-2-ylidene)acetaldehyde (1) 88
B.4 I9TBT: 2-((Z)-4-tert-butyl-5-((E)-2-(3,3-dimethyl-1-nonylindolin-2-ylidene)ethylidene)thiazol-2(5H)-ylidene)malononitrile 89
B.5 UVvis absorption spectra of I8TBT solution in various solvents of varying polarity and a neat film for comparison. 92
B.6 Raw unnormalized UV-vis absorption spectra of InTBT:PCBM films. 92
B.7 GIXRD of PCBM Film. Each peak fit with Pseudo-Voigt. 94
B.8 GIXRD of I6TBT Film. Each peak fit with Pseudo-Voigt. 95
B.9 GIXRD of I6TBT:PCBM Film. Each peak fit with Pseudo-Voigt. 96
B.10 GIXRD of I7TBT Film. Each peak fit with Pseudo-Voigt. 98
B.11 GIXRD of I7TBT:PCBM Film. Each peak fit with Pseudo-Voigt. 99
B.12 GIXRD of I8TBT Film. Each peak fit with Pseudo-Voigt. 101
B.13 GIXRD of I8TBT:PCBM Film. Each peak fit with Pseudo-Voigt. 102
B.14 GIXRD of I9TBT Film. Each peak fit with Pseudo-Voigt. 104

B.15 GIXRD of I9TBT:PCBM Film. Each peak fit with Pseudo-Voigt. 105
B.16 GIXRD of I10TBT Film. Each peak fit with Pseudo-Voigt. 107
B.17 GIXRD of I10TBT:PCBM Film. Each peak fit with Pseudo-Voigt. 108
B.18 GIXRD of I11TBT Film. Each peak fit with Pseudo-Voigt. 110
B.19 GIXRD of I11TBT:PCBM Film. Each peak fit with Pseudo-Voigt. 111
B.20 GIXRD of I12TBT Film. Each peak fit with Pseudo-Voigt. 113
B.21 GIXRD of I12TBT:PCBM Film. Each peak fit with Pseudo-Voigt. 114
B.22 GIXRD of IHDTBT Film. Each peak fit with Pseudo-Voigt. 116
B.23 GIXRD of IHDTBT:PCBM Film. Each peak fit with Pseudo-Voigt. 117
B.24 Lognormal distribution of short ellipsoid radii. 122
B.25 Lognormal distribution of long ellipsoid radii. 123
B.26 IHDTBT SANS data fit with fuzzy spherical form factor at low Q and spherical form factor at high Q. 124
B.27 Gaussian distribution of the fuzzy sphere radii for IHDTBT fit. 125
B.28 Lognormal distribution of the blue grain sizes. 126
B.29 Lognormal distribution of the red grain sizes. 127

C.1 Chemical Structures of P3HT, PDPP-2T, $FeCl_3$, and LiTFSI. 130
C.2 Full UV-Vis-NIR spectral fits of P3HT films soaked in a solution various $FeCl_3$ concentrations in n-butyl acetate. 134
C.3 Full UV-Vis-NIR spectral fits of P3HT films soaked in a solution with 0.1 mM LiTFSI and various $FeCl_3$ concentrations in n-butyl acetate. 135
C.4 Full UV-Vis-NIR spectral fits of P3HT films soaked in a solution with 1 mM LiTFSI and various $FeCl_3$ concentrations in n-butyl acetate. 136
C.5 Full UV-Vis-NIR spectral fits of P3HT films soaked in a solution with 10 mM LiTFSI and various $FeCl_3$ concentrations in n-butyl acetate. 137
C.6 Full UV-Vis-NIR spectral fits of P3HT films soaked in a solution with 25 mM LiTFSI and various $FeCl_3$ concentrations in n-butyl acetate. 138
C.7 Full UV-Vis-NIR spectral fits of P3HT films soaked in a solution with 50 mM LiTFSI and various $FeCl_3$ concentrations in n-butyl acetate. 139

C.8 Full UV-Vis-NIR spectral fits of P3HT films soaked in a solution with 75 mM LiTFSI and various $FeCl_3$ concentrations in n-butyl acetate. 140
C.9 Full UV-Vis-NIR spectral fits of P3HT films soaked in a solution with 100 mM LiTFSI and various $FeCl_3$ concentrations in n-butyl acetate. 141
C.10 Full UV-Vis-NIR spectral fits of PDPP-2T films soaked in a solution with various $FeCl_3$ concentrations in n-butyl acetate. The unknown state is discussed in section S4. 141
C.11 Full UV-Vis-NIR spectral fits of PDPP-2T films soaked in a solution with 100 mM LiTFSI and various $FeCl_3$ concentrations in n-butyl acetate. 142
C.12 a) 3D and b) 2D scatter plots of Θ extracted from UV-vis-NIR and corresponding anion exchange isotherm fit, c) shows the Θ fit contour with respect to the prepared $FeCl_3$ and LiTFSI concentrations, and d) depicts the percentage of doped P3HT sites with $TFSI^-$ anions. The gray region in d) corresponds to the range in which no P3HT sites are doped. 150
C.13 Contour plot of residuals from Anion Exchange Isotherm Fit to P3HT θ extracted from UV-vis. 151
C.14 Comparison of the Θ fit using one P3HT monomer site size and a four P3HT monomer site size. 152
C.15 Comparison of the Θ fit using one P3HT monomer site size (colored lines) and a four P3HT monomer site size (black dashed lines). 153
C.16 3D scatter plot of Θ calculated from UV-Vis-NIR of doped P3HT films with respect to prepared $FeCl_3$ and LiTFSI concentrations, assuming 1) the population of holes is related to the sum of the P1, P2, and P3 integrals and 2) cation site size corresponds to four P3HT monomers. 154
C.17 2D scatter plot of Θ calculated from UV-Vis-NIR of P3HT films with respect to prepared $FeCl_3$ (at 100 mM LiTFSI), assuming 1) the population of holes is related to the sum of the P1, P2, and P3 integrals and 2) cation site size corresponds to four P3HT monomers. 155

C.18 a) Simulated Θ using the Anion Exchange Isotherm and c) corresponding percentage of doped polymer sites with exchanged anions for a P3HT film doped with a stronger dopant than $FeCl_3$ exchanged with an anion with a 40x larger K_2. b) Simulated Θ and d) corresponding percentage of doped polymer sites with exchanged anions for a polymer doped with a weaker dopant (K_1=0.5 mM^{-1}) and exchanged with an anion with a 40x larger K_2. Note: K_I and K_{II} are given in units of mM^{-1} 157
C.19 UV-Vis-NIR spectra of PDPP-2T film, before and after soaking in 100 mM LiTFSI in nBA. 159
C.20 High energy UV-Vis zoomed into $FeCl_3$ spectral peaks in doped P3HT films, and the absence of $FeCl_3$ peaks in doped PDPP-2T film. 160
C.21 IV curves from P3HT films doped with various $FeCl_3$ and LiTFSI concentrations 162
C.22 IV curves from PDPP-2T films doped with 0.5, 1, and 5 mM $FeCl_3$ and 100 mM LiTFSI concentrations 163
C.23 X-ray photoelectron spectroscopy of PDPP-2T film doped with 5 mM $FeCl_3$ and 100 mM LiTFSI in the range of iron and fluorine 166
C.24 X-ray photoelectron spectroscopy of PDPP-2T film doped with 5 mM $FeCl_3$ and 100 mM LiTFSI, full survey spectrum. 167

D.1 Temperature dependent SANS data of neutral and doped P3HT solutions. . . . 175
D.2 Fits to the Neutral P3HT SANS data. 176
D.3 Illustration of high temperature dissolved P3HT fit parameters. 177
D.4 Illustration of low temperature P3HT fiber fit parameters. 177
D.5 Temperature dependence UV-vis of 2mg/mL P3HT in 3:1 tol:oct solution as the solution is cooled down at a 20C/hr ramp rate, with 30 min soaks at 60, 40, and 20C. 178
D.6 Temperature dependence UV-vis of 2mg/mL P3HT in 3:1 tol:oct solution as the solution is heated up at a 20C/hr ramp rate, with 30 min soaks at 20, 40, and 60C. 179

D.7 GISANS data from a neat P3HT film swollen with dCB as a function of wavelength. 180
D.8 GISANS data from an F4TCNQ doped P3HT film swollen with dCB as a function of wavelength. 180
D.9 Illustration of phase segregation upon cooling a mixed P3HT/PEO melt. 181
D.10 (top) Temperature dependent SANS P3HT:PEO mixtures, fit with an ellipsoidal form factor. (bottom) Extracted ellipsoidal radii. 182
D.11 (top)Temperature dependent SANS P3HT:PEO mixtures, fit the lamellar peak at high Q. (bottom) Extracted P3HT Lamellar Spacing. 183
D.12 Illustration morphology extracted from SANS. P3HT ellipsoids surrounded by a matrix of mixed P3HT/PEO domains. 184
D.13 Extracted volume fraction of pure P3HT ellipsoidal domains and the volume fraction of P3HT in the mixed P3HT:PEO matrix. 185
D.14 Image of fabricated blade coater, including automatic linear stage actuator, and custom temperature controller. 186
D.15 Schematics of a) the first prototype of projection photothermal lithography setup and b) the final projection photothermal lithography microscope. 189
D.16 AFM height image of ghost pattern artifact. 190
D.17 AFM height images of P3HT films patterned with initial prototype equipment. Pattern depth is adjusted Solvent quality was tuned by the adjusting the mixing ratio THF and DCB. Three different exposure times 192
D.18 Dissolution Temperature of P3HT film, immersed in a binary solvent mixture of chlorobenzene (CB) and cyclohexanone(CHN). 193
D.19 AFM height images of patterned P3HT with DCB:CHN solvent ratios a) 20:80, b)25:75, c) 30:70. d) and e) depict AFM cross sections from the 25:75 and 30:70 ratio images respectively. 193
D.20 Hexagonal Matrix of 20um holes, 5um separation. 195
D.21 Hexagonal Matrix of 5um islands, 20um separation. 195
D.22 Simple Cubic Matrix of 20um holes, 5um separation. 195

D.23 Simple Cubic Matrix of 5um islands, 20um separation. 196
D.24 Simple Cubic matrix of 20x20um transistors, 20 um edges, 20um separation. . 196
D.25 Optical Grating 20um Slit, 12.5um spacing. 196
D.26 Optical Grating 20um slit, 30um spacing. 197
D.27 Trident transistor 1000um channel width, 20um channel length. 197
D.28 Doped Electrode Trident Transistor: 20um transistor length, 10220um transistor width. 197
D.29 Grating(nanowires): 200um slit, 20um spacing. 198
D.30 Grating (nanowires): 100um slit, 20um spacing. 198
D.31 Grating (nanowires): 200um slit, 10um spacing. 198
D.32 Grating(nanowires): 100um slit, 10um spacing. 199
D.33 Optical grating: 20um slit, 5um spacing. 199
D.34 Optical grating: 20um slit, 1um spacing. 199
D.35 Hexagonal matrix of 20um holes, 1um separation. 200
D.36 Hexagonal matrix of 10um holes, 1um separation. 200
D.37 Simple cubic matrix of targets, 20um diameter center transparent ring, 5um solid rings (10 total), 20um transparent separation, 50um spacing between targets. 201
D.38 Smallest achieved feature size. P3HT, 405nm 5W laser diode, new photomasks 203
D.39 a) Illustration of film deposition and patterning steps for creating a bulk heterojunction organic photovoltaic. b) Final desired OPV architecture. 204
D.40 Flourescence of 1000nm thick P3HT film, neat, with ITIC layer deposited ontop, and after thermally annealing at 100°C for 10 minutes. Measurements were made in reflection mode with light incident through both the glass interface (P3HT rich side), and the air interface (ITIC rich side). 205
D.41 Florescence of a 1000nm thick P3HT film, as deposited, exposed to MC, and thermally annealed. 206
D.42 UVvis of ITIC film, as deposited, annealed in glove box, or annealed in air. . . 207
D.43 UVvis of 500 nm blade coated P3HT film, with and without ITIC spun coat ontop. Note: film too thick for spectrometer range (see noise above 3.5 A.U.). . 208

D.44 AFM of Blade Coated 1000 nm thick P3HT film deposited from 3:1 CF:CB (blade height: 0.9mm, Acceleration: 200 mms^{-}2, Velocity: 30mms^{-1}, Stage Temperature 40C). Patterned with 445nm laser (Photomask: hexagonal lattice of 20μm holes with 5μm separation) through 10x Objective Lens, five 5s pulses (2s wait between pulses) 210
D.45 Scheme for transferring patterned film from transparent substrate to silicon substrate to perform SEM. 210
D.46 Cross section SEM image of P3HT:ITIC bilayer after zinc ALD. 211
D.47 SEM image of FIBed patterned P3HT:ITIC bilayer cross section. 212

LIST OF TABLES

2.1 Solvent volume fraction and percent film thickness increase obtained from NR fits. 19

2.2 P3HT and dedoped P3HT π-π stacking distance and lamellar spacing from grazing incidence wide-angle x-ray scattering. 22

3.1 Best performance data of I*n*TBT:PCBM OPVs in the standard device setup (composition 2:3). 40

3.2 Bragg's d-spacing and Scherrer's coherence length L_C extracted from most prominent I*n*TBT peak (in the range of 2θ $\sim$4-10°) from pure and mixed I*n*TBT:PCBM films. 42

3.3 Volume fraction of I7TBT and I8TBT in ellipsoidal and mixed domains obtained from SANS fits, and volume fraction of PCBM in mixed domains from sample preparation. 45

A.1 Preliminary Profilometer thickness measurements of thin films deposited from same processing conditions and at the time the NR films were made. 75

A.2 Scattering length densities of materials in model 75

B.1 Ionization energy of pure InTBT films obtained by UPS on films (thickness below 20 nm) on ITO/MoO_3. 91

B.2 Unit cell information extracted from single crystal XRD data. 93

B.3 I6TBT Peak location and d-spacing from GIXRD. 97

B.4 I6TBT:PCBM Peak location and d-spacing from GIXRD. 97

B.5 I7TBT Peak location and d-spacing from GIXRD. 100

B.6 I7TBT:PCBM Peak location and d-spacing from GIXRD. 100

B.7 I8TBT Peak location and d-spacing from GIXRD. 103

B.8 I8TBT:PCBM Peak location and d-spacing from GIXRD. 103

B.9 I9TBT Peak location and d-spacing from GIXRD. 106

B.10 I9TBT:PCBM Peak location and d-spacing from GIXRD. 106

B.11 I10TBT Peak location and d-spacing from GIXRD. 109
B.12 I10TBT:PCBM Peak location and d-spacing from GIXRD. 109
B.13 I11TBT Peak location and d-spacing from GIXRD. 112
B.14 I11TBT:PCBM Peak location and d-spacing from GIXRD. 112
B.15 I12TBT Peak location and d-spacing from GIXRD. 115
B.16 I12TBT:PCBM Peak location and d-spacing from GIXRD. 115
B.17 IHDTBT Peak location and d-spacing from GIXRD. 118
B.18 IHDTBT:PCBM Peak location and d-spacing from GIXRD. 118
B.19 Bragg's d-spacing and coherence length extracted from the PCBM peak from pure PCBM and mixed 2:3 InTBT:PCBM films. 119
B.20 Calculated scattering length density of pure domains. Based on crystal structure information. 121

C.1 Θ fit statistics. 149
C.2 Θ fit parameters for P3HT film, defining site size as one P3HT monomer or four P3HT monomers. 153
C.3 Comparison of Θ fit parameters for P3HT films, using either P1 or the sum of P1, P2, and P3 to define Θ. 156

D.1 Dissolved P3HT fit parameters. Showing the ensemble average chain width, height, contour length, and kuhn length. The dimensionless fractal parameter (D_f) fits to the low Q region of the SANS data. 177
D.2 P3HT Fiber fit parameters. Showing the ensemble average fiber width, height, contour length, and kuhn length. 178
D.3 Description of designed photomasks. 194

ABSTRACT

Correlating Processing to Structure-Function Relationships of Organic Semiconductors

Organic semiconductors (OSCs), including semiconducting small molecules (SSMs), polymers (SPs) and carbon nanotubes (s-CNTs), are a versatile class of materials. Their compatibility with low-cost solution processing techniques and potential for producing lightweight, flexible, electronic devices has already begun to revolutionize several technologies. Typical organic devices, including thermoelectrics (OTEs), photovoltaics (OPVs), field-effect transistors (OFETs), and light-emitting diodes (OLEDs) can be fabricated with flexible OSCs, and has spawned several novel applications including wearable electronics, foldable low-temperature thermoelectrics, and flexible displays. While the future of OSC technology is promising, several structure-property relationships remain poorly understood, likewise the link between molecular doping level and OSC carrier density is underdeveloped. In my dissertation, I demonstrate new solution processing techniques, connect processing methods to structure formation using X-ray and neutron scattering probes, and correlate processing and structure formation to vital optoelectronic properties. I begin by demonstrating an additive solution process for depositing multiple layers of mutually soluble SP films without disrupting layer continuity. I use neutron reflectometry to quantify film thickness changes during processing steps and demonstrate the fabrication of a 4-layered device. Next, I perform a hierarchal structural analysis of bulk heterojunction SSM OPVs using grazing incidence X-ray diffraction and small angle neutron scattering, and correlate peak OPV performance to an inflection in film crystallinity and phase purity. Third, I refined a doping process, termed anion exchange doping, and show its effectiveness for doping high ionization energy polymers. During which I developed the framework for quantifying and predicting doping levels and carrier densities in SPs.

ACKNOWLEDGMENTS

I would like to thank the many people; mentors, teachers, emotional supporters; who've helped support me along the fulfilling – and often tenuous – journey of completing my dissertation. First and foremost, I would like to thank my parents, Stacy and Lloyd, my grandparents, Norma and Jim, and Loretta and Jack, and my sisters, Morgan, Sydney, and Taylor, for their guidance over the years. I would not be the man that I am today without their love and support. Next, I would like to thank my PhD advisor, Dr. Adam Moulé, for continuously pushing me to expand the limit of my capabilities, for always supporting my ideas no matter how strange/wild they sound, and always providing exceptional guidance when needed. I could always count on Adam to causally show up in the student offices on a random Thursday afternoon and turn the rest of the day into a (sometimes aimless) discussion about whatever science was on his mind; although frustrating at times (deadlines are deadlines), it was almost always a nice break and kept science fun. I'd also like to thank Adam for giving me my first opportunity to leave the United States; working in Germany and Israel allowed me to recognize the "cultural bubble" that encompasses the United States. Next, I'd like to thank the Moulé research group for countless scientific discussions and emotional support, particularly Dr. Tommy Harrelson, Meghna Jha, and Dr. Zaira Bedolla-Valdez. I'd like to thank my army of undergraduate researchers for aiding many projects in the lab, specifically Justin Mulvey, Owen Lee, and Alice Fergerson. I'd also like to thank a few of my friends that kept me sane during my PhD, including but not limited to Alecksey, Dr. Jennifer Staton, and Dr. Antonio Rossi. And saving the best for last, I would like to thank my partner, Lauren Klein, for everything she has done for me. Honestly, meeting her has been the highlight of my time at Davis. She makes the worst times bearable, and she somehow makes the best times even better. I am lucky to have met her and continue to have her in my life.

Chapter 1

Introduction

1.1 Preamble

My dissertation contains three of my publications. Each publication focuses on developing new processing techniques and connects structural properties to optoelectronic functions in organic semiconductors. Each chapter is seemingly unrelated beyond this central theme. The purpose of this section is to provide a broad introduction to organic semiconductors, while each chapter contains more focused introductory background information.

1.2 Introduction

Over the past few decades, organic semiconductors (OSCs) have received enormous attention due to their compatibility with low-cost, large-area, solution processing techniques and their unique combination of optoelectronic and mechanical properties that enable flexible electronics. OSCs have shown promise as a key component in several electronic applications including organic light emitting diodes (OLEDs), organic field-effect transistors (OFETs)[1, 2, 3, 4], organic photovoltaics (OPVs))[5, 6, 7], microfluidic devices[8], and biosensors[9, 10, 6]. As of 2019, the global organic electronics market size reached $46.12 billion and is expected to grow to $145.3 billion by 2026.[11]

At a fundamental level, OSCs are a collection of conjugated, carbon-based molecules and polymers that derive their semiconducting properties from alternating single and double bonds.[12] This alternating structure causes a delocalization of π-orbitals and lowers the energy difference between the electronic ground and excited states. This small energy difference ($<$ 3eV), typically referred to as a 'band gap', defines a material as a semiconductor and gives rise to its unique optical and electronic properties.[13] For context, materials with no band gap are considered electronic conductors and materials with large band gaps ($>$ 3eV) are considered electronic insulators. Unlike typical rigid inorganic semiconductors, where all elements are connected through strong covalent bonds, OSCs are dominated by weak intermolecular van der Waals (London Dispersion) interactions. This enables the formation of mechanically flexible, semi-crystalline and amorphous networks in solid state. The rich chemical flexibility of OSCs allows myriad possible chemical modifications for tuning optoelectronic band gap and hierarchical structure formation ($\mathring{A}$-μm), while also making it incredibly challenging to predict

specific solid-state morphologies.[14, 15]

Solid-state morphology, in general, refers to any observable structural motif in a material in solid-state (ie. not liquid, gas, or dissolved into solution). OSCs form very complex solid-state morphologies and require a combination of state-of-the-art structural characterization techniques to obtain a comprehensive analysis. These techniques typically involve various forms of X-ray, electron, and neutron scattering probes.[16, 17, 18, 19] Specific measurable structural properties include crystal structure, percent crystallinity (amorphous vs crystalline content), paracrystallinity (the amount of disorder within a crystalline domain), crystalline orientation, domain size distribution, and domain composition (in bulk and near film interfaces).[20, 21, 22] To further complicate structural characterization, OSC morphologies are highly sensitive to deposition and post deposition processing. Common solution deposition techniques, including spin coating and blade coating, often create metastable solid-state morphologies.[23] While, exposure to external stimuli, typically thermal or solvent annealing, causes changes to all the above listed structural properties. Therefore, it is vital to control and correlate the exact processing conditions of a given OSC film to its measured morphological properties.

The optoelectronic properties of a given OSC can also be tuned through chemical doping. Unlike doped inorganic semiconductors, where individual atoms are substituted with either an electron withdrawing (p-type) or donating (n-type) atom, chemical doping of OSCs occurs by introducing molecular impurities. These impurities undergo spontaneous charge transfer, either stealing (p-type) or donating (n-type) an electron from/to an OSC. For p-type charge transfer to be spontaneous, the molecular dopant must have a larger electron affinity (EA) than the OSC's ionization energy (IE). Likewise, for spontaneous n-type charge transfer, the molecular dopant must have a lower IE than the OSC's EA. Molecular doping causes multiple observable changes to OSC material properties.[24] (1) It increases charge carrier densities which, in turn, can increase OSC film conductivities by > 7 orders of magnitude. (2) As carriers are introduced to the OSC the intrinsic optical absorption and photoluminescence quench while broad red shifted carrier (polaron) absorptions grow in. Finally, (3) the charges introduced by molecular doping form dipoles between the charged OSCs and oppositely charged dopants. This introduces polar intermolecular interactions into the material and significantly changes the miscibility/solubility

of the OSC with a given solvent system.

This provides a good transition into my dissertation. Chapter 2 introduces a novel solution based deposition process that enables the multilayer deposition of mutually soluble semiconducting polymers (SPs).[25] This process takes advantage of dopant induced solubility changes in SPs to prevent mixing between sequentially deposited polymer layers. Multi-layered films are inherent in all modern day electronic devices. Hole transporting layers are most relevant to this new process. Many OLEDs and OPVs use the polar polymer PEDOT:PSS as their hole transporting layer. PEDOT:PSS is non-miscible with the majority of SPs, making it insoluble in the conventional nonpolar/polarizable solvents used to deposit the SPs. This makes it possible to sequentially deposit active layers on it without inducing mixing. This new multilayer deposition process expands the list of SPs available for vertically layered organic devices by providing a method for tuning SP solubility. In the publication, I use neutron reflectometry to quantify film thickness changes during processing steps and demonstrate the fabrication of a four layered device.

Chapter 3 provides a hierarchal structural analysis of a series of bulk heterojunction films and correlates domain size and purity to OPV efficiency.[26] Bulk heterojunction OPVs are composed of a mixture of two OSCs, an electron donor and an electron acceptor. When a photon enters the film and is absorbed, it creates an exciton. The exciton must diffuse to a donor/acceptor interface before dissociating into a free hole and electron. The electron (hole) then travels through the acceptor (donor) phase until it can be collected at an electrode. The solid state morphology of these donor/acceptor mixtures has an enormous impact on film optoelectronic properties. Domain size and purity are particularly critical for optimizing exciton dissociation and charge carrier transport. In this publication, I study a series of novel chemically modified electron donor molecules called merocyanines, coupled with the conventional acceptor molecule, PCBM. Merocyanines are a class of small molecules composed of an electron donating group connected to an electron withdrawing group through a conjugated carbon-carbon double bond. These kind of molecules are typically referred to as donor-acceptor (D-A) molecules. D-A molecules tend to form strong dipoles and often couple to neighboring D-A molecules. This causes the formation of large crystalline domains, inhibits mixing with accep-

tor molecules in a BHJ, and limits OPV performance. This chapter demonstrates that domain size and purity, and in turn OPV performance, can be optimized by chemically modifying the merocyanine aliphatic side chain length. I use grazing incidence X-ray diffraction and small angle neutron scattering to correlate an inflection in crystallinity, phase purity, and domain size to a peak in OPV performance.

In chapter 4, I refine an anion exchange doping process and demonstrate its effectiveness for doping high IE polymers.[27] This process works by immersing a SP film in a solution with a molecular dopant and more abundant electrolyte. The solvent system used must be orthogonal to the SP to prevent the film from dissolving, while remaining miscible with both the dopant and the electrolyte. After the film is immersed, the dopant enters the film, charge transfers with the SP, then gets exchanged with the more abundant electrolyte anion. I demonstrate that anion exchange can increase an SP film doping level by up to 70% at a given dopant/electrolyte concentration. In this publication I developed a simple thermodynamic isotherm for quantifying and predicting equilibrium doping levels and carrier densities in SPs. This chapter is particularly impactful in the field of OSCs, as it demonstrates maximum conductivity records (as of 2020) for two semiconducting polymer systems and enables p-type doping of polymers that have previously been undopable due to their high IE.

During my PhD, I also collected a large ensemble of unpublished data for several collaborative projects. Most of which are presented in Appendix D. I am currently preparing three manuscripts for publication. The first is a follow-up on my anion exchange research. It focuses on addressing how anion exchange influences solid state morphology and doping stability in donor-acceptor copolymers. In the second, I develop a new scalable patterning process called 'Projection Photothermal Lithography'. This process enables rapid high resolution patterning of SP films with sub-micron resolution. Finally, the third focuses on thermal and electronic transport of molecularly doped semiconducting single walled carbon nanotubes. I collected the data for this publication during a six month National Science Foundation internship at the National Renewable Energy Laboratory in 2020. I expect all three of these manuscripts to publish by the end of 2021.

REFERENCES

[1] G. Orecchini, R. Zhang, J. Agar, D. Staiculescu, M. M. Tentzeris, L. Roselli, and C. P. Wong, "Inkjet printed organic transistors for sustainable electronics," in *2010 Proceedings 60th Electronic Components and Technology Conference (ECTC)*, pp. 985–989, June 2010.

[2] J. S. Chang, A. F. Facchetti, and R. Reuss, "A circuits and systems perspective of organic/printed electronics: Review, challenges, and contemporary and emerging design approaches," *IEEE Journal on Emerging and Selected Topics in Circuits and Systems*, vol. 7, pp. 7–26, March 2017.

[3] G. Mattana, A. Loi, M. Woytasik, M. Barbaro, V. Nol, and B. Piro, "Inkjet-printing: A new fabrication technology for organic transistors," *Advanced Materials Technologies*, vol. 2, no. 10, p. 1700063, 2017.

[4] H. Sirringhaus, "25th anniversary article: Organic field-effect transistors: The path beyond amorphous silicon," *Advanced Materials*, vol. 26, no. 9, pp. 1319–1335, 2014.

[5] S.-I. Na, S.-S. Kim, J. Jo, S.-H. Oh, J. Kim, and D.-Y. Kim, "Efficient polymer solar cells with surface relief gratings fabricated by simple soft lithography," *Advanced Functional Materials*, vol. 18, no. 24, pp. 3956–3963, 2008.

[6] S. Park, S. W. Heo, W. Lee, D. Inoue, Z. Jiang, K. Yu, H. Jinno, D. Hashizume, M. Sekino, T. Yokota, K. Fukuda, K. Tajima, and T. Someya, "Self-powered ultra-flexible electronics via nano-grating-patterned organic photovoltaics," *Nature*, vol. 561, no. 7724, pp. 516–521, 2018.

[7] K. S. Nalwa, J.-M. Park, K.-M. Ho, and S. Chaudhary, "On realizing higher efficiency polymer solar cells using a textured substrate platform," *Advanced Materials*, vol. 23, no. 1, pp. 112–116, 2011.

[8] G. Jenkins, Y. Wang, Y. L. Xie, Q. Wu, W. Huang, L. Wang, and X. Yang, "Printed elec-

tronics integrated with paper-based microfluidics: new methodologies for next-generation health care," *Microfluidics and Nanofluidics*, vol. 19, no. 2, pp. 251–261, 2015.

[9] S. R. A. Ruth, V. R. Feig, H. Tran, and Z. Bao, "Microengineering pressure sensor active layers for improved performance," *Advanced Functional Materials*, vol. 30, no. 39, p. 2003491, 2020.

[10] S. Park, Y. J. Kang, and S. Majd, "A review of patterned organic bioelectronic materials and their biomedical applications," *Advanced Materials*, vol. 27, no. 46, pp. 7583–7619, 2015.

[11] M. Malaga, "Global organic electronics market by material, application, and region: Industry analysis and forcast 2020-2026," tech. rep., Marqual IT Solutions Pvt. Ltd, 2020.

[12] M. Jaiswal and R. Menon, "Polymer electronic materials: a review of charge transport," *Polymer International*, vol. 55, no. 12, pp. 1371–1384, 2006.

[13] R. E. Hummel, *Electronic Properties of Materials*. Springer, 4 ed., 2011.

[14] S. R. Forrest, *Organic Electronics Foundations to Applications*. Oxford University Press, Oct. 2020.

[15] X. Guo, M. Baumgarten, and K. Mllen, "Designing -conjugated polymers for organic electronics," *Progress in Polymer Science*, vol. 38, no. 12, pp. 1832–1908, 2013. Topical issue on Conductive Polymers.

[16] D. I. S. L. A. Feigin, *Structure Analysis by Small-Angle X-Ray and Neutron Scattering*. Springer, 1987.

[17] I. Toyoko, K. Toshiji, F. Michihiro, and T. Naoya, *Neutrons in Soft Matter*. Wiley, 2011.

[18] J. Penfold and R. K. Thomas, "The application of the specular reflection of neutrons to the study of surfaces and interfaces," *Journal of Physics: Condensed Matter*, vol. 2, no. 6, p. 1369, 1990.

[19] W. H. Bragg and W. L. Bragg, "The reflection of x-rays by crystals," *Proc. Roy. Soc. London*, vol. 88, no. 605, pp. 428–438, 1913.

[20] J. Rivnay, R. Noriega, R. J. Kline, A. Salleo, and M. F. Toney, "Quantitative analysis of lattice disorder and crystallite size in organic semiconductor thin films," *Phys. Rev. B*, vol. 84, p. 045203, Jul 2011.

[21] A. L. Patterson, "The scherrer formula for x-ray particle size determination," *Phys. Rev.*, vol. 56, pp. 978–982, Nov 1939.

[22] C. Poelking and D. Andrienko, "Effect of polymorphism, regioregularity and paracrystallinity on charge transport in poly(3-hexylthiophene) [p3ht] nanofibers," *Macromolecules*, vol. 46, pp. 8941–8956, Nov. 2013.

[23] Y. Diao, L. Shaw, Z. Bao, and S. C. B. Mannsfeld, "Morphology control strategies for solution-processed organic semiconductor thin films," *Energy Environ. Sci.*, vol. 7, pp. 2145–2159, 2014.

[24] I. E. Jacobs and A. J. Moulé, "Controlling molecular doping in organic semiconductors," *Advanced Materials*, vol. 29, no. 42, pp. 1703063–n/a, 2017. 1703063.

[25] T. L. Murrey, K. Guo, J. T. Mulvey, O. A. Lee, C. Cendra, Z. I. Bedolla-Valdez, A. Salleo, J.-F. Moulin, K. Hong, and A. J. Moulé, "Additive solution deposition of multi-layered semiconducting polymer films for design of sophisticated device architectures," *J. Mater. Chem. C*, vol. 7, pp. 953–960, 2019.

[26] T. L. Murrey, D. Hertel, J. Nowak, R. Bruker, T. Limbck, J. Neudrfl, S. Rth, J. Schelter, S. Olthof, A. Radulescu, A. J. Moul, and K. Meerholz, "Investigation of hierarchical structure formation in merocyanine photovoltaics," *J. Phys. Chem. C*, vol. 124, pp. 19457–19466, Sept. 2020.

[27] T. L. Murrey, M. A. Riley, G. Gonel, D. D. Antonio, L. Filardi, N. Shevchenko, M. Mascal, and A. J. Moul, "Anion exchange doping: Tuning equilibrium to increase doping efficiency in semiconducting polymers," *J. Phys. Chem. Lett.*, vol. 12, pp. 1284–1289, Feb. 2021.

Chapter 2

Additive Solution Deposition of Multi-Layered Semiconducting Polymer Films for Design of Sophisticated Device Architectures

2.1 Preface

In this chapter, I am reprinting an article I wrote on how to fabricate multilayered semiconducting polymer films; DOI: 10.1039/C8TC05652H. Many organic electronic devices require vertically layered structures to operate. This manuscript demonstrates an additive solution process for depositing multiple layers of semiconducting polymer (SP) films by controlling film solubility with molecular dopants. During multi-layer deposition the bottom layers are exposed to a series of solvent environments that swell the SP films. We use neutron reflectometry (NR) to quantify the film thickness change and solvent content during solvent exposure in a single poly-3-hexylthiophene (P3HT) layer. The film thickness increases by 40-80% with exposure to good solvents. Four layer thin-films composed of alternating protonated and deuterated P3HT layers were additively coated from solution. NR measurements reveal high individual layer purity and that extensive solvent soaking induces no mixing between layers. Finally, two-point conductivity measurements demonstrate that P3HT:P3HT layer interfaces have no effect on vertical conductivity. This facile process enables additive layering of mutually soluble SP films and can be used to design novel electronic device architectures.

2.2 Introduction

Semiconducting polymers (SPs) have received enormous attention due to low-cost scalable solution-processing, and the potential for creating light-weight flexible electronic devices.[1] Most working organic devices consist of several layers of material, each having a specific optical and/or electronic function. One universal design constraint for complicated device architectures, like organic field effect transistors (OFETs), organic photovoltaics (OPVs) and red-green-blue organic light emitting diode (OLED) displays is that they require multiple components patterned laterally and vertically to operate.[2, 3, 4] Currently, many of these components are comprised of non-flexible inorganic materials. Typical OFETs have an organic channel and inorganic source, drain, and gate electrodes.[3, 4] In order to move towards flexible all organic electronic devices, there is a need to develop high precision vertical and lateral patterning methods that are compatible with solution processing. Until now, solution processing multiple layers of SP's has been difficult because most SP's are soluble in similar solvents; coating a second

layer dissolves the first layer. Thus, there is a need to develop a multilayer solution processing method that is compatible with a variety of SP's.

Unlike small molecules, polymers cannot be evaporated into multilayers.[5] One previously demonstrated method for creating multiple SP layers is by lamination. This process involves coating an SP layer onto a sacrificial substrate like poly(3,4ethylenedioxythiophene):polystyrene sulfonate (PEDOT:PSS) or poly(sodium 4−styrenesulfonate) (PSSNa)) then dissolving the substrate in water.[6, 7] Water is a poor solvent for most SPs so the film is left floating on the water's surface, available to be placed onto another SP film. This method is useful for laboratory experiments but is not compatible with high-throughput scalable solution processing techniques because it forms inconsistent contact area between the two films, leading to small bi-layer areas. A more robust method for vertical patterning utilizes a stamping technique. A polydimethylsiloxane (PDMS) stamp can mechanically bind to a film, lift it off a poorly wetted substrate, and deposit the film onto a different SP film. This process enables both vertical and lateral patterning of polymer films and has been used to fabricate OFETs, OPVs, and OLED displays.[8, 9, 10] Drawbacks to stamping techniques include mechanical damage, structural imperfections, and incompatibility with high throughput coating.[11]

The Moulé group recently demonstrated a patterning technique that enables lateral patterning of SPs and dopants in thin films, called dopant induced solubility control (DISC).[12, 13] For DISC patterning, molecular p-type dopants like 2,3,5,6-Tetrafluoro-7,7,8,8- tetracyanoquinodimethane (F4TCNQ) are sequentially introduced into a SP film using an orthogonal solvent. For example, a poly(3-hexylthiophene-2,5-diyl) (P3HT) film can be deposited from chlorobenzene (CB) then sequentially doped from a poor solvent for the polymer, such as acetonitrile (AN).[14, 15] The choice of orthogonal solvent can be optimized by the degree in which it swells the polymer film. The solvent must swell the polymer to allow the dopant to diffuse through the entire film. Under specific processing conditions P3HT/F4TCNQ systems form charge transfer (CT) states.[16] However, in the P3HT/F4TCNQ system explored in this manuscript the dopants undergo integer charge transfer with the polymer leaving a dopant anion and a cationic hole state on the polymer.[17, 15] The doped polymer is rendered insoluble by the charged states[12] and can be patterned laterally by exciting a photoinduced reaction between

the F4TCNQ and tetrahydrofuran (THF).[18] While submersed in THF the dedoped polymer dissolves into the solvent leaving a negative pattern in the film with smallest feature size on the order of the patterning wavelength.[13, 19] Since the doped polymer is insoluble and stable in solution over days, DISC patterning can easily be adapted to other coating methods, like blade or roll coating. Here we demonstrate that DISC processing steps can also be used to create a multi-layer SP film with facile solution deposition from common solvents. In order to validate this technique for creating sophisticated layered device architectures, it is critical to quantify whether sequential solvent processing steps introduce mixing between layers.

Figure 2.1 shows a schematic of the additive solution processing method demonstrated here. In step (1) a multi-layer stack of N p-doped P3HT layers has already been deposited. Next, a layer of P3HT is coated on top from a good solvent for P3HT. For this study we exclusively spin coated the P3HT from CB. In step (2) the addition of P3HT solution causes the preexisting doped layers to swell with solvent. Next in step (3), the solvent evaporates leaving a new undoped P3HT layer on top of the doped P3HT layer stack. In order to render the new layer insoluble, (4) a dopant, like F4TCNQ, is introduced to the film in an orthogonal solution, like AN. Presumably, the AN swells all of the polymer layers by some amount since we know that the solvent can carry a dopant several hundreds of nm into the film. Any anhydrous orthogonal solvent for P3HT will work as a carrier solvent for the dopant. Anhydrous solvents are necessary because H_2O and/or base will react with F4TCNQ and other strong electron acceptors. In previous experiments methylene chloride, cyclohexanone, and alcohols were used to introduce F4TCNQ to polymer films. (5) The orthogonal solvent evaporates leaving a multi-layer stack of $N+1$ doped P3HT films. At this point another film layer could be deposited by repeating steps 1 through 5. Alternatively, (6) all of the dopants could be deactivated by reacting F4TCNQ with a primary amine.[19] A typical dedoping solution is 10 vol% 1-butylamine and 90 vol% cyclohexanone, acetone, or AN. Again these orthogonal solvents are expected to swell all of the P3HT layers. Most of the deactivated dopant molecules are removed into the dedoping solution since the reaction product of F4TCNQ with 1-butylamine is more soluble than F4TCNQ (full dedoping takes 15 minutes).[19] (7) The final sample is a stack of $N+1$ intrinsic P3HT layers.

Creating a four layer stack of doped films using the DISC processing steps requires that

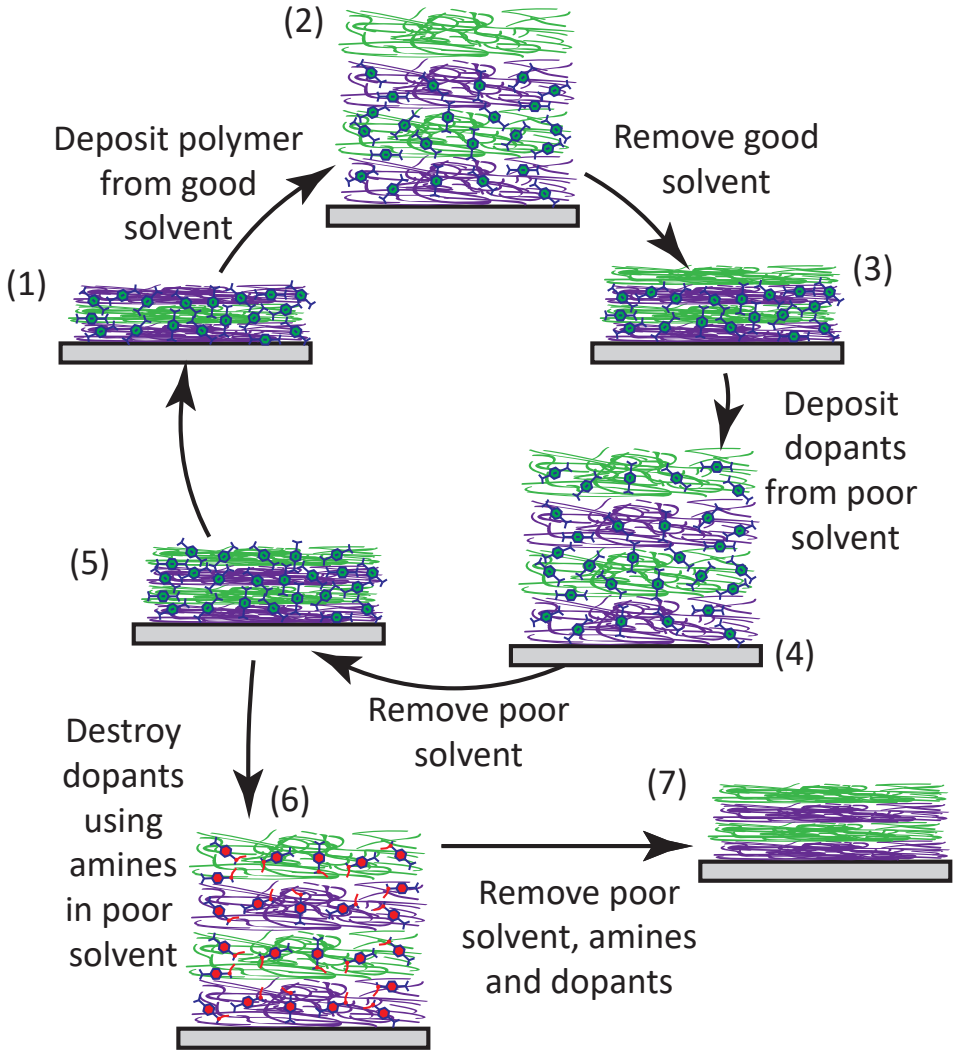

Figure 2.1. **Multilayer DISC patterning:** This schematic displays the additive solution deposition of multiple SP layers. (1) shows an initial stack of three alternating layers of doped polymer on a substrate. In (2) a fourth undoped polymer layer is deposited from solution and (3) the solvent is removed. In (4) the top polymer layer is sequentially doped from solution and (5) the solvent is removed. Step (6) demonstrates the chemical process to dedope the polymer film and (7) depicts the final stack of neutral polymer layers.

the bottom film be solvent swollen three times by a good solvent and four times by an orthogonal solvent. De-doping requires an additional solvent swelling step. It is necessary to question whether these sequential solvent processing steps result in mixing between the P3HT layers. Reptation between amorphous polymer films has been well studied, where thermal activation causes mixing between polymer layers.[20, 21, 22] However, the reptation model is only

quantitative when applied to amorphous polymers with molecular weights larger than the entanglement molecular weight; regioregular P3HT is a semi-crystalline polymer. During DISC processing, the deposition solvent swells the film leaving a larger free volume for polymer reorganization and should promote polymer diffusion. At a fundamental level we investigate the degree of swelling in P3HT and doped P3HT films when exposed to good and poor solvents in order to quantify a change in free volume. At a practical level, we investigate if the dopants prevent polymer layers from mixing during multiple solution processing steps.

2.3 Experimental

2.3.1 Materials

For neutron reflectometry (NR) and grazing incidence wide-angle x-ray scattering (GIWAXS) measurements, P3HT (Mn=54-75 kDa, 99.995% trace metals basis, >98% Regioregularity) was purchased from Sigma Aldrich. F4TCNQ was purchased from TCI America. Fully deuterated P3HT (dP3HT) (Mn = 14.2 kDa, PDI=1.17) was synthesized by Kunlun Hong at Center for Nanophase Materials Sciences (CNMS) (Batch: hy080414). Deuterated chlorobenzene (d-CB) and deuterated acetonitrile (d-AN) were purchased from Sigma Aldrich. For conductivity measurements P3HT (MW=85-100 kDa, 99.995% trace metals basis, >90% Regioregularity) was purchased from Sigma Aldrich.

2.3.2 Thin Film Fabrication, Profilometer, and UV-Vis Measurements

For NR measurements a single P3HT film and a multi-layered P3HT film were fabricated on 4 inch Si wafers. The substrates were cleaned in a series of 45 minute ultrasonic baths in acetone, 10 % mucasol:DI water, and DI water before being blown dry with nitrogen and UV-ozone treated for 20 min. All spin coating occurred in a nitrogen glove box (<5 ppm H_2O, O_2). The single P3HT film was spun coat from a 20 mg/ml solution in CB at 1000 RPM for 60 seconds. The film was sequentially swollen with d-AN vapor and d-CB vapor during NR collection. The film was then doped with F4TCNQ by dipping in a 0.1 mg/ml F4TCNQ/AN solution for 10 seconds. The film was again sequentially swollen with d-AN and d-CB vapor during NR collection. Between each vapor swelling step the film was put under vacuum for 5 min. to remove excess solvent.

The four layer film was prepared with alternating deuterated P3HT (d-P3HT) and protonated P3HT layers. All four layers were spun coat at 1000 RPM for 3 seconds then 100 RPM for 60 sec. The layers were deposited from the following CB solutions listed in the order of deposition 14 mg/mL d-P3HT, 7.25 mg/mL P3HT, 12 mg/ml d-P3HT, 6.5 mg/mL P3HT. Between each P3HT layer deposition the top layer was doped by covering the film stack with a 0.1 mg/mL solution of F4TCNQ in AN for 10 seconds before spinning off the excess solution at 3000 RPM for 30 seconds. The excess F4TCNQ deposits on the polymer/air interface were removed by spin coating pure AN solvent at 3000 RPM for 30 sec. After the first NR was collected the four layer film was soaked in a CB bath at room temperature for 4 hours before vacuuming off excess solvent for 5 min. Preliminary thickness measurements of films deposited from these sample conditions were made using a Veeco Dektak 150 Profilometer (Table S1). UV-Vis measurements were taken of P3HT and doped P3HT films during exposure to solvent vapor (Figure: S1) on a Perkin Elmer Lambda 750 Spectrometer.

For GIWAXS measurements, two 300 nm P3HT films were spin coated at 1000 RPM for 3 seconds then 100 RPM for 60 seconds onto one inch native oxide silicon substrates from 25 mg/ml solution in CB. One film was sequentially doped by covering the film with a 0.1 mg/mL solution of F4TCNQ in AN for 10 seconds before spinning off the excess solution at 3000 RPM for 30 seconds then chemically dedoped by soaking in butylamine:acetone (1:10 vol%) solution for 15 min.

2.3.3 Neutron Reflectometry

The NR measurements were carried out using the REFSANS beamline at the reactor Heinz Maier-Leibnitz (FRM II)[23]. This instrument makes use of a double chopper system which allows for time of flight (TOF) measurements. A collimation length of 8680 mm and sample-detector distance of 5827 mm and two incident angles were chosen 0.6° and 1.8°. Reflectivity is measured as a function of momentum change perpendicular to the surface, $Q_z = \frac{4\pi}{\lambda}\sin\theta$ where λ is the neutron wavelength. Instrument resolution was $\frac{dQ}{Q} = 0.0335$ Reflectivity was fit with a genetic algorithm using Igor based MOTOFIT, in which the reflectivity profile is calculated with the Abeles matrix method. The scattering length densities of the bulk materials are shown in Table S2.

2.3.4 Grazing Incidence Wide-Angle X-ray Scattering

GIWAXS measurements were carried out at the Stanford Synchrotron Radiation Lightsource (SSRL) on beam line 11-3 using an area detector (Rayonix MAR-225) and incident energy of 12.73 keV. The incidence angle (0.1°) was larger than the critical angle, ensuring that we sampled the full depth of the film. A sample-detector distance of 314.99 mm was chosen and calibrated using a LaB6 polycrystalline standard. All measurements were performed under a Helium environment to minimize air scattering and beam damage to samples. Raw data was normalized by monitor counts and thickness. Data was reduced and analyzed using a combination of Nika 1D SAXS[24] and WAXStools software packages in Igor Pro[25]. Scattering data are presented in terms of scattering vector $Q = \frac{4\pi}{\lambda}\sin\theta$, where θ is half the scattering angle and λ is the wavelength of incident x-rays. The terms Q_{xy} and Q_z denote the component of scattering vector in-plane and out-of-plane with the substrate, respectively.

2.3.5 Conductivity Measurements

Two-point vertical conductivity measurements were performed in the dark under nitrogen (<5 ppm H_2O, O_2), using a Keithley 2420 source-meter, film device geometry is shown in Figure S4. Electrode area was 19.635 mm^2.

2.4 Results and Discussion

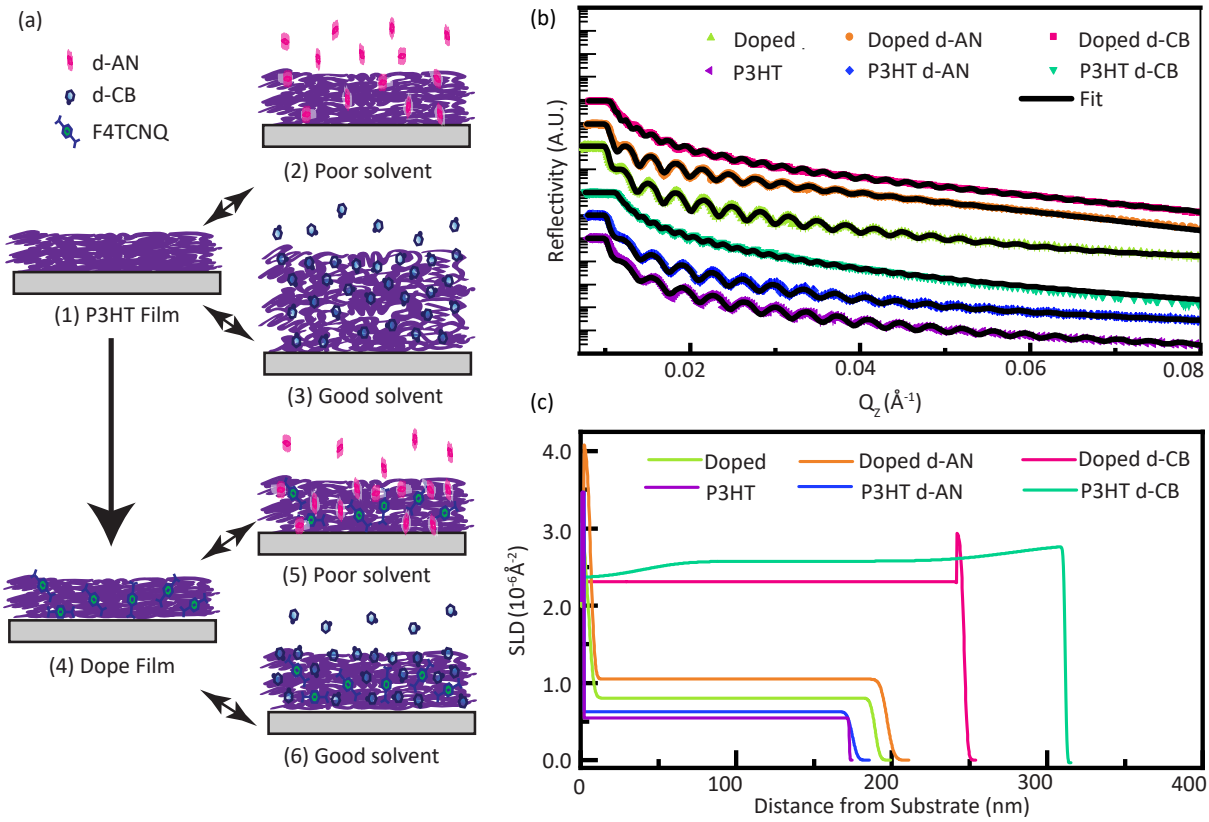

Figure 2.2. (a) Processing steps for the single P3HT film sequentially swollen with saturated d-AN vapor and d-CB vapor, then doped with F4TCNQ and sequentially swollen with d-AN vapor and d-CB vapor. (b) Neutron reflectivity data and best fit (c) vertical scattering length density profiles from NR fits.

To elucidate the changes that may occur during subsequent solvent exposure steps we used NR[23] to study a single P3HT thin film exposed to a series of saturated d-CB and d-AN vapor environments, before and after sequentially doping the film to 7 mol% with 0.1 mg/ml F4TCNQ/AN. Deuterated solvents were used to increase the scattering length density (SLD) contrast between the polymer and solvent. Analysis of NR data allows determination of the film thickness and SLD.[26] A volume balance (Equations A.1-A.4) can be applied to the measured SLD to determine the volume fraction of solvent in the film (Table 2.1). Figure 2.2 (a) illustrates the series of processing steps performed on the same P3HT film. Figure 2.2 (b) reveals the q-dependence of the scattering intensity from the film for each of the processing condition (offset vertically). Figure 2.2 (c) shows the corresponding vertical SLD profiles obtained from fits to the NR data.

Step (1) begins with a neutral P3HT film spin coated onto an Si:SiO_2 substrate from a CB solution. In (2), the neutral P3HT film was exposed to a saturated vapor of d-AN. As mentioned above d-AN is an orthogonal solvent for P3HT; the film thickness only increases 1.1 $\pm$ 1.0 % when exposed to d-AN vapor. The small increase in SLD corresponds to 2 $\pm$ 1 vol% of d-AN penetrating the free space in the amorphous regions of the polymer film. This exhibits a necessary requirement for sequential doping, the carrier solvent for the dopant must swell the polymer enough to promote diffusion of the dopant through the entirety of the film, however if mixing between this solvent and the polymer is too thermodynamically favorable it will result in unwanted changes to film morphology or dissolution. In (3), the neutral P3HT film was exposed to a saturated vapor of d-CB causing the film to swell significantly, with d-CB occupying 49 $\pm$ 2 vol% of the film and causing an 81.4 $\pm$ 6.4 % thickness increase. Since d-CB is a good solvent for P3HT, the film swells as much as entanglement allows. The volume percent of d-CB in the film decreases near the substrate due to attractive substrate-polymer interactions.[27] Between each solvent swelling step the film was placed under vacuum to remove residual solvent.

After the first three NR measurements, the same P3HT film was sequentially doped with F4TCNQ by dipping in a 0.1 mg/ml solution of F4TCNQ/AN (4). Due to technical challenges during collection, the NR of the doped film was collected after the swelling experiments with the doped film. However, since there was no heating or removal of solvent other than by evaporation, we are confident that the dopant concentration is identical in all three experiments. The doped film has higher SLD due to the scattering from the nitrogen and fluorine atoms on the F4TCNQ. The doped film swelled 43.4 $\pm$ 4.6 % during d-CB vapor exposure and did not collapse back to its initial thickness after exposure, remaining 9.9 $\pm$ 2.2 % thicker than the undoped film. This increased layer thickness after solvent exposure only occurs in the presence of the dopant. The original neutral P3HT film was deposited from CB. Further exposure of an undoped P3HT film to CB does not permanently affect film thickness. Our group previously showed that sequential addition of F4TCNQ to a P3HT film results in addition of dopants to amorphous domains. Only with secondary exposure to CB do the dopants intercalate to crystalline domains causing the $\pi - \pi$ stacking dimension to shrink from 0.39 nm to 0.38 nm.[14] More recently, Chew et.al. showed that adding F4TCNQ to P3HT via sequential doping results

Table 2.1. Solvent volume fraction and percent film thickness increase obtained from NR fits.

Film	Solvent	$\phi_{solvent}$	ΔT
P3HT	d-AN	0.02 ± 0.01	1.1 ± 1 %
	d-CB	0.49 ± 0.02	81.4 ± 6.4 %
Doped	d-AN	0.06 ± 0.01	14.3 ± 2.5 %
P3HT	d-CB	0.39 ± 0.01	43.4 ± 4.6 %

in significant stiffening of tie-chains between crystalline domains.[28] These results together suggest that when the doped film is solvent swollen, F4TCNQ redistributes in the film and stiffens sections of the P3HT chains. When the solvent evaporates, the film is less dense due to inefficient packing of these stiffer chain sections. The sharp increase in SLD near the silicon interface corresponds to the formation of a F4TCNQ mono-layer. Several studies have shown that F4TCNQ p-type dopes silicon.[29, 30] In (5), the doped P3HT film was exposed to a saturated vapor of d-AN. When exposed to d-AN vapor the doped film swells 14.3 ± 2.5 % and contains 6 ± 1 vol% d-AN. In (6), the doped P3HT film was exposed to a saturated vapor of d-CB. When exposed to d-CB vapor the doped film swelled 43.4 ± 4.6 % containing 39 ± 1 vol% d-CB. This is 21 % thinner than the neutral d-CB swollen P3HT film.

The Hansen Solubility parameters for CB and AN representing dispersion, polar, and hydrogen bonding forces are ($\delta_d = 9.28,\ \delta_p = 2.1,\ \delta_h = 1.0$) and ($\delta_d = 7.5,\ \delta_p = 8.8,\ \delta_h = 3.0$) respectively.[31] AN has higher polar bonding forces than CB. Since F4TCNQ forms cation/anion pairs with P3HT increasing the polarity of select regions of the film, it is reasonable to consider that the doped film would swell more in AN. Likewise, increasing the polarity of the film should reduce miscibility with CB.

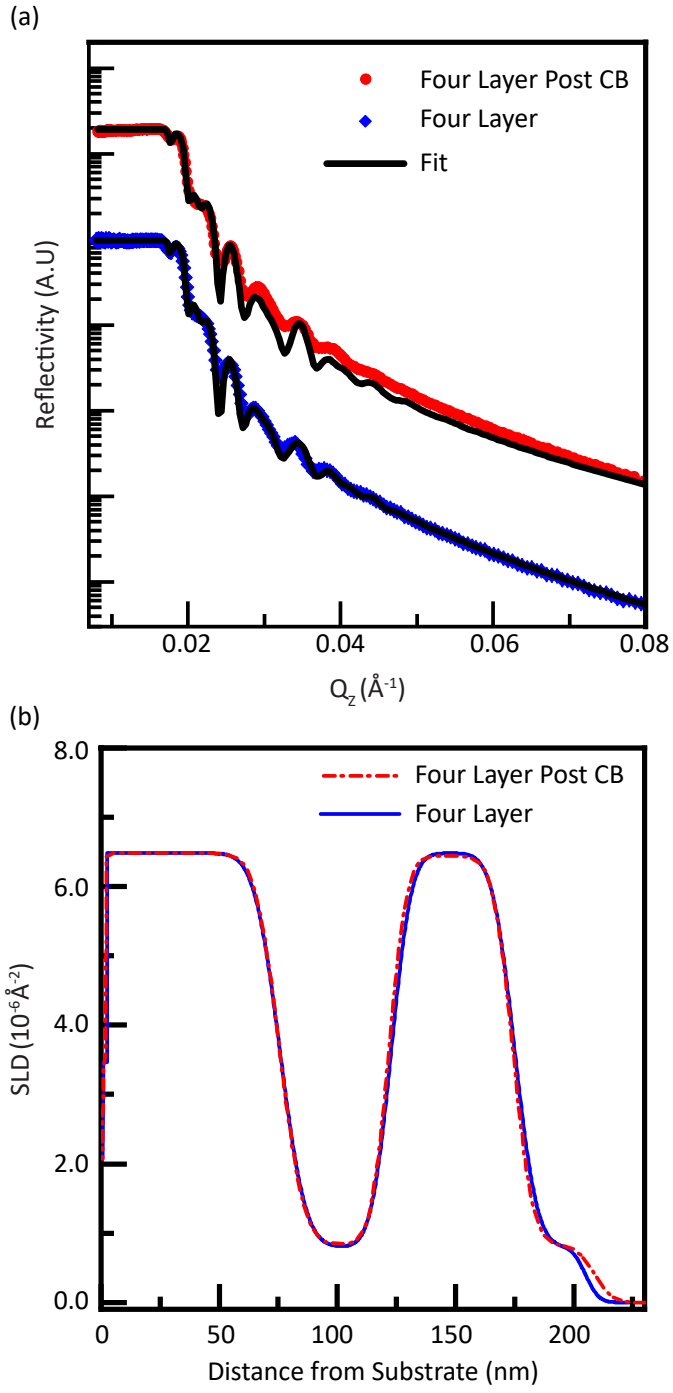

Figure 2.3. (a) Neutron Reflectivity from a four layered doped P3HT film with alternating deuterated and protonated layers before and after soaking in CB bath for 4 hours, (b) vertical scattering length density profiles from NR fits.

To demonstrate our multilayer deposition process, we created a doped four-layer P3HT film stack with alternating deuterated (d-P3HT) and protonated (p-P3HT) layers. The layer thicknesses were characterized using NR. Figure 2.3 (a) presents the q-dependence of the scattering intensity and Figure 2.3 (b) displays the vertical SLD profiles obtained from the fits. The SLD profile reveals four distinct layers that are purely d-P3HT or p-P3HT. The average layer interface width is 7.58 ± 0.65 nm. Although the bottom d-P3HT:p-P3HT interface was solvent swollen more times than subsequent interfaces (see Figure 2.1) there is no additional mixing. The overall interface roughness is elevated compared to previous bi-layer experiments using polystyrene because P3HT is semi-crystalline.[32] Also, the roughness is measured over a 8-10 cm strip in the film; any thickness change over several cm increases the apparent interface roughness over the measured length scale. We were not able to optimize the deposition conditions to minimize the interface roughness due to a limited supply of d-P3HT. Nevertheless, the data clearly shows pure layered films with sharp interfaces and constant roughness with respect to the number of solution processing steps.

After the first NR measurement, the four-layer film was soaked in a bath of liquid CB at room temperature for 4 hours. The sample was then removed from the bath, dried under vacuum, and a second NR measurement was performed. The top doped P3HT layer thickness increased after soaking because, unlike the bottom three layers, it had not been exposed to CB since it was deposited. The presence of F4TCNQ in the layer prevents the film from collapsing back to its original thickness, as was shown in the solvent swelling experiment in Figure 2.2 (c). The data also shows that solvent soaking did not induce mixing between the layers; the layer thicknesses, purity of the layers, and interface widths remain constant after soaking in CB. As shown above, a doped P3HT film swollen with d-CB has a volume increase of $43.4 \pm 4.6\%$. Assuming the entirety of this increase adds to the free volume around the polymer chains, we expected to observe a sharp increase in diffusion at the layer interfaces, even without a temperature increase. Without considering the effects of dopants, polymer diffusion and solubility are known to decrease with increasing molecular weight. [20, 21, 33] Since our d-P3HT has a lower molecular weight of 14.4 kDa, we expected layer mixing to result from diffusion of the d-P3HT into the higher molecular weight p-P3HT ($\sim$ 65 kDa). However, there is no observable

Table 2.2. P3HT and dedoped P3HT π-π stacking distance and lamellar spacing from grazing incidence wide-angle x-ray scattering.

Sample	π-π Stacking Distance (Å)	Coherence Length (nm)	Lamellar Spacing (Å)
P3HT	3.86 ± 0.01	8.0 ± 0.1	16.29 ± 0.01
Dedoped P3HT	3.85 ± 0.01	7.3 ± 0.1	16.26 ± 0.01

mixing between layers during the explored timescale. All things considered, the presence of the dopant:

1. Prevents the film from swelling as much as the undoped polymer film.
2. Prevents mixing at d-P3HT:p-P3HT interfaces during solution deposition.
3. Prevents the film from collapsing back to its original thickness after swelling with a good solvent.

Since the ultimate goal of this multilayer deposition process is to demonstrate its viability for creating sophisticated layered device architectures, we explore whether the presence of polymer:polymer interfaces significantly changes the electronic properties of the film. We prepared a series of single, double, and quadruple layer p-P3HT films with a 200 nm total thickness. We then performed two-point conductivity measurements vertically through the film to explore whether the polymer:polymer interfaces have any effect on the vertical conductivity of a multilayer film. Device architecture is located in Figure A.4 and I-V curves are located in Figures A.5-A.10. We compare samples that are doped to samples in which the F4TCNQ was removed using a reaction with butylamine.[19] We further characterized the morphology of P3HT and chemically dedoped P3HT films using GIWAXS. (Table: 2.2, Figures: A.2A.3). The lattice spacings extracted from fitting the diffraction peak positions of the lamellar (200) and π-π stacking (010) spacings show that the film microstructure is not affected by chemical dedoping. For the π-π direction, the coherence length can be calculated using peak widths and the Scherrer equation. Chemical dedoping produces a small decrease in the coherence length. Figure 2.4 shows the conductivity as a function of the number of p-P3HT layers. The error bars were generated by multiple measurements of several samples with small thickness variations. For both doped and dedoped samples, there is no statistically significant change in the out-of plane

conductivity as a function of the number of layer interfaces. The overall conductivity of the dedoped P3HT samples is consistent with literature values for neutral P3HT.[34] However our doped film conductivity is a few orders of magnitude lower than previous observations.[14, 15] Zuo et al. obtained high in-plane conductivities on the order of 10^2 S/m from sequentially deposited P3HT:F4TCNQ films. [35] This discrepancy is likely the result of using different measurement techniques. Two-point conductivity measurements are susceptible to high contact resistance.[36] Our NR data shows F4TCNQ forms a monolayer on an Si:SiO_2 substrate. F4TCNQ is known to form a surface layer on gold that increases the work function and thus the extraction barrier for holes from doped P3HT.[37] A further complication is that F4TCNQ undergoes significant drift in P3HT resulting in a non-linear current voltage characteristic.[38] Here we used low voltages (-0.01 to 0.01 V) to minimize any contribution to resistivity from dopant drift. Regardless, the data shows identical conductivity for all three doped and all three de-doped samples. We can safely conclude that the presence of polymer:polymer interfaces in a vertical multi-layer stack makes no significant contribution to vertical conductivity.

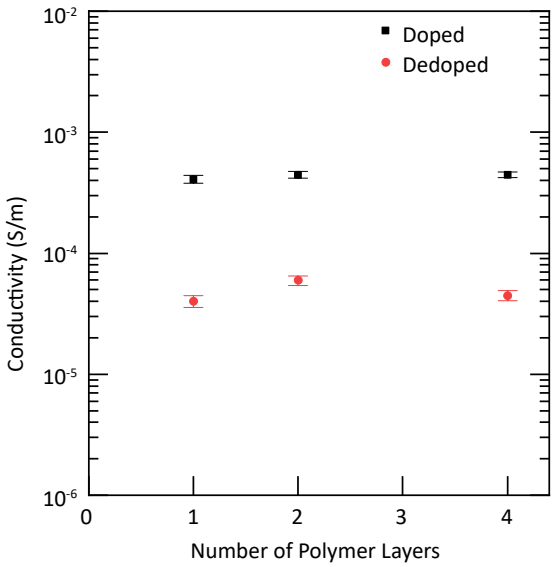

Figure 2.4. Two-point vertical conductivity measurements of doped and dedoped single, double, and quadruple P3HT layer devices.

2.5 Conclusion

This manuscript demonstrates a novel solution deposition process for multi-layered SP films. Each sequential solution processing step swells the polymer film and is quantified with NR. Doped P3HT swells to >40% in a good solvent but does not dissolve. We fabricated a four layer stack of alternating deuterated and protonated P3HT layers using the DISC method. NR shows all four layers are pure with negligible mixing between sequential layers. Solvent soaking in CB for 4 hours swells the layer stack but does not result in any additional mixing between layers. This shows that sequential solvent processing does not induce layer mixing and that DISC patterning is a viable technique for roll-to-roll compatible coating processes including dip coating, blade coating, spin coating, and/or ink jet printing. Finally, we measured the vertical conductivity as a function of the number of P3HT:P3HT layer interfaces and found that interfaces did not affect the vertical conductivity. We want to emphasize that this simple additive deposition technique facilitates the design of novel layered architectures by allowing the sequential deposition of mutually soluble SP films. With chemical dedoping one may create doped or dedoped layered architectures for various electronic applications. We expect this technique to be compatible with other SP/dopant systems and may one day be used to design multi-layered all-organic electronic devices.

2.6 Conficts of Interest

There are no conficts of interest to declare.

2.7 Acknowledgments

This project was supported by the U.S. Department of Energy, Office of Basic Energy Sciences, Division of Materials Sciences and Engineering, under Award No. DE-SC0010419. Thanks to the Jülich Centre for Neutron Science at Heinz Maier-Leibnitz Zentrum in Garching, Germany for Neutron Reflectometry measurement time and salary for J.F.M. Thanks to the Center for Nanophase Materials Science at Oak Ridge National Lab for synthesis of d-P3HT and salary for K.H. X-ray diffraction measurement were carried out at the Stanford Synchrotron Radiation Lightsource, a national user facility operated by Stanford University on behalf of the U.S. De-

partment of Energy, Office of Basic Energy Sciences. The x-ray measurements, performed by C.C. and A.S. were supported by the National Science Foundation award No. 1636385. Z.I.B.V thanks SENER-CONACyT project No. 291145 for postdoctoral support. Thanks to the China Scholarship Council for support for K.G. and to the Wasson Family thesis program for support for J.M.

REFERENCES

[1] C. Wang, H. Dong, W. Hu, Y. Liu, and D. Zhu, "Semiconducting π-conjugated systems in field-effect transistors: A material odyssey of organic electronics," *Chemical Reviews*, vol. 112, no. 4, pp. 2208–2267, 2012.

[2] F. Guo, A. Karl, Q.-F. Xue, K. C. Tam, K. Forberich, and C. J. Brabec, "The fabrication of color-tunable organic light-emitting diode displays via solution processing," *Light: Science &Amp; Applications*, vol. 6, p. e17094, 2017.

[3] B. Lüssem, C.-M. Keum, D. Kasemann, B. Naab, Z. Bao, and K. Leo, "Doped organic transistors," *Chemical Reviews*, vol. 116, no. 22, pp. 13714–13751, 2016.

[4] H. Sirringhaus, "25th anniversary article: Organic field-effect transistors: The path beyond amorphous silicon," *Advanced Materials*, vol. 26, no. 9, pp. 1319–1335, 2014.

[5] U. Heider, "Oled and merck's respective position (a deep dive into merck's lc & oled business)," tech. rep., Merck, June 2013.

[6] A. Karim, G. P. Felcher, and T. P. Russell, "Interdiffusion of polymers at short times," *Macromolecules*, vol. 27, no. 23, pp. 6973–6979, 1994.

[7] K. Nakano and K. Tajima, "Organic planar heterojunctions: From models for interfaces in bulk heterojunctions to high-performance solar cells," *Advanced Materials*, vol. 29, no. 25, p. 1603269.

[8] M. Ikawa, T. Yamada, H. Matsui, H. Minemawari, J. Tsutsumi, Y. Horii, M. Chikamatsu, R. Azumi, R. Kumai, and T. Hasegawa, "Simple push coating of polymer thin-film transistors," *Nature Communications*, vol. 3, p. 1176, 2012.

[9] A. L. Shu, A. Dai, H. Wang, Y.-L. Loo, and A. Kahn, "Electronic structure and carrier transport at laminated polymer homojunctions," *Organic Electronics*, vol. 14, no. 1, pp. 149 – 155, 2013.

[10] J. Li, L. Xu, C. W. Tang, and A. A. Shestopalov, "High-resolution organic light-emitting diodes patterned via contact printing," *ACS Applied Materials & Interfaces*, vol. 8, no. 26, pp. 16809–16815, 2016.

[11] A. C. Arias, J. D. MacKenzie, I. McCulloch, J. Rivnay, and A. Salleo, "Materials and applications for large area electronics: Solution-based approaches," *Chemical Reviews*, vol. 110, no. 1, pp. 3–24, 2010. doi: 10.1021/cr900150b.

[12] I. E. Jacobs, J. Li, S. L. Berg, D. J. Bilsky, B. T. Rotondo, M. P. Augustine, P. Stroeve, and A. J. Moule, "Reversible optical control of conductive polymer solubility with sub-micrometer resolution," *ACS Nano*, vol. 9, no. 2, pp. 1905–1912, 2015.

[13] I. E. Jacobs, E. W. Aasen, D. Nowak, J. Li, W. Morrison, J. D. Roehling, M. P. Augustine, and A. J. Moulé, "Direct-write optical patterning of p3ht films beyond the diffraction limit," *Advanced Materials*, vol. 29, no. 2, p. 1603221, 2017.

[14] I. E. Jacobs, E. W. Aasen, J. L. Oliveira, T. N. Fonseca, J. D. Roehling, J. Li, G. Zhang, M. P. Augustine, M. Mascal, and A. J. Moulé, "Comparison of solution-mixed and sequentially processed p3ht:f4tcnq films: effect of doping-induced aggregation on film morphology," *J. Mater. Chem. C*, vol. 4, pp. 3454–3466, 2016.

[15] D. T. Duong, C. Wang, E. Antono, M. F. Toney, and A. Salleo, "The chemical and structural origin of efficient p-type doping in p3ht," *Organic Electronics*, vol. 14, no. 5, pp. 1330 – 1336, 2013.

[16] I. E. Jacobs, C. Cendra, T. F. Harrelson, Z. I. Bedolla Valdez, R. Faller, A. Salleo, and A. J. Moul, "Polymorphism controls the degree of charge transfer in a molecularly doped semiconducting polymer," *Mater. Horiz.*, vol. 5, no. 4, pp. 655–660, 2018.

[17] J. Gao, J. D. Roehling, Y. Li, H. Guo, A. J. Moulé, and J. K. Grey, "The effect of 2,3,5,6-tetrafluoro-7,7,8,8-tetracyanoquinodimethane charge transfer dopants on the conformation and aggregation of poly(3-hexylthiophene)," *J. Mater. Chem. C*, vol. 1, pp. 5638–5646, 2013.

[18] J. Fuzell, I. E. Jacobs, A. Ackling, T. F. Harrelson, D. M. Huang, D. S. Larsen, and A. J. Moule, "Optical dedoping mechanism for p3ht/f4tcnq mixtures," *Journal of physical Chemistry Letters*, vol. 7, pp. 4297–4303, 2016.

[19] I. E. Jacobs, F. Wang, N. Hafezi, C. Medina-Plaza, T. F. Harrelson, J. Li, M. P. Augustine, M. Mascal, and A. J. Moulé, "Quantitative dedoping of conductive polymers," *Chemistry of Materials*, vol. 29, no. 2, pp. 832–841, 2017.

[20] T. P. Russell, V. R. Deline, W. D. Dozier, G. P. Felcher, G. Agrawal, R. P. Wool, and J. W. Mays, "Direct observation of reptation at polymer interfaces," *Nature*, vol. 365, p. 235, 1993.

[21] P. G. de Gennes, "Reptation of a polymer chain in the presence of fixed obstacles," *The Journal of Chemical Physics*, vol. 55, no. 2, pp. 572–579, 1971.

[22] M. Doi and S. F. Edwards, "Dynamics of concentrated polymer systems. part 3.-the constitutive equation," *J. Chem. Soc., Faraday Trans. 2*, vol. 74, pp. 1818–1832, 1978.

[23] M. H. Heinz Maier-Leibnitz Zentrum, Jean-Francois Moulin, "Refsans: Reflectometer and evanescent wave small angle neutron spectrometer," *Journal of large-scale research facilities*, 2015.

[24] J. Ilavsky, "*Nika*: software for two-dimensional data reduction," *Journal of Applied Crystallography*, vol. 45, pp. 324–328, Apr 2012.

[25] S. D. Oosterhout, V. Savikhin, J. Zhang, Y. Zhang, M. A. Burgers, S. R. Marder, G. C. Bazan, and M. F. Toney, "Mixing behavior in small molecule:fullerene organic photovoltaics," *Chemistry of Materials*, vol. 29, no. 7, pp. 3062–3069, 2017.

[26] J. Penfold and R. K. Thomas, "The application of the specular reflection of neutrons to the study of surfaces and interfaces," *Journal of Physics: Condensed Matter*, vol. 2, no. 6, p. 1369, 1990.

[27] Y. Guo, X. Ma, and Z. Su, "Interfacial interactions between poly(3-hexylthiophene) and substrates," *Macromolecules*, vol. 46, no. 7, pp. 2733–2739, 2013.

[28] A. R. Chew, R. Ghosh, Z. Shang, F. C. Spano, and A. Salleo, "Sequential doping reveals the importance of amorphous chain rigidity in charge transport of semi-crystalline polymers," *The Journal of Physical Chemistry Letters*, vol. 8, no. 20, pp. 4974–4980, 2017. PMID: 28949140.

[29] S. Yoshimoto, M. Furuhashi, T. Koitaya, Y. Shiozawa, K. Fujimaki, Y. Harada, K. Mukai, and J. Yoshinobu, "Quantitative analysis of chemical interaction and doping of the si(111) native oxide surface with tetrafluorotetracyanoquinodimethane," *Journal of Applied Physics*, vol. 115, no. 14, p. 143709, 2014.

[30] M. Furuhashi and J. Yoshinobu, "Charge transfer and molecular orientation of tetrafluorotetracyanoquinodimethane on a hydrogen-terminated si(111) surface prepared by a wet chemical method," *The Journal of Physical Chemistry Letters*, vol. 1, no. 10, pp. 1655–1659, 2010.

[31] C. M. Hansen, *The three dimensional solubility parameter and solvent diffusion coefficient: Their importance in surface coating formulation*. 1967.

[32] T. P. Russell, A. Karim, A. Mansour, and G. P. Felcher, "Specular reflectivity of neutrons by thin polymer films," *Macromolecules*, vol. 21, no. 6, pp. 1890–1893, 1988.

[33] B. A. Miller-Chou and J. L. Koenig, "A review of polymer dissolution," *Progress in Polymer Science*, vol. 28, no. 8, pp. 1223 – 1270, 2003.

[34] V. Skrypnychuk, N. Boulanger, V. Yu, M. Hilke, S. C. B. Mannsfeld, M. F. Toney, and D. R. Barbero, "Enhanced vertical charge transport in a semiconducting p3ht thin film on single layer graphene," *Advanced Functional Materials*, vol. 25, no. 5, pp. 664–670.

[35] G. Zuo, O. Andersson, H. Abdalla, and M. Kemerink, "High thermoelectric power factor from multilayer solution-processed organic films," *Applied Physics Letters*, vol. 112, no. 8, p. 083303, 2018.

[36] I. Miccoli, F. Edler, H. Pfnür, and C. Tegenkamp, "The 100th anniversary of the four-

point probe technique: the role of probe geometries in isotropic and anisotropic systems," *Journal of Physics: Condensed Matter*, vol. 27, no. 22, p. 223201, 2015.

[37] G. M. Rangger, O. T. Hofmann, L. Romaner, G. Heimel, B. Bröker, R.-P. Blum, R. L. Johnson, N. Koch, and E. Zojer, "F4tcnq on cu, ag, and au as prototypical example for a strong organic acceptor on coinage metals," *Phys. Rev. B*, vol. 79, p. 165306, 2009.

[38] L. Muller, S.-Y. Rhim, V. Sivanesan, D. Wang, S. Hietzschold, P. Reiser, E. Mankel, S. Beck, S. Barlow, S. R. Marder, A. Pucci, W. Kowalsky, and R. Lovrincic, "Electric field controlled dopant distribution in organic semiconductors," *Advanced Materials*, vol. 29, no. 30, p. 1701466.

Chapter 3

Investigation of Hierarchical Structure Formation in Merocyanine Photovoltaics

3.1 Preface

In this chapter, I am reprinting an article I wrote on correlating hierarchical structure formation to photovoltaic performance in merocyanine/fullerene blends; DOI: 10.1021/acs.jpcc.0c04988. Merocyanines (MC) are a versatile class of small molecule dyes. Their optoelectronic properties are easily tunable by chemically controlling their donor-acceptor strength, and their structural properties can be tuned by simple side chain substitution. This manuscript demonstrates a novel series of MC featuring an indoline donor with varying hydrocarbon side chain length (from 6 to 12 carbons) and a tert-butyl-thiazole acceptor, labeled I*n*TBT. Bulk heterojunction organic photovoltaics are fabricated with a PCBM acceptor and characterized. Films composed of I8TBT:PCBM and I9TBT:PCBM produced the the highest power conversion efficiency of 4.5%, which suggests that the morphology is optimized by controlling the side chain length. Hierarchical structure formation in I*n*TBT:PCBM films are studied using grazing incidence x-ray diffraction (GIXRD), small angle neutron scattering (SANS), and atomic force microscopy (AFM). When mixed with PCBM, I*n*TBTs with ≤ 8 side chain carbons form pure crystalline domains, while I*n*TBTs with ≥ 9 side chain carbons mix well with PCBM. SANS demonstrates that increasing side chain length increases I*n*TBT rich domain size. In addition, a branched hexyl-dodecyl side chain IHDTBT:PCBM film was studied and found to exhibit the worst performance OPV device. The large branched side chain inhibited mixing between IHDTBT and PCBM resulting in large segregated phases.

3.2 Introduction

An increasing number of donor candidate molecules for organic photovoltaics (OPV) with alternating electron donor (D) and acceptor (A) subunits have been reported in recent years.[1, 2, 3, 4] Among simple dyes, dipolar merocyanines (MCs) are an interesting and versatile class of functional materials.[5, 6] MC donor-acceptor (D-A) groups can be easily changed to tune their absorption from the blue to IR spectral region, with ground state dipole moments ranging from 3 to 15 D. MCs have been applied as active component in bulk heterojunction (BHJ) OPV devices.[7, 8, 9, 10] A previous study by Kronenberg et al. showed that BHJ OPVs composed of indoline based MCs donors and [6,6]-phenyl-C_{61}-butyric acid methyl ester (PCBM) or C_{60}

acceptors manifest large open circuit voltages (V_{OC}) and short circuit currents (J_{SC}) of 0.9, 0.76 V and 5.3 , 6.3 $\frac{mA}{cm^2}$ respectively. However poor charge transport gave rise to low fill factors (FF) ($\sim$30%) resulting in power conversion efficiencies (PCE) of 1.5 and 1.7%.[11] Subsequently, Steinmann et al. created a tandem OPV using the same materials resulting in an very high V_{OC} of 2.1 V and PCE of 4.8%, but retained a low FF.[12] So far the highest PCE reported from an indoline based D-A device with a simple BHJ architecture is 6.1% (FF 47%) from a vacuum deposited MC:PCBM device, while the record for solution processed device is 4.5%.[13, 14] Both of those devices benefited from improved FFs of 47% and 44% respectively.

Morphology control is currently a major limitation for D-A OPVs. A variety of structural motifs have been obtained for several D-A subunits with varying dipole strength, including but not limited to, simple isolated anti-parallel dimers, stacked dimers (1D), and slipped/staircase like structures.[15, 14] Due to the complexity of interactions between neighboring molecules (i.e.: competing sterical interactions, intermolecular van der Waals/dipolar forces, and substrate interactions) there is currently no set of guidelines capable of predicting the solid-state packing from molecular structure. Recently, many new small molecule architectures have been developed to prevent D-A dipole alignment and improve π-π stacking including donor-acceptor-donor (D-A-D), and acceptor-donor-acceptor (A-D-A).[16] The current BHJ OPV record for a small molecule device is held by an A-D-A donor molecule with π-conjugated bridges between the groups denoted as A-π-D-π-A, with a PCE of 14.3%.[17] The cost of synthesizing A-π-D-π-A molecules is considerably larger than for simple D-A compounds. Research into improving BHJ morphology with simple D-A donors is necessary.

Optimizing the structural properties of D-A BHJ OPVs is challenging. To enable efficient charge separation and collection, p-type MC donors must be mixed with an n-type acceptor (i.e. PCBM). The mixture of MC:PCBM in solid state can create a multiphase system with pure MC, pure PCBM, and mixed domains. Domain size, crystal structure, and domain purity must be optimized to promote efficient exciton dissociation, charge transport, and extraction.[18]

In this article, we report a comprehensive investigation of a series of structurally related D-A MC dyes, with varying hydrocarbon side chain length (Figure 3.1). The choice of MC is based on previous studies which obtained best results, in terms of PV performance, with indoline

based donor groups.[2, 3] The thiazol-di-cyanovinylene acceptor group was chosen because its high acceptor strength enables H/J type coupling,[19] shows high mobility in crystalline OFETs, and yields a high V_{OC} with PCBM due to favorable ionization energy.[3] By tuning side chain length we are able to control solubility, molecular packing, and phase segregation in MC:PCBM BHJ OPV devices. The BHJ films are characterized in OPV devices to obtain J-V curves and structural information is obtained using grazing incidence x-ray diffraction (GIXRD), small-angle neutron scattering (SANS), and atomic force microscopy (AFM). Similar to previous studies[20, 21, 22] we show that by tuning hydrocarbon side chain length we can control hierarchical structure formation to improve charge extraction in MC based OPVs.

3.3 Methods

3.3.1 Sample Processing:

All OPVs were fabricated on indium-tin oxide (ITO, 125 nm) coated glass. The substrates were exposed to ozone for 3 min and transferred to the evaporation chamber to evaporate 10 nm MoO_3. Substrates were transfered into a glove box to spin coat 70 nm thick active layers from chloroform solutions of 13 to 15 mg/mL mixed in a ratio of 2:3 (I*n*TBT to $PC_{61}BM$). The device fabrication was completed by thermal evaporation of 5 nm Ca then 100 nm Ag.

3.3.2 UV-Vis:

Absorption measurements were performed using a Lambda 1050 (Perkin Elmer) UV/vis spectrometer. A molar concentration of 10^{-4}-10^{-6} mol/L were used for performing optical absorption measurements in solution.

3.3.3 Single Crystal XRD:

Measurement of single crystals was done using a Bruker D8 Venture (with software APEX3) in kappa geometry equipped with a copper microfocus source and a Photon100 detector. SADABS[23] was used for analysis, scaling and absorption correction. SHELXT and SHELXL[24] were used for I*n*TBT structure refinement.

3.3.4 GIXRD:

GIXRD was collected using a Panalytical Empyrean system with a Cu Kα anode λ=1.54056 Å^{-1}. Glass was used as amorphous substrate. The incidence angle was optimized for every measurement to reduce scattering from substrate and air interfaces. Initially a survey was conducted from $\theta \sim$5 to 15° with $\omega = 0.2°$. The most intense $\theta \sim$ peak was used to find the optimal ω for signal and background measurement.[25]

3.3.5 SANS:

The SANS experiments were completed on KWS-2 SANS instrument at the Heinz Maier-Leibnitz Zentrum (MLZ), Garching, Germany. Three instrument conditions were used to provide Q-values ranging from 0.16 to 0.003 Å^{-1}, where $Q = \frac{4\pi}{\lambda}\sin(\frac{\theta}{2})$; λ is the neutron wavelength and θ is the scattering angle. The first two conditions were collected with a collimation length of 4 m with neutron wavelength 4.66 Å and a sample-detector distances of 1.61m and 3.61 m. For the third condition, the collimation length was 20 m with neutron wavelength 5 Å and sample-detector distance at 19.51 m.

3.3.6 AFM:

The AFM measurements were performed on a MFP-3d Infinity from Asylum Research. All measurements were conducted in amplitude-modulated alternating contact mode utilizing micro cantilevers of the type OMCL-AC200TS from Olympus Micro Cantilevers. All measurements were conducted under ambient conditions in air.

3.4 Results

The procedures to synthesize the MC donors can be found in the Supporting Information. We synthesized a series of MCs with varied side chain length on the indolene from hexyl to dodecyl and a derivative with a branched hexyl-dodecyl chain. For the ease of labeling we number the MCs according to the side chain length, i.e. I*n*TBT, with I6TBT for the hexyl side chain and so on to I12TBT and IHDTBT for the branched derivative See Figure 3.1. The I*n*TBTs with n $>$ 6 have a much higher FF (FF $>$ 0.6) compared to typical MC cells processed from solution/or vacuum of comparable thickness (Figure 3.3 a)).[26]

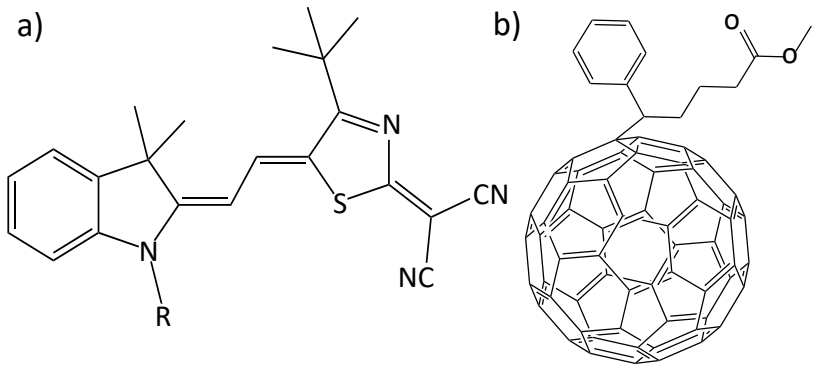

Figure 3.1. Chemical structures of compounds used in this study: a) a series of MC featuring an indoline donor with varying hydrocarbon side chain length (R) and a tert-butyl-thiazole acceptor, labeled I*n*TBT. b) $PC_{61}BM$.

The side chain affects both the solubility and crystal packing but does not change the optical or electronic properties of the dye itself. All I*n*TBT samples have nearly identical UV-vis absorbance at the same molar concentration and solvent quality in solution. The absorption spectra of I8TBT in solutions with varying polarity are shown in Figure B.5. The data shows a clear progression from a blue-shifted spectrum in hexane to red-shifted J-aggregates in more polar solvents. Since the I*n*TBT's are less soluble in nonpolar solvents, this progression also shows that a red-shifted UV-vis spectrum with increased 0-0 to 0-1 peak ratio indicates the presence of ordered crystalline aggregates in the film.[19, 10] Figure 3.2 shows UV-vis absorption spectra of all 2:3 wt.% I*n*TBT:PCBM films normalized to the central peak at 590 nm. In these aggregates the coupling between nearest neighbors is strongly influenced by the side chain length.

A clear side chain length trend can be observed in the UV-vis data. The OPV films all share three MC vibronic peaks at $\sim$650 nm (0-0), $\sim$600 nm (0-1), and $\sim$550 nm (0-2) as well as a PCBM peak at $\sim$350 nm. The linear side chain samples also share an amorphous absorption at $\sim$500 nm. The spectra are normalized to the central peak of the MC, which allows us to probe the symmetry of the D-A aggregations to be more H-like or J-like and provides information on delocalization. The ratio of the 0-0 to 0-1 transitions ($\frac{0-0}{0-1}$) is fairly constant for all the I*n*TBTs with linear side chains, meaning the aggregations are similar in orientation. As the linear side chain increases in length the 0-2 peak and amorphous absorption increase, indicating that the I*n*TBTs with longer side chains experience additional geometries. The 0-0 and 0-1 transition

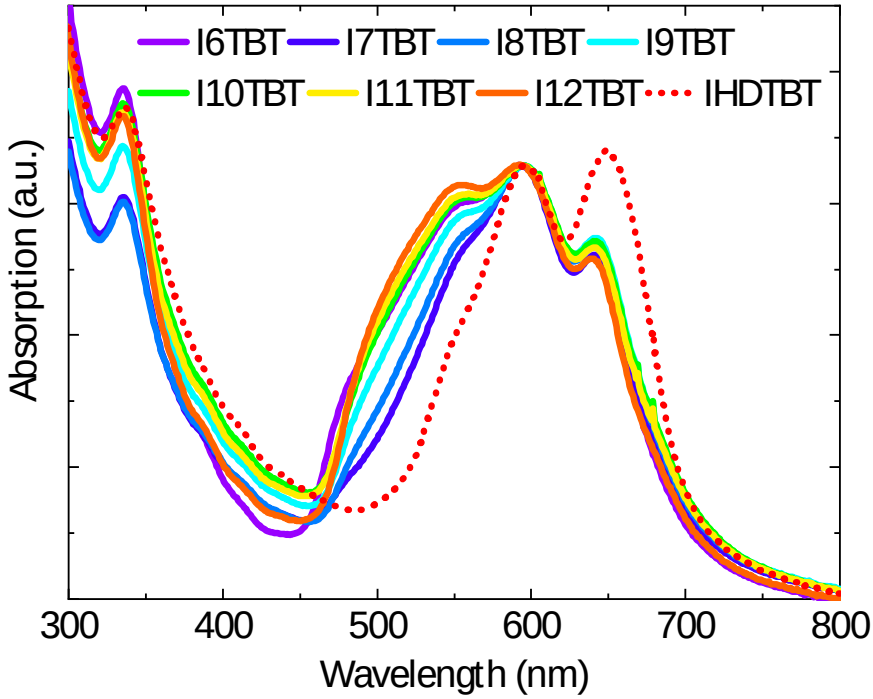

Figure 3.2. UV-vis absorption spectra of I*n*TBT:PCBM films normalized to the common peak at 594 nm.

ratio in the IHDTBT:PCBM film depicts a J-like configuration indicating minimal mixing with PCBM.

We fabricated BHJ OPV devices from solution with I*n*TBT:PCBM in a composition ratio of 2:3 by weight, which means the molar ratio changes as a function of side chain length.[27] The active layer thickness was kept at a constant 70 nm for all the devices due to the limited solubility of the short and very long side-chain derivatives. The hole collection layer is 10 nm MoO_3 evaporated onto ITO[3] and the anode is composed of 5 nm Ca/100 nm Ag. All of the device fabrication details are in the experimental section. Typical AM1.5 solar simulator JV curves are shown in Figure 3.3 (a) for all MCs. The JV characteristics are listed in Table 3.1 and PCE as a function of side chain length is shown in Figure 3.3 b).

As I*n*TBT side chain length is increased from 6 to 12 carbons, the V_{OC} increases to a maximum at 0.90 $\pm$ 0.01 V for I9TBT, I10TBT, and I11TBT before decreasing again. The I6TBT device has the highest short circuit current density (J_{sc}) at 8.29 $\pm$ 0.38 $\frac{mA}{cm^2}$ because it has the highest absorbance integral (shortest side chain) seen in the unnormalized UV-vis Figure B.6. I11TBT has the highest FF at 0.67 $\pm$ 0.01, indicating the most favorable balance of hole

and electron transport.[28, 29] The highest PCE of $4.5 \pm 0.1\%$ was extracted from devices with I8TBT and I9TBT. These films exhibited the best combination of J_{sc} and FF, balancing increased optical absorbance for short side chains and favorable morphology for longer chains. Higher PCE devices could be obtained by optimizing layer thickness and the mixing ratio for I8TBT-I12TBT, however this is not the goal of this study. Rather we focus on explaining how the side chain length affects the morphology in this material class. The MC with the branched side chain IHDTBT exhibited the worst device performance in spite of the most favorable absorbance.

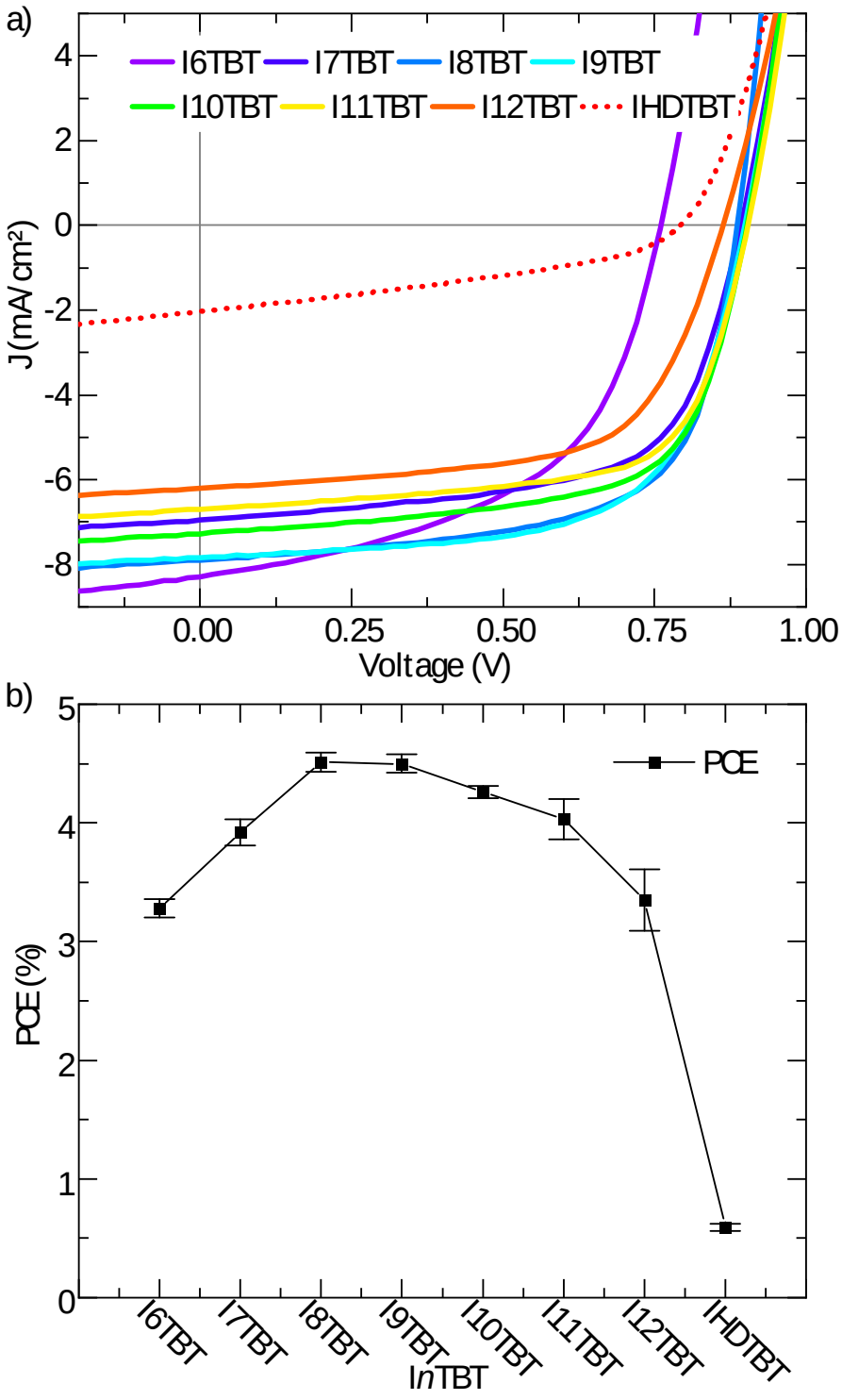

Figure 3.3. (a) JV curves and (b) extracted power conversion efficiencies from 3:2 by wt. I*n*TBT:PCBM devices.

Table 3.1. Best performance data of I*n*TBT:PCBM OPVs in the standard device setup (composition 2:3).

Merocyanine	V_{OC} (V)	J_{sc} (mA/cm^2)	FF	PCE (%)
I6TBT	0.76 ± 0.01	8.29 ± 0.38	0.52 ± 0.02	3.3 ± 0.1
I7TBT	0.89 ± 0.01	6.95 ± 0.15	0.63 ± 0.01	3.9 ± 0.1
I8TBT	0.89 ± 0.01	7.90 ± 0.24	0.64 ± 0.02	4.5 ± 0.1
I9TBT	0.90 ± 0.01	7.83 ± 0.22	0.64 ± 0.02	4.5 ± 0.1
I10TBT	0.90 ± 0.01	7.28 ± 0.13	0.65 ± 0.01	4.3 ± 0.1
I11TBT	0.90 ± 0.01	6.69 ± 0.28	0.67 ± 0.01	4.0 ± 0.1
I12TBT	0.86 ± 0.01	6.20 ± 0.3	0.63 ± 0.02	3.4 ± 0.3
IHDTBT	0.79 ± 0.01	2.03 ± 0.06	0.37 ± 0.02	0.6 ± 0.1

To probe the smallest length scale structures (Å) in pure I*n*TBT and 2:3 I*n*TBT:PCBM films we use grazing incidence x-ray diffraction (GIXRD) (Figures: B.7 − B.23). Diffraction peaks were fit with a Pseudo-Voigt model to extract peak positions and widths.[30, 31] Bragg's Law was used to calculate crystal d-spacing and the Scherrer equation was used to calculate coherence length (L_C) for the most prominent I*n*TBT and PCBM peaks (Tables: 3.2, B.19).[32, 33, 34] GIXRD of the pure PCBM film shows two peaks at $2\theta \sim 19.5^\circ$ and $\sim 9.7^\circ$, in accordance with literature.[35]

In the pure I*n*TBT films, the samples with side chains $n \leq 8$ form larger crystals with L_C (> 14 nm) (Table: 3.2). In I*n*TBT samples with side chain $n \geq 9$ (and IHDTBT) the side chain is long enough to impede crystal growth, thereby reducing the L_C (< 8.2 nm). In the I*n*TBT:PCBM films, the I*n*TBT L_C decreases significantly in all of the studied samples suggesting that I*n*TBTs form smaller more disordered crystals when mixed with PCBM (Table: 3.2). The L_C of the PCBM peak at $2\theta \sim 19.5^\circ$ remains consistent ($\sim$ 1.6 nm) in all of the I*n*TBT:PCBM films (Table: B.19), which shows that pure PCBM crystalline domains form in all films. The ratio of the prominent I*n*TBT to PCBM peak intensity in the mixed films are shown in Figure 3.4. I*n*TBTs with $n \leq 8$ and $n =$HD form pure I*n*TBT crystalline domains in the presence of PCBM. Their prominent diffraction peak intensity around $\sim 7.5^\circ$ are 2 to 6 times greater then their corresponding PCBM peak intensity. As the linear side chain is in-

creased to $n \geq 9$, the I*n*TBT peaks broaden significantly and the prominent peak height ratio ($\frac{\text{I}n\text{TBT Peak Height}}{\text{PCBM Peak Height}}$) decreases below unity (Figures: 3.4 and B.14-B.21). A similar drop in the prominent peak integration ratio ($\frac{\text{I}n\text{TBT Peak Integration}}{\text{PCBM Peak Integration}}$) is observed, although the change is less discernible due to the broadening of the InTBT diffraction peaks and the large FWHM of the PCBM peak. This suggests that I*n*TBTs with linear side chains $n \geq 9$ undergo significant mixing with PCBM and form amorphous structures that do not have long range order.

I*n*TBT diffraction peaks for n $\leq$ 8 broaden and shift when mixed with PCBM resulting in minor shifts in the prominent I*n*TBT d-spacing (Table 3.2). I6TBT d-spacing decreases from 12.0 to 11.5 Å while both I7TBT and I8TBT d-spacings increase from 11.1 and 12.6 to 12.5 and 12.8 Å respectively. More significant changes upon mixing are observed for I*n*TBTs with n $\geq$ 9. The I9TBT peaks at 2θ= 4.64°, 5.31°, 7.06°, and 9.11° merge into a single broad peak at 7.63° when mixed with PCBM resulting in the apparent I*n*TBT:PCBM d-spacing of 11.6 Å. The I10TBT peaks at 7.16° and 8.66° merge into the broad peak at 7.95° when mixed with PCBM resulting in the apparent I*n*TBT:PCBM d-spacing of 11.1 Å. Upon mixing with PCBM, I11TBT peaks broaden and merge but are still distinguishable; the peaks at 4.25° and 5.05° shift to 4.02° and 4.95°, increasing the d-spacing to 22 and 17.8 Å respectively. The peaks at 7.19° and 8.49° shift to 7.27° and 8.24° changing the d-spacing to 12.2 and 10.7 Å. The I12TBT peaks at 4.04° and 4.93° merge into the broad peak at 4.26° when mixed with PCBM resulting in the apparent I12TBT:PCBM d-spacing of 20.7 Å. Finally, upon mixing with PCBM the IHDTBT peak shifts from 4.25° to 4.18° resulting in a d-spacing 21.2 Å. In summary, when mixed with PCBM the I*n*TBTs with n $\leq$ 8 remain phase segregated and show minor broadening and shifting of their prominent diffraction peaks. While I*n*TBTs with n $\geq$ 9 allow intercalation of PCBM into the I*n*TBT crystals causing significant broadening of their diffraction peaks due to reduced long range order.

Table 3.2. Bragg's d-spacing and Scherrer's coherence length L_C extracted from most prominent I*n*TBT peak (in the range of 2θ ~4-10°) from pure and mixed I*n*TBT:PCBM films.

I*n*TBT	I*n*TBT d-Spacing (Å)	I*n*TBT L_C (Å)	I*n*TBT:PCBM d-Spacing (Å)	I*n*TBT:PCBM L_C (Å)
I6TBT	12.0 ± 0.1	147 ± 2	11.5 ±0.1	41 ± 1
I7TBT	11.1 ± 0.1	220 ± 6	12.5 ± 0.1	75 ± 8
I8TBT	12.6 ± 0.1	181 ± 8	12.8±0.1	87 ± 6
I9TBT	9.7 ± 0.1	56 ± 37	11.6±0.1	11 ± 8
I10TBT	10.2 ± 0.1	39 ± 8	11.1±0.1	17 ± 15
I11TBT	17.5 ± 0.1	82 ± 4	17.8±0.1	42 ± 4
I12TBT	17.9 ± 0.1	40 ± 6	20.7±0.1	39 ± 25
IHDTBT	20.8 ± 0.1	82 ± 3	21.1±0.1	48 ± 27

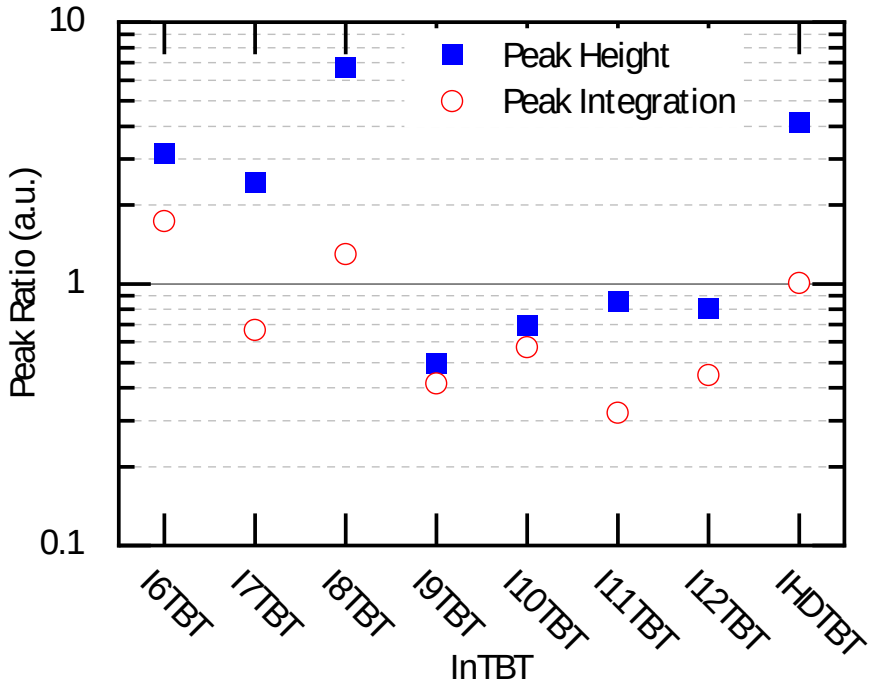

Figure 3.4. GIXRD: Ratio of prominent I*n*TBT peak over prominent PCBM peak (peak heights and peak integrations) in mixed 3:2 by wt. I*n*TBT:PCBM films.

We use SANS to probe the size, shape, and composition of nanoscale (3-200 nm) domains in I*n*TBT:PCBM films ($7 \leq n \geq 11$).[36] Differences in the ^{1}H density between I*n*TBT and PCBM lead to a neutron scattering contrast. Figure 3.5 (a) shows SANS data (I(Q) vs Q),

where I is intensity and Q is momentum transfer in units of $Å^{-1}$. This scattering data is fit to a model that determines statistical length scale correlations and relative density differences between domains. SANS is not sensitive to crystallinity, which allows us to probe structural and compositional density distributions of the full bulk sample, not just the crystalline regions as for x-ray diffraction analysis.

The I*n*TBTs with linear side chains form elongated domains that are best fit with an ellipsoidal form factor.[37] We therefore use a model that assumes elongated I*n*TBT rich domains surrounded by PCBM rich material. Figure 3.5 (b) depicts the parameters extracted from the fit, where R_S is the mean radius along the short axis of the ellipsoid, R_L is the mean radius along the long axis of the ellipsoid, and the scattering length density (SLD) contrast is a parameter describing the compositional difference between the ellipsoids and surrounding matrix. The lognormal domain size-dispersity (SD) of R_S and R_L is displayed in Figures B.24 and B.25.

From the previously discussed GIXRD, I7TBT and I8TBT MCs form pure crystalline phases when mixed with PCBM. Since the SLD for neutrons depends on the atomic density and composition of each phase, the ellipsoid SLDs (Table B.20) are estimated from unit cell information obtained from single crystal simulations (Table B.2). The SLD of a pure crystalline PCBM domain is also shown in Table B.20.[38] The expected SLD contrast for pure I*n*TBT and PCBM domains is 3.3-3.4 $\times 10^{-6}$ $Å^{-2}$. Since the measured SLD contrast between the ellipsoidal I*n*TBT domains and the surrounding matrix is much smaller than expected for pure domains ($\sim$1.2 $\times 10^{-6}$ $Å^{-2}$) and since PCBM forms pure clusters that are too small to be detected with SANS (Table B.19), the matrix is assumed to be a mixed I*n*TBT:PCBM domain. For I7TBT and I8TBT, the total volume fraction of the ellipsoidal domains ($\phi_{Ellipsoid}$) are determined with Equations B.3 and B.7 (Table 3.3), where the partial volume fractions of PCBM and I*n*TBT are known from solution concentrations. As the linear I*n*TBT side chain is increased from 7 to 8 carbons R_S decreases from 5.3 $\pm$ 0.1 to 3.0 $\pm$ 0.5 nm and R_L remains consistent at 13.5 $\pm$0.4 and 13.4 $\pm$ 0.6 nm respectively. So the needle length is maintained but the diameter narrowed. I8TBT also has more I*n*TBT dispersed in the mixed phase as seen in the decreased SLD contrast from 1.26 to 1.18 $\times 10^{-6} Å^{-2}$. This means that I8TBT has a reduced volume percent of ellipsoidal I*n*TBT domains of 26% compared to 28% for I7TBT.

As shown by GIXRD, I*n*TBTs with linear side chains $n \geq 9$ allow PCBM to intercalate into the I*n*TBT crystalline domains resulting in a further reduction in the SLD contrast. Thus the model now corresponds to mixed I*n*TBT-rich I*n*TBT:PCBM ellipsoids in a matrix of amorphous PCBM-rich mixed domain. As the linear I*n*TBT side chain is increased from 9 to 10 carbons, R_L increases from 15.6 $\pm$ 1.5 to 21.8 $\pm$ 0.5 nm and R_S remains consistent at 4.3 $\pm$ 0.2 and 4.2 $\pm$ 0.2 nm respectively. So the mixed crystalline I*n*TBT:PCBM needles become longer while maintaining roughly the same diameter as I8TBT and I7TBT. Interestingly, the I11TBT sample contained the largest ellipsoids in both dimensions with a R_S of 7.1 $\pm$ 0.1 nm and an R_L of 23.1 $\pm$ 0.5 nm. All of the I*n*TBT films show an increasing scattering intensity through the low Q detector limit. The slope of the intensity increase at low Q follows Porod's Law [39] which suggests the presence of larger structures ($>$ 200 nm) in the films that are outside our instruments measurement range.

SANS data was also collected for IHDTBT:PCBM. The intensity profile was best fit to two models (Figure B.26). A spherical form factor was fit to the bend in the spectrum at Q=.05 $Å^{-1}$ and a fuzzy sphere (FS) form factor was fit to the low Q intensity, the combined fit is shown in Figure 3.5.[37] The spherical radius is 4.8 $\pm$ 0.2 nm, plotted as R_S, and the mean FS radius is 52.2 $\pm$ 0.2 nm, plotted as R_L. The surface of the FS is smeared with a Gaussian to obtain a gradual drop off in SLD, the width of the smeared surface interface is 3.7 $\pm$ 0.3 nm. Similar to the I*n*TBTs with linear side chains, IHDTBT forms a distribution of domain sizes ranging from 20 - 80 nm (Figure B.27). IHDTBT:PCBM films are more phase segregated resulting in the increased SLD contrast between the FS and the surrounding matrix of 1.89×10^{-6} $Å^{-2}$.

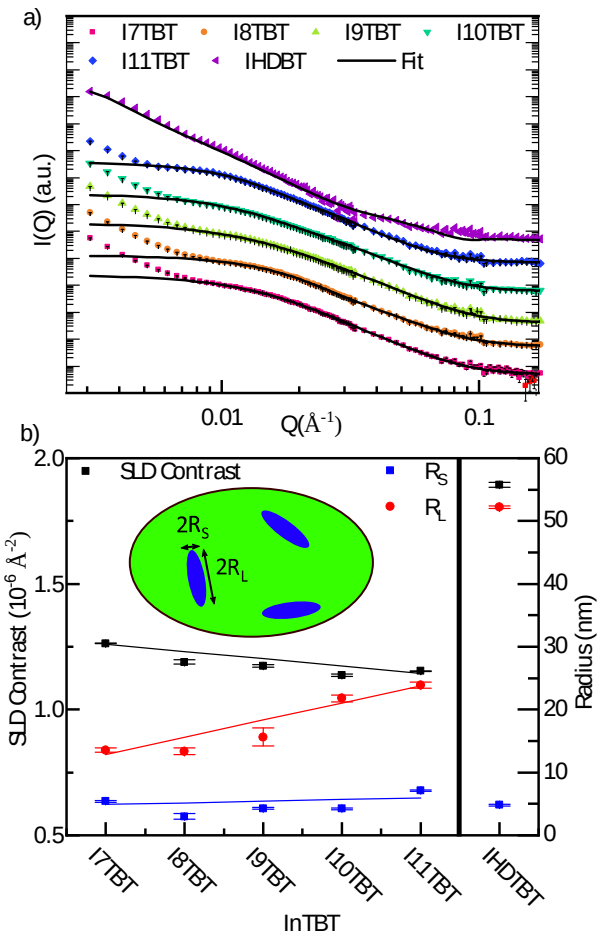

Figure 3.5. a) Small Angle Neutron Scattering data (offset for clarity) of I*n*TBT:PCBM films. I*n*TBTs with linear side chain were fit to an ellipsoidal form factor. IHDTBT was fit with a fuzzy sphere form factor at low Q and a spherical form factor at high Q, the combined fit is plotted. b)(Left axis) Scattering length density (SLD) contrast (black squares) between the form factor and surrounding matrix. (Right axis) Mean short (R_S)(blue squares) and long (R_L)(red dots) ellipsoidal radii from linear I*n*TBT fits. For IHDTBT, the mean fuzzy sphere radii is plotted as (R_L), and the spherical radii is plotted as (R_S).

Table 3.3. Volume fraction of I7TBT and I8TBT in ellipsoidal and mixed domains obtained from SANS fits, and volume fraction of PCBM in mixed domains from sample preparation.

Merocyanine	$\Phi^{InTBT}_{Ellipsoid}$	Φ^{InTBT}_{Mixed}	Φ^{PCBM}_{Mixed}
I7TBT	0.28	0.21	0.52
I8TBT	0.26	0.24	0.50

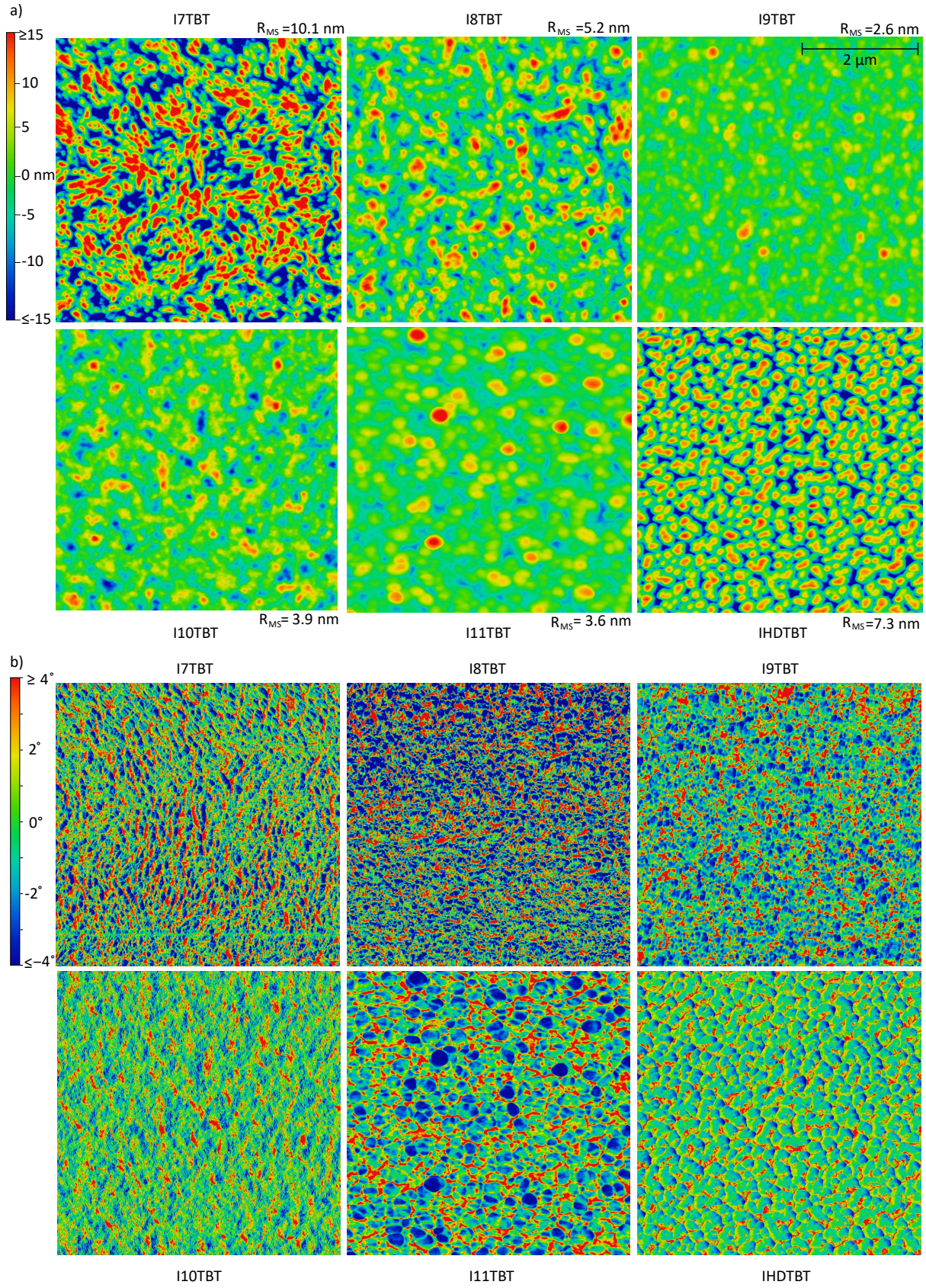

Figure 3.6. Atomic Force Microscope (a) height images with mean square roughness (R_{MS}) and (b) phase images of I*n*TBT:PCBM films.

We use AFM to study the mesoscale (25 nm$-$ 5 μm) surface structures on InTBT:PCBM films ($7 \leq n \leq 11$, and $n =$ HD). Figure 3.6 (a) depicts the height profile and root mean square roughness (R_{MS}) of the films. I7TBT:PCBM and IHDTBT:PCBM have the largest R_{MS} of 10.1 $\pm$0.5 nm and 7.3 $\pm$0.5 nm respectively. These films exhibit depressions in the surface that dig $>$ 50% down into the 70 nm films. This is in agreement with SANS and GIXRD; I7TBT and IHDTBT phase segregate when mixed with PCBM resulting in increased surface roughness. The I7TBT:PCBM surface shows a connected network of elongated domains with lateral size variations 200 $\pm$ 110 nm, while the IHDTBT surface shows round unconnected domains on the order of 240 $\pm$ 80 nm. I8TBT:PCBM film surface forms elongated domains (on the size of 210 $\pm$ 100 nm) that are less pronounced than the I7TBT:PCBM film and has an R_{MS} of 5.2 $\pm$0.5 nm. The similar domain size but reduced fraction of InTBT domains is consistent with the SANS analysis of I7TBT:PCBM and I8TBT:PCBM. Pure InTBT crystals are still present as the side chain is increased to $n = 8$ but the longer side chain begins to reduce mesoscopic phase segregation. In accordance with GIXRD and SANS, the I9TBT:PCBM, I110TBT:PCBM and I11TBT:PCBM films form large mixed domains that result in a low R_{MS} of 2.6 $\pm$0.5, 3.9 $\pm$0.5, and 3.6 $\pm$0.5 nm respectively.

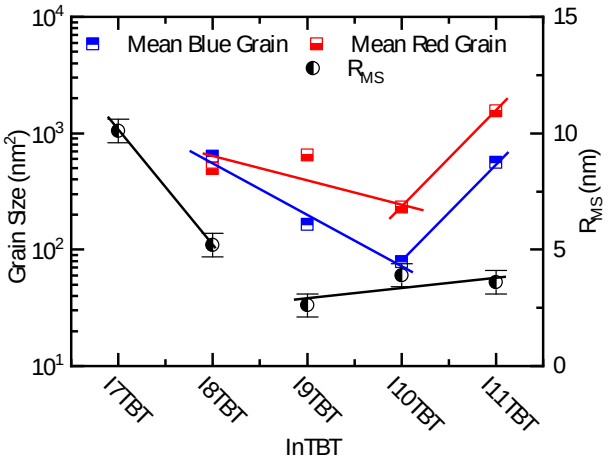

Figure 3.7. (Left) Mean grain size from AFM phase images of InTBT:PCBM films. Grains are defined by a cutoff phase shift; red (InTBT-rich) grains have greater than 4° phase shift and blue (PCBM-rich) grains have less than -4° phase shift. (Right) Root mean square roughness (R_{MS}) from corresponding AFM height images.

The phase images provide finer detail of the surface composition. Figure 3.6 (b) shows the corresponding AFM phase images. It is clear that the phase domains for I7TBT:PCBM,

I11TBT:PCBM, and IHDTBT:PCBM directly correlate to features observed in the height images. Since I7TBT:PCBM and IHDTBT:PCBM films have the roughest surface topography and the phase shift has a pattern of increasing and decreasing($\pm 10^{\circ}$ for I7TBT and $\pm 7.5^{\circ}$ for IHDTBT) on the edges of raised surface domains, the observed phase shift is likely an instrument artifact; the tapping AFM tip phase shifts as the tip travels up over a raised surface domain and shifts in the opposite direction as the tip travels down into a depression in the film surface. For this reason we choose to exclude those films from the following phase analysis. This is not observed in the I11TBT:PCBM film due to its lower surface roughness. For I11TBT:PCBM the raised domains in the height image are compositionally different from the surrounding film. Figure 3.7 compares the mean grain sizes extracted from the phase images and R_{MS} from height images. The grains are defined by a cutoff phase shift. Red grains have $> 4^{\circ}$ phase shift, corresponding to I*n*TBT-rich domains, and blue grains have $< -4^{\circ}$ phase shift, corresponding to PCBM-rich domains. Figure 3.7 depicts mean blue (PCBM-rich) and red (I*n*TBT-rich) grain size; grain size distributions are shown in Figures B.28 and B.29. Starting with the shortest side chain film the I8TBT phase image shows networks of interconnected domains resulting in the relatively large mean PCBM-rich grain size of 630 nm^2, and a mean I*n*TBT-rich grain size of 500 nm^2. As the side chain is increased, I9TBT forms domains with reduced connectivity resulting in mean PCBM-rich and I*n*TBT-rich grain sizes of 160 and 650 nm^2 respectively. I10TBT forms a well mixed film surface resulting the smoothest phase images with mean PCBM-rich and I*n*TBT-rich grain sizes of 80 and 230 nm^2. As the side chain is increased further, the I11TBT films begin to form large disconnected domains with mean PCBM-rich and I*n*TBT-rich grain sizes of 560 and 1540 nm^2.

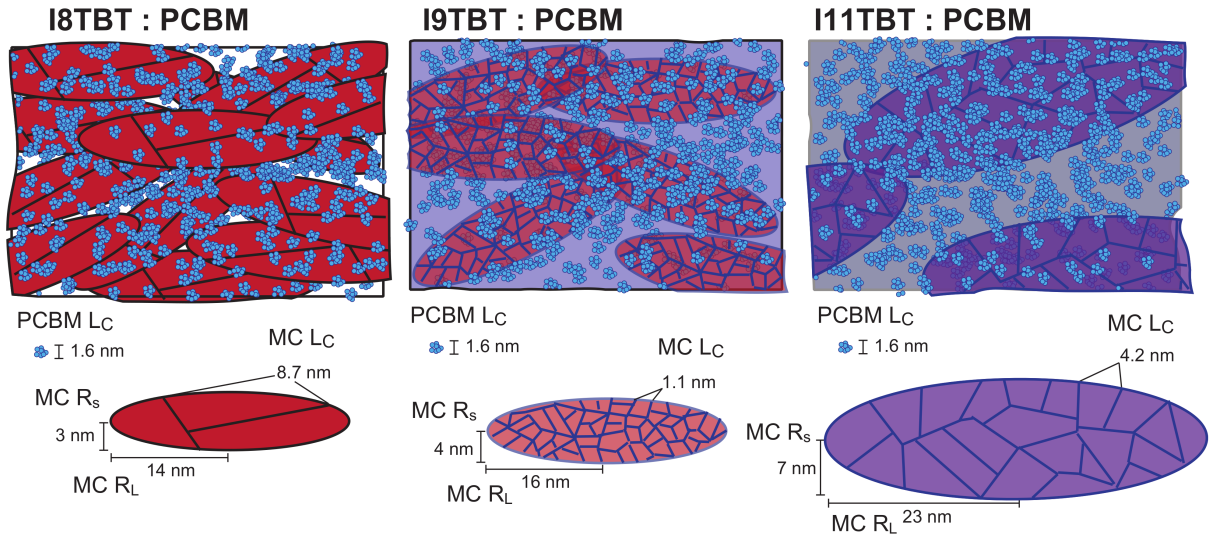

Figure 3.8. Illustration representing the bulk morphological differences observed between I8TBT:PCBM, I9TBT:PCBM, and I11TBT:PCBM films. L_C is coherence length from GIXRD, R_S and R_L are the short and long ellipsoidal radii from SANS.

3.5 Discussion

This series of I*n*TBTs with varying linear side chain length demonstrate the morphologically controlled balance between exciton dissociation, charge carrier transport, and recombination. A generated exciton can diffuse up to 10 nm before geminate recombination (GR) occurs.[40, 41] Charge separation is maximized when I*n*TBT domain size is minimized to increase the probability of an exciton being generated within 5-10 nm of a I*n*TBT/PCBM interface.[40, 41] However there is a necessary balance between exciton dissociation and free charge carrier transport. Small disconnected I*n*TBT domains reduce hole transport through the film and increase trap sites for free charge carriers increasing nongeminate recombination (NGR) rates.[42]

Figure 3.8 illustrates the bulk morphologies reported by GIXRD and SANS for I8TBT:PCBM, I9TBT:PCBM, and I11TBT:PCBM. The PCBM coherence length remains constant at 1.6 nm. I8TBT:PCBM films form pure MC ellipsoids (R_S = 3 nm, R_L = 14 nm) composed of crystalline MC domains with a large MC coherence length (8.7 nm), that are surrounded by a mixed MC:PCBM domain. I9TBT:PCBM films form larger mixed ellipsoids (R_S = 4 nm, R_L = 16 nm) with a shorter MC coherence length (1.1 nm), also surrounded by a mixed MC:PCBM domain. Finally, I11TBT:PCBM films form even larger, more mixed ellipsoids (R_S = 7 nm, R_L = 23 nm), composed of MC crystalline regions with increased coherence length (4.2 nm).

GIXRD shows that I6TBT through I8TBT form pure crystalline phases in InTBT:PCBM films. When the side chain length is increased to $n \geq 9$, PCBM mixes with InTBT significantly broadening the observed diffraction peaks. Of the InTBTs with linear side chains, I6TBT:PCBM films have the lowest FF and V_{OC}. GIXRD demonstrates the presence of small unmixed I6TBT domains (L_C = 4.1 nm) which results in high geminate recombination rates. Since our BHJs were fabricated with a 2:3 InTBT:PCBM weight fraction and I6TBT has the lowest molecular weight out of the studied materials, BHJs with I6TBT have the highest molar ratio of InTBT to PCBM. This resulted in a stronger absorbance and the highest J_{SC} of 8.29 $\frac{mA}{cm^2}$. Likewise, I12TBT:PCBM films have the lowest molar ratio of InTBT to PCBM resulting in the lowest J_{SC} of 6.20 $\frac{mA}{cm^2}$. GIXRD shows that the 12 carbon linear side chain on I12TBT allows strong mixing between I12TBT and PCBM, which resulted in lower V_{OC} and FF. Since BHJs with I6TBT and I12TBT show reduced PCE due to little and too much mixing respectively, we chose to exclude I6TBT and I12TBT from further morphological analysis.

I7TBT and I8TBT BHJs have the same V_{OC}= 0.89 V. They both form pure crystalline domains when mixed with PCBM with a L_C of 7.5 and 8.7 nm respectively. The SANS data shows R_L of $\sim$5 nm for all films, which should mean that all excitons can reach a donor/acceptor interface, minimizing GR. The topography of the I7TBT:PCBM film shows a larger surface roughness than I8TBT:PCBM due to decreased miscibility. The I8TBT:PCBM film has fewer pure InTBT domains and more InTBT in the mixed phase leading to increases in J_{SC} and FF. Finally the I8TBT:PCBM film has the highest PCE of 4.5%, due to a combination of high J_{SC} and FF.

OPV devices with I9TBT, I10TBT, and I11TBT have the same V_{OC} = 0.90 V. They do not form pure crystalline domains when mixed with PCBM and have a much lower coherence length than I7TBT or I8TBT BHJs for both InTBT and PCBM rich domains. Curiously, in spite of the increased domain size and the onset of InTBT:PCBM mixing with increased side chain length, the JV characteristics show a remarkably consistent and smooth trend in device characteristics with V_{OC} peaking for $n = 9 - 11$, J_{SC} peaking for $n = 8$, and FF peaking for $n = 11$. Thus I9TBT:PCBM films also produce the highest PCE of 4.5%, even though GIXRD and AFM show they form an entirely different structural motif compared to I8TBT:PCBM films. SANS demonstrates InTBTs with $n \geq 9$ form ellipsoidal InTBT domains with reduced

SLD contrast due to the presence of PCBM in both the ellipsoid and the surrounding matrix. The J_{SC} decreases with $n > 8$ because the increased side chain length effectively means lower absorption coefficient for the 2:3 I*n*TBT:PCBM film. The increase of FF with increased n may be due to a relative $v\%$ increase in acceptor.[43]

In spite of the most favorable absorbance, the branched side IHDTBT:PCBM device exhibited the worst OPV performance due to unfavorable morphology across several orders of magnitude. GIXRD shows the long branched side chains inhibit intercalation of the PCBM into IHDTBT domains. This is confirmed by the increased SLD contrast from SANS. It should be noted that an increased SLD contrast is also caused by increased ^{1}H density on the longer side chains. SANS demonstrates the presence of small $\sim$10 nm IHDTBT domains however both SANS and AFM show IHDTBT forms large pure domains on the order of 100-240 nm significantly increasing the geminate recombination rates which results in the low J_{SC} of 2.03 $\frac{mA}{cm^2}$ and PCE of 0.6%.

It is useful to speculate what the device optimization and morphology assessment performed here indicates about the device efficiency limits for I*n*TBT:PCBM OPVs. V_{OC} is quite high at 0.9 V and essentially the same for all linear I*n*TBTs, therefore it does not need to be optimized. Our analysis fixed the OPV layer thickness at 70 nm and wt. ratio of I*n*TBT:PCBM at 2:3 because these parameters came from a prior optimization of MC:PCBM solubility.[27] The trend in FF indicates that the hole and electron currents are well balanced with little bimolecular recombination in films up to 70 nm device thickness. With such high FF and no optimization of the mixing ratio, it is likely that layer thicknesses of up to $\sim$ 200 nm would still have FF above 0.6. Given the absorbance up to $\sim$ 725 nm (which is $\sim$ 1.7 eV) one could expect J_{SC} of up to 15 $\frac{mA}{cm^2}$ under AM1.5 illumination and an optimized PCE of 6.5-8%.[44]

Another intriguing series of future experiments should focus on mixing multiple different I*n*TBTs with fullerenes. Since the I*n*TBTs form mixed structures for $n \geq 9$ and $n \leq 8$ form pure domains, one could exert far more control over the morphology using a combination of I*n*TBTs with mixed side chain lengths to obtain even greater improvements to the FF.

Although PCEs reported in this manuscript could be considered relatively low compared to recent record small molecule devices, we point out that D-A MC dyes are extremely inex-

pensive. Previous small molecule OPV studies claim that D-A-D like structures are needed to prevent dipole alignment between neighboring molecules in order to obtain high PCEs. However, we demonstrate that decent PCEs can be obtained through morphological optimization of D-A systems and that the miscibility with a PCBM acceptor can be tuned through a range of domain sizes and mixing ratios.

3.6 Conclusions

This manuscript demonstrates a novel series of MC dyes with varying hydrocarbon side chain length. BHJ OPV devices were fabricated with 2:3 wt. ratio I*n*TBT:PCBM and characterized as a function of side chain length. A maximum PCE of $4.5 \pm 0.1\%$ was extracted from I8TBT:PCBM and I9TBT:PCBM devices. As expected, tuning the side chain length allows careful adjustment of the miscibility between the donor and acceptor, thereby enabling optimization of film morphology and OPV performance characteristics. Hierarchical structure formation was studied using GIXRD (Å), SANS (3-200 nm), and AFM (25 nm$-$ 5 μm). When mixed with PCBM, I*n*TBTs with ≤ 8 side chain carbons form pure crystalline domains, while I*n*TBTs with ≥ 9 side chain carbons form mixed domains with PCBM. SANS demonstrates that increasing side chain length increases I*n*TBT-rich domain size while at the same time allowing for mixed domains for n ≥ 9. The branched side chain IHDTBT:PCBM film was also studied and was found to exhibit the worst performance OPV device, the large side chain inhibited mixing between IHDTBT and PCBM resulting in large segregated phases. Further optimization of the mixing ratios and layer thickness could nearly double the OPV performance. Ternary mixtures of I*n*TBTs with different side chain length could enable even more control over BHJ morphology.

3.7 Supporting Information

Synthesis, ultraviolet visible spectroscopy, crystal Stacking, grazing incidence x-ray diffraction analysis, small angle neutron scattering analysis, atomic force microscopy analysis

3.8 Acknowledgments

This project was supported by the U.S. Department of Energy, Office of Basic Energy Sciences, Division of Materials Sciences and Engineering, under Award No. DE-SC0010419, and the German Federal Office of Science and Technology (BMBF, MEDOS FKZ: 03EK3505I). Thanks to the Alexander von Humboldt Foundation and to the Universität zu Köln alumni fellowship fund. for sabbatical funding for A.J.M.. Thanks to the Jülich Centre for Neutron Science at Heinz Maier-Leibnitz Zentrum in Garching, Germany for Small-Angle Neutron Scattering measurement time. This work benefited from the use of the SasView application, originally developed under NSF award DMR-0520547. SasView contains code developed with funding from the European Unions Horizon 2020 research and innovation programme under the SINE2020 project, grant agreement No 654000

3.9 Conflicts of Interest

There are no conflicts of interest to declare.

REFERENCES

[1] J. Roncali, P. Leriche, and P. Blanchard, "Molecular materials for organic photovoltaics: Small is beautiful," *Adv. Mater.*, vol. 26, no. 23, pp. 3821–3838, 2014.

[2] R. Augulis, A. Devizis, D. Peckus, V. Gulbinas, D. Hertel, and K. Meerholz, "High electron mobility and its role in charge carrier generation in merocyanine/fullerene blends," *J. Phys. Chem. C*, vol. 119, pp. 5761–5770, Mar. 2015.

[3] A. Arjona-Esteban, J. Krumrain, A. Liess, M. Stolte, L. Huang, D. Schmidt, V. Stepanenko, M. Gsanger, D. Hertel, K. Meerholz, and F. Wurthner, "Influence of solid-state packing of dipolar merocyanine dyes on transistor and solar cell performances," *J. Am. Chem. Soc.*, vol. 137, pp. 13524–13534, Oct. 2015.

[4] N. M. Kronenberg, H. Bürckstümmer, M. Deppisch, F. Würthner, and K. Meerholz, "Optimized solution-processed merocyanine:pcbm organic bulk heterojunction solar cell," *J. Photonics Energy*, vol. 1, no. 1, pp. 1 – 8 – 8, 2011.

[5] A. K. Ghosh and T. Feng, "Merocyanine organic solar cells," *J. Appl. Phys.*, vol. 49, no. 12, pp. 5982–5989, 1978.

[6] F. Würthner and K. Meerholz, "Systems chemistry approach in organic photovoltaics," *Chemistry A European Journal*, vol. 16, no. 31, pp. 9366–9373, 2010.

[7] A. Mishra and P. Bauerle, "Small molecule organic semiconductors on the move: Promises for future solar energy technology," *Angew. Chem. Int. Ed.*, vol. 51, pp. 2020–2067, Feb. 2012.

[8] Y. Lin, Y. Li, and X. Zhan, "Small molecule semiconductors for high-efficiency organic photovoltaics," *Chem. Soc. Rev.*, vol. 41, pp. 4245–4272, 2012.

[9] Y. Li, Q. Guo, Z. Li, J. Pei, and W. Tian, "Solution processable d-a small molecules for bulk-heterojunction solar cells," *Energy Environ. Sci.*, vol. 3, pp. 1427–1436, 2010.

[10] A. Liess, A. Arjona-Esteban, A. Kudzus, J. Albert, A.-M. Krause, A. Lv, M. Stolte, K. Meerholz, and F. Wrthner, "Ultranarrow bandwidth organic photodiodes by exchange narrowing in merocyanine h- and j-aggregate excitonic systems," *Adv. Funct. Mater.*, vol. 29, no. 21, p. 1805058, 2019.

[11] N. M. Kronenberg, M. Deppisch, F. Würthner, H. W. A. Lademann, K. Deing, and K. Meerholz, "Bulk heterojunction organic solar cells based on merocyanine colorants," *Chem. Commun.*, pp. 6489–6491, 2008.

[12] V. Steinmann, N. M. Kronenberg, M. R. Lenze, S. M. Graf, D. Hertel, H. Bürckstümmer, F. Würthner, and K. Meerholz, "A simple merocyanine tandem solar cell with extraordinarily high open-circuit voltage," *Appl. Phys. Lett.*, vol. 99, no. 19, p. 193306, 2011.

[13] V. Steinmann, N. M. Kronenberg, M. R. Lenze, S. M. Graf, D. Hertel, K. Meerholz, H. Bürckstümmer, E. V. Tulyakova, and F. Würthner, "Simple, highly efficient vacuum-processed bulk heterojunction solar cells based on merocyanine dyes," *Adv. Energy Mater.*, vol. 1, no. 5, pp. 888–893, 2011.

[14] H. Bürckstümmer, E. V. Tulyakova, M. Deppisch, M. R. Lenze, N. M. Kronenberg, M. Gsanger, M. Stolte, K. Meerholz, and F. Würthner, "Efficient solution-processed bulk heterojunction solar cells by antiparallel supramolecular arrangement of dipolar donor-acceptor dyes," *Angew. Chem. Int. Ed.*, vol. 50, pp. 11628–11632, Dec. 2011.

[15] N. Gräß er, S. Wolf, F. Holzmüller, O. Zeika, K. Vandewal, and K. Leo, "Heteroquinoid merocyanine dyes with high thermal stability as absorber materials in vacuum-processed organic solar cells," *Eur. J. Org. Chem.*, vol. 2019, no. 4, pp. 845–851, 2019.

[16] Z. Wang, L. Zhu, Z. Shuai, and Z. Wei, "A-π-d-π-a electron-donating small molecules for solution-processed organic solar cells: A review," *Macromol. Rapid Commun.*, vol. 38, no. 22, p. 1700470, 2017.

[17] R. Zhou, Z. Jiang, C. Yang, J. Yu, J. Feng, M. A. Adil, D. Deng, W. Zou, J. Zhang, K. Lu, W. Ma, F. Gao, and Z. Wei, "All-small-molecule organic solar cells with over 14morphologies," *Nat. Commun.*, vol. 10, p. 5393, Nov. 2019.

[18] S. M. Menke and R. J. Holmes, "Exciton diffusion in organic photovoltaic cells," *Energy Environ. Sci.*, vol. 7, pp. 499–512, 2014.

[19] N. J. Hestand and F. C. Spano, "Expanded theory of h- and j-molecular aggregates: The effects of vibronic coupling and intermolecular charge transfer," *Chem. Rev.*, vol. 118, no. 15, pp. 7069–7163, 2018. PMID: 29664617.

[20] M. Chang, L. Meng, Y. Wang, X. Ke, Y.-Q.-Q. Yi, N. Zheng, W. Zheng, Z. Xie, M. Zhang, Y. Yi, H. Zhang, X. Wan, C. Li, and Y. Chen, "Achieving an efficient and stable morphology in organic solar cells via fine-tuning the side chains of small-molecule acceptors," *Chem. Mater.*, vol. 32, no. 6, pp. 2593–2604, 2020.

[21] B. Qiu, S. Chen, L. Xue, C. Sun, X. Li, Z.-G. Zhang, C. Yang, and Y. Li, "Effects of alkoxy and fluorine atom substitution of donor molecules on the morphology and photovoltaic performance of all small molecule organic solar cells," *Front. Chem.*, vol. 6, p. 413, 2018.

[22] M. J. Jurow, B. A. Hageman, E. DiMasi, C.-Y. Nam, C. Pabon, C. T. Black, and C. M. Drain, "Controlling morphology and molecular packing of alkane substituted phthalocyanine blend bulk heterojunction solar cells," *J. Mater. Chem. A*, vol. 1, pp. 1557–1565, 2013.

[23] L. Krause, R. Herbst-Irmer, G. M. Sheldrick, and D. Stalke, "Comparison of silver and molybdenum microfocus x-ray sources for single-crystal structure determination," *J. Appl. Crystallogr.*, vol. 48, pp. 3–10, Feb 2015.

[24] G. M. Sheldrick, "*SHELXT* – Integrated space-group and crystal-structure determination," *Acta Crystallogr., Sect. A: Found. Crystallogr.*, vol. 71, pp. 3–8, Jan 2015.

[25] C. Elschner, A. A. Levin, L. Wilde, J. Grenzer, C. Schroer, K. Leo, and M. Riede, "Determining the c60 molecular arrangement in thin films by means of x-ray diffraction," *J. Appl. Crystallogr.*, vol. 44, pp. 983–990, Oct 2011.

[26] N. M. Kronenberg, V. Steinmann, H. Bürckstümmer, J. Hwang, D. Hertel, F. Würthner, and K. Meerholz, "Direct comparison of highly efficient solution- and vacuum-processed

organic solar cells based on merocyanine dyes," *Adv. Mater.*, vol. 22, no. 37, pp. 4193–4197, 2010.

[27] M. R. Lenze, N. M. Kronenberg, F. Würthner, and K. Meerholz, "In-situ modification of pedot:pss work function using alkyl alcohols as secondary processing solvents and their impact on merocyanine based bulk heterojunction solar cells," *Org. Electron.*, vol. 21, pp. 171 – 176, 2015.

[28] B. Qi and J. Wang, "Fill factor in organic solar cells," *Phys. Chem. Chem. Phys.*, vol. 15, pp. 8972–8982, 2013.

[29] M.-H. Jao, H.-C. Liao, and W.-F. Su, "Achieving a high fill factor for organic solar cells," *J. Mater. Chem. A*, vol. 4, pp. 5784–5801, 2016.

[30] F. Sánchez-Bajo and F. L. Cumbrera, "The Use of the Pseudo-Voigt Function in the Variance Method of X-ray Line-Broadening Analysis," *J. Appl. Crystallogr.*, vol. 30, pp. 427–430, Aug 1997.

[31] J. Olivero and R. Longbothum, "Empirical fits to the voigt line width: A brief review," *J. Quant. Spectrosc. Radiat. Transfer*, vol. 17, no. 2, pp. 233 – 236, 1977.

[32] W. H. Bragg and W. L. Bragg, "The reflection of x-rays by crystals," *Proc. Roy. Soc. London*, vol. 88, no. 605, pp. 428–438, 1913.

[33] A. L. Patterson, "The scherrer formula for x-ray particle size determination," *Phys. Rev.*, vol. 56, pp. 978–982, Nov 1939.

[34] J. Rivnay, R. Noriega, R. J. Kline, A. Salleo, and M. F. Toney, "Quantitative analysis of lattice disorder and crystallite size in organic semiconductor thin films," *Phys. Rev. B*, vol. 84, p. 045203, Jul 2011.

[35] R. Mens, S. Chambon, S. Bertho, G. Reggers, B. Ruttens, J. D'Haen, J. Manca, R. Carleer, D. Vanderzande, and P. Adriaensens, "Description of the nanostructured morphology of [6,6]-phenyl-c61-butyric acid methyl ester (pcbm) by xrd, dsc and solid-state nmr," *Magn. Reson. Chem.*, vol. 49, no. 5, pp. 242–247, 2011.

[36] I. Toyoko, K. Toshiji, F. Michihiro, and T. Naoya, *Neutrons in Soft Matter*. Wiley, 2011.

[37] D. I. S. L. A. Feigin, *Structure Analysis by Small-Angle X-Ray and Neutron Scattering*. Springer, 1987.

[38] A. J. Clulow, A. Armin, K. H. Lee, A. K. Pandey, C. Tao, M. Velusamy, M. James, A. Nelson, P. L. Burn, I. R. Gentle, and P. Meredith, "Determination of fullerene scattering length density: A critical parameter for understanding the fullerene distribution in bulk heterojunction organic photovoltaic devices," *Langmuir*, vol. 30, pp. 1410–1415, Feb. 2014.

[39] S. K. Sinha, E. B. Sirota, S. Garoff, and H. B. Stanley, "X-ray and neutron scattering from rough surfaces," *Phys. Rev. B*, vol. 38, pp. 2297–2311, Aug 1988.

[40] L. Dou, J. You, Z. Hong, Z. Xu, G. Li, R. A. Street, and Y. Yang, "25th anniversary article: A decade of organic/polymeric photovoltaic research," *Adv. Mater.*, vol. 25, pp. 6642–6671, Dec. 2013.

[41] M. Wojcik, A. Nowak, and K. Seki, "Geminate electron-hole recombination in organic photovoltaic cells. a semi-empirical theory," *J. of Chem. Phys.*, vol. 146, no. 5, p. 054101, 2017.

[42] C. Gohler, A. Wagenpfahl, and C. Deibel, "Nongeminate recombination in organic solar cells," *Adv. Electron. Mater.*, vol. 4, p. 1700505, Oct. 2018.

[43] A. J. Moulé, J. B. Bonekamp, and K. Meerholz, "The effect of active layer thickness and composition on the performance of bulk-heterojunction solar cells," *J. Appl. Phys.*, vol. 100, no. 9, p. 094503, 2006.

[44] M. Scharber, D. Mhlbacher, M. Koppe, P. Denk, C. Waldauf, A. Heeger, and C. Brabec, "Design rules for donors in bulk-heterojunction solar cellstowards 10% energy-conversion efficiency," *Adv. Mater.*, vol. 18, no. 6, pp. 789–794, 2006.

Chapter 4

Anion Exchange Doping: Tuning Equilibrium to Increase Doping Efficiency in Semiconducting Polymers

4.1 Preface

In this chapter, I am reprinting a Letter I wrote on a novel doping process that improves doping efficiencies in semiconducting polymers; DOI: 10.1021/acs.jpclett.0c03620. High electron affinity (EA) molecules p-type dope low ionization energy (IE) polymers resulting in an equilibrium doping level based on the energetic driving force (IE-EA), reorganization energy, and dopant concentration. Anion exchange doping (AED) is a process whereby the dopant anion is exchanged with a stable ion from an electrolyte. We show that AED level can be predicted using an isotherm equilibrium model. The exchange of the dopant anion ($FeCl_3^-$) for bis(trifluoromethanesulfonamide) ($TFSI^-$) anion in the polymers poly(3-hexylthiophene-2,5-diyl) (P3HT) and poly[3-(2,2-bithien-5-yl)-2,5-bis(2-hexyldecyl)-2,5-dihydropyrrolo[3,4-c]pyrrole-1,4-dione-6,5-diyl] (PDPP-2T) highlights two cases in which the process is non-spontaneous and spontaneous, respectively. For P3HT, $FeCl_3$ provides a high doping level but an unstable counter ion, so exchange results in an air stable counter ion with a marginal increase in doping. For PDPP-2T, $FeCl_3$ is a weak dopant, but the exchange of $FeCl_3^-$ for $TFSI^-$ is spontaneous, so the doping level increases by $>$10x with AED.

4.2 Introduction

Sequential doping of semiconducting polymers (SPs) is a well studied method for tuning SP film conductivity and solubility, while maintaining a film morphology that is ideal for efficient charge transport.[1, 2, 3, 4] Multiple studies have demonstrated that morphology control and sequential doping are essential for obtaining efficient electronic devices, including organic thermoelectrics, organic field effect transistors, and organic electrochemical transistors.[5, 6, 7, 8, 9] Recently, Yamashita et al. demonstrated an improvement to molecular doping efficiency through a process termed Anion Exchange Doping (AED).[10] By immersing a poly(2,5-bis(3-tetradecylthiophen-2-yl)thieno[3,2-b]thiophene) (PBTTT) film into a solution with the molecular dopant 2,3,5,6-tetrafluoro-7,7,8,8-tetracyanoquinodimethane (F4TCNQ) and various electrolytes they sequentially doped the polymer and exchanged the $F4TCNQ^-$ anion for the electrolyte anion. This process yields two advantages. First, the anion exchange enables the choice of a stable counter ion. Common p-type dopant anions often react with H_2O and O_2. Thus,

AED can be used to create air stable films. Second, AED enables increased film dopant levels compared to conventional doping.[10, 11] Although AED yields significant advantages, there are fundamental knowledge gaps. Currently, there is no method for predicting the equilibrium doping level or the fraction of exchanged anions. Likewise, the link between doping level and carrier density is poorly understood.

In this manuscript, first we study the relationship between solution concentrations of molecular dopants and electrolyte ions on P3HT film doping level using the dopant $FeCl_3$ and electrolyte lithium bis(trifluoromethanesulfonyl)imide (LiTFSI) pair, as developed by Jacobs et al.[11] We derive a novel anion exchange isotherm to model equilibrium processes occurring during AED and extract equilibrium constants for both doping and the subsequent anion exchange. This model predicts high p-type doping efficiency is possible in systems with low chemical potential for doping. P-type doping high IE polymers has previously been limited by inherent challenges in the synthesis of stable high EA dopants.[12, 1]. By optimizing the AED process, we reduce the need to develop stable, high EA dopants. We demonstrate that high doping levels are achieved using AED with the high IE donor-acceptor polymer poly[3-(2,2-bithien-5-yl)-2,5-bis(2-hexyldecyl)-2,5-dihydropyrrolo[3,4-c]pyrrole-1,4-dione- 6,5-diyl] (PDPP-2T).

4.3 Results and Discussion

Figure 4.1a-c illustrates the two equilibrium processes occurring during AED. The Langmuir model, when applied to sequential doping, assumes a fixed and finite number of polymer sites are available for doping and simplifies the complex morphologies present in solid state SPs by assuming that all sites have an identical energy landscape. In reality, solid state P3HT contains crystalline and amorphous regions with a variety of configurations. In Figure 4.1a, a 180 nm thick P3HT film is immersed in an 8 mL solution of 5 mM $FeCl_3$ in anhydrous n-butyl acetate (nBA). The solvent swells the film allowing $FeCl_3$ to penetrate and undergo charge transfer with P3HT resulting in $P3HT^{+}FeCl_3^{-}$, with equilibrium constant K_I (Equation C.3).[4] In Figures 4.1b and 4.1c, a P3HT film is immersed in 8 mL of 5 mM $FeCl_3$ nBA solution, this time with either 50 mM or 100 mM LiTFSI concentrations, respectively. LiTFSI dissociates into Li^{+} and $TFSI^{-}$ in nBA. $FeCl_3$ dopes the film with the same equilibrium constant, however, the charged

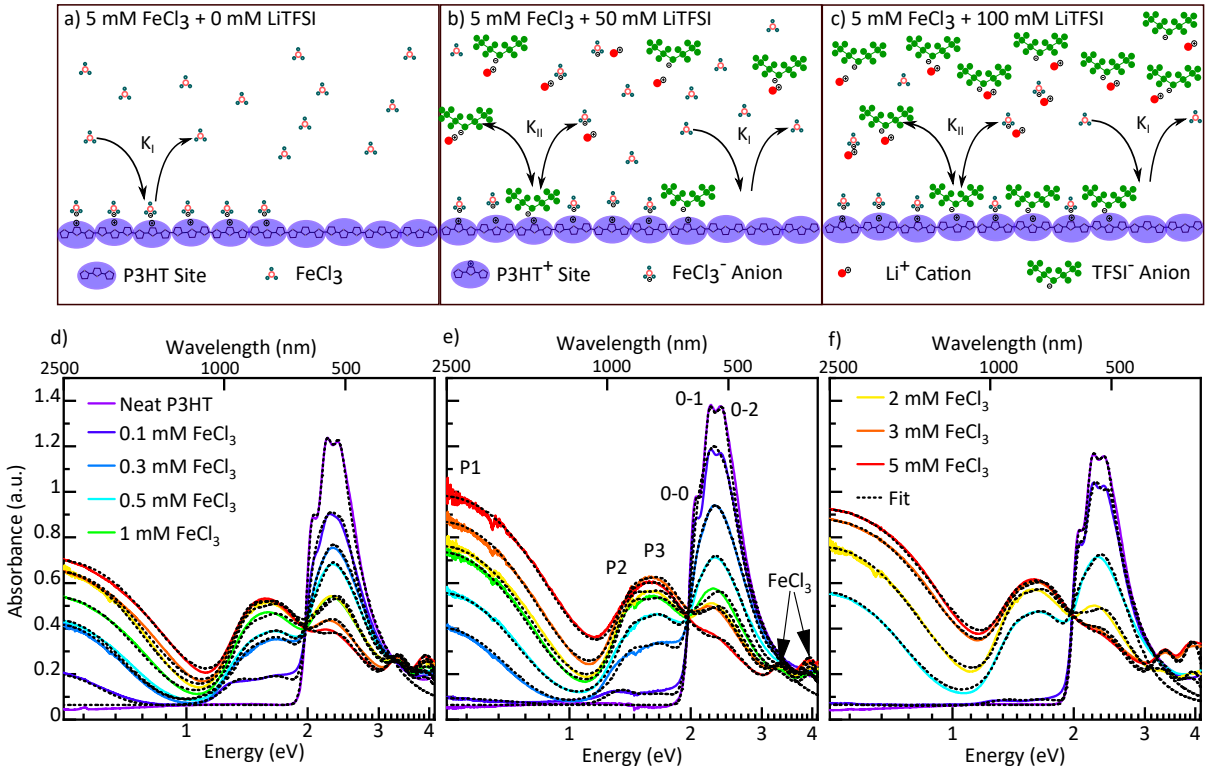

Figure 4.1. a) Illustration of $FeCl_3$ doping P3HT sites with equilibrium constant K_I. b) and c) illustrates $FeCl_3$ doping P3HT sites, where $FeCl_3^-$ is subsequently exchanged by $TFSI^-$ with equilibrium constant K_{II}. UV-Vis-NIR absorption spectra for P3HT films doped with various $FeCl_3$ solution concentrations and d) 0 mM, e) 50 mM, and f) 100 mM LiTFSI solutions, respectively.

$FeCl_3^-$ anion is now exchanged for $TFSI^-$ anion with an equilibrium constant K_{II} (Equation C.4). LiTFSI is inert towards P3HT so no third equilibrium is required.

$$\mathrm{P3HT^{(SS)} + FeCl_3{}^{(Sol.)} \rightleftharpoons P3HT^{+}/FeCl_3{}^{-(SS)}} \tag{4.1}$$

$$\mathrm{P3HT^{+}/FeCl_3{}^{-(SS)} + TFSI^{-(Sol.)} + Li^{+(Sol.)} \rightleftharpoons P3HT^{+}/TFSI^{-(SS)} + FeCl_3{}^{-(Sol.)} + Li^{+(Sol.)}} \tag{4.2}$$

Figure 4.1d shows ultraviolet-visible-near-infrared spectroscopy (UV-Vis-NIR) of sequentially doped P3HT films[2, 3] with various $FeCl_3$ solutions. Neat P3HT shows three vibronic transitions at ~2 eV (0-0), ~2.2 eV (0-1), and ~2.4 eV (0-2) in accordance with the literature.[13] As P3HT is doped to higher doping levels the neat 0-0, 0-1, and 0-2 peaks bleach and broaden while three broad $P3HT^+$ absorbance peaks grow in at 0.47 (P1), 1.25 (P2), and 1.5 (P3) eV

[14, 15, 16, 17]. As the doping level is increased, an $FeCl_3$ peak becomes apparent at $\sim$3.9 eV and an $FeCl_3^-$ peak appears at $\sim$3.4 eV.[18] UV-Vis-NIR of P3HT films sequentially doped with mixtures of $FeCl_3$ and 50 mM or 100 mM LiTFSI show similar trends (Figures 4.1e and 4.1f). Key differences are observed in the extent of bleaching of the neat P3HT vibronic transitions and corresponding growth of the broad $P3HT^+$ polaron peaks (P1, P2, and P3) with anion exchanged films yielding a 10-50% higher doping level with respect to $FeCl_3$ solutions without an electrolyte present.

Since the P3 absorbance at 1.5 eV (780 nm) overlaps the neutral P3HT absorbance, we deconvoluted overlapping peaks by globally fitting the spectral signatures between 0.5 and 4.2 eV. The cumulative fits for the 0, 50, and 100 mM LiTFSI series are shown in Figure 4.1d-4.1f, and their corresponding individual peak fits and the remaining fits for the 0.1, 1.0, 10.0, 25.0, and 75.0 mM LiTFSI concentrations are in Figures C.2-C.9. Similar to previous studies,[16] we constrained the peak positions to remain constant across all studied samples. Our discussion of the UV-Vis-NIR peak fitting is in Supporting Information Section S4.

To simplify these spectral changes with respect to doping level we define Θ as the fraction of doped P3HT sites over the total available P3HT sites. Θ is linearly approximated from optical absorbance by $\theta = \frac{A_P}{A_P + A_N}$, where A_N is the integral of the neutral P3HT absorption peaks and A_P is the integral of P1. The calculated Θ from the UV-Vis-NIR data is shown in Figure 4.2a and 4.2b. In films sequentially doped with 5 mM $FeCl_3$ concentration and no LiTFSI present, 63 $\pm$3 % of the polymer sites are doped ($\Theta = 0.63 \pm 0.03$). As LiTFSI concentration increases to 100 mM at constant 5 mM $FeCl_3$ concentration, the doping level increases to 75% ($\Theta = 0.75 \pm 0.04$).

To determine the equilibrium coefficients K_I and K_{II}, we derive a generalized Anion Exchange Isotherm (Equation 4.3) in terms of known quantities. This model represents the fraction of doped sites over total sites (Θ) for a polymer undergoing charge transfer with a molecular dopant, followed by a subsequent exchange of anions with a monovalent electrolyte. Further description of the extracted Θ and isotherm parameters are in Supporting Information Section S6. The isotherm derivation is in the Supporting Information Equations C.3-C.25.

$$\Theta = S\frac{K_I([D]-w[C^+A^-]) + \frac{K_I K_{II}([D]-w[C^+A^-])([C^+A^-]-w[C^+A^-])}{\Theta C_t^0 - K_I([D]-w[C^+A^-])(1-\Theta)C_t^0}}{1 + K_I([D]-w[C^+A^-]) + \frac{K_I K_{II}([D]-w[C^+A^-])([C^+A^-]-w[C^+A^-])}{\Theta C_t^0 - K_I([D]-w[C^+A^-])(1-\Theta)C_t^0}} \tag{4.3}$$

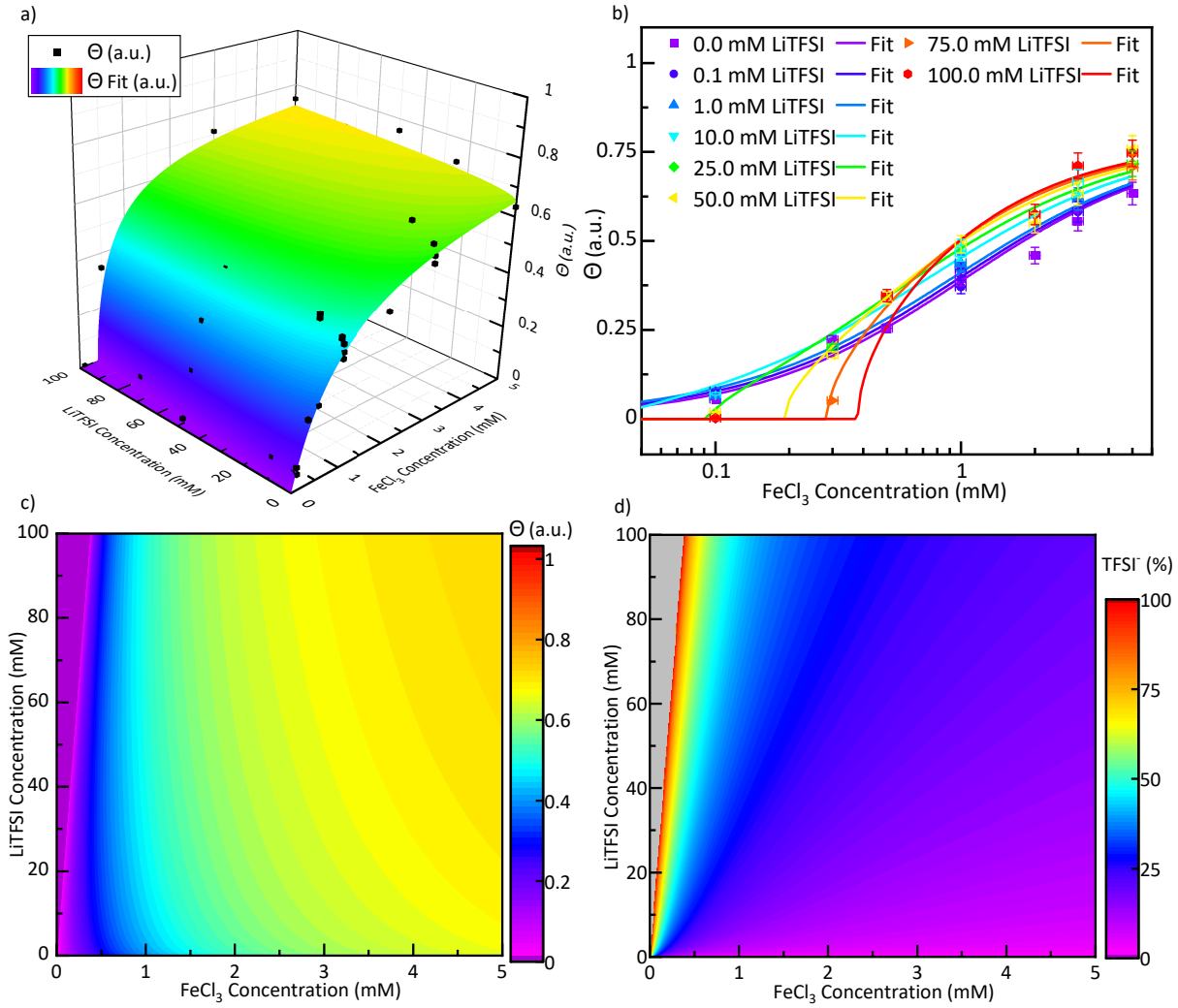

Figure 4.2. a) 3D and b) 2D scatter plots of Θ extracted from UV-Vis-NIR and corresponding anion exchange isotherm fit, c) shows the Θ fit contour with respect to the prepared $FeCl_3$ and LiTFSI concentrations, and d) depicts the percentage of doped P3HT sites with $TFSI^-$ anions. The gray region in d) corresponds to the range in which no P3HT sites are doped.

The anion exchange isotherm was fit to the concentration dependent data.[19, 20] The best fit is shown in Figures 4.2a and 4.2b, with residuals displayed in Figure C.13. The extracted K_I and K_{II} are 971 ± 85 and 0.2 ± 0.06 M^{-1} corresponding to ΔG_I° and ΔG_{II}° of -0.177 ± 0.002 and 0.04 ± 0.007 eV, respectively. As expected, charge transfer between $FeCl_3$ and P3HT is spontaneous. At room temperature the anion exchange process is non-spontaneous, but a new equilibrium is established between $FeCl_3^-$ and $LiTFSI^-$ counter ions. Figure 4.2c shows the contour of the anion exchange isotherm fit. Θ reduces to zero at low $FeCl_3$ and high LiTFSI concentrations because the water contamination ($w = 0.0038 \pm 2.3 * 10^{-4}$) exceeds the pre-

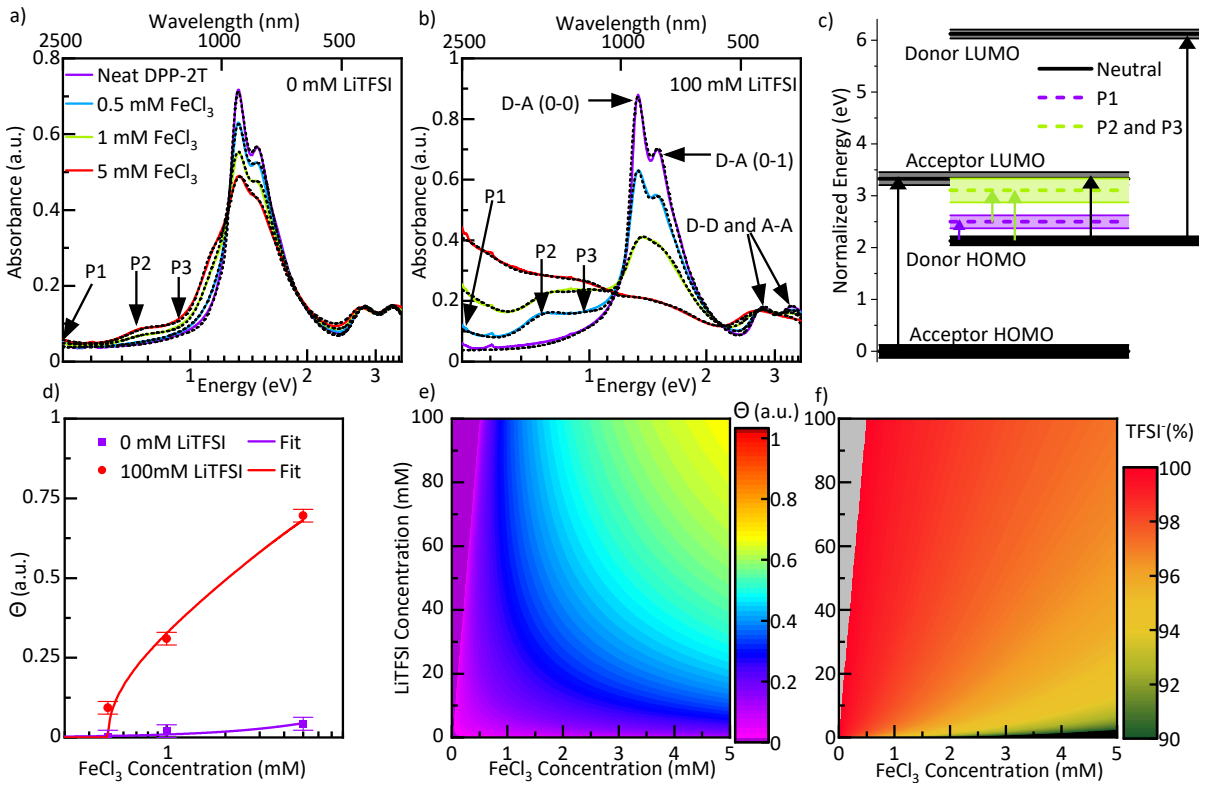

Figure 4.3. UV-Vis-NIR absorption spectra of PDPP-2T films sequentially doped with varying $FeCl_3$ concentrations and either 0 mM a) or 100 mM b) of LiTFSI. All spectra are fit with with cumulative Gaussian fits (dashed lines) to determine state populations. c) Depicts energy transitions for p-doped alternating D/A copolymers. d) Depicts a 2D scatter plot of Θ extracted from the absorption data and the corresponding Anion Exchange Isotherm fit. e) Shows fit Θ for PDPP-2T as a function of the $FeCl_3$ and LiTFSI concentrations, and f) depicts the percentage of doped polymer sites with $TFSI^-$ anions. The gray region in f) corresponds to the range in which no polymer sites are doped.

pared $FeCl_3$ concentration. At the maximum combined dopant/electrolyte concentrations of 5 mM $FeCl_3$ and 100 mM LiTFSI, the calculated Θ approaches a saturation doping level of 79%, meaning that $\sim$20% of the neutral P3HT sites cannot be sequentially doped, likely due to disordered dihedral bends along the polymer backbone and/or excluded volume interactions at the substrate or air interfaces. The percent of doped sites occupied by $TFSI^-$ is shown in Figure 4.2d. Interestingly, in films exposed to 100 mM LiTFSI solutions, the percent of sites with $TFSI^-$ anions remains below $\sim$50% for all $FeCl_3$ concentrations above $\sim$1 mM. At 1 mM $FeCl_3$ and 100 mM LiTFSI approximately half of the doped sites are occupied by $TFSI^-$.

Figure C.18 demonstrates that AED can be used to effectively dope SPs with a relatively weak chemical potential for doping. We tested this prediction by attempting the doping of

PDPP-2T with $FeCl_3$ in the presence of LiTFSI. PDPP-2T has a higher IE (IE^{CV} = 5.4 eV)[21] than P3HT (IE^{CV} = 5.0 eV), reducing the chemical potential for doping with $FeCl_3$. As a result, doping PDPP-2T with $FeCl_3$ yields low doping efficiency. Figure 4.3a shows raw unnormalized UV-Vis-NIR of 80± 5 nm thick PDPP-2T films sequentially doped at room temperature with 0.5, 1, and 5 mM $FeCl_3$ solutions. As the doping level is increased, the neutral vibronic (0-0), and (0-1) transitions at 1.3 and 1.5 eV slightly bleach and polaron transitions P1, P2, and P3 grow in at 0.33 eV, 0.75 eV, and 0.98 eV. An unknown feature grows in with increasing $FeCl_3$ concentration at 1.13 eV, this is discussed in Supporting Information Section S5. The two high energy D-D and A-A transitions at 2.8 eV and 3.3 eV mildly broaden. On the other hand, Figure 4.3b shows UV-Vis-NIR of PDPP-2T films sequentially doped with the same 0.5, 1, and 5 mM $FeCl_3$ with the addition of 100 mM LiTFSI. The D-A (0-0) and (0-1) transitions bleach more significantly and only the P1, P2, and P3 polaron transitions grow in. At the highest doping level the high energy D-D and A-A transitions quench and broaden, with an increased red shifted absorbance. Figure 4.3c depicts the corresponding energy transitions.

Discussion of the spectral and isotherm fitting of PDPP-2T is in Supporting Information Section S6.1.The cumulative fits are shown as the dashed line in Figures 4.3a and 4.3b. We calculate Θ from the absorption data (Figure 4.3d). As expected, with no LiTFSI present the higher energetic barrier for charge transfer limits the doping efficiency, reaching a 4.3% doping level (θ=0.043) with a 5 mM $FeCl_3$ solution. However, in the presence of 100 mM LiTFSI, PDPP-2T reached a 70% doping level (θ=0.70) at 5mM $FeCl_3$. We fit Θ for the PDPP-2T samples with the Anion Exchange Isotherm model (Figures 4.3d and 4.3e). The extracted K_I and K_{II} are 9.41 ± 1.62 and 2.92 ± 0.61 M^{-1} corresponding to ΔG_I° and ΔG_{II}° of -0.058 ± 0.004 and -0.028 ± 0.005 eV, respectively. Unlike P3HT, PDPP-2T approaches a saturated doping level of ∼100%. Figure 4.3f shows the calculated % $TFSI^-$ anions in the PDPP-2T film after AED. Unlike the P3HT sample, >90% of doped sites have exchanged $FeCl_3^-$ with $TFSI^-$.

We performed four-point probe collinear sheet resistance measurements on P3HT films with respect to $FeCl_3$ concentration at various LiTFSI concentrations (Figure 4.4a). P3HT films doped with only $FeCl_3$ ranged in conductivity from 0.066 ± 0.002 S/cm at 0.1 mM $FeCl_3$ up to 140 ± 20 S/cm at 5 mM $FeCl_3$. Anion exchanged P3HT films doped with 0.1 mM $FeCl_3$

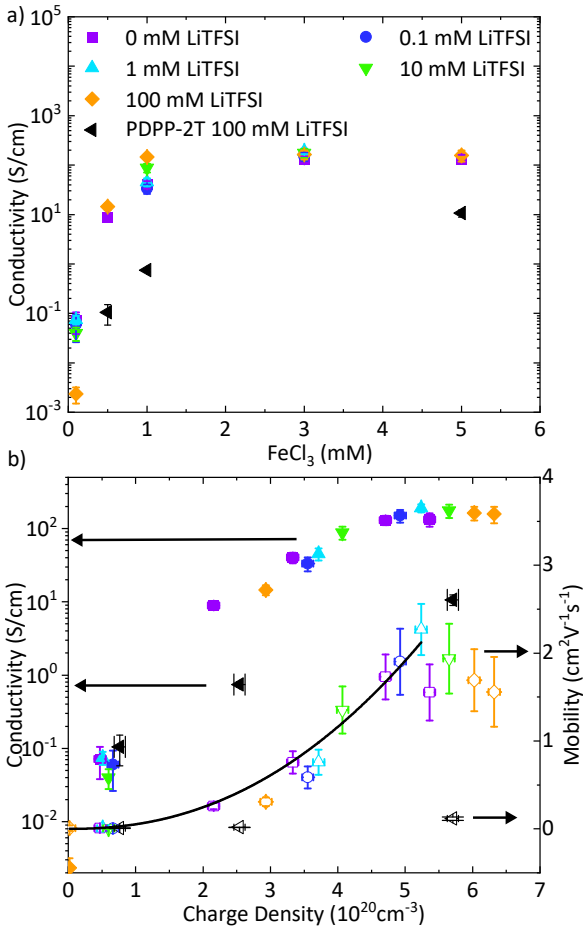

Figure 4.4. a) Four-point probe conductivity of P3HT films with respect to $FeCl_3$ solution concentration at various LiTFSI concentrations, and one conductivity series of PDPP-2T films with respect to $FeCl_3$ solution concentrations with 100 mM LiTFSI. b) Conductivity (filled symbols) and mobility (empty symbols) as a function of charge density.

and 100 mM LiTFSI have the lowest conductivity at $\sim 10^{-3}$ S/cm, due to traces of water in LiTFSI. The presence of LiTFSI led to the largest enhancement in conductivity at 1 mM $FeCl_3$, where the measured conductivity increased from 31$\pm$ 6 S/cm at 0 mM LiTFSI to 80 $\pm$ 6 S/cm at 100 mM LiTFSI. For this sample, 43% of the $P3HT^+$ sites have $TFSI^-$ and 57% have $FeCl_3^-$. Discussion of conductivity enhancement is in Supporting Information Section S13.

Carrier density is proportional to the fraction of polymer sites that possess a hole (Θ). To estimate the hole density from Θ, we estimate the minimum site size, which we define as the minimum number of monomer units that can hold a hole state. For the PDPP-2T polymer, we assume that each monomer T-DPP-T is a single site. This assumption is justified by recent first-principle simulations of alternating co-polymers.[22] Using a film density of 1.1 g/cm^3,

we estimate a maximum hole density (p_{max}) of 8.2x10^{20} holes/cm^3 for PDPP-2T. A 10% uncertainty in film mass density translates to a 10% uncertainty in maximum carrier density. For P3HT, we assume the minimum site size is a four thiophene (4T) monomer section, and yields an estimated maximum hole density of 8.5x10^{20} holes/cm^3, nearly identical to that of PDPP-2T. We recognize that more accurate estimates of the minimum site size and maximum carrier density will improve our model's predictive power. Discussion of carrier density is in Supporting Information Section S14.

Scaling these maximum hole densities by the fraction of sites that are doped (Θ) allows us to compare film conductivity (σ) to hole density and estimate hole mobility (Equation 4.4),

$$\mu = \frac{\sigma}{p_{max}\Theta e} \tag{4.4}$$

where e is the elemental charge (Figure 4.4b). The P3HT hole mobility is fit to the variable range hopping model (VRHM) (Equation C.27),[23, 24, 25] where the pre-factor for conductivity ($\sigma_0 = 1.6$ S/m), the effective overlap parameter between localized states ($\alpha^{-1} = 0.16$ nm), and the critical number for the onset of percolation ($B_c = 2.8$) are identical to previous P3HT mobility studies.[23, 26] Our sample has an increased width of the exponential density of states ($T_0 = 665$ K) compared to previous fits to P3HT. This analysis shows that μ_h increases with doping density until it saturates at 2.3 cm^{2}V^{-1}s^{-1} at a doping density of $\sim 5\times 10^{20}$ cm^{-3}. At higher doping levels, μ_h deviates from the VRHM due to increased structural disorder induced by the presence of counter ions.[8]

We were unable to measure the conductivity of the PDPP-2T films doped with only $FeCl_3$ because it was below the detection limit of our equipment ($< 10^{-3}$ S/cm). The conductivity of PDPP-2T films anion exchange doped at 100 mM LiTFSI ranged from 0.1 $\pm$ 0.05 S/cm with 0.5 mM $FeCl_3$ up to 10.7$\pm$ 1.8 S/cm with 5 mM $FeCl_3$ (Figure 4.4 a)). IV curves are in Figure C.22. The estimated hole density and mobility are in Figure 4.4b. The estimated PDPP-2T mobility increased from 0.009 to 0.117 cm^{2}V^{-1}s^{-1} at 0.5 mM and 5 mM $FeCl_3$, respectively.

In summary, we demonstrate sequential AED of P3HT and PDPP-2T films with the dopant $FeCl_3$ and electrolyte LiTFSI. In P3HT, AED is non-spontaneous and doping efficiency increases by 10% to 50% in the presence of LiTFSI. We demonstrate control over the exchange

of $FeCl_3^-$ for $TFSI^-$ on $P3HT^+$ sites between 0 and 100%. Sheet resistance measurements reveal record P3HT film conductivities of $\sim$140 S/cm can be obtained at high $FeCl_3$ doping levels, and remains the same in AED P3HT. In PDPP-2T, AED is spontaneous, doping efficiency increases $>$10x in the presence of LiTFSI, and conductivity increases by $>$4 orders of magnitude. Therefore, AED enables high p-type doping efficiency in systems with low chemical potential for doping. Future research is needed on AED polymers to address the affects that anion exchange has on polaron delocalization, the stability doping density in the presence of external stimuli, and how anion exchange affects the polymer film morphology.

4.4 Acknowledgments

This research was funded by the National Science Foundation Scalable Nanomanufacturing Program, Award # CMMI 1636385. We thank the National Science Foundation Division of Materials Research (award no. MRI-182838) for funding the acquisition of the XPS instrument used in this work, and Ian Jacobs for helping with dopant formulation and processing techniques.

4.5 Supporting Information

Molecular Structure of Materials, Experimental Methods, PDPP-2T Synthesis, UV-Vis-NIR Full Gaussian Fits, PDPP-2T $FeCl_3$ Absorption Discussion, Fractional Doping Level (Θ) and Isotherm Fitting, Discussion of ΔG°, P3HT Anion Exchange (Assuming one monomer site), Anion Exchange Isotherm Site Size Comparison, Discussion of Θ: Is $\Theta \propto P1$ or $\propto \sum(P1, P2, P3)$?, Anion Exchange Simulations, Extra UV-Vis-NIR Tests, Sheet Resistance IV Curves and Discussion of Conductivity Enhancements, Discussion of Carrier Density, X-ray Photoelectron Spectroscopy.

REFERENCES

[1] I. E. Jacobs and A. J. Moulé, "Controlling molecular doping in organic semiconductors," *Adv. Mater.*, vol. 29, no. 42, p. 1703063, 2017.

[2] I. E. Jacobs, E. W. Aasen, J. L. Oliveira, T. N. Fonseca, J. D. Roehling, J. Li, G. Zhang, M. P. Augustine, M. Mascal, and A. J. Moulé, "Comparison of solution-mixed and sequentially processed p3ht:f4tcnq films: Effect of doping-induced aggregation on film morphology," *J. Mater. Chem. C*, vol. 4, pp. 3454–3466, 2016.

[3] D. T. Scholes, P. Y. Yee, J. R. Lindemuth, H. Kang, J. Onorato, R. Ghosh, C. K. Luscombe, F. C. Spano, S. H. Tolbert, and B. J. Schwartz, "The effects of crystallinity on charge transport and the structure of sequentially processed f4tcnq-doped conjugated polymer films," *Adv. Funct. Mater.*, vol. 27, no. 44, p. 1702654, 2017.

[4] T. L. Murrey, K. Guo, J. T. Mulvey, O. A. Lee, C. Cendra, Z. I. Bedolla-Valdez, A. Salleo, J.-F. Moulin, K. Hong, and A. J. Moulé, "Additive solution deposition of multi-layered semiconducting polymer films for design of sophisticated device architectures," *J. Mater. Chem. C*, vol. 7, pp. 953–960, 2019.

[5] S. N. Patel, A. M. Glaudell, K. A. Peterson, E. M. Thomas, K. A. O'Hara, E. Lim, and M. L. Chabinyc, "Morphology controls the thermoelectric power factor of a doped semiconducting polymer," *Sci. Adv.*, vol. 3, no. 6, p. e1700434, 2017.

[6] A. I. Hofmann, R. Kroon, S. Zokaei, E. Järsvall, C. Malacrida, S. Ludwigs, T. Biskup, and C. Müller, "Chemical doping of conjugated polymers with the strong oxidant magic blue," *Adv. Electron. Mater*, vol. 6, no. 8, p. 2000249, 2020.

[7] K. Kang, S. Watanabe, K. Broch, A. Sepe, A. Brown, I. Nasrallah, M. Nikolka, Z. Fei, M. Heeney, D. Matsumoto, K. Marumoto, H. Tanaka, S.-i. Kuroda, and H. Sirringhaus, "2d coherent charge transport in highly orderedconducting polymers doped by solid state-diffusion," *Nat. Mater.*, vol. 15, no. 8, pp. 896–902, 2016.

[8] S. Fratini, M. Nikolka, A. Salleo, G. Schweicher, and H. Sirringhaus, "Charge transport in high-mobility conjugated polymers and molecular semiconductors," *Nat. Mater.*, vol. 19, no. 5, pp. 491–502, 2020.

[9] J. Rivnay, S. Inal, A. Salleo, R. M. Owens, M. Berggren, and G. G. Malliaras, "Organic electrochemical transistors," *Nat. Rev. Mater*, vol. 3, no. 2, p. 17086, 2018.

[10] Y. Yamashita, J. Tsurumi, M. Ohno, R. Fujimoto, S. Kumagai, T. Kurosawa, T. Okamoto, J. Takeya, and S. Watanabe, "Efficient molecular doping of polymeric semiconductors driven by anion exchange," *Nature*, vol. 572, no. 7771, pp. 634–638, 2019.

[11] I. E. Jacobs, G. D'Avino, Y. Lin, V. Lemaur, Y. Huang, X. Ren, D. Simatos, W. Wood, C. Chen, T. Harrelson, T. Mustafa, C. A. O'Keefe, L. Spalek, D. Tjhe, M. Statz, L. Lai, P. A. Finn, W. G. Neal, J. Strzalka, C. B. Nielsen, J.-K. Lee, S. Barlow, S. R. Marder, I. McCulloch, S. Fratini, D. Beljonne, and H. Sirringhaus, "Ion-exchange doped polymers at the degenerate limit: What limits conductivity at 100% doping efficiency?," 2021.

[12] B. Lüssem, C.-M. Keum, D. Kasemann, B. Naab, Z. Bao, and K. Leo, "Doped organic transistors," *Chem. Rev.*, vol. 116, pp. 13714–13751, Nov. 2016.

[13] K. Rahimi, I. Botiz, J. O. Agumba, S. Motamen, N. Stingelin, and G. Reiter, "Light absorption of poly(3-hexylthiophene) single crystals," *RSC Adv.*, vol. 4, pp. 11121–11123, 2014.

[14] R. Österbacka, C. P. An, X. M. Jiang, and Z. V. Vardeny, "Two-dimensional electronic excitations in self-assembled conjugated polymer nanocrystals," *Science*, vol. 287, p. 839, Feb. 2000.

[15] O. J. Korovyanko, R. Österbacka, X. M. Jiang, Z. V. Vardeny, and R. A. J. Janssen, "Photoexcitation dynamics in regioregular and regiorandom polythiophene films," *Phys. Rev. B*, vol. 64, p. 235122, Nov 2001.

[16] C. Wang, D. T. Duong, K. Vandewal, J. Rivnay, and A. Salleo, "Optical measurement

of doping efficiency in poly(3-hexylthiophene) solutions and thin films," *Phys. Rev. B*, vol. 91, p. 085205, Feb 2015.

[17] I. Salzmann, G. Heimel, M. Oehzelt, S. Winkler, and N. Koch, "Molecular electrical doping of organic semiconductors: Fundamental mechanisms and emerging dopant design rules," *Acc. Chem. Res.*, vol. 49, pp. 370–378, Mar. 2016.

[18] H. Abderrazak, M. Dachraoui, and B. Lendl, "A novel flow injection procedure for determination of phosphate in industrial raw phosphoric acid," *Analyst*, vol. 125, pp. 1211–1213, 2000.

[19] K. Levenberg, "A method for the solution of certain non-linear problems in least squares," *Quart. Appl. Math.*, vol. 2, pp. 164–168, 1944.

[20] D. W. Marquardt, "An algorithm for least-squares estimation of nonlinear parameters," *J. Soc. Ind. Appl*, vol. 11 (2), pp. 431–441, 1963.

[21] Y. Li, B. Sun, P. Sonar, and S. P. Singh, "Solution processable poly(2,5-dialkyl-2,5-dihydro-3,6-di-2-thienyl-pyrrolo[3,4-c]pyrrole-1,4-dione) for ambipolar organic thin film transistors," *Org. Electron.*, vol. 13, no. 9, pp. 1606 – 1613, 2012.

[22] M. Balooch Qarai, X. Chang, and F. C. Spano, "Vibronic exciton model for low bandgap donoracceptor polymers," *J. Chem. Phys*, vol. 153, no. 24, p. 244901, 2020.

[23] C. Tanase, E. J. Meijer, P. W. M. Blom, and D. M. de Leeuw, "Unification of the hole transport in polymeric field-effect transistors and light-emitting diodes," *Phys. Rev. Lett.*, vol. 91, p. 216601, Nov 2003.

[24] W. F. Pasveer, J. Cottaar, C. Tanase, R. Coehoorn, P. A. Bobbert, P. W. M. Blom, D. M. de Leeuw, and M. A. J. Michels, "Unified description of charge-carrier mobilities in disordered semiconducting polymers," *Phys. Rev. Lett.*, vol. 94, p. 206601, May 2005.

[25] M. C. J. M. Vissenberg and M. Matters, "Theory of the field-effect mobility in amorphous organic transistors," *Phys. Rev. B*, vol. 57, pp. 12964–12967, May 1998.

[26] C. H. Seager and G. E. Pike, “Percolation and conductivity: A computer study. ii,” *Phys. Rev. B*, vol. 10, pp. 1435–1446, Aug 1974.

Appendix A

Supporting information for “Additive Solution Deposition of Multi-Layered Semiconducting Polymer Films for Design of Sophisticated Device Architectures”

Table A.1. Preliminary Profilometer thickness measurements of thin films deposited from same processing conditions and at the time the NR films were made.

Film	Layer	Thickness (nm)
Multilayer film	1st layer	75 ± 4
	2nd layer	39 ± 4
	3rd layer	47 ± 2
	4th layer	32 ± 4
Single Layer P3HT Film	NA	187 ± 8

Material	SLD ($10^{-6}\AA^{-2}$)
Air	0
Silicon	2.07
Silicon Oxide	3.47
P3HT	0.55
F4TCNQ	4.88
d-CB	4.91
d-AN	4.92

Table A.2. Scattering length densities of materials in model

A.1 SLD Volume Balance

Calculated solvent volume fraction ($\phi_{solvent}$) from layer SLD obtained from fitting NR.

$$\phi_{solvent} = 1 - (\frac{\rho^L - \rho^S}{\rho^P \tau - \rho^S}) \tag{A.1}$$

Where ρ^L is measured layer SLD, ρ^S is calculated solvent SLD based on density at room temperature. ρ^P is measured P3HT layer SLD from the pure P3HT sample and τ is a thickness normalization to correct the P3HT SLD to its expanded volume in the swollen state.

$$\tau = \frac{T^P}{T^{SP}} \tag{A.2}$$

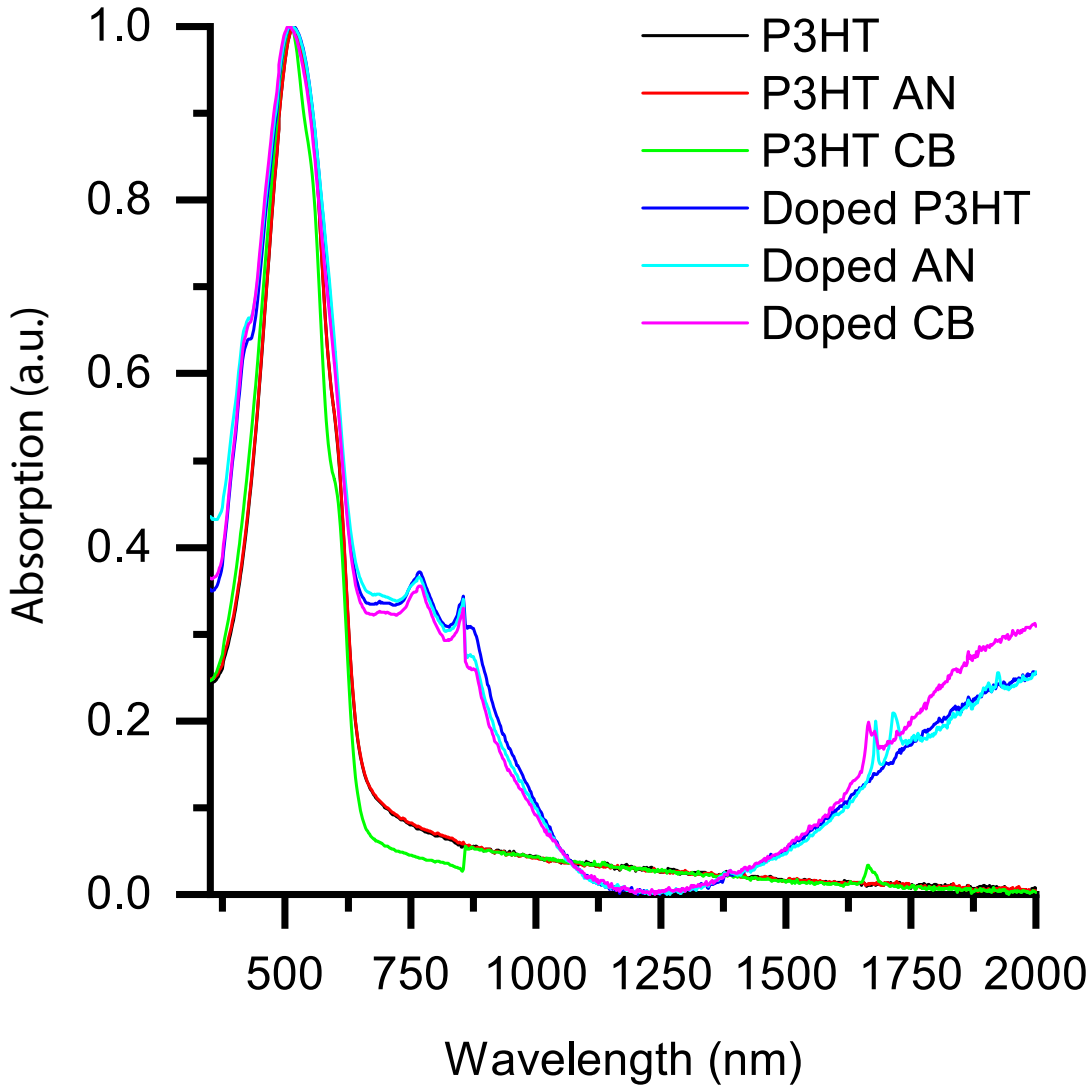

Figure A.1. Normalized UV-Vis absorption profile of neat and doped P3HT films under saturated AN and CB vapor environments

Where, T^P is the neutral P3HT layer thicknesses before swelling, and T^{SP} is the thickness in the solvent swollen state.

The solvent Volume Fraction for doped film

$$\phi_{solvent} = 1 - \left(\frac{\rho^L - \rho^S}{\rho^{DP}\gamma - \rho^S}\right) \tag{A.3}$$

Where ρ^{DP} is the measured SLD of the doped polymer layer and γ is a thickness normalization

to correct the Doped P3HT SLD to its expanded volume in the swollen state.

$$\gamma = \frac{T^{DP}}{T^{SDP}} \tag{A.4}$$

Where, $T^{D}P$ is the Doped P3HT layer thicknesses before swelling, and T^{SDP} is the thickness in the solvent swollen state.

A.2 Grazing Incidence Wide Angle X-ray Scattering

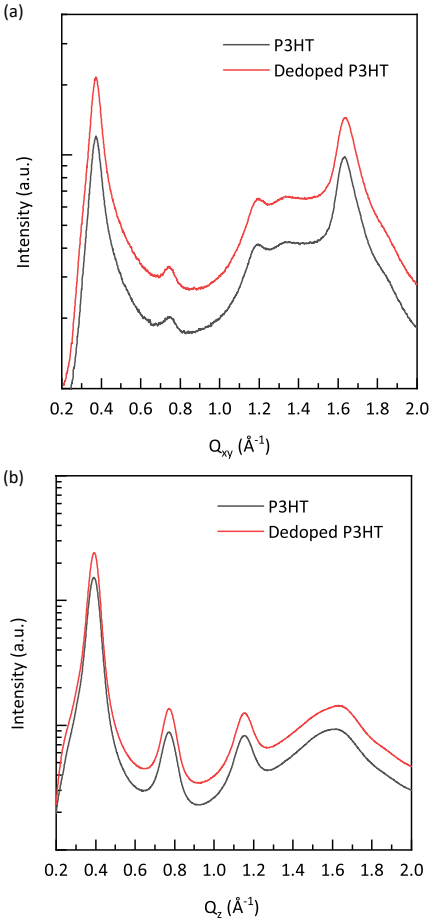

Figure A.2. (a) In-plane (Q_{xy}) and (b) out-of-plane (Q_z) GIWAXS of neat and dedoped P3HT film.

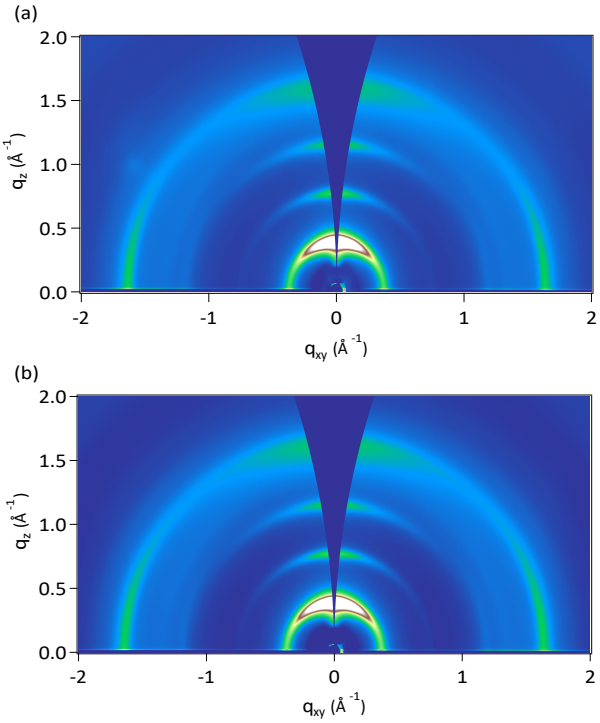

Figure A.3. 2D GIWAXS patterns of (a) neat P3HT and (b) chemically dedoped P3HT. (Note: Q_z is approximate)

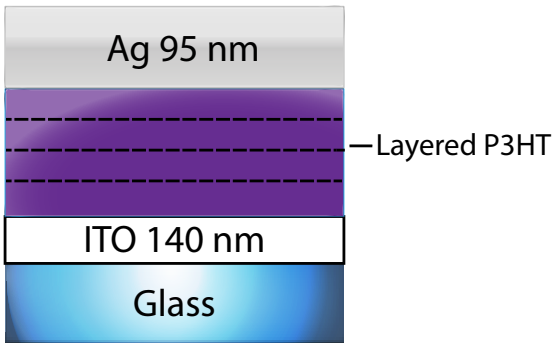

Figure A.4. Device architecture for two-point conductivity test

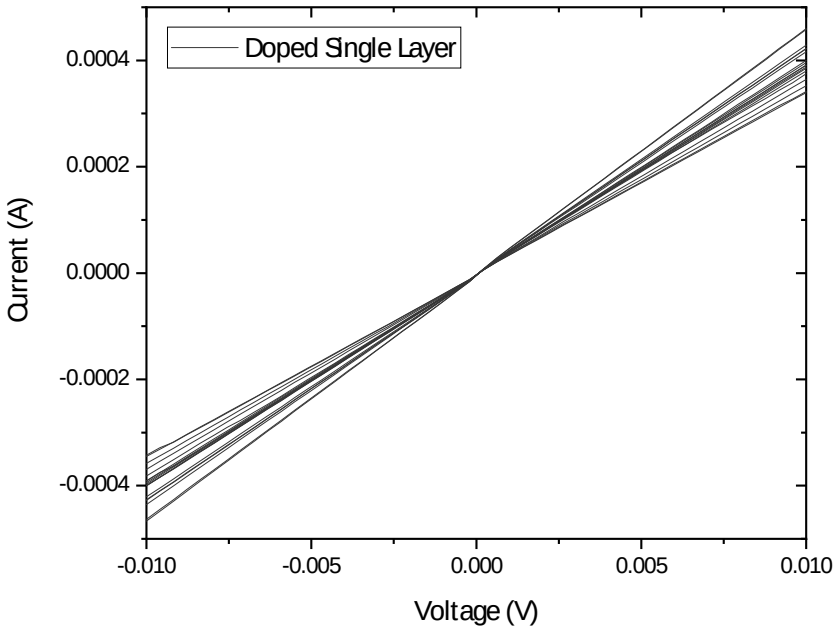

Figure A.5. IV Data of doped single layer P3HT film from several substrates, 6 electrodes per substrate. Omitted data from electrodes where good electrical connection could not be obtained.

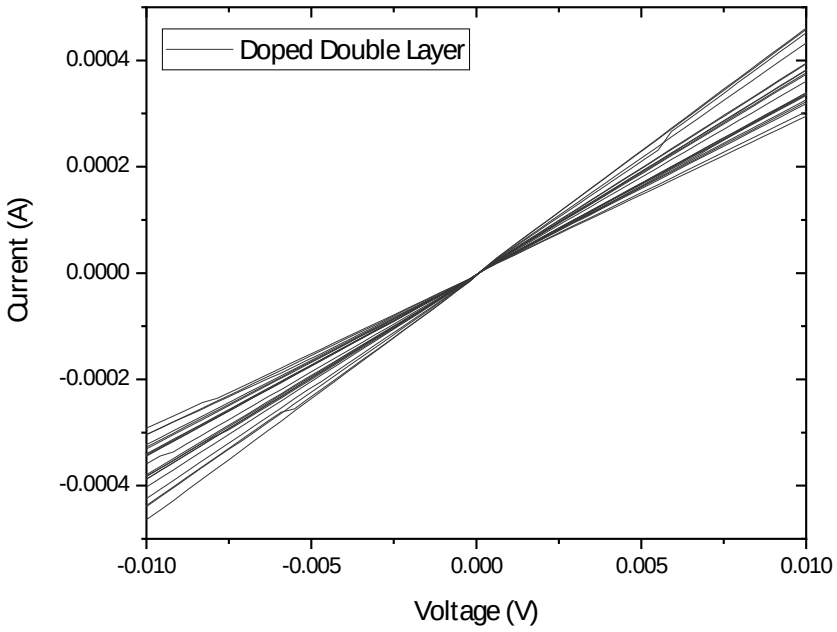

Figure A.6. IV Data of doped double layer P3HT film from several substrates, 6 electrodes per substrate. Omitted data from electrodes where good electrical connection could not be obtained.

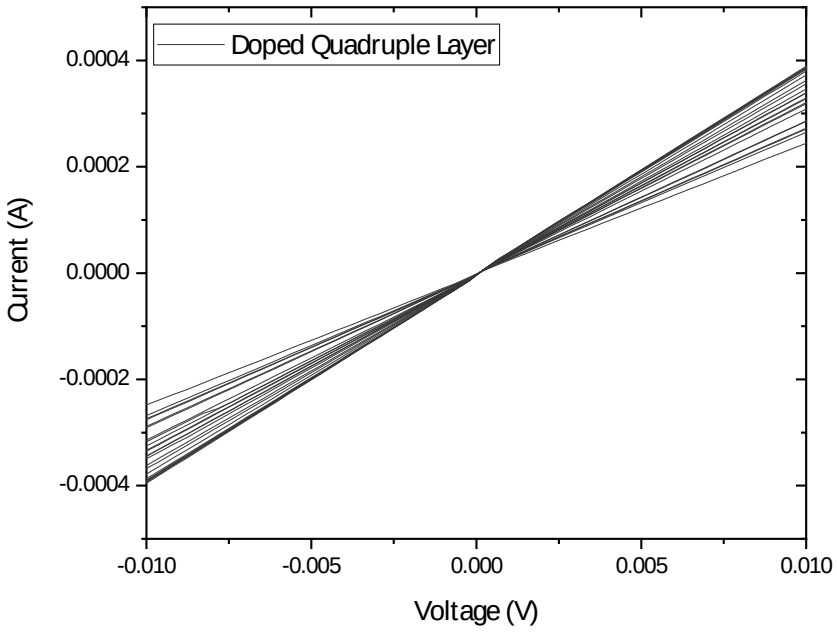

Figure A.7. IV Data of doped quadruple layer P3HT film from several substrates, 6 electrodes per substrate. Omitted data from electrodes where good electrical connection could not be obtained.

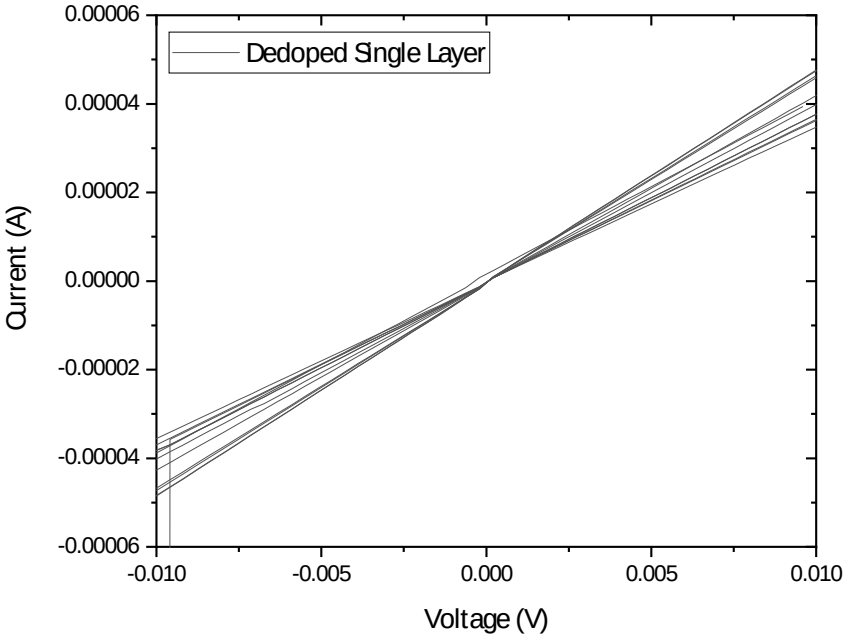

Figure A.8. IV Data of dedoped single layer P3HT film from several substrates, 6 electrodes per substrate. Omitted data from electrodes where good electrical connection could not be obtained.

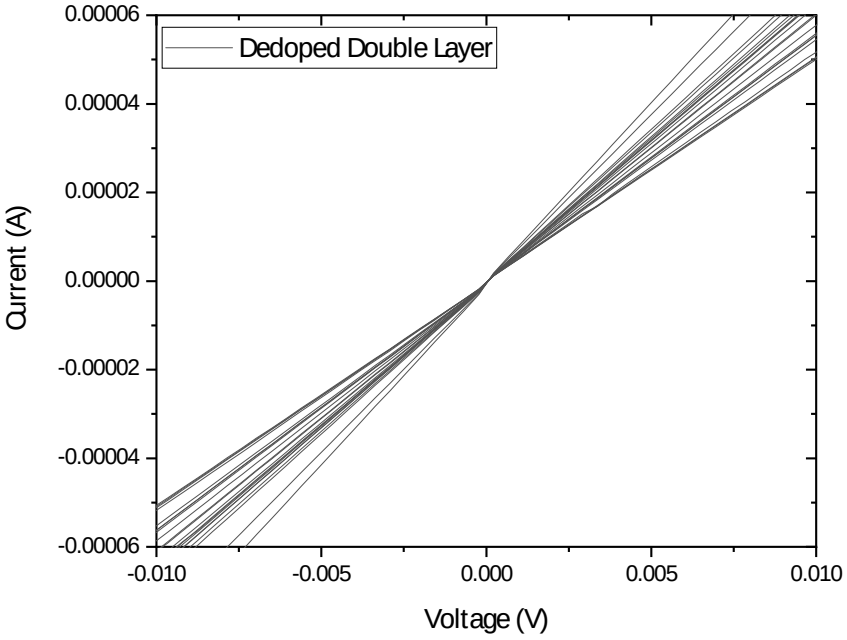

Figure A.9. IV Data of dedoped double layer P3HT film from several substrates, 6 electrodes per substrate. Omitted data from electrodes where good electrical connection could not be obtained.

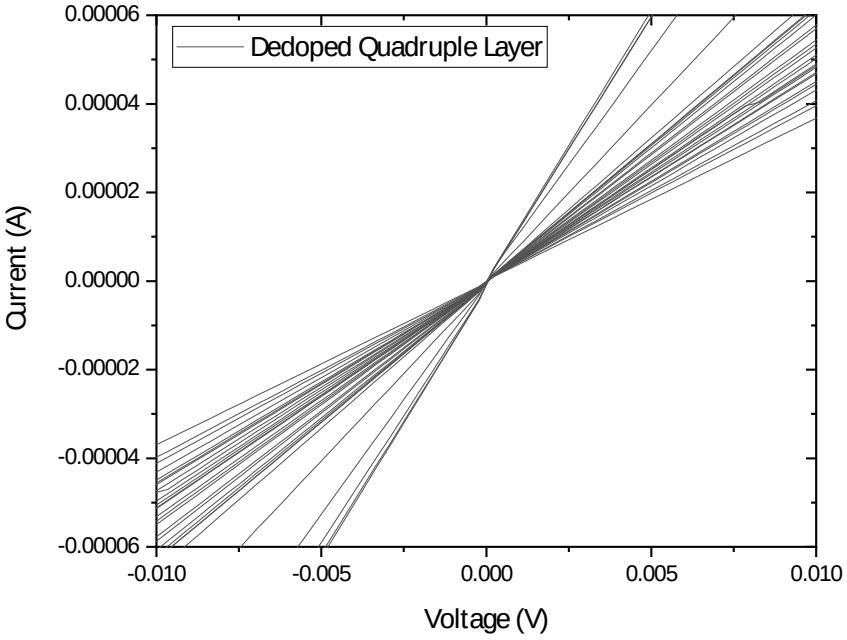

Figure A.10. IV Data of dedoped quadruple layer P3HT film from several substrates, 6 electrodes per substrate. Omitted data from electrodes where good electrical connection could not be obtained.

REFERENCES

Appendix B

Supporting information for “Investigation of Hierarchical Structure Formation in Merocyanine Photovoltaics”

B.1 Synthesis

B.1.1 I7TBT

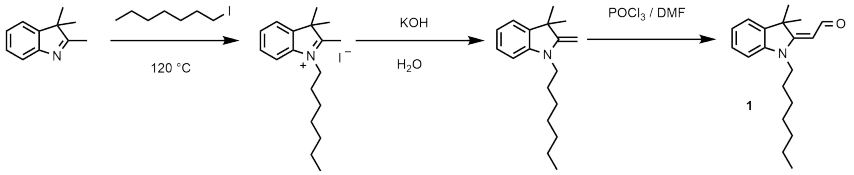

Figure B.1. I7TBT: (E)-2-(1-heptyl-3,3-dimethylindolin-2-ylidene)acetaldehyde (1)

2,3,3-trimethylindolenine (10.0 g, 62.8 mmol) and 1-iodoheptane (14.2 g, 62.8 mmol) were heated under an argon atmosphere to 120 ° C for 24 hours. After cooling to room temperature the residue was dissolved in dichloromethane and a 1 M aqueous solution of potassium hydroxide (180 ml) was added. The mixture was stirred at room temperature for 1 h and the crude product (1-heptyl-3,3-dimethyl-2-methyleneindoline) was extracted with dichloromethane. After drying the organic phase over $MgSO_4$ the solvent was removed under reduced pressure. The crude product was used immediately without any further purification. Under an argon atmosphere dry dimethylformamide (11.5 ml) was cooled to 0 ° C and phosphorous oxychloride (10.8 g, 70.1 mmol) was slowly added. The crude 1-heptyl-3,3-dimethyl-2-methyleneindoline was dissolved in dry dimethylformamide (14.5 ml) and added dropwise to the $POCl_3$ / DMF mixture. The reaction mixture was stirred at 40 ° C for 1 h and then added to 1 L of water containing ice. After adjusting the pH to 10 with a diluted sodium hydroxide solution the mixture was heated under reflux for 30 minutes. The crude product was extracted with dichloromethane, the organic phase was dried over $MgSO_4$ and the solvent was removed under reduced pressure.

Column chromatography on silica with toluene / ethyl acetate (4:1) as eluent yielded a red oil (12.9 g, 45.2 mmol, 72 %).

^{1}H NMR (acetone-d_6, 300 MHz): δ / ppm = 10.00 (1H, d, ^{3}J = 8.4 Hz); 7.38 (1H, m); 7.27 (1H, m); 7.08 6.99 (2H); 5.33 (1H, d, ^{3}J = 8.4 Hz); 3.78 (2H, t, ^{3}J = 7.5 Hz); 1.70 (2H, m); 1.65 (6H, s); 1.50 1.23 (8H); 0.87 (3H, m).

A mixture of 1 (See Figure B.2)(1.60 g, 5.62 mmol),2-(4-tert-butylthiazol-2(3H)-ylidene) malononitrile[1] (1.05 g, 5.09 mmol) and acetic anhydride (6 ml) was heated to 90 ° C for 1

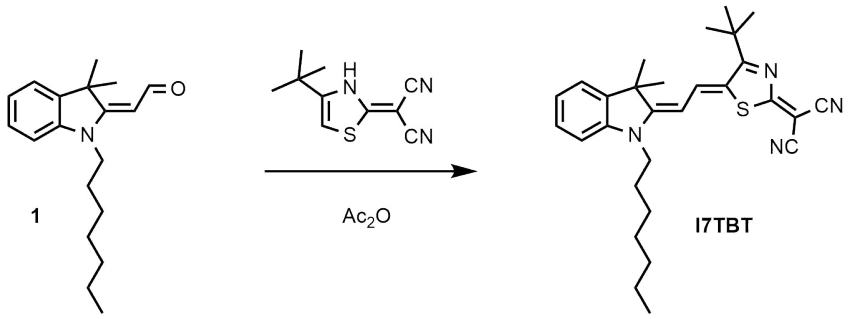

Figure B.2. I7TBT: 2-((Z)-4-tert-butyl-5-((E)-2-(1-heptyl-3,3-dimethylindolin-2-ylidene)ethylidene)thiazol-2(5H)-ylidene)malononitrile

h. After cooling to room temperature n-hexane was added and the precipitate was collected by filtration, washed with 2-propanol and n-hexane and dried in vacuum. Subsequent purification by column chromatography on silica with dichloromethane as eluent yielded a blue powder (1.62 g, 3.43 mmol, 61 %). ^{1}H NMR (CD_2Cl_2, 300 MHz): δ / ppm = 8.32 (1H, d, ^{3}J = 13.5 Hz); 7.43 7.35 (2H), 7.24 (1H, m), 7.08 (1H, m), 5.64 (1H, d, ^{3}J = 13.5 Hz), 3.93 (2H, t, ^{3}J = 7.5 Hz), 1.81 (2H, m), 1.68 (6H, s), 1.55 (9H, s), 1.49 1.24 (8H), 0.88 (3H, m). ^{13}C NMR APT (CD_2Cl_2, 75 MHz): δ / ppm = 185.2 (C_q), 179.4 (C_q), 172.6 (C_q), 142.5 (C_q), 140.8 (C_q), 138.8 (CH), 129.0 (CH), 126.7 (C_q), 125.3 (CH), 122.5 (CH), 118.2 (C_q), 116.0 (C_q), 110.7 (CH), 99.3 (CH), 49.3 (C_q), 44.6 (CH_2), 38.3 (C_q), 31.9 (CH_2), 31.5 (CH_3), 29.3 (CH_2), 28.4 (CH_3), 27.4 (CH_2), 27.3 (CH_2), 22.9 (CH_2), 14.1 (CH_3).

B.1.2 I9TBT

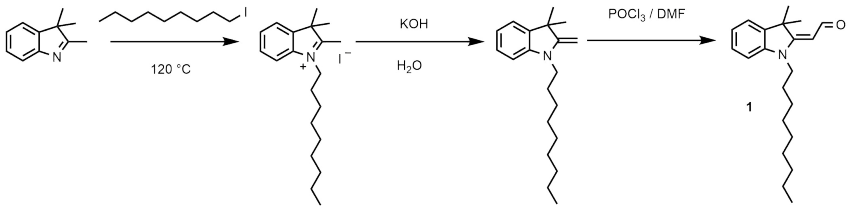

Figure B.3. I9TBT: (E)-2-(3,3-dimethyl-1-nonylindolin-2-ylidene)acetaldehyde (1)

2,3,3-trimethylindolenine (5.00 g, 31.4 mmol) and 1-iodononane (7.98 g, 31.4 mmol) were heated under an argon atmosphere to 120 ° C for 24 hours(Figure B.3). After cooling to room temperature the residue was dissolved in dichloromethane and a 1M aqueous solution of potassium hydroxide (90 ml) was added. The mixture was stirred at room temperature for 1 h and the crude product (1-heptyl-3,3-dimethyl-2-methyleneindoline) was extracted with

dichloromethane. After drying the organic phase over $MgSO_4$ the solvent was removed under reduced pressure. The crude product was used immediately without any further purification. Under an argon atmosphere dry dimethylformamide (5.5 ml) was cooled to 0 ° C and phosphorous oxychloride (5.37 g, 35.0 mmol) was slowly added. The crude 3,3-dimethyl-1-nonyl-2-methyleneindoline was dissolved in dry dimethylformamide (7.5 ml) and added dropwise to the $POCl_3$ / DMF mixture. The reaction mixture was stirred at 40 ° C for 1 h and then added to water containing ice (30 ml). After adjusting the pH to 10 with a diluted sodium hydroxide solution the mixture was heated under reflux for 30 minutes. The crude product was extracted with dichloromethane, the organic phase was dried over $MgSO_4$ and the solvent was removed under reduced pressure. Column chromatography on silica with toluene / ethyl acetate (5:1) as eluent yielded a red oil (7.36 g, 23.5 mmol, 75 %). ^{1}H NMR (acetone-d_6, 300 MHz): δ / ppm = 10.00 (1H, d, ^{3}J = 8.5 Hz); 7.38 (1H, m); 7.27 (1H, m); 7.07 6.99 (2H); 5.33 (1H, d, ^{3}J = 8.5 Hz); 3.78 (2H, t, ^{3}J = 7.5 Hz); 1.70 (2H, m); 1.65 (6H, s); 1.50 1.23 (12H); 0.86 (3H, m).

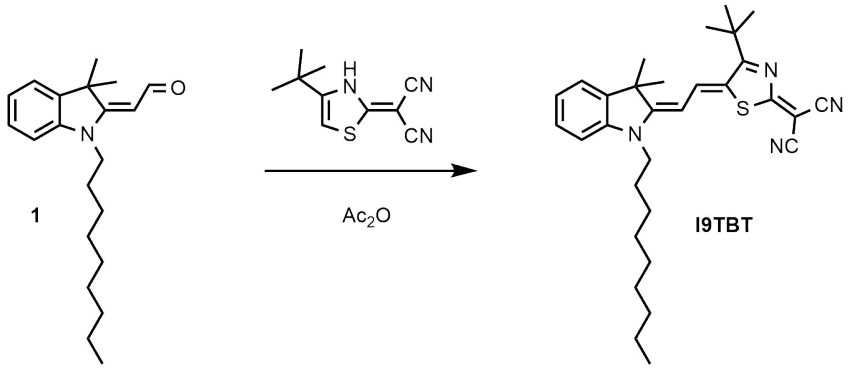

Figure B.4. I9TBT: 2-((Z)-4-tert-butyl-5-((E)-2-(3,3-dimethyl-1-nonylindolin-2-ylidene)ethylidene)thiazol-2(5H)-ylidene)malononitrile

A mixture of 1 (see Figure B.4) (1.76 g, 5.62 mmol), 2-(4-tert-butylthiazol-2(3H)-ylidene)malononitrile[1] (1.05 g, 5.09 mmol) and acetic anhydride (6 ml) was heated to 90 ° C for 1 h. After cooling to room temperature n-hexane was added and the precipitate was collected by filtration, washed with 2-propanol and n-hexane and dried in vacuo. Subsequent purification by column chromatography on silica with dichloromethane / ethyl acetate (99 : 1) as eluent yielded a blue powder (1.47 g, 2.94 mmol, 52 %). ^{1}H NMR (CD_2Cl_2, 500 MHz): δ / ppm = 8.33 (1H, d, ^{3}J = 13.4 Hz); 7.45 7.34 (2H), 7.25 (1H, m), 7.09 (1H, m), 5.65 (1H, d, ^{3}J = 13.4 Hz), 3.94 (2H, t, ^{3}J = 7.3 Hz), 1.81 (2H, m), 1.69 (6H, s), 1.55 (9H, s), 1.48 1.21 (8H), 0.87 (3H, m). ^{13}C NMR

(CD_2Cl_2, 125 MHz): δ / ppm = 185.0 (C_q), 179.4 (C_q), 172.4 (C_q), 142.4 (C_q), 140.6 (C_q), 138.3 (CH), 128.9 (CH), 126.5 (C_q), 125.2 (CH), 122.5 (CH), 118.2 (C_q), 116.1 (C_q), 110.7 (CH), 99.2 (CH), 55.5 (C_q), 49.1 (C_q), 44.5 (CH_2), 38.1 (C_q), 32.1 (CH_2), 31.4 (CH_3), 29.5 (3xCH_2), 28.4 (CH_3), 27.3 (CH_2), 27.2 (CH_2), 22.9 (CH_2), 14.1 (CH_3).

B.2 Ultraviolet Photoelectron Spectroscopy

The ionization energies of InTBT films processed from two different solvents, chloroform (CF) and dichloromethane (DCM) are probed with Ultraviolet Photoelectron Spectroscopy (UPS) (Table B.1). We expect similar HOMO levels for all the InTBTs since the electronically relevant part of the molecule is the same and the side chains have similar electron donating properties. Only a slight influence (100 meV) from the packing occurs when processed from CF or DCM (5.5 to 5.7 eV (Table B.1)) . The ionization energies of InTBT films processed from two different solvents, chloroform (CF) and dichloromethane (DCM) are probed with Ultraviolet Photoelectron Spectroscopy (UPS) (Table B.1). We expect similar HOMO levels for all the InTBTs since the electronically relevant part of the molecule is the same and the side chains have similar electron donating properties. Only a slight influence (100 meV) from the packing occurs when processed from CF or DCM. UV- photoelectron spectroscopy (UPS) measurements were performed under ultrahigh vacuum (base pressure 1×10^{-10} mbar) using a helium plasma excitation source (VG). The measurements were done with the He I α excitation line at 21.22 eV and a sample bias of 8V. The kinetic energy of the emitted photoelectrons were recorded using a hemispherical electron analyzer (Specs, Phoibos 100).

Table B.1. Ionization energy of pure InTBT films obtained by UPS on films (thickness below 20 nm) on ITO/MoO_3.

Merocyanine	Solvent	IE (eV)
I6TBT	CF	5.31
I8TBT	CF	5.33
	DCM	5.2
I9TBT	CF	5.23
	DCM	5.2
I10TBT	CF	5.35
I12TBT	CF	5.33
IHDTBT	CF	5.21

B.3 UV-Vis

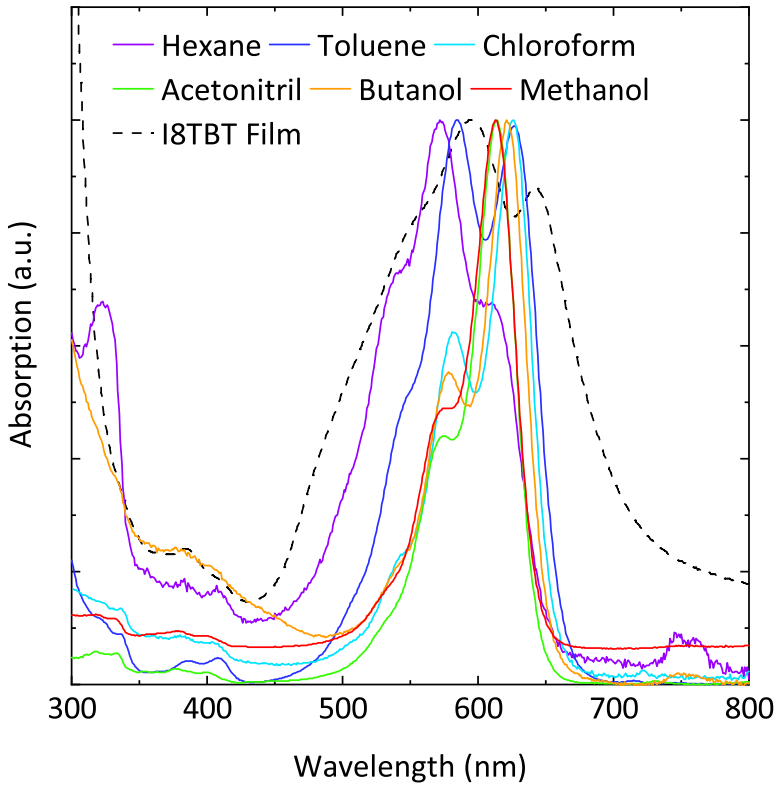

Figure B.5. UVvis absorption spectra of I8TBT solution in various solvents of varying polarity and a neat film for comparison.

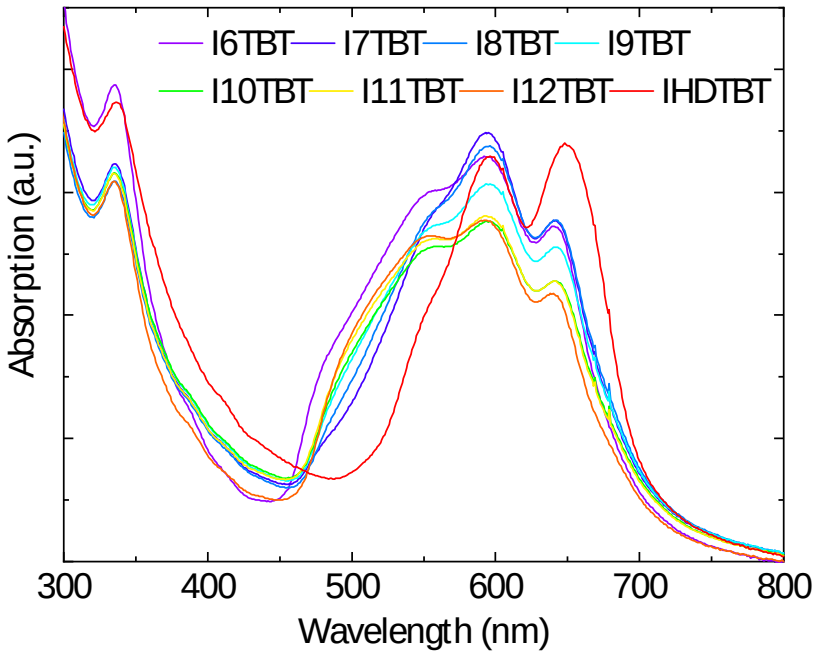

Figure B.6. Raw unnormalized UV-vis absorption spectra of InTBT:PCBM films.

B.4 Crystal Stacking

Table B.2. Unit cell information extracted from single crystal XRD data.

Merocyanine:	I7TBT	I8TBT
Chemical Formula:	$C_{29}H_{36}N_4S$	$C_{30}H_{38}N_4S$
Description:	needles	needles
Space group:	P 2_1/n (14)	P 1 (2)
a (Å):	19.40(4)	7.31(5)
b (Å):	6.96(9)	14.89(14)
c (Å):	22.82(4)	15.51(2)
α°:	90	105.82(4)
β°:	107.40(5)	90.58(6)
γ°:	90	91.26(5)
Volume ($Å^3$):	2943	1626

B.5 Grazing Incidence X-ray Diffraction

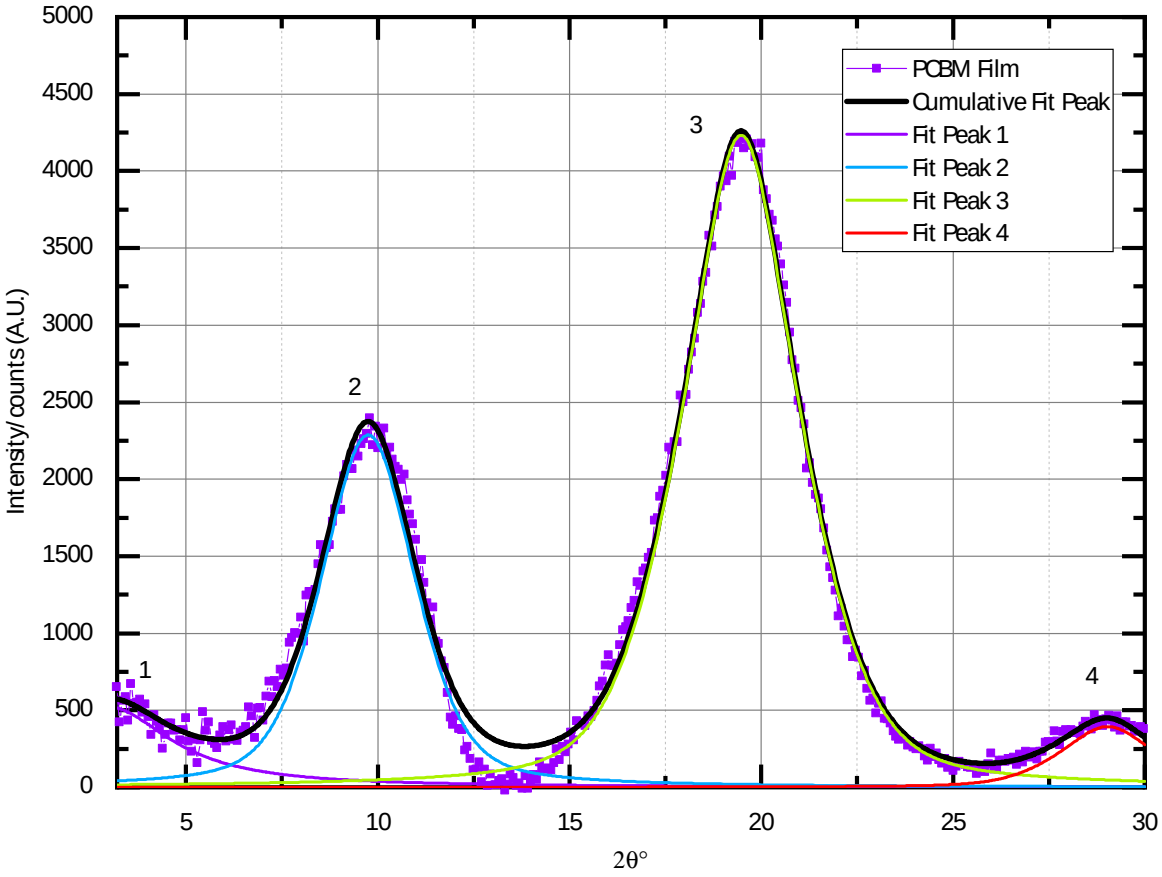

Figure B.7. GIXRD of PCBM Film. Each peak fit with Pseudo-Voigt.

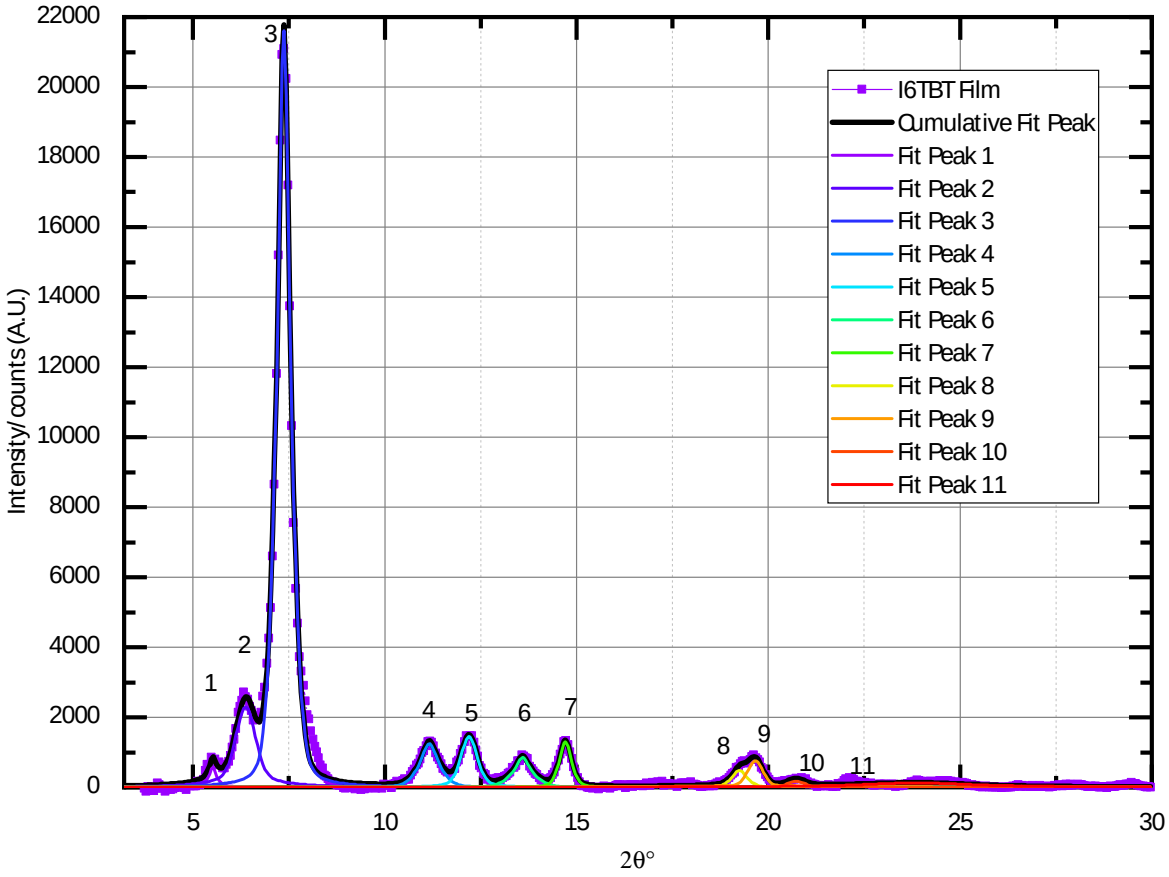

Figure B.8. GIXRD of I6TBT Film. Each peak fit with Pseudo-Voigt.

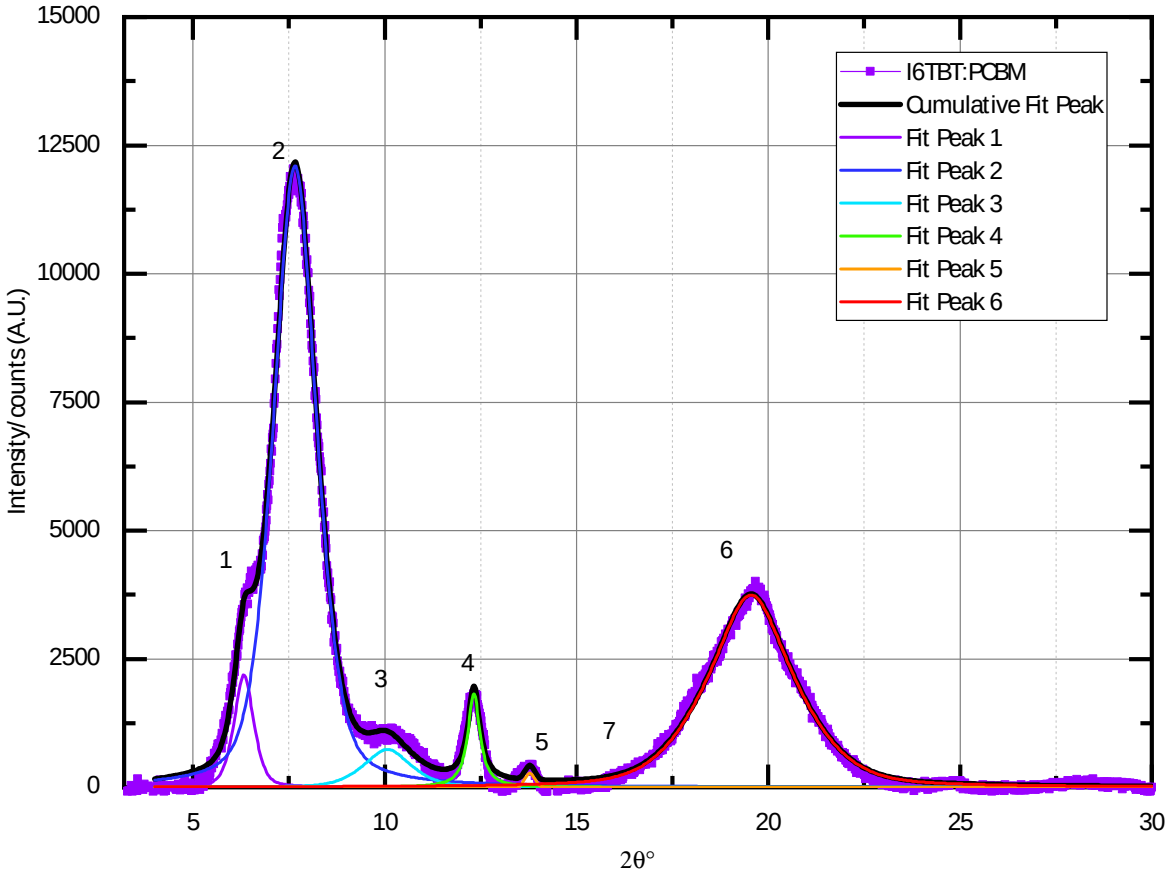

Figure B.9. GIXRD of I6TBT:PCBM Film. Each peak fit with Pseudo-Voigt.

Table B.3. I6TBT Peak location and d-spacing from GIXRD.

I6TBT Peak Index	$2\theta^\circ$	d-Spacing ($\pm$0.1)(Å)
1	5.51	16.03
2	6.37	13.88
3	7.37	12.00
4	11.16	7.26
5	12.19	7.26
6	13.60	6.51
7	14.71	6.02
8	19.25	4.61
9	19.66	4.52
10	20.73	4.29
11	23.87	3.72

Table B.4. I6TBT:PCBM Peak location and d-spacing from GIXRD.

I6TBT:PCBM Peak Index	$2\theta^\circ$	d-Spacing ($\pm$0.1)(Å)
1	6.33	14.0
2	7.66	11.5
3	10.06	8.8
4	12.32	7.2
5	13.78	6.4
6 (PCBM)	19.55	4.5

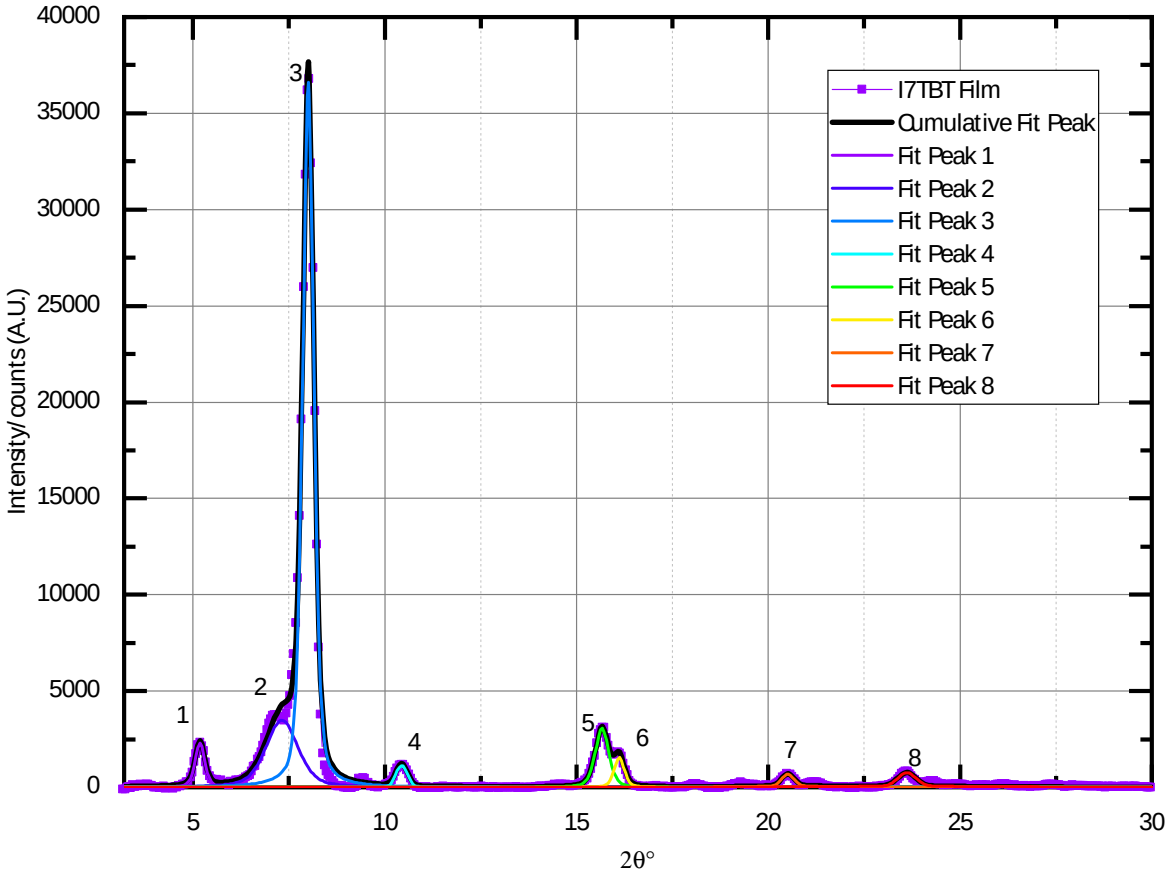

Figure B.10. GIXRD of I7TBT Film. Each peak fit with Pseudo-Voigt.

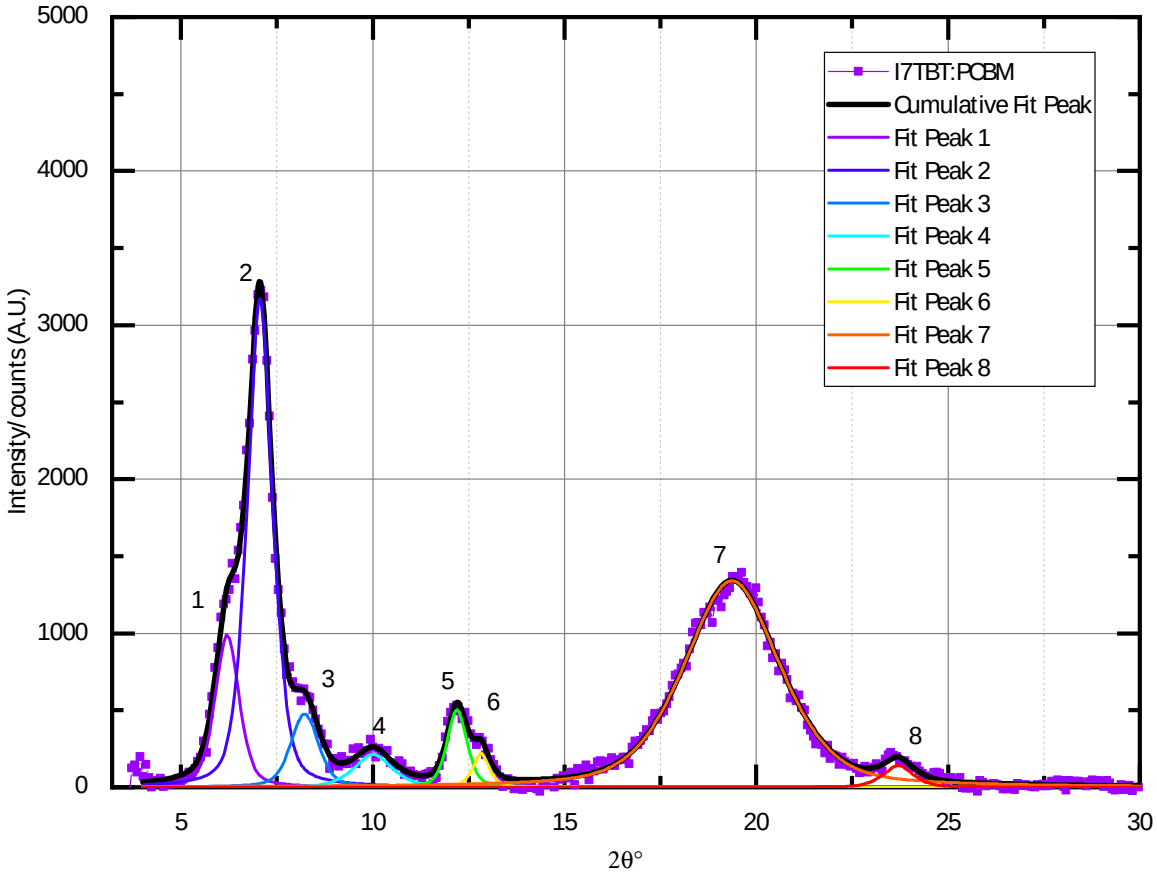

Figure B.11. GIXRD of I7TBT:PCBM Film. Each peak fit with Pseudo-Voigt.

Table B.5. I7TBT Peak location and d-spacing from GIXRD.

I7TBT Peak Index	$2\theta^\circ$	d-Spacing ($\pm$0.1) (Å)
1	5.18	17.1
2	7.32	12.1
3	8.00	11.1
4	10.44	8.5
5	15.66	5.7
6	16.11	5.5
7	20.51	4.3
8	23.61	3.8

Table B.6. I7TBT:PCBM Peak location and d-spacing from GIXRD.

I7TBT:PCBM Peak Index	$2\theta^\circ$	d-Spacing ($\pm$0.1) (Å)
1	6.20	14.3
2	7.06	12.5
3	8.22	10.8
4	10.01	8.8
5	12.20	7.3
6	12.82	6.9
7 (PCBM)	19.36	4.6
8	23.70	3.8

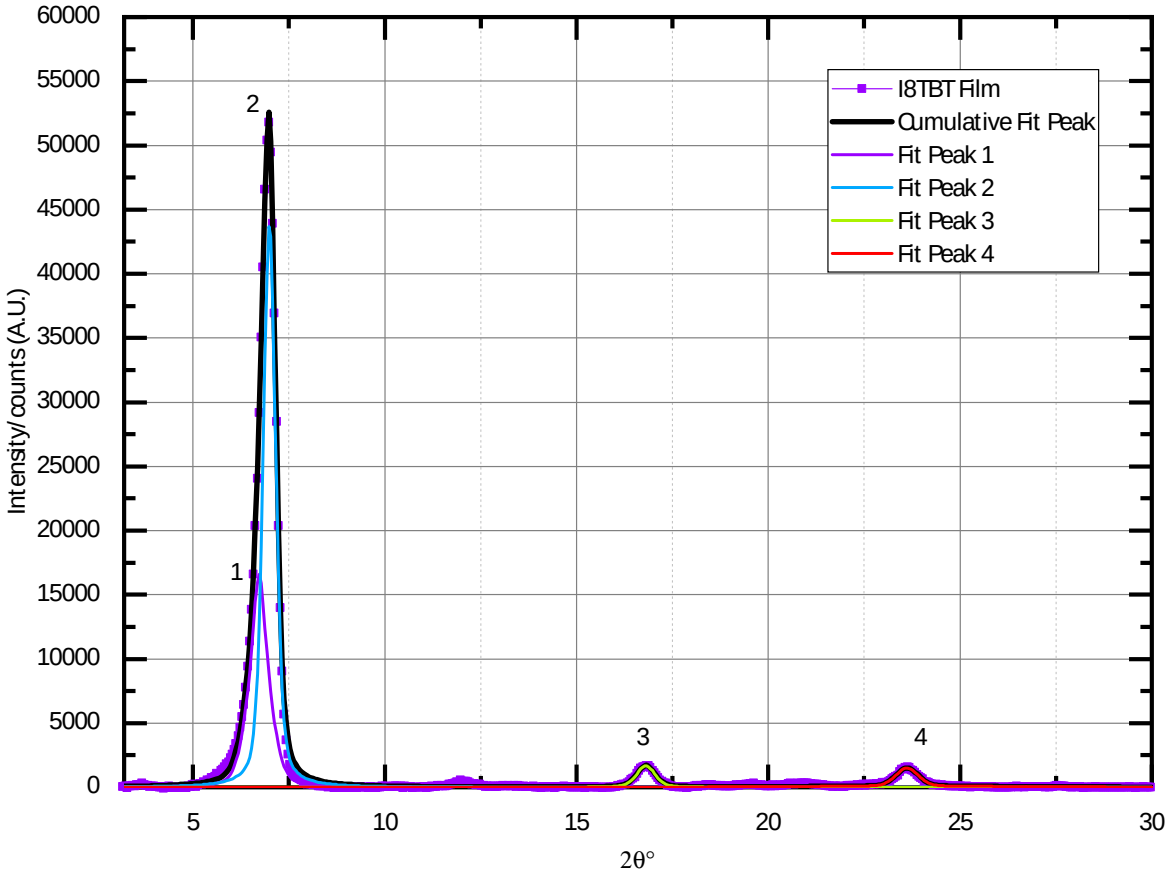

Figure B.12. GIXRD of I8TBT Film. Each peak fit with Pseudo-Voigt.

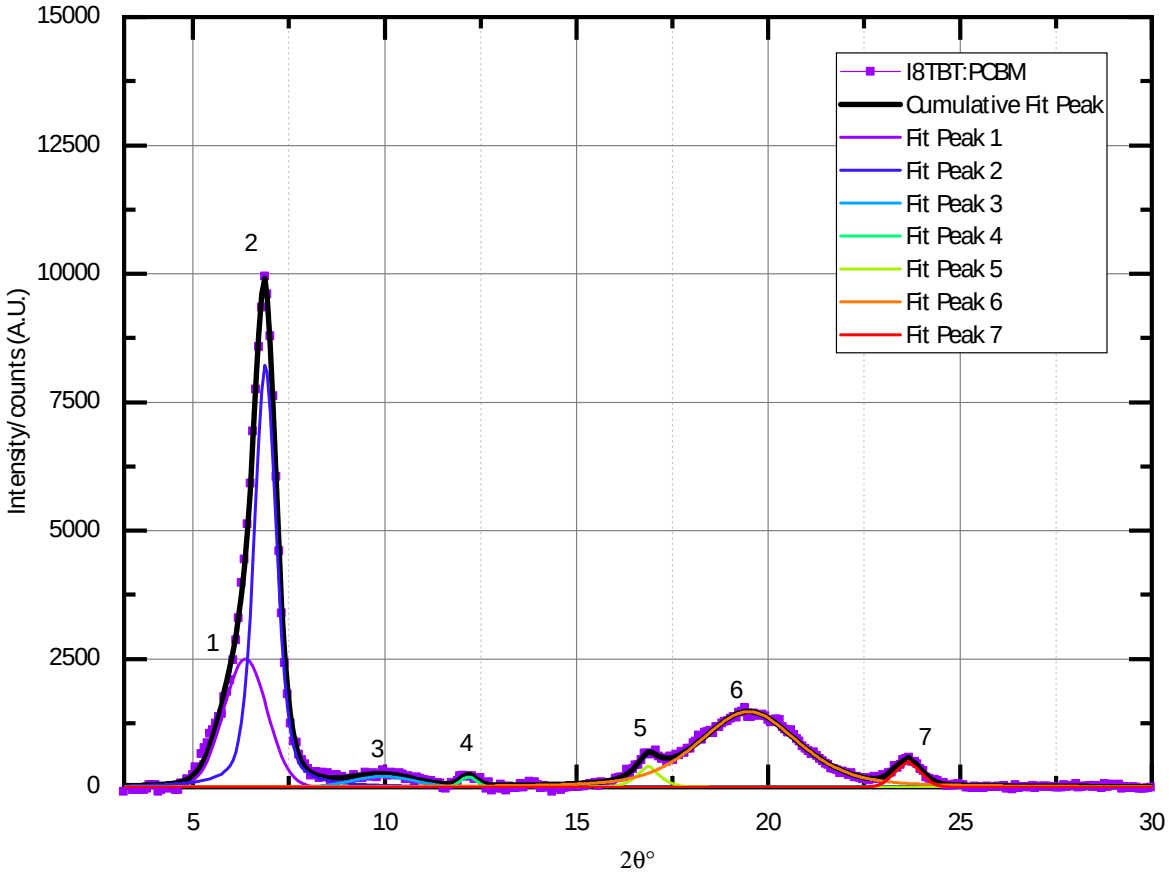

Figure B.13. GIXRD of I8TBT:PCBM Film. Each peak fit with Pseudo-Voigt.

Table B.7. I8TBT Peak location and d-spacing from GIXRD.

I8TBT Peak Index	$2\theta^\circ$	d-Spacing ($\pm$0.1) (Å)
1	6.72	13.1
2	7.00	12.6
3	16.81	5.3
4	23.62	3.8

Table B.8. I8TBT:PCBM Peak location and d-spacing from GIXRD.

I8TBT:PCBM Peak Index	$2\theta^\circ$	d-Spacing ($\pm$0.1) (Å)
1	6.36	13.9
2	6.88	12.8
3	9.95	8.9
4	12.18	7.3
5	16.87	5.3
6 (PCBM)	19.48	4.6
7	23.64	3.8

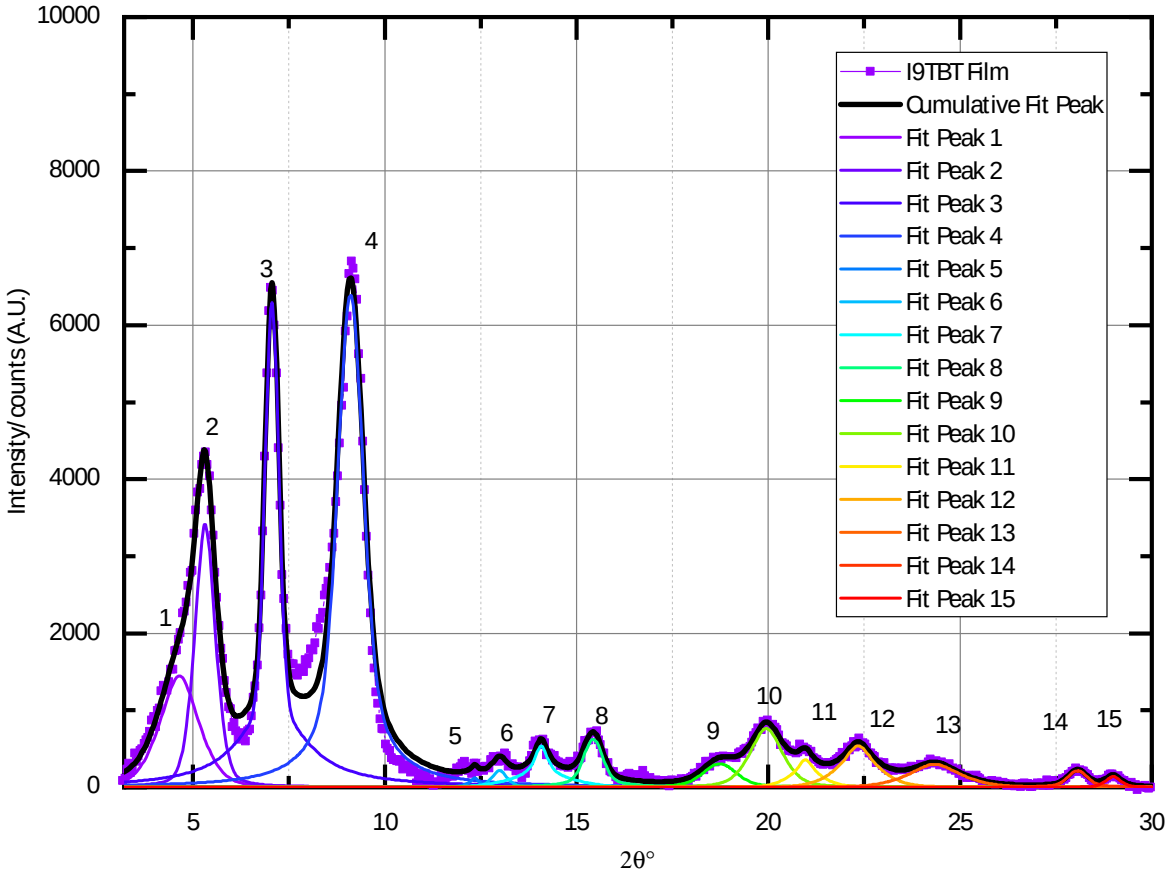

Figure B.14. GIXRD of I9TBT Film. Each peak fit with Pseudo-Voigt.

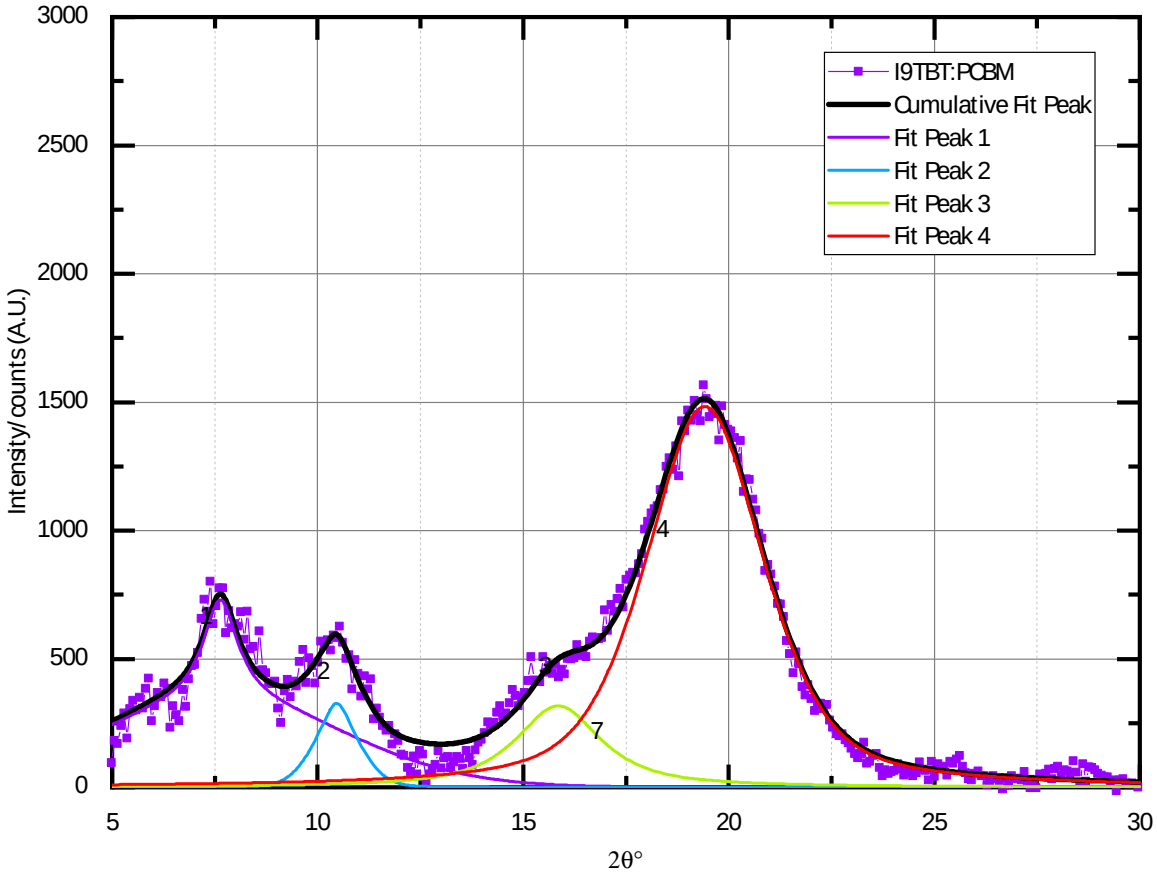

Figure B.15. GIXRD of I9TBT:PCBM Film. Each peak fit with Pseudo-Voigt.

Table B.9. I9TBT Peak location and d-spacing from GIXRD.

I9TBT Peak Index	$2\theta^\circ$	d-Spacing ($\pm$0.1) (Å)
1	4.64	19.0
2	5.31	16.6
3	7.06	12.5
4	9.11	9.7
5	12.34	7.2
6	12.99	6.8
7	14.08	6.3
8	15.43	5.7
9	18.73	4.7
10	19.95	4.5
11	20.97	4.2
12	22.34	4.0
13	24.34	3.7
14	28.07	3.2
15	28.99	3.1

Table B.10. I9TBT:PCBM Peak location and d-spacing from GIXRD.

I9TBT:PCBM Peak Index	$2\theta^\circ$	d-Spacing ($\pm$0.1) (Å)
1	7.63	11.6
2	10.46	8.5
3	15.85	5.6
4 (PCBM)	19.42	4.6

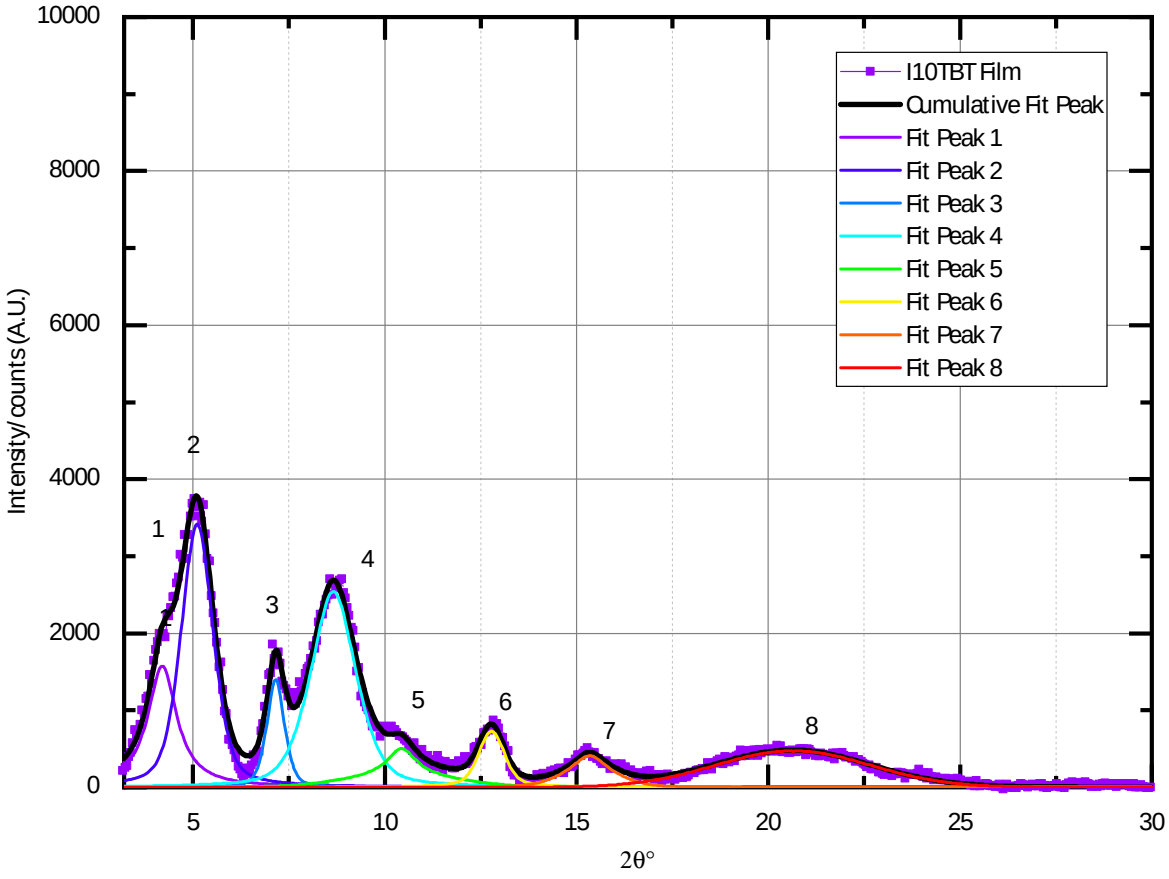

Figure B.16. GIXRD of I10TBT Film. Each peak fit with Pseudo-Voigt.

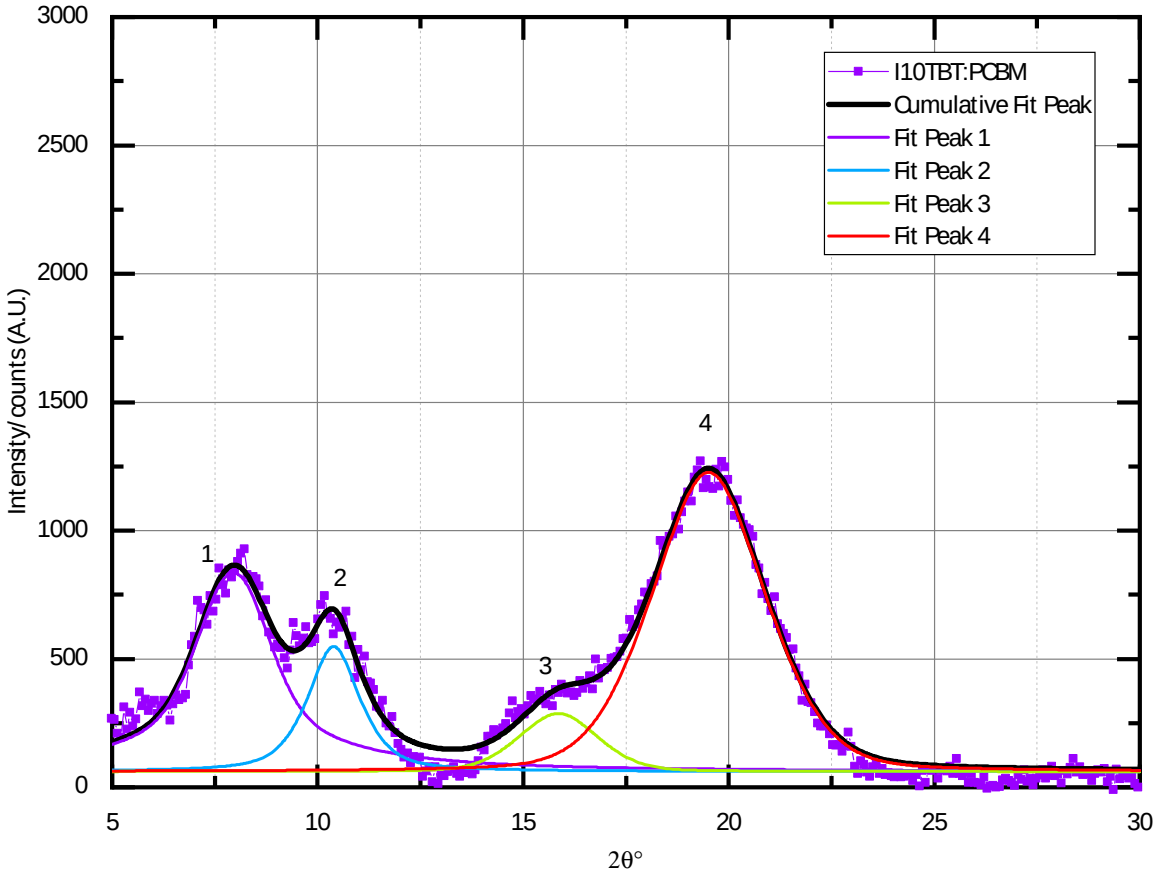

Figure B.17. GIXRD of I10TBT:PCBM Film. Each peak fit with Pseudo-Voigt.

Table B.11. I10TBT Peak location and d-spacing from GIXRD.

I10TBT Peak Index	$2\theta^\circ$	d-Spacing ($\pm$0.1) (Å)
1	4.20	21.0
2	5.12	17.3
3	7.15	12.4
4	8.66	10.2
5	10.43	8.5
6	12.78	6.9
7	15.34	5.8
8	20.64	4.3

Table B.12. I10TBT:PCBM Peak location and d-spacing from GIXRD.

I10TBT:PCBM Peak Index	$2\theta^\circ$	d-Spacing ($\pm$0.1) (Å)
1	7.95	11.1
2	10.39	8.5
3	15.85	5.6
4 (PCBM)	19.51	4.5

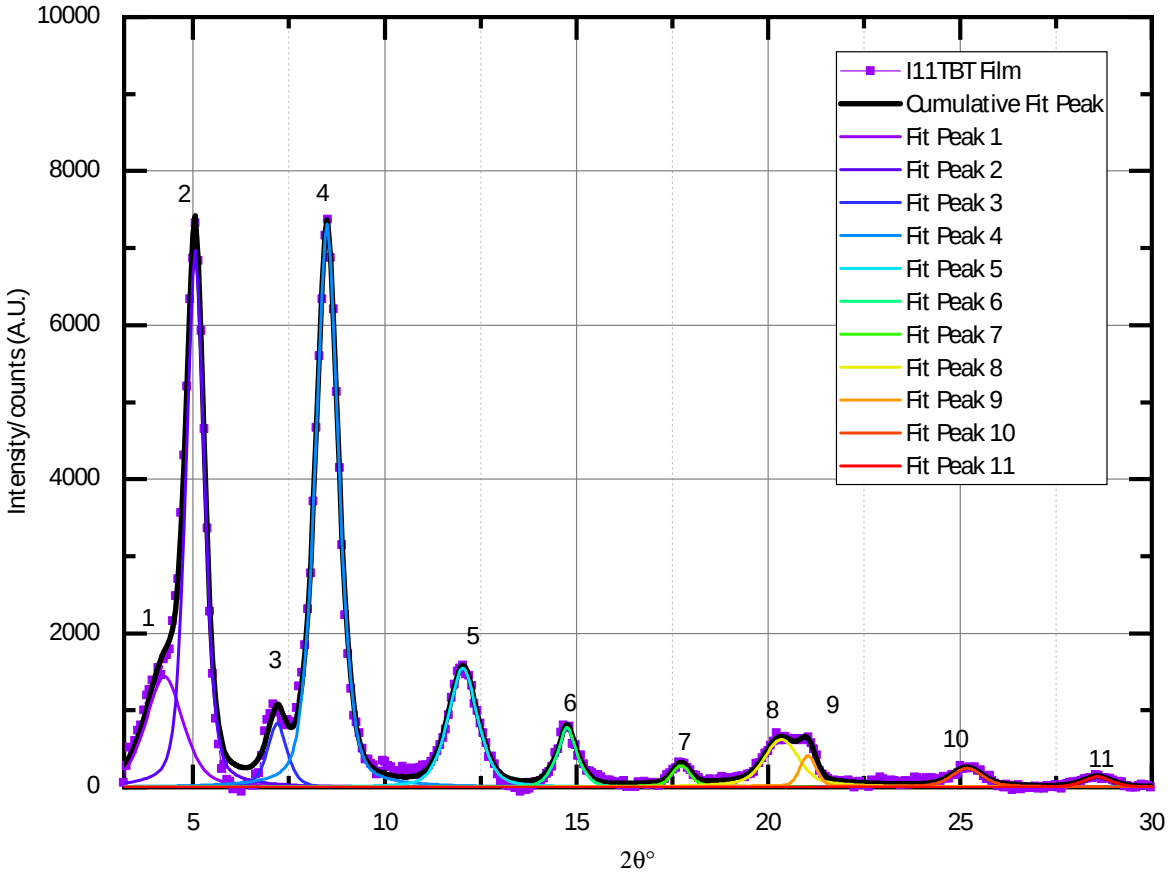

Figure B.18. GIXRD of I11TBT Film. Each peak fit with Pseudo-Voigt.

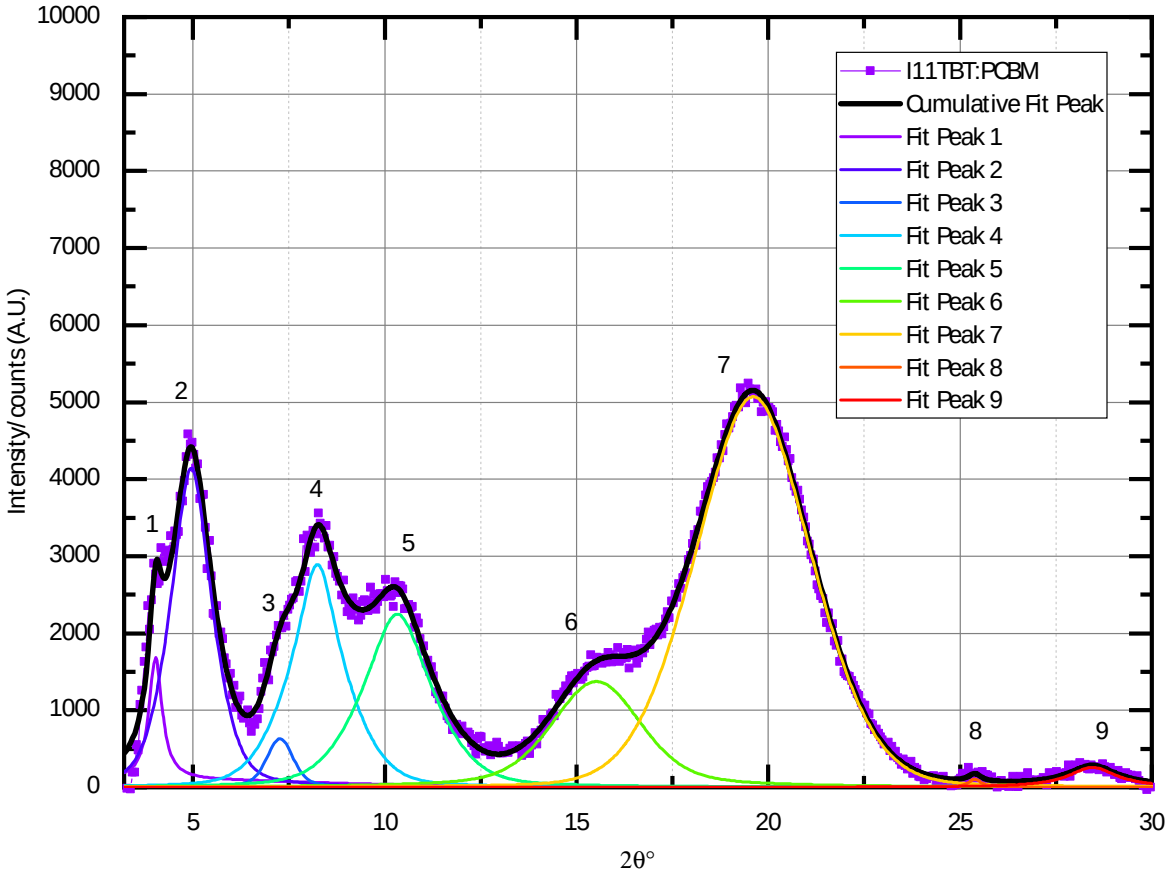

Figure B.19. GIXRD of I11TBT:PCBM Film. Each peak fit with Pseudo-Voigt.

Table B.13. I11TBT Peak location and d-spacing from GIXRD.

I11TBT Peak Index	$2\theta^\circ$	d-Spacing ($\pm$0.1) (Å)
1	4.25	20.8
2	5.05	17.5
3	7.19	12.3
4	8.49	10.4
5	12.03	7.4
6	14.75	6.0
7	17.73	5.0
8	20.34	4.4
9	21.04	4.2
10	25.18	3.5
11	28.58	3.1

Table B.14. I11TBT:PCBM Peak location and d-spacing from GIXRD.

I11TBT:PCBM Peak Index	$2\theta^\circ$	d-Spacing ($\pm$0.1) (Å)
1	4.02	22.0
2	4.95	17.8
3	7.27	12.2
4	8.24	10.7
5	10.33	8.6
6	15.52	5.7
7 (PCBM)	19.61	4.5
8	25.38	3.5
9	28.45	3.1

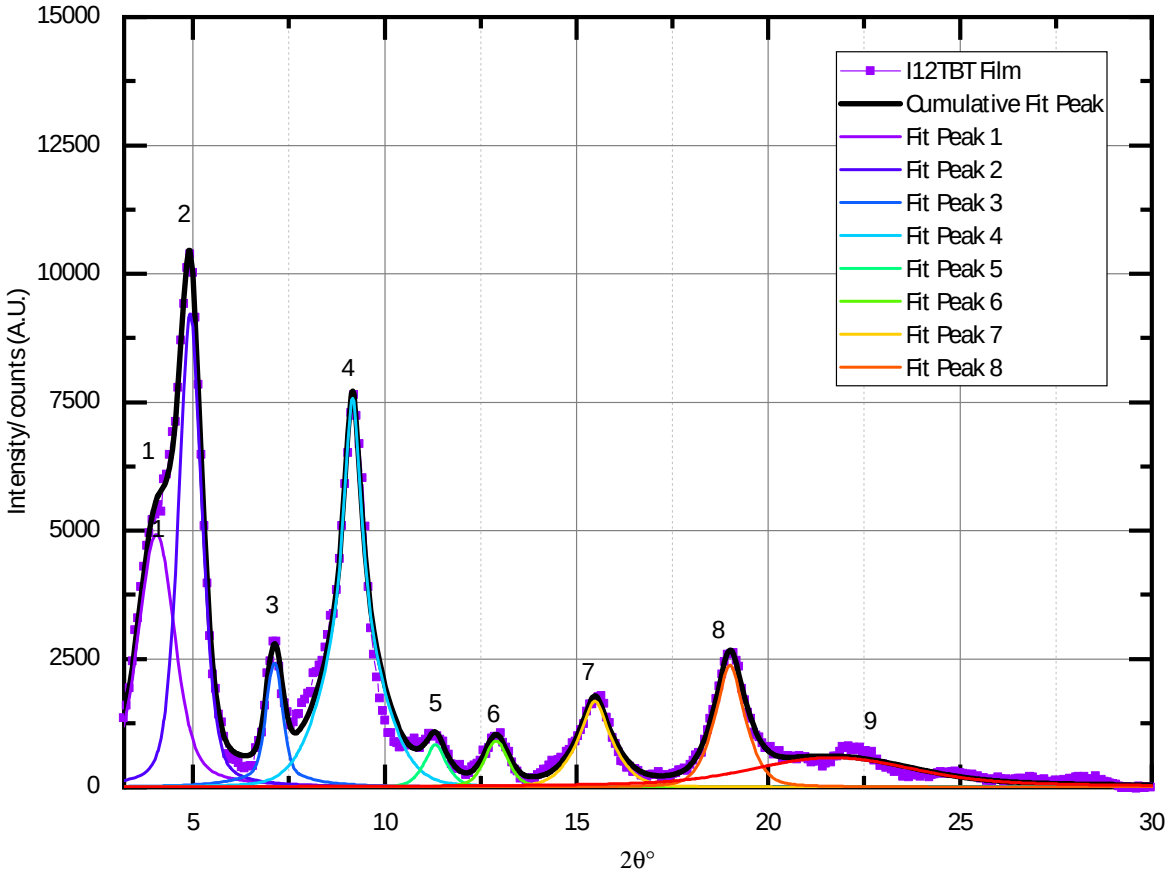

Figure B.20. GIXRD of I12TBT Film. Each peak fit with Pseudo-Voigt.

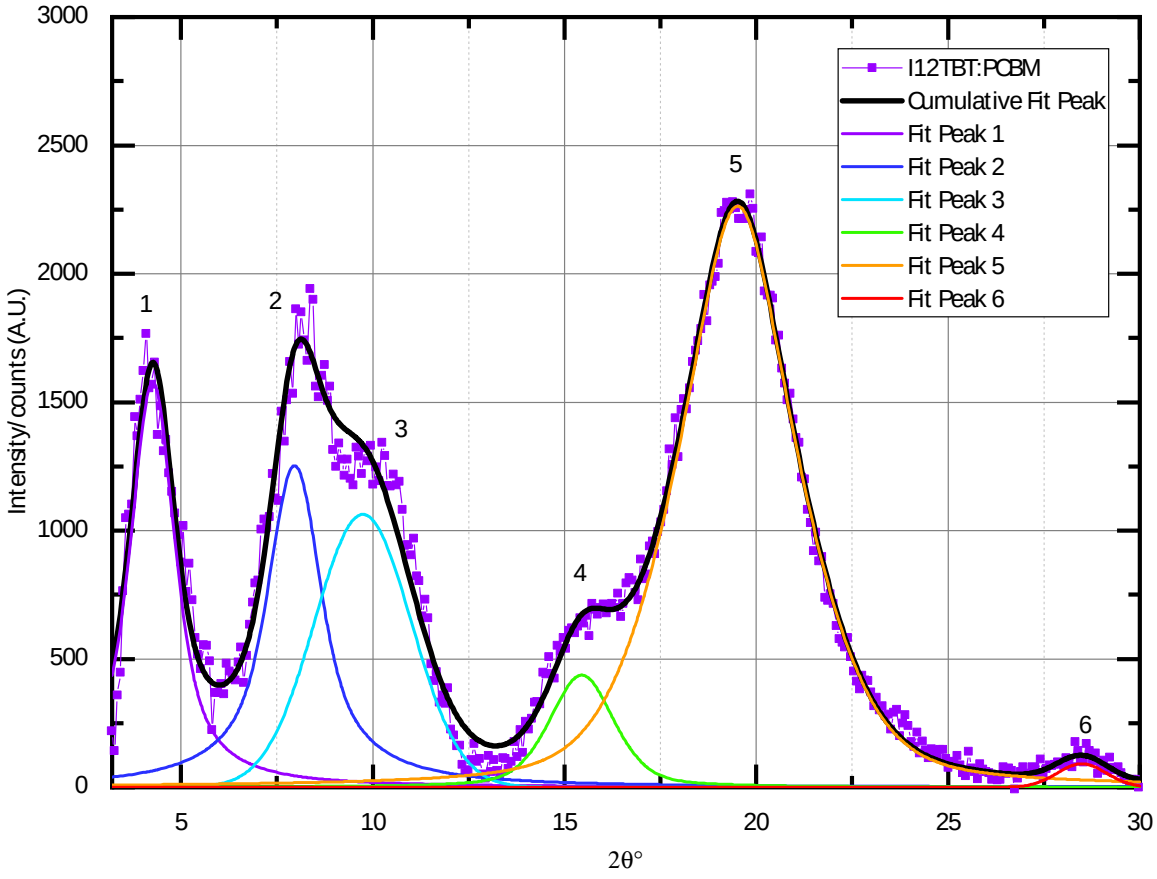

Figure B.21. GIXRD of I12TBT:PCBM Film. Each peak fit with Pseudo-Voigt.

Table B.15. I12TBT Peak location and d-spacing from GIXRD.

I12TBT Peak Index	$2\theta^\circ$	d-Spacing ($\pm$0.1) (Å)
1	4.04	21.8
2	4.93	17.9
3	7.12	12.4
4	9.16	9.7
5	11.32	7.8
6	12.90	6.9
7	15.48	5.7
8	19.00	4.7
9	21.68	4.1

Table B.16. I12TBT:PCBM Peak location and d-spacing from GIXRD.

I12TBT:PCBM Peak Index	$2\theta^\circ$	d-Spacing ($\pm$0.1) (Å)
1	4.26	20.74
2	7.96	11.11
3	9.74	9.08
4	15.45	5.74
5 (PCBM)	19.51	4.55
6	28.49	3.13

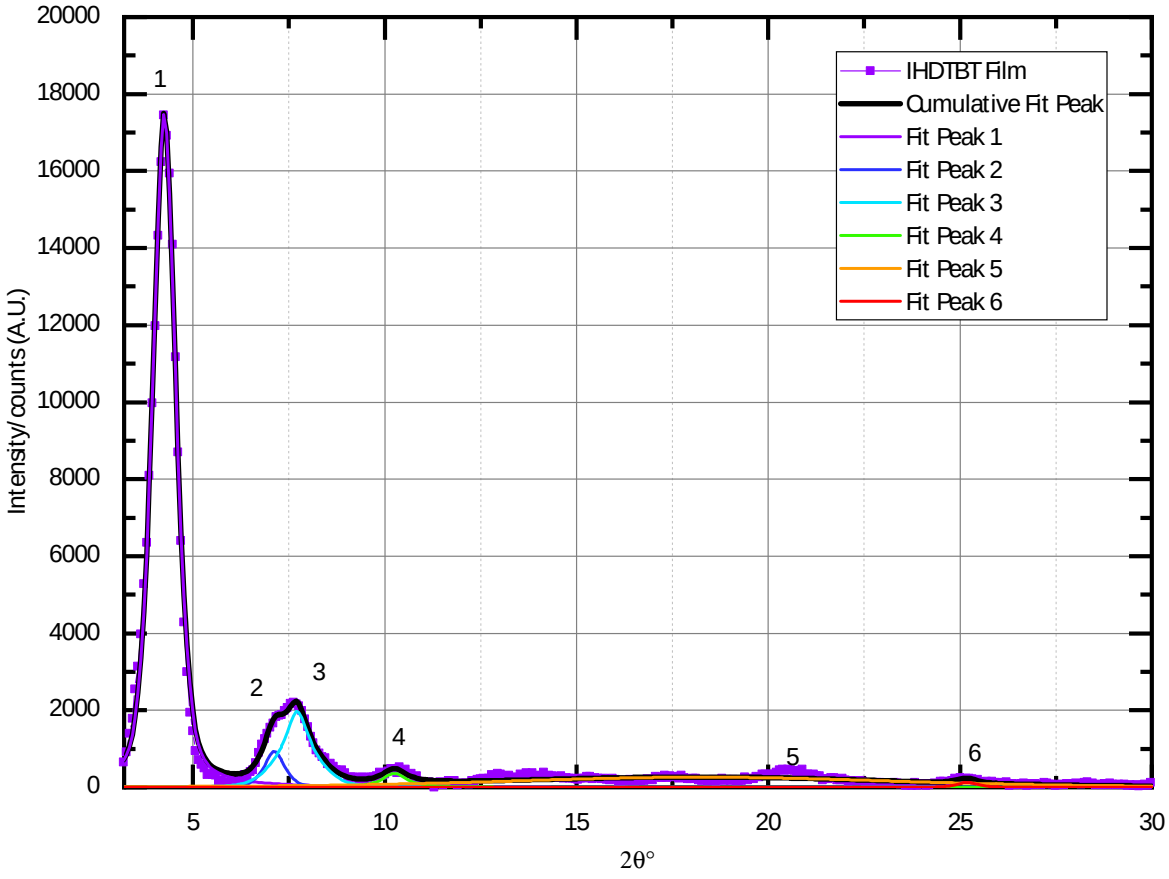

Figure B.22. GIXRD of IHDTBT Film. Each peak fit with Pseudo-Voigt.

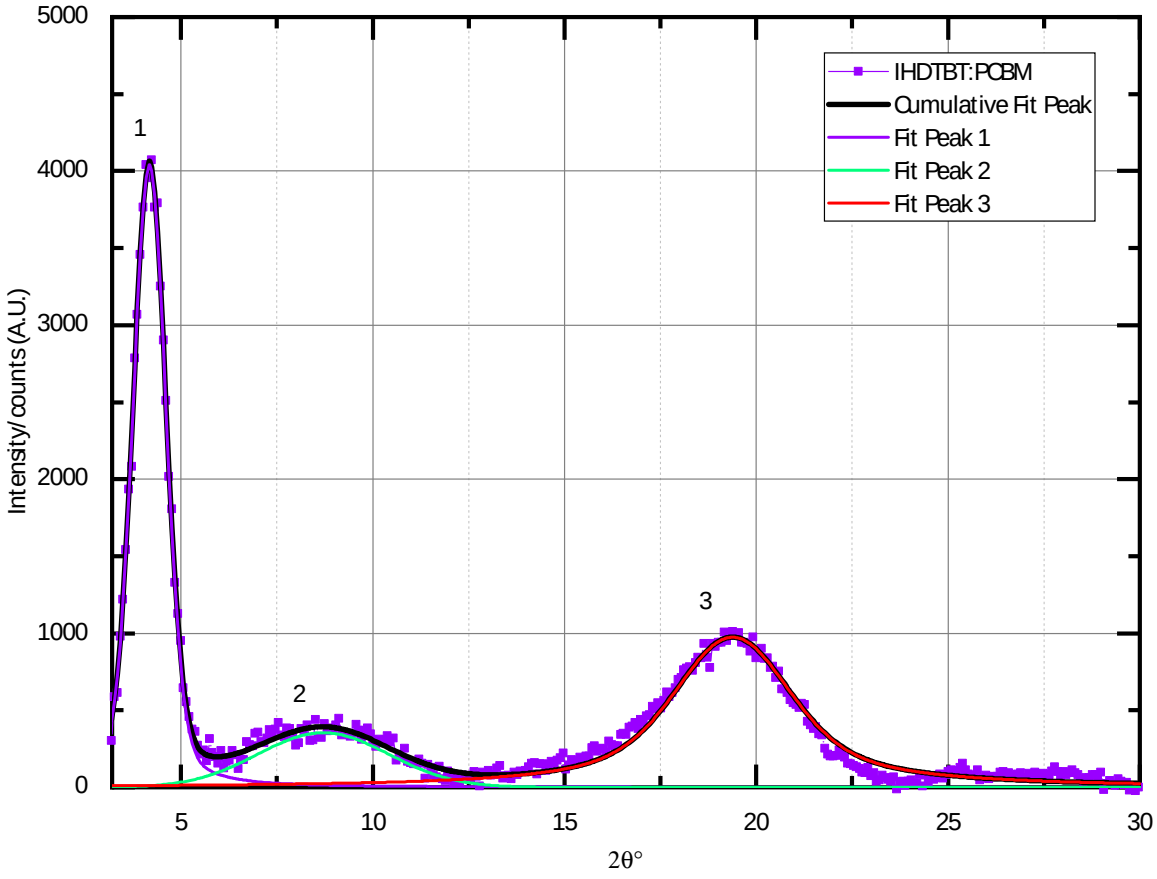

Figure B.23. GIXRD of IHDTBT:PCBM Film. Each peak fit with Pseudo-Voigt.

Table B.17. IHDTBT Peak location and d-spacing from GIXRD.

IHDTBT Peak Index	$2\theta^\circ$	d-Spacing ($\pm$0.1) (Å)
1	4.25	20.8
2	7.12	12.4
3	7.71	11.5
4	10.25	8.6
5	18.24	4.9
6	25.19	3.5

Table B.18. IHDTBT:PCBM Peak location and d-spacing from GIXRD.

IHDTBT:PCBM Peak Index	$2\theta^\circ$	d-Spacing ($\pm$0.1) (Å)
1	4.18	21.2
2	8.71	10.2
3	19.38	4.6

Table B.19. Bragg's d-spacing and coherence length extracted from the PCBM peak from pure PCBM and mixed 2:3 InTBT:PCBM films.

Sample	d-Spacing (Å)	Coherence Length (nm)
PCBM	4.6±0.1	1.4±0.3
I6TBT:PCBM	4.5 ±0.1	1.9 ±0.2
I7TBT:PCBM	4.6 ± 0.1	1.8±0.6
I8TBT:PCBM	4.6±0.1	1.7±0.9
I9TBT:PCBM	4.6±0.1	1.5±0.8
I10TBT:PCBM	4.5±0.1	1.7±0.8
I11TBT:PCBM	4.5±0.1	1.6±0.8
I12TBT:PCBM	4.5±0.1	1.4±0.3
IHDTBT:PCBM	4.6±0.1	1.3±0.7

B.6 Small-Angle Neutron Scattering

B.6.1 Volume Balance

Volume fraction of InTBT in mixed and ellipsoidal domains was determined with the following volume balance.

$$1 = \phi_{Ellipsoid}^{InTBT} + \phi_{Mixed} \tag{B.1}$$

$$\phi_{Mixed} = \phi_{Mixed}^{InTBT} + \phi_{Mixed}^{PCBM} \tag{B.2}$$

$$1 = \phi_{Ellipsoid}^{InTBT} + \phi_{Mixed}^{InTBT} + \phi_{Mixed}^{PCBM} \tag{B.3}$$

The volume fraction of InTBT (ϕ^{InTBT}) in the film is determined by the initial weight ratio 40:60 InTBT:PCBM in the solution prior to film deposition. We assume this ratio remains constant when the film is created. The volume fraction of InTBT is calculated by:

$$\phi^{InTBT} = \phi_{Ellipsoid}^{InTBT} + \phi_{Mixed}^{InTBT} = \frac{\frac{W_{InTBT}}{\rho_{InTBT}}}{\frac{W_{InTBT}}{\rho_{InTBT}} + \frac{W_{PCBM}}{\rho_{PCBM}}} \tag{B.4}$$

Where w_{InTBT} and ρ_{InTBT} are the weight fractions and solid state mass densities of InTBT, and w_{PCBM} and ρ_{PCBM} are the weight fractions and solid state mass densities of PCBM. The estimated volume fractions are $\phi^{InTBT} = 0.484$ and 0.498 for I7TBT and I8TBT; and, $\phi_{Mixed}^{PCBM} =$ 0.516 and 0.502 for I7TBT and I8TBT.

The volume fraction of ellipsoids and the scattering length density contrast (ΔSLD) are both scalars in the Ellipsoidal form factor. Where,

$$\Delta SLD = \mid SLD_{Ellisoids} - SLD_{Mixed} \mid \tag{B.5}$$

Since the ellipsoids are assumed to be composed of pure InTBT in the the I7TBT and I8TBT samples, $SLD_{Ellisoids}$ are estimated using the atomic density from single crystal XRD simulation (Table A.2). ΔSLD is fit and SLD_{Mixed} is calculated using Equation B.5. SLD_{Mixed} can be split into its components (InTBT and PCBM):

$$SLD_{Mixed} = \frac{\phi_{Mixed}^{InTBT}}{\phi_{Mixed}} SLD^{InTBT} + \frac{\phi^{PCBM}}{\phi_{Mixed}} SLD^{PCBM} \tag{B.6}$$

Rearrange for ϕ_{Mixed}^{InTBT}:

$$\frac{\left(SLD_{Mixed} - SLD^{PCBM}\left(\frac{\phi_{Mixed}^{PCBM}}{\phi^{Mixed}}\right)\right)\phi^{Mixed}}{SLD^{InTBT}} = \phi_{Mixed}^{InTBT} \tag{B.7}$$

We calculate ϕ_{Mixed}^{InTBT} from scattering length densities and the ellipsoid volume fraction from a given fit, plug back into Equation B.3 to check that it remains balanced.

Variables:

$\phi_{Ellipsoid}^{InTBT}$: Volume fraction of InTBT in ellipsoidal domains

ϕ_{Mixed}^{InTBT}: Volume fraction of InTBT in mixed domains

ϕ_{Mixed}^{PCBM}: Volume fraction of PCBM in mixed domains (for I7TBT, I8TBT, and I9TBT this is also the total volume fraction of PCBM in the film)

$\phi^{Mixed} = \phi_{Mixed}^{InTBT} + \phi_{Mixed}^{PCBM}$

SLD_{Mixed}: Scattering length density of mixed domain.

SLD^{PCBM}: Scattering length density of pure PCBM(calculated from PCBM atomic density)[2]

SLD^{InTBT}: Scattering length density of pure InTBT domains (calculated from atomic density determined by measured unit cell dimensions)

Lognormal Distribution used in ellipsoidal models:

$$f(r,\sigma) = \frac{1}{Norm}\frac{1}{r*\sigma} exp\left(-\frac{1}{2}\left(\frac{ln(r) - ln(r_{med})}{\sigma}\right)^2\right) \tag{B.8}$$

Table B.20. Calculated scattering length density of pure domains. Based on crystal structure information.

Material	SLD ($*10^{-6}\AA^{-2}$)
PCBM	4.66
I7TBT	1.34
I8TBT	1.25
I9TBT	Can't assume pure ellipsoids
I10TBT	Can't assume pure ellipsoids
I11TBT	Can't assume pure ellipsoids
IHDTBT	Need Crystal Structure Unit cell

With radius (r), median radius (r_{med}), distribution width (σ). The mean radius (r_{Mean}) is given by:

$$r_{Mean} = exp\left(ln(r_{med}) + \frac{\sigma^2}{2}\right) \tag{B.9}$$

The peak of the distribution is located at:

$$r_{Max} = exp\left(ln(r_{med}) - \sigma^2\right) \tag{B.10}$$

The ellipsoidal scattering intensity is normalized by the distribution such that

$$P(q) = \frac{scale}{V}\int f(r,\sigma)F^2(q,r)dr + background \tag{B.11}$$

Where $F(q,\alpha)$ is the ellipsoidal form factor.

$$F(q,\alpha) = \Delta SLD * V\frac{3\left(sin(q*y) - q*ycos(q*y)\right)}{(q*y)^3} \tag{B.12}$$

Where,

$$y = \left(R_s^2 sin^2\alpha + R_p^2 cos^2\alpha\right)^{1/2} \tag{B.13}$$

α is the angle between the axis of the ellipsoid and q. R_s is the short axis of the ellipsoid, and R_L is the long axis of the ellipsoid.

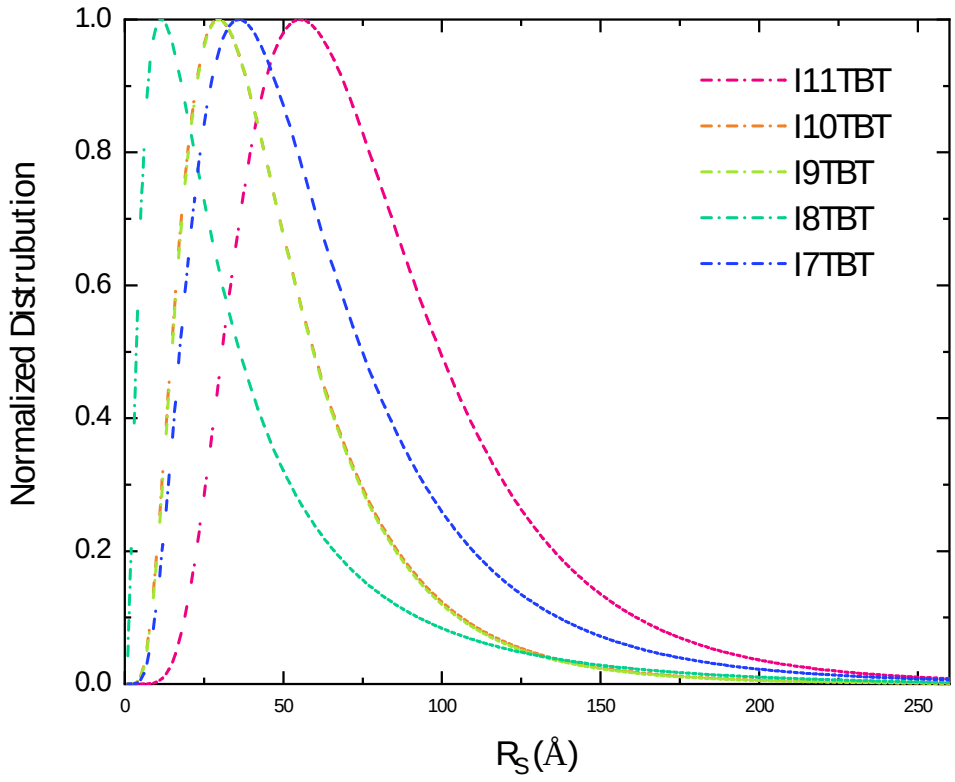

Figure B.24. Lognormal distribution of short ellipsoid radii.

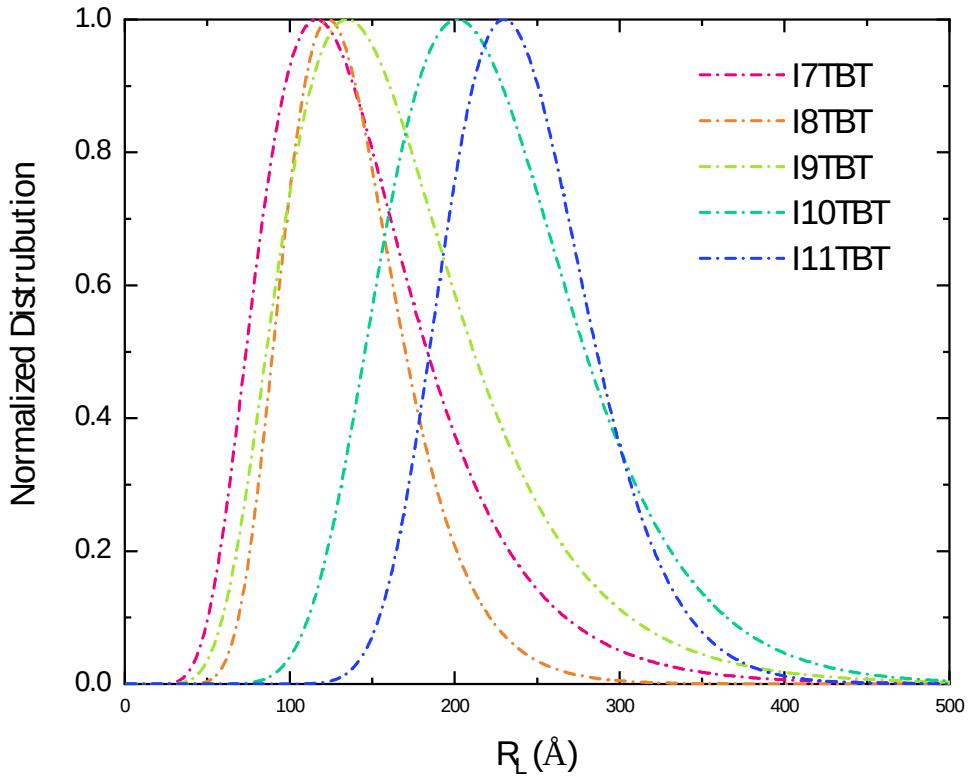

Figure B.25. Lognormal distribution of long ellipsoid radii.

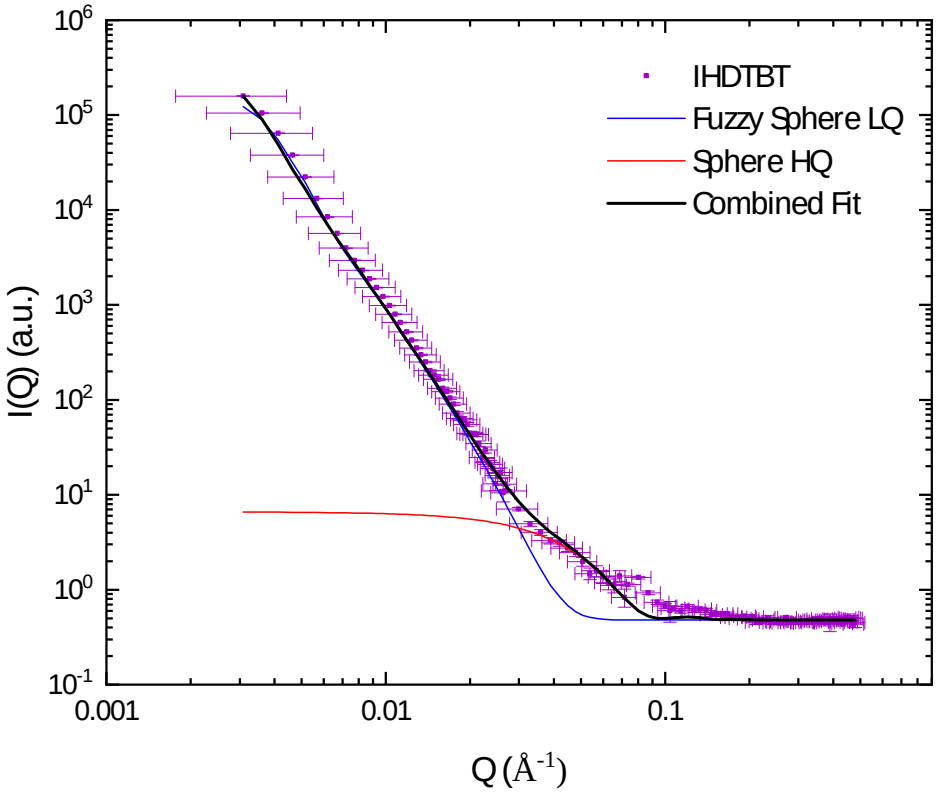

Figure B.26. IHDTBT SANS data fit with fuzzy spherical form factor at low Q and spherical form factor at high Q.

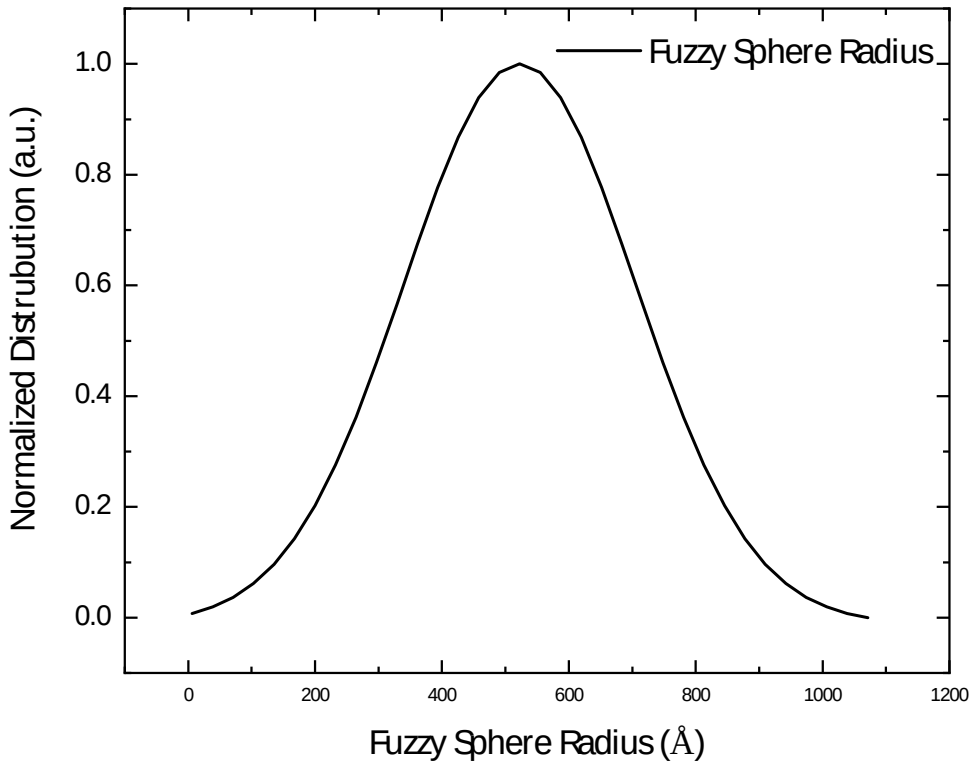

Figure B.27. Gaussian distribution of the fuzzy sphere radii for IHDTBT fit.

B.7 Atomic Force Microscopy

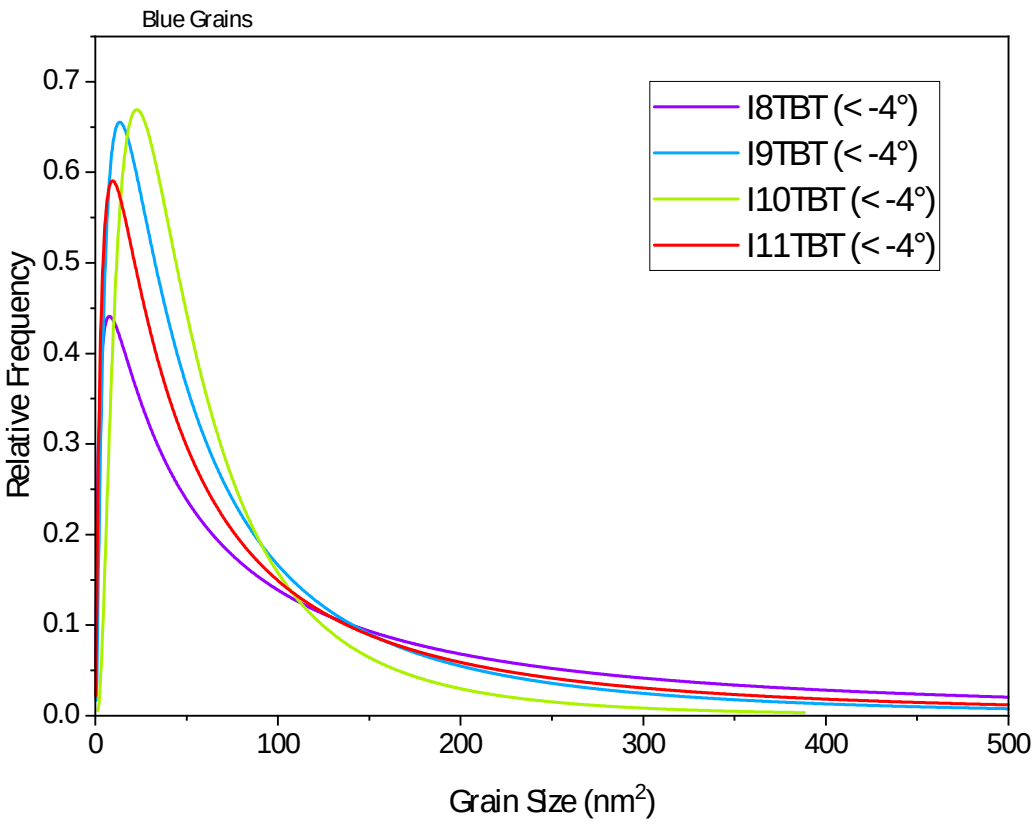

Figure B.28. Lognormal distribution of the blue grain sizes.

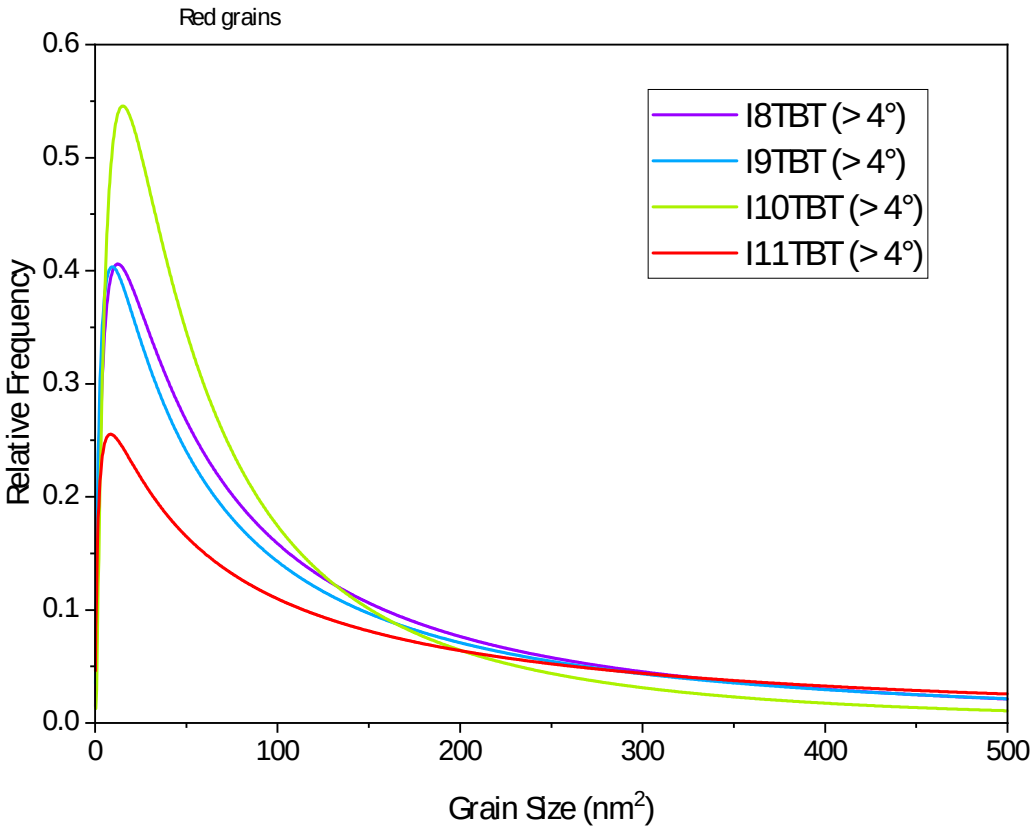

Figure B.29. Lognormal distribution of the red grain sizes.

REFERENCES

[1] H. Bürckstümmer, E. V. Tulyakova, M. Deppisch, M. R. Lenze, N. M. Kronenberg, M. Gsanger, M. Stolte, K. Meerholz, and F. Würthner, "Efficient solution-processed bulk heterojunction solar cells by antiparallel supramolecular arrangement of dipolar donor-acceptor dyes," *Angew. Chem. Int. Ed.*, vol. 50, pp. 11628–11632, Dec. 2011.

[2] A. J. Clulow, A. Armin, K. H. Lee, A. K. Pandey, C. Tao, M. Velusamy, M. James, A. Nelson, P. L. Burn, I. R. Gentle, and P. Meredith, "Determination of fullerene scattering length density: A critical parameter for understanding the fullerene distribution in bulk heterojunction organic photovoltaic devices," *Langmuir*, vol. 30, pp. 1410–1415, Feb. 2014.

Appendix C

Supporting information for "Anion Exchange Doping: Tuning Equilibrium to Increase Doping Efficiency in Semiconducting Polymers"

C.1 Molecular Structure of Materials

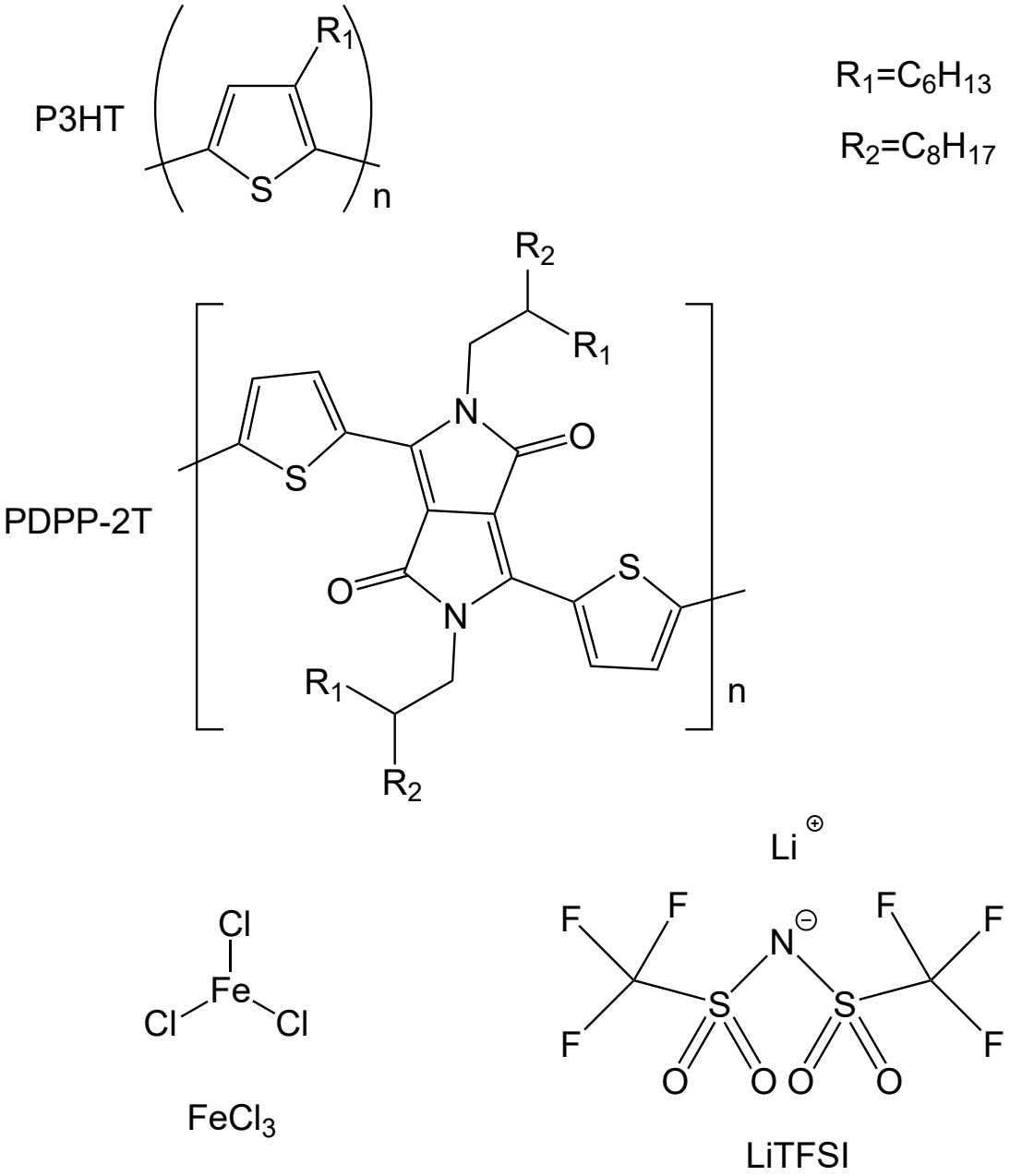

Figure C.1. Chemical Structures of P3HT, PDPP-2T, $FeCl_3$, and LiTFSI.

C.2 Experimental Methods

Electronic grade poly(3-hexylthiophene-2,5-diyl) (P3HT) (regioregular $\geq$96%, MW = 83 kDa) was purchased from Rieke. Anhydrous lithium bis(trifluoromethanesulfonimide) (Li-TFSI) was

purchased from TCI America. Anhydrous iron(III) chloride ($FeCl_3$) was purchase from Alfa Aesar. Anhydrous n-butyl acetate (nBA), anhydrous chloroform (CF), anhydrous chlorobenzene (CB), and anhydrous dichlorobenzene (DCB) were purchased from Sigma Aldrich. All chemicals were used without further purification. PDPP-2T was synthesized in house and synthetic procedures are listed in Supporting Information section S2. Quartz substrates were purchased from Quartz Scientific Inc., and silicon wafers were purchased from University Wafers.

Quartz and silicon substrates were cleaned in a series of ultrasonic baths of acetone, methanol, isopropanol and deionized water, then dried with nitrogen and exposed to UV/ozone for 30 min. P3HT films were prepared by spin coating 25 mg mL^{-1} solutions in DCB at 600 rpm for 60 s, then 2000 rpm for 30 s. Film thicknesses of 180 nm were confirmed using a Veeco Dektak 150 surface Profilometer. P3HT films were submerged in 8 mL nBA solutions with varying combinations of LiTFSI (0-100 mM) and $FeCl_3$ (0.1-5 mM) concentrations for 5 min at RT. After removing samples from solution, they were spun at $\sim$5000 rpm for 30 s to remove excess solvent. Spin coating and film doping were performed in a nitrogen-filled glovebox (O_2 level < 10 ppm, H_2O level < 5 ppm). PDPP-2T films were prepared by dynamic spin coating 5 mg mL^{-1} solutions in 4:1 CF:CB at 1000 RPM for 45 s, then thermally annealing in a nitrogen glovebox at 125°C for 1 h. Film thicknesses of 80 nm were confirmed using a Veeco Dektak 150 surface Profilometer. PDPP-2T films were submerged in 8 mL nBA solutions with 0 mM or 100 mM LiTFSI and 0.5 to 5 mM $FeCl_3$ concentrations for 5 min at RT then thermally annealed at 50°C for 30 min to evaporate the solvent. 200μL of nBA was spun coat at 2000 RPM for 60 s on each film to remove excess LiTFSI and $FeCl_3$ deposits. UV-vis-NIR and conductivity measurements were carried out on doped samples. UV-Vis-NIR spectra were measured under atmospheric conditions using a PerkinElmer Lambda 750 spectrometer. Four-point probe collinear sheet resistance measurements were performed in a nitrogen-filled glovebox. A Keithley 2420 source meter was used for P3HT sheet resistance measurements. For the P3HT samples, electrodes (5 nm Cr/95 nm Au, 1 5 mm^2, 1 mm spacing) were deposited on Si wafers via thermal evaporation prior to spin coating the films. A Keithley 2450 source meter in combination with a Signatone 4-point probe system was used for PDPP-2T sheet resistance measurements.

X-ray photoelectron spectroscopy (XPS) was performed using a Kratos AXIS Supra spec-

trometer equipped with a monochromatic Al Kα anode (1486.6 eV), hemispherical analyzer, and a 128 channel delay-line detector. Samples were fastened onto the sample bar and loaded from air into a flexi-lock. The flexi-lock was pumped down to 10^{-7} torr prior to automatic transfer of samples to the analysis chamber. The pressure of the analysis chamber was kept below 5x10^{-8} torr throughout experimentation. An electron gun with a bias of 1.2V and current of 0.45A was used as a charge neutralizer. All binding energies were charge corrected by referencing the C1s peak to 284.8 eV. The data were processed and analyzed using Kratos ESCApe software.

C.3 PDPP-2T Synthesis

C.3.1 Materials and Methods

All chemicals were purchased from the Millipore Sigma and were used without further purification unless noted otherwise. Catalyst components Ni(COD)2 (bis(1,5-cyclooctadiene)nickel(0)) and BBBPY (4,4-di-tert-butyl-2,2-dipyridyl) were purchased from the Millipore Sigma and stored in a nitrogen-filled glovebox ($<$ 0.5 ppm O_2, $<$ 0.5 ppm H_2O). Anhydrous THF, the polymerization solvent, was purchased from Sigma-Aldrich and was degassed prior to transfer to the glovebox. 3,6-Bis(5-bromothiophen-2-yl)-2,5-bis(2-hexyldecyl)- 2,5-dihydropyrrolo[3,4-c]pyrrole-1,4-dione was synthesized according to reported procedures.[1]

Polymer molecular weight was determined on an Agilent 1260 Infinity II GPC/SEC system equipped with a set of two PLgel 5 μm mixed-C columns using chloroform (stabilized with 250 ppm of ethanol) as eluent at 50°C and calibrated with polystyrene standards. Polymer samples were pre-dissolved at 0.50 mg/mL concentration in chloroform under stirring at 50°C overnight.

C.3.2 PDPP-2T

A Yamamoto polymerization reaction was set up in a nitrogen-filled glovebox ($<$0.5 ppm O_2, $<$0.5 ppm H_2O) following the modified protocol described in previous reports.[2, 3, 4] An oven-dried 10 mL Wheaton V-vial equipped with a stir bar was charged with the solution of $Ni(COD)_2$ (109 mg, 0.397 mmol), BBBPY (4,4-di-tert-butyl-2,2-dipyridyl) (106.5 mg, 0.397 mmol) and 3,6-bis(5-bromothiophen-2-yl)-2,5-bis(2-hexyldecyl)-2,5-dihydropyrrolo[3,4-c]pyrrole-1,4-dione (300 mg, 0.33 mmol) in 10 mL of THF. The vial was sealed with a Teflon-lined Mininert pres-

sure screw cap and transferred out of the glove box. The reaction mixture was stirred at room temperature for 24 h. The resulting polymer was precipitated into 100 mL of methanol containing 5 mL 12 N HCl with vigorously stirring. After 1 h, the polymer was filtered through a cellulose extraction thimble and subjected to Soxhlet extraction using methanol, acetone, hexane, and chloroform, in that order. After the final extraction, the chloroform solution of the polymer was precipitated into 100 mL of methanol with vigorous stirring. The polymer product was collected by filtration through a nylon membrane and dried overnight under high vacuum (100 mTorr) at 60°C to afford the PDPP-2T polymer (221.6 mg, 89.4%, M_n = 95400, M_w/M_n = 4.5).

C.4 UV-Vis-NIR Full Gaussian Fits

Similar to previous studies,[5] we constrained the peak positions to remain constant across all of the studied samples. Previous studies have determined that increased doping level can increase or decrease the structural and energetic disorder of the polymer.[6, 7, 8, 9] Upon increased doping, we measure a blue-shift in the remaining neutral P3HT sites absorbance. This blue–shift is interpreted as first doping the band edge states at lower doping concentrations before doping sites with increased structural disorder. The width of the P2 and P3 transitions remains constant and the peak areas increase with increasing doping level until the doping level saturates at $\sim$ 1 mM $FeCl_3$ concentration. P1 provides the best measure of polaron absorbance across all spectra with a peak center position at 0.47 eV. The P1 width and area increase as a function of the doping level up through the 5 mM $FeCl_3$ concentration. Again, the increased peak width indicates that $P3HT^+$ sites are not identical. The increased absorbance width of the P1 peak along with the blue-shift of the neutral P3HT absorbance both indicate that highly planar polymer sites are preferentially doped at low doping concentrations to yield similar polaron structure/absorbance. With increased dopant density, less favorable neutral sites are doped and yield polaron sites with greater structural/energetic heterogeneity.[10]

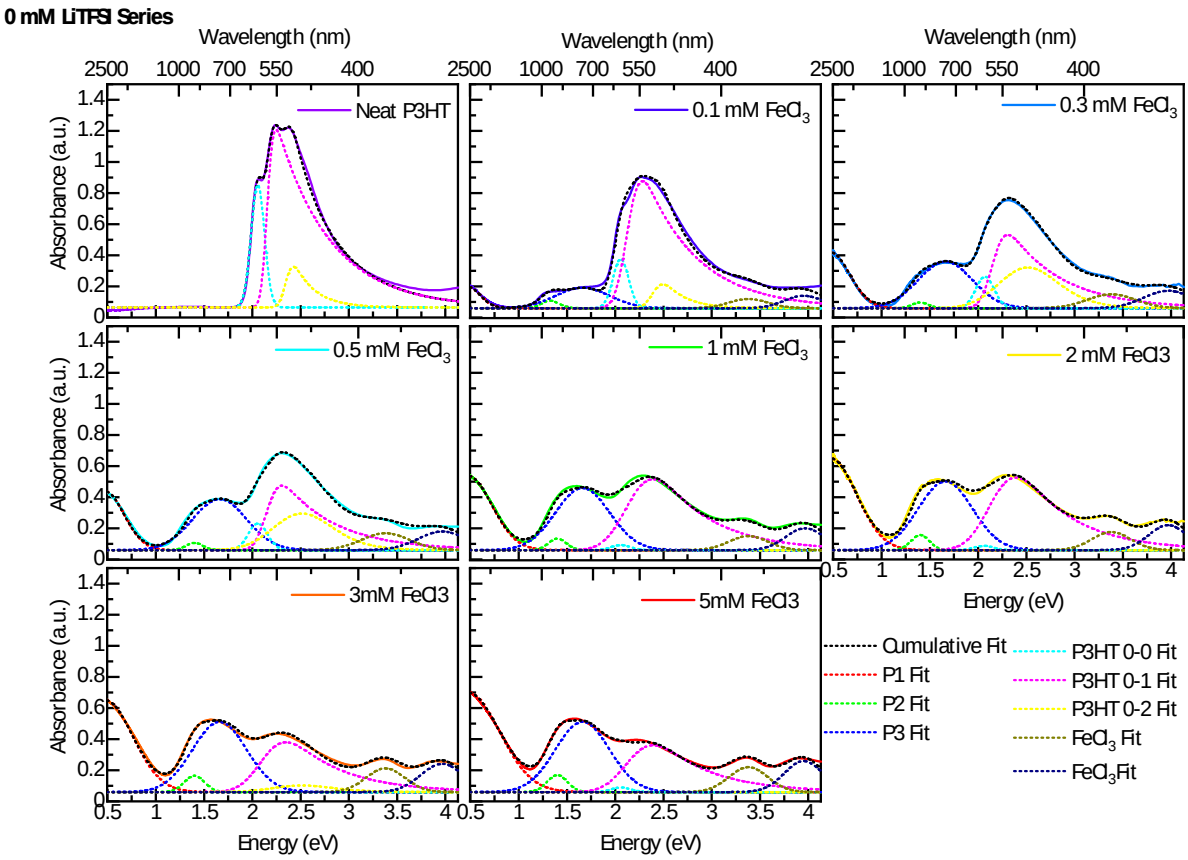

Figure C.2. Full UV-Vis-NIR spectral fits of P3HT films soaked in a solution various $FeCl_3$ concentrations in n-butyl acetate.

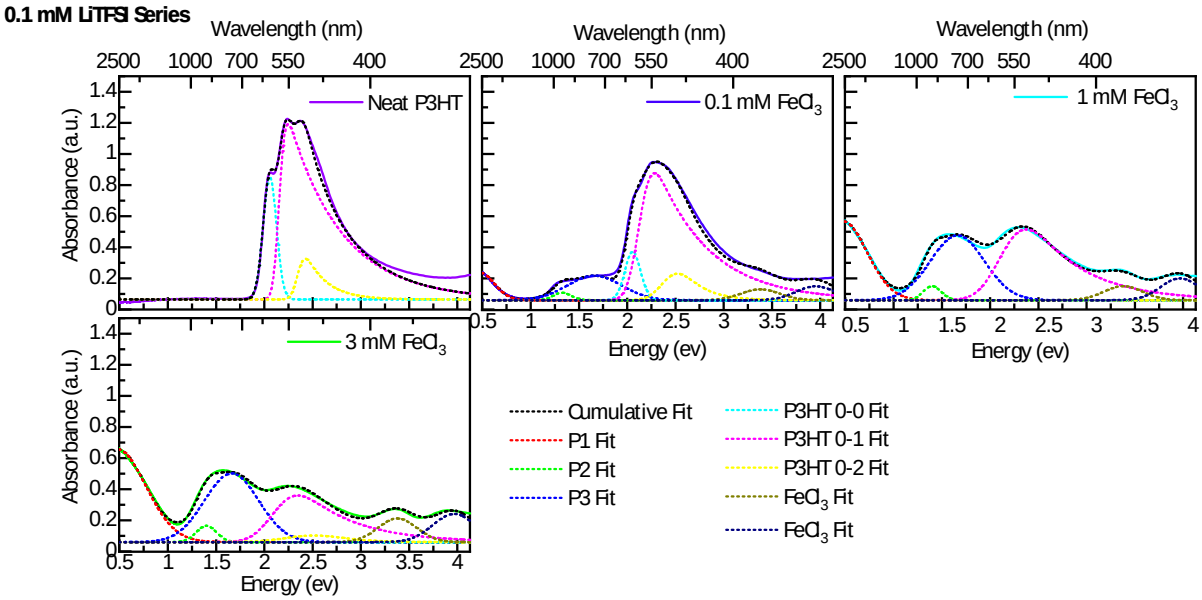

Figure C.3. Full UV-Vis-NIR spectral fits of P3HT films soaked in a solution with 0.1 mM LiTFSI and various $FeCl_3$ concentrations in n-butyl acetate.

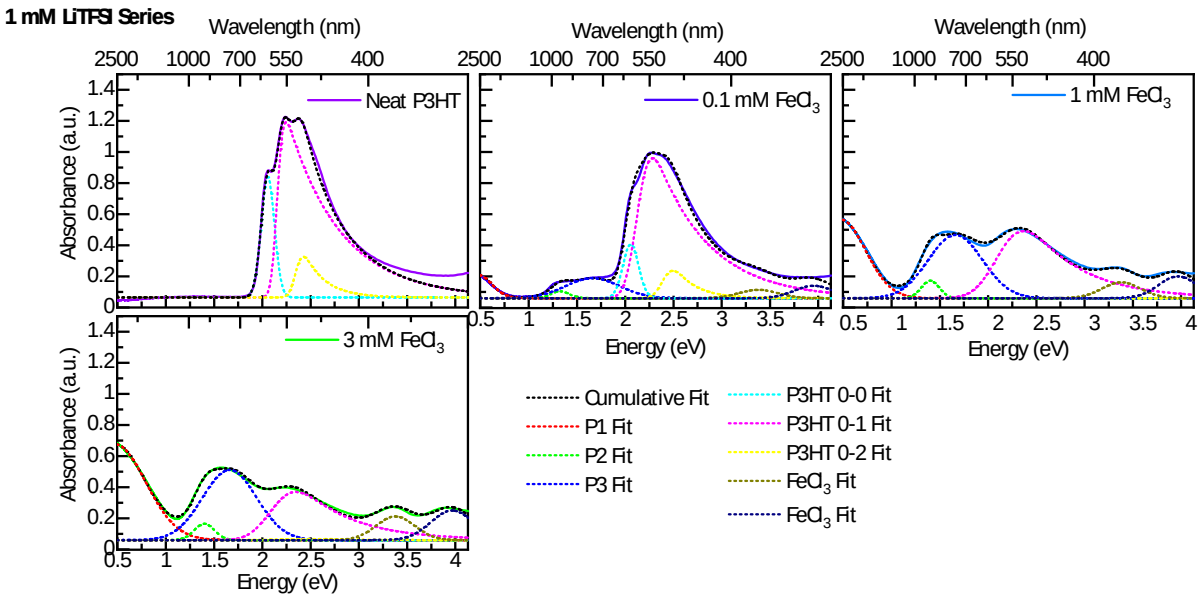

Figure C.4. Full UV-Vis-NIR spectral fits of P3HT films soaked in a solution with 1 mM LiTFSI and various $FeCl_3$ concentrations in n-butyl acetate.

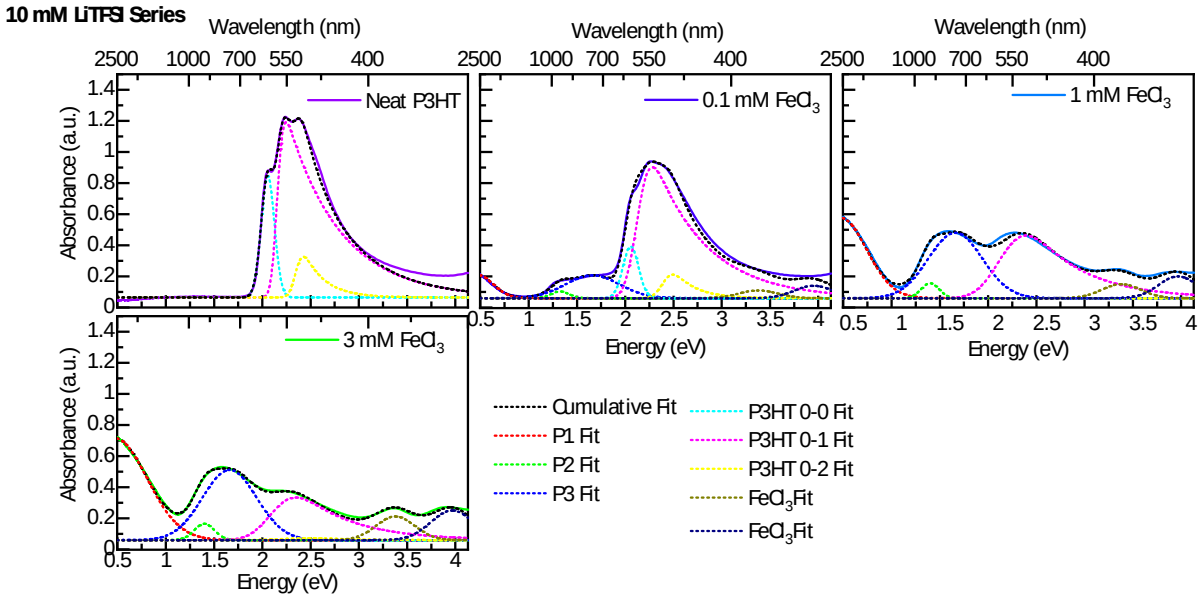

Figure C.5. Full UV-Vis-NIR spectral fits of P3HT films soaked in a solution with 10 mM LiTFSI and various $FeCl_3$ concentrations in n-butyl acetate.

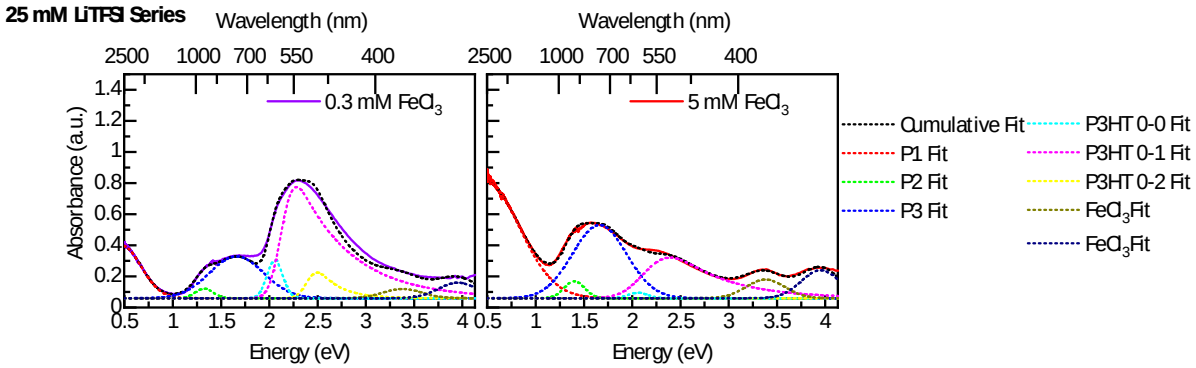

Figure C.6. Full UV-Vis-NIR spectral fits of P3HT films soaked in a solution with 25 mM LiTFSI and various $FeCl_3$ concentrations in n-butyl acetate.

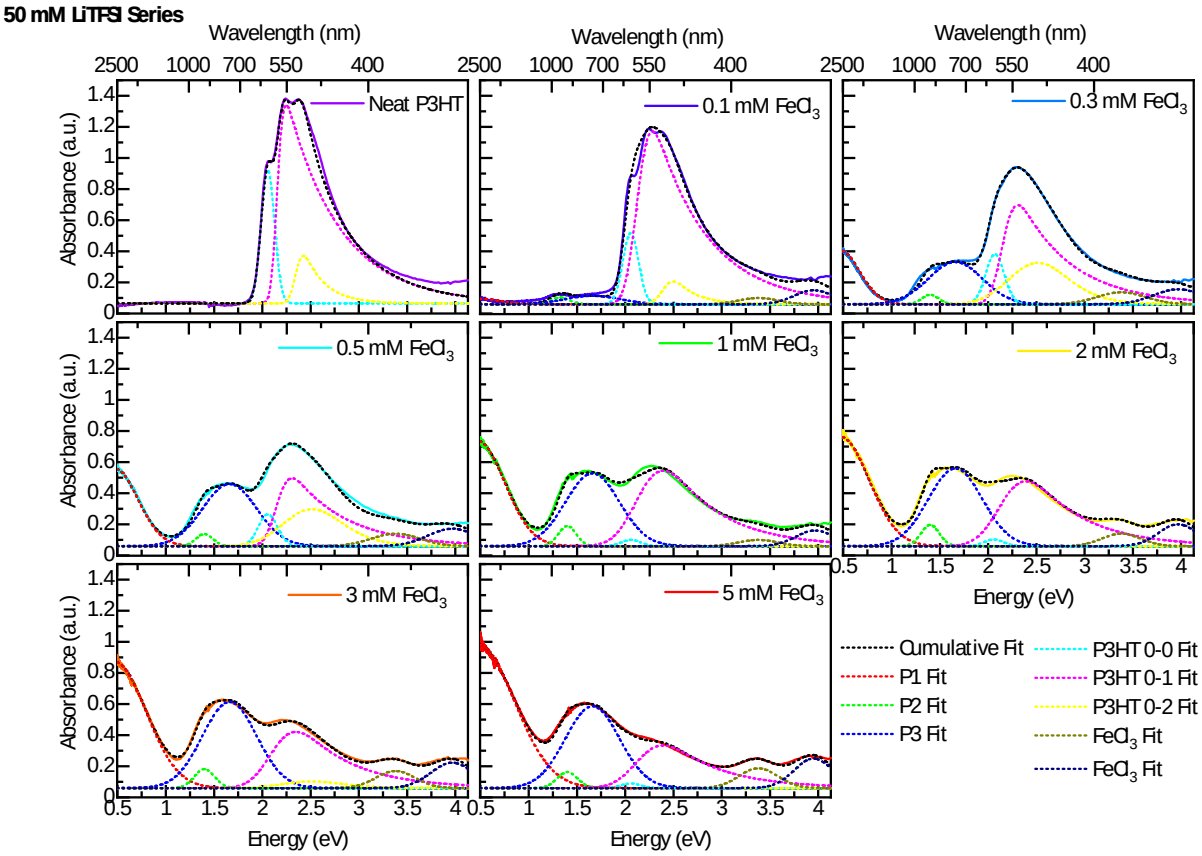

Figure C.7. Full UV-Vis-NIR spectral fits of P3HT films soaked in a solution with 50 mM LiTFSI and various $FeCl_3$ concentrations in n-butyl acetate.

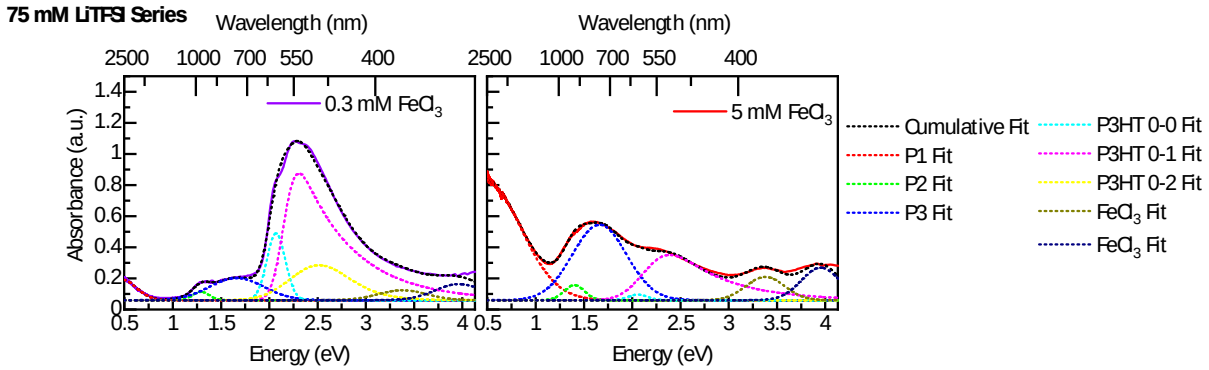

Figure C.8. Full UV-Vis-NIR spectral fits of P3HT films soaked in a solution with 75 mM LiTFSI and various $FeCl_3$ concentrations in n-butyl acetate.

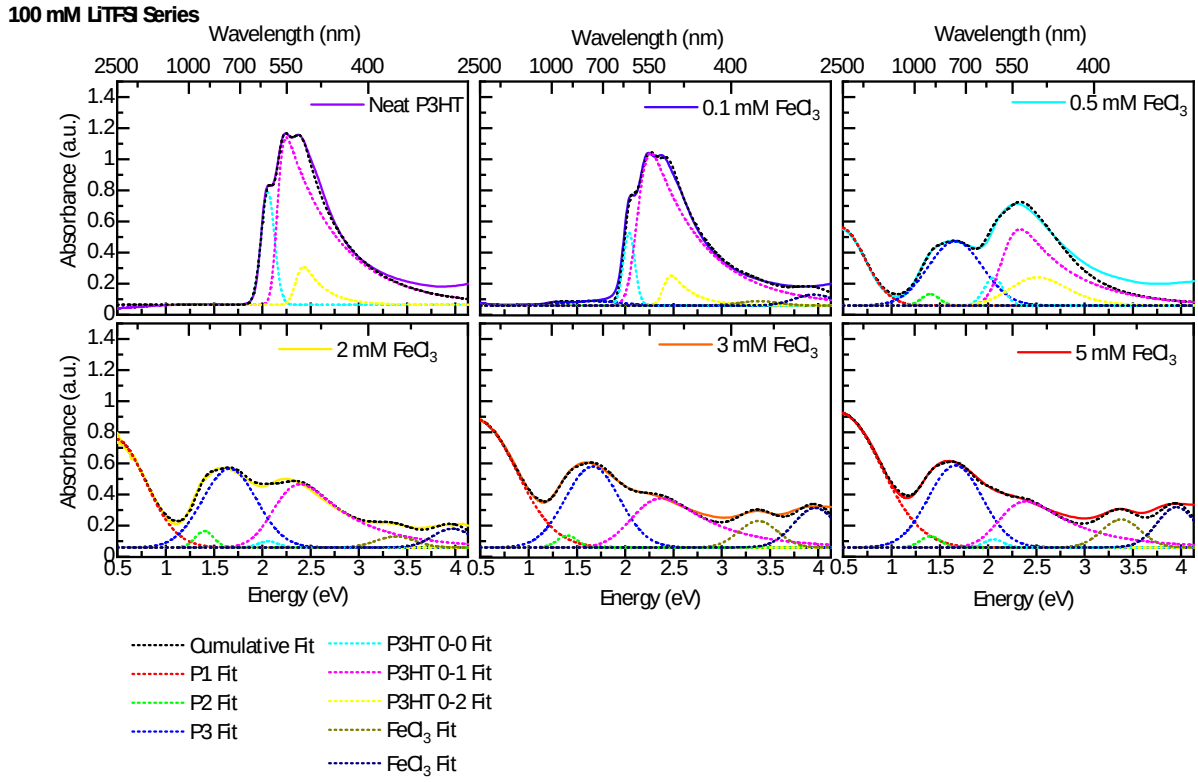

Figure C.9. Full UV-Vis-NIR spectral fits of P3HT films soaked in a solution with 100 mM LiTFSI and various $FeCl_3$ concentrations in n-butyl acetate.

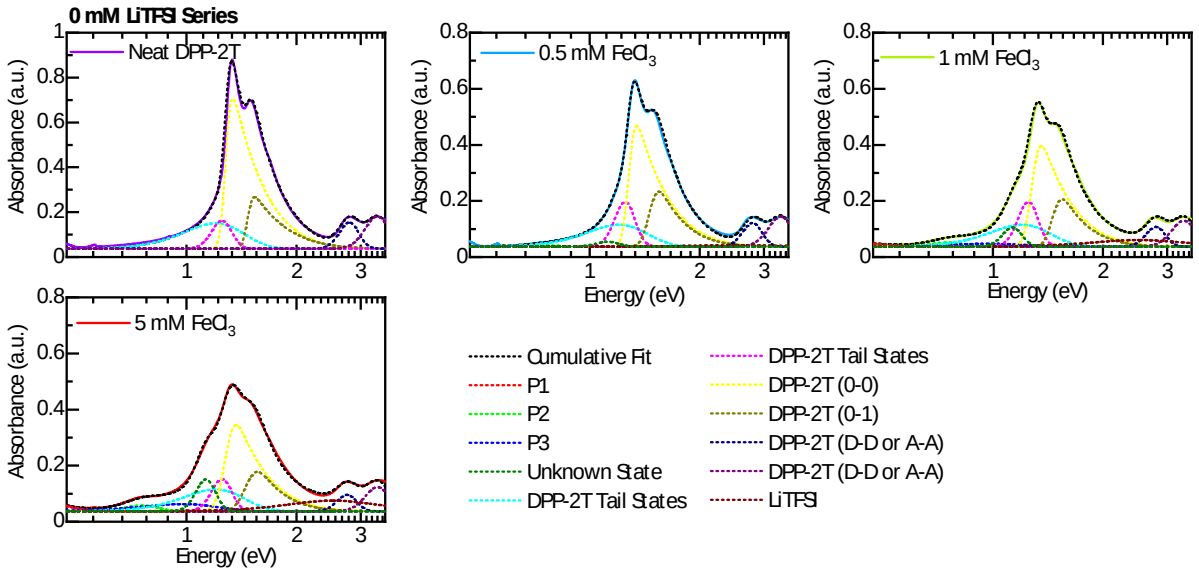

Figure C.10. Full UV-Vis-NIR spectral fits of PDPP-2T films soaked in a solution with various $FeCl_3$ concentrations in n-butyl acetate. The unknown state is discussed in section S4.

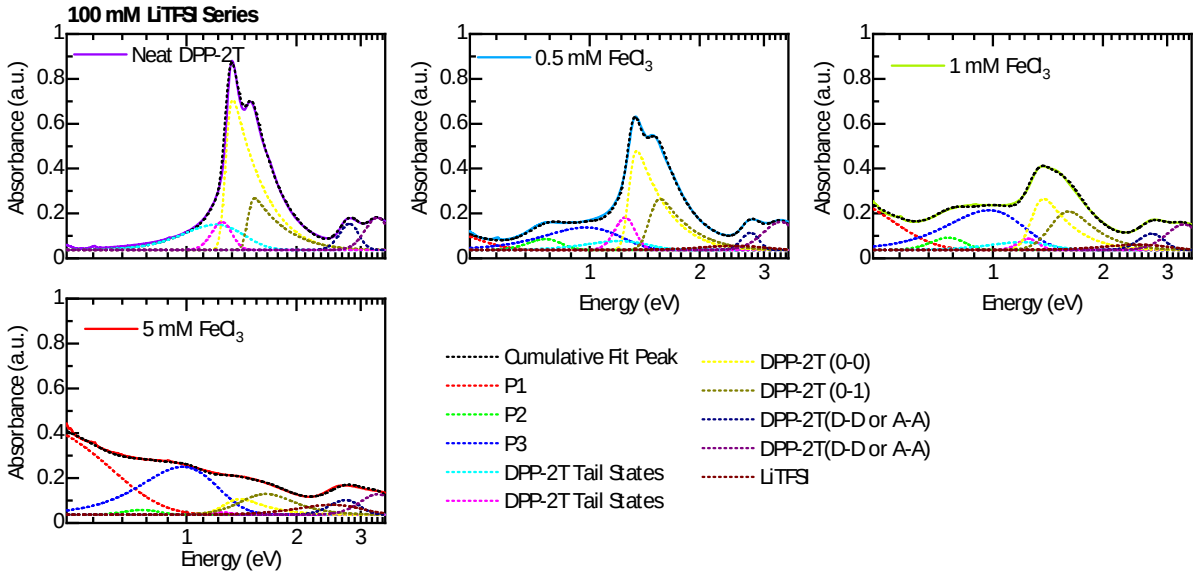

Figure C.11. Full UV-Vis-NIR spectral fits of PDPP-2T films soaked in a solution with 100 mM LiTFSI and various $FeCl_3$ concentrations in n-butyl acetate.

C.5 PDPP-2T $FeCl_3$ Absorption Discussion

There is a unique feature at 1.13 eV in the PDPP-2T films doped with only $FeCl_3$. Like the polaron peaks P1, P2, and P3, this feature grows in with increasing $FeCl_3$ concentration. Since it is spectroscopically different from P3 and doesn't appear to have free charges associated with it, it may corresponds to a new species. We cannot confirm what this transition corresponds to, it could be a charge transfer state or might be the result of a change in morphology, but it is clearly not associated with free holes.

C.6 Fractional Doping Level (Θ) and Isotherm Fitting

To simplify these spectral changes with respect to doping level we define Θ as the fraction of doped P3HT sites over the total available P3HT sites. Θ can be linearly approximated from optical absorbance by $\theta = \frac{A_P}{A_P + A_N}$, where A_N represents the neutral P3HT sites (sum of the 0-0, 0-1, and 0-2 peak integrals) and A_P represents the charged $P3HT^+$ sites (integral of P1). Although this approximation assumes that polaron and neutral absorbances have identical oscillation strength, Θ allows us to directly compare the extent of doping between multiple samples. The calculated Θ from the UV-Vis-NIR data is shown in Figure 4.2a and 4.2b. Each data point corresponds to an individual P3HT film, doped by soaking in a bath with either $FeCl_3$ or mixed $FeCl_3$/LiTFSI solutions. In films sequentially doped with 5 mM $FeCl_3$ concentration and no LiTFSI present, 63 $\pm$3 % of the polymer sites are doped ($\Theta = 0.63 \pm 0.03$). As LiTFSI concentration is increased to 100 mM at constant 5 mM $FeCl_3$ concentration, the percentage of doped sites increases to 75% ($\Theta = 0.75 \pm 0.04$). As $FeCl_3$ concentration is decreased from 5 mM, Θ remains larger in samples with LiTFSI present until a threshold is crossed at $\sim$ 0.5 mM $FeCl_3$. This lower threshold is encountered due to water contamination in LiTFSI. $FeCl_3$ undergoes hydrolysis in the presence of water and since LiTFSI has a high affinity for water, it is a likely source of contamination. This explains the quicker drop off in Θ as $FeCl_3$ concentration approaches zero for samples with large quantities of LiTFSI.

To determine the equilibrium coefficients K_I and K_{II}, we derive a generalized Anion Exchange Isotherm model (Equation C.1) in terms of known quantities. This model represents the fraction of doped sites over total sites (Θ) for a polymer system undergoing charge transfer

with a molecular dopant, followed by a subsequent exchange of anions with a monovalent ionic liquid. The derivation is located in the Supporting Information (Equations C.3-C.25).

$$\Theta = S\frac{K_I([D]-w[C^+A^-]) + \frac{K_I K_{II}([D]-w[C^+A^-])([C^+A^-]-w[C^+A^-])}{\Theta C_t^0 - K_I([D]-w[C^+A^-])(1-\Theta)C_t^0}}{1+K_I([D]-w[C^+A^-]) + \frac{K_I K_{II}([D]-w[C^+A^-])([C^+A^-]-w[C^+A^-])}{\Theta C_t^0 - K_I([D]-w[C^+A^-])(1-\Theta)C_t^0}} \tag{C.1}$$

Where, S is the saturated doping level (0 to 1), $[D]$ is the prepared dopant concentration ($[FeCl_3]$), $[C^+A^-]$ is the prepared electrolyte concentration ([LiTFSI]), w is the fraction of water contamination in the electrolyte, and C_t^0 is the concentration of total polymer sites extrapolated over the volume of the dopant solution. The concentration of P3HT sites is estimated assuming four monomers per site using the film volume (γ), film monomer density (ρ), the number of monomers per site (n), and dopant solution volume (V) with $C_t^0 = \frac{\gamma\rho}{nV}$ mM, assuming a film mass density of 1.1 mg^1cm^{-3}. Discussion on how estimated site size influences this isotherm fit is located in Supporting Information section S9. When there is no dopant present (ie: $[D]=0$) then $\Theta = \frac{0+0}{1+0+0} = 0$, and when there is no electrolyte present (ie: $[C^+A^-]=0$) Eq. 4.3 simplifies to the Langmuir Isotherm (Equation C.2), previously used to model sequential doping in SPs.[11]

$$\Theta = S\frac{K_I[D]}{1+K_I[D]} \tag{C.2}$$

The equilibrium constants can be used to calculate the standard state free energy change (ΔG°) for doping and subsequent anion exchange.[12] For the purpose of this manuscript we use it to determine the spontaneity of the doping and exchange processes. Discussion on the meaning of ΔG° is located in Supporting Information Section S7.

C.6.1 PDPP-2T Θ and Isotherm Fitting

Each PDPP-2T spectrum was fit with a series of Gaussians using the methods discussed above. For simplicity, the PDPP-2T P1 peak center was best fit at 0.33 eV and kept constant between samples. The peak center position has minimal effect on the analyzed fit peak area. However further study is needed to explore the evolution of P1 in the infrared as a function of doping level.[13] The cumulative fits are shown as the dashed line in Figures 3a and 3b. Fits to each individual spectrum are located in Figures C.10 and C.11. We calculate Θ from the absorption data (Figure 3d). As expected, with no LiTFSI present the higher energetic barrier for charge

transfer limits the doping efficiency, reaching only a 4.3% doping level (θ=0.043) with a 5 mM $FeCl_3$ solution. However, in the presence of 100 mM LiTFSI, PDPP-2T reached a 70% doping level (θ=0.70) at 5mM $FeCl_3$. Exposing PDPP-2T to 100 mM LiTFSI without $FeCl_3$ has minimal effect on the PDPP-2T absorbance. (Figure C.19)

We fit Θ for the PDPP-2T samples with the Anion Exchange Isotherm model (Figures 3d and 3e). The concentration of the PDPP-2T D-A monomers (C_t^0) is estimated at 0.00878mM. The extracted K_I and K_{II} are 9.41 ± 1.62 and 2.92 ± 0.61 M^{-1} corresponding to ΔG_I° and ΔG_{II}° of -0.058 ± 0.004 and -0.028 ± 0.005 eV, respectively. Unlike P3HT, PDPP-2T approaches a saturated doping level of $\sim$100%. We hypothesize that the stiff, ribbon like configuration of the PDPP-2T polymer likely provides easier access to all the polymer sites by reducing the excluded volume which is caused by high-torsion dihedral angles along the polymer backbone.[3, 8] In other words, we believe that reducing structural disorder enables higher doping levels. Future studies are needed to address the influence of morphology on AED. Figure 3f shows the calculated % $TFSI^-$ anions in the PDPP-2T film after AED. Unlike the P3HT sample, >90% of doped sites have exchanged $FeCl_3^-$ with $TFSI^-$. This calculation is confirmed by the absence of $FeCl_3$ absorbance in the AED doped PDPP-2T films and x-ray photo-electron spectroscopy (Figures C.20 and C.23).

C.6.2 Anion Exchange Doping Isotherm Derivation

$$FeCl_3 + P3HT \overset{K_1}{\rightleftharpoons} P3HT^+FeCl_3^- \tag{C.3}$$

$$P3HT^+FeCl_3^- + Li^+TFSI^- \overset{K_2}{\rightleftharpoons} P3HT^+TFSI^- + Li^+FeCl_3^- \tag{C.4}$$

Equation C.3 shows the charge transfer reaction between P3HT and $FeCl_3$. Equation C.4 shows the anion exchange mechanism replacing the $FeCl_3^-$ counter ion with $TFSI^-$.

This can be generalized to any polymer/dopant/electrolyte system:

$$D + P \overset{K_I}{\rightleftharpoons} P^+D^- \tag{C.5}$$

$$P^+D^- + C^+A^- \overset{K_{II}}{\rightleftharpoons} P^+A^- + C^+D^- \tag{C.6}$$

Where P represents unoccupied polymer sites, D is the molecular dopant, and C and A represent the electrolyte cation and anion. The equilibrium constants generated from equations C.5 and C.6 are:

$$K_I = \frac{[P^+D^-]}{[P][D]} \tag{C.7}$$

$$K_{II} = \frac{[P^+A^-][C^+D^-]}{[P^+D^-][C^+A^-]} \tag{C.8}$$

To model the equilibrium composition, we assume that all available polymer sites are energetically equivalent and the energy of adsorption is equal for all sites. Additionally, species adsorbed to adjacent sites do not interact with each other and polymer sites can only be occupied by a single adsorbate, whether it be D^- or A^-. We now define Θ as the fraction of occupied (doped polymer sites) over all sites. Θ is related to species concentrations by equation C.9.

$$\Theta = S\frac{\text{Doped Sites}}{\text{Total Sites}} = S\frac{[P^+D^-]+[P^+A^-]}{[P]+[P^+D^-]+[P^+A^-]} \tag{C.9}$$

Θ can be experimentally measured using UV-Vis-NIR absorption spectroscopy by

$$\Theta = \frac{A_P}{A_P + A_N} \tag{C.10}$$

where A_P and A_N are integral of the P1 polaron and the sum of the integrals of the neutral polymer absorption peaks, respectively. Now we can rewrite Eq. C.9 in terms of the equilibrium constants. First rearrange Eq. C.8 to:

$$[P^+A^-] = \frac{K_{II}[P^+D^-][C^+A^-]}{[C^+D^-]} \tag{C.11}$$

Now plug Eq. C.11 into C.9 to get:

$$\Theta = \frac{[P^+D^-] + \frac{K_{II}[P^+D^-][C^+A^-]}{[C^+D^-]}}{[P]+[P^+D^-] + \frac{K_{II}[P^+D^-][C^+A^-]}{[C^+D^-]}} \tag{C.12}$$

Next, rearrange Eq. C.7 to :

$$[P^+D^-] = K_I[P][D] \tag{C.13}$$

Now plug Eq. C.13 into C.12 and simplify to get:

$$\Theta = \frac{K_I[D] + \frac{K_IK_{II}[D][C^+A^-]}{[C^+D^-]}}{1 + K_I[D] + \frac{K_IK_{II}[D][C^+A^-]}{[C^+D^-]}} \tag{C.14}$$

Eq. C.14 needs to be written in terms of known concentrations. The concentrations of dopant $[D]$ and electrolyte $[C^+A^-]$ are know from the processing conditions. The volume of the prepared dopant electrolyte solution is in excess, therefore the concentrations are assumed to be constant. The concentration of the exchanged dopant anion $[C^+D^-]$ is unknown. We now define the concentration of doped sites C_d as

$$C_d = \Theta C_t^0 = [P^+D^-] + [P^+A^-] \tag{C.15}$$

where C_t^0 is the concentration of total polymer sites (millimoles of monomer in film per volume of processing solution), known from processing conditions. The number of monomers in the film is estimated from film density and thickness. Now plug Eq. C.13 into C.15 and rearrange for $[P^+A^-]$.

$$[P^+A^-] = \Theta C_t^0 - K_I[P][D] \tag{C.16}$$

Now the concentration of available polymer sites $[P]$ is related to Θ by:

$$[P] = (1-\Theta)C_t^0 \tag{C.17}$$

and

$$[P^+A^-] = [C^+D^-] \tag{C.18}$$

Plug Eq. C.17 into C.16 and rearrange for to $[C^+D^-]$.

$$[C^+D^-] = \Theta C_t^0 - K_I[D](1-\Theta)C_t^0 \tag{C.19}$$

Now plug Eq. C.19 into C.14.

$$\Theta = S\frac{K_I[D] + \frac{K_IK_{II}[D][C^+A^-]}{\Theta C_t^0 - K_I[D](1-\Theta)C_t^0}}{1 + K_I[D] + \frac{K_IK_{II}[D][C^+A^-]}{\Theta C_t^0 - K_I[D](1-\Theta)C_t^0}} \tag{C.20}$$

$FeCl_3$, like many other molecular dopants, is highly susceptible water contamination. Since the electrolyte is likely the source of water contamination, we add an additional term to correct the prepared concentrations to the actual concentration. We assume all water contamination reacts with the dopant and correct the dopant concentration to $[D]^* = ([D] - w * [C^+A^-])$ and in turn we correct the electrolyte concentration to $[C^+A^-]^* = ([C^+A^-] - w * [C^+A^-])$, where w

is the water contamination in the electrolyte in mol%. By plugging those two expressions into equation C.20 we get:

$$\Theta = S\frac{K_I([D]-w[C^+A^-]) + \frac{K_I K_{II}([D]-w[C^+A^-])([C^+A^-]-w[C^+A^-])}{\Theta C_t^0 - K_I([D]-w[C^+A^-])(1-\Theta)C_t^0}}{1+K_I([D]-w[C^+A^-]) + \frac{K_I K_{II}([D]-w[C^+A^-])([C^+A^-]-w[C^+A^-])}{\Theta C_t^0 - K_I([D]-w[C^+A^-])(1-\Theta)C_t^0}} \tag{C.21}$$

When there is no electrolyte present (ie:$[C^+A^-]=0$) Eq. C.21 simplifies to the Langmuir Isotherm[]:

$$\Theta = \frac{K_I[D]}{1+K_I[D]} \tag{C.22}$$

Now rearrange the expression for Θ.

$$\Theta = S\frac{\sqrt{-[C^+A^-]K_1K_2\,(D-[C^+A^-]w)\,(w-1)\,M} + 2D^2C_t^0{K_1}^2 + 2DC_t^0K_1 + 2[C^+A^-]^2C_t^0{K_1}^2w^2 + N}{2C_t^0D^2{K_1}^2 - 4C_t^0D[C^+A^-]{K_1}^2w + 4C_t^0DK_1 + 2C_t^0[C^+A^-]^2{K_1}^2w^2 - 4C_t^0[C^+A^-]K_1w + 2C_t^0} \tag{C.23}$$

with

$$\begin{aligned} M = (&4C_t^0 + 4[D]C_t^0K_1 - [C^+A^-]^2K_1K_2w + [C^+A^-]^2K_1K_2w^2 + \ldots \\ &\ldots + [D][C^+A^-]K_1K_2 - 4[C^+A^-]C_t^0K_1w - [D][C^+A^-]K_1K_2w) \end{aligned} \tag{C.24}$$

and

$$\begin{aligned} N = ([C^+A^-]^2K_1K_2w - [C^+A^-]^2K_1K_2w^2 - [D][C^+A^-]K_1K_2 - 2[C^+A^-]C_t^0K_1w + \ldots \\ \ldots + [D][C^+A^-]K_1K_2w - 4[D][C^+A^-]C_t^0{K_1}^2w) \end{aligned} \tag{C.25}$$

Source code for fitting can be found at https://github.com/kul-group/Anion-Exchange-Doping-Isotherms/.

C.6.3 % TFSI Calculation

Using the extracted equilibrium constants K_I and K_{II}, the concentration of $P3HT^+$ sites with $FeCl_3^-$ counter anions ($[P^+D^-]$) can be calculated using Equations C.7 and C.17. Subsequently, the concentration of $P3HT^+$ sites with an exchanged $TFSI^-$ anion ($[P^+A^-]$) can be calculated using Equation C.8. The percentage of $P3HT^+$ sites with exchanged anions (ie: the percent of doped sites with $TFSI^-$ anion) is shown in Equation C.26.

$$[P^+A^-](\%) = \frac{[P^+A^-]}{[P^+A^-]+[P^+D^-]} * 100 \tag{C.26}$$

C.7 Discussion of ΔG°

The equilibrium constants can be used to calculate the standard state free energy change.[12] ΔG_I° is a measure of the charge transfer between the solvent swollen polymer with dissolved dopants and the dopant moving from solution to the solid state. ΔG_{II}° is a measure of the exchange of one ion from solution with a different ion in solid state. Both processes are highly influenced by solvent miscibility with the electrolyte, the dopant, the dopant counter ion, and the polymer. We've previously demonstrated that the presence of dopants changes the degree to which a P3HT film swells in a given solvent, with doped films swelling more/less than undoped films in polar/nonpolar solvents.[14] Additionally, miscibility differences between the dopant counter ion and the electrolyte cation also influences this equilibrium. The anion exchange isotherm simplifies all of these processes to a simple equilibrium expression and allows us to determine the spontaneity of the doping and subsequent exchange processes in a given system at a particular state point.

C.8 P3HT Anion Exchange (Assuming one monomer site)

Table C.1. Θ fit statistics.

Parameter	Value
Number of Points	35
Degrees of Freedom	31
Reduced Chi-sqr	0.00122
Residual Sum of Squares	0.03771
R-Square (COD)	0.98034
Root-MSE (SD)	0.0.03488

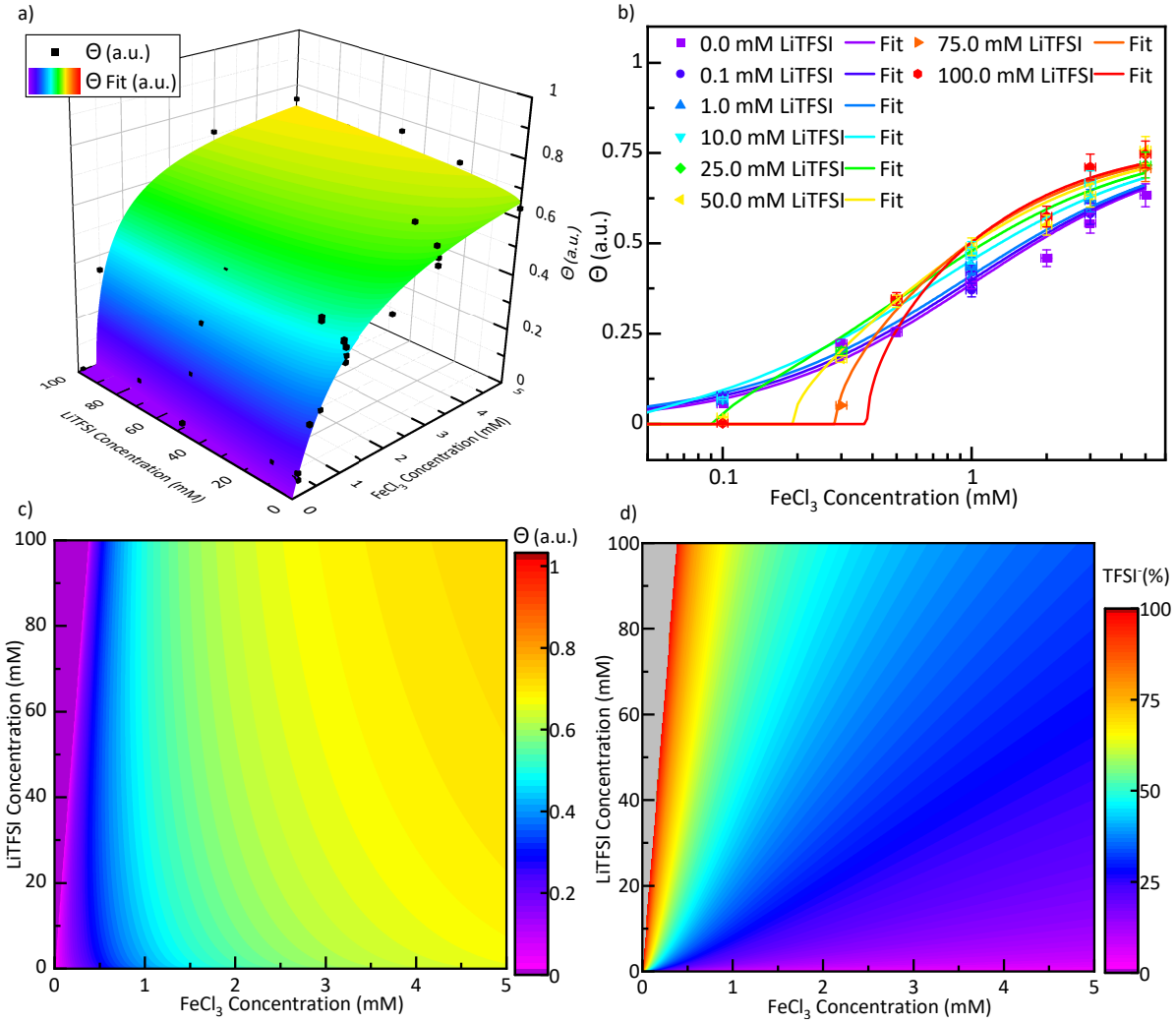

Figure C.12. a) 3D and b) 2D scatter plots of Θ extracted from UV-vis-NIR and corresponding anion exchange isotherm fit, c) shows the Θ fit contour with respect to the prepared $FeCl_3$ and LiTFSI concentrations, and d) depicts the percentage of doped P3HT sites with $TFSI^-$ anions. The gray region in d) corresponds to the range in which no P3HT sites are doped.

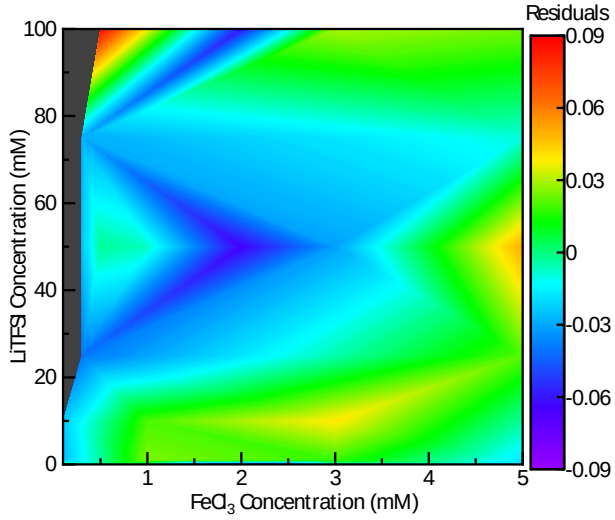

Figure C.13. Contour plot of residuals from Anion Exchange Isotherm Fit to P3HT θ extracted from UV-vis.

C.9 Anion Exchange Isotherm Site Size Comparison

K_{II} and estimated polymer site concentration (C_t^0) are mutually dependent parameters in our anion exchange isotherm. This makes the fit to K_{II} dependent on the estimated C_t^0. We designed our experiments so that the dopants/electrolytes are more abundant than the polymer sites; since all of our films are less than 200nm thick and they were doped by immersing in a much larger volume of dopant/electrolyte solutions (8 mL), changes in C_t^0 should have a minor influence on the extracted equilibrium constants. Assuming the site size is one or four P3HT monomers corresponds to a C_t^0 of 0.096 and 0.024 mM respectively. Increasing the size of the P3HT site from one to four monomers provides the same fit quality with our isotherm model, shown in figures C.14 and C.15. Using the larger site size our isotherm fits to a reduced K_{II} of 0.2 ± 0.06 M^{-1} and a ΔG_{II}° or 0.04 ± 0.007 eV (Table C.2) compared to one monomer site size.

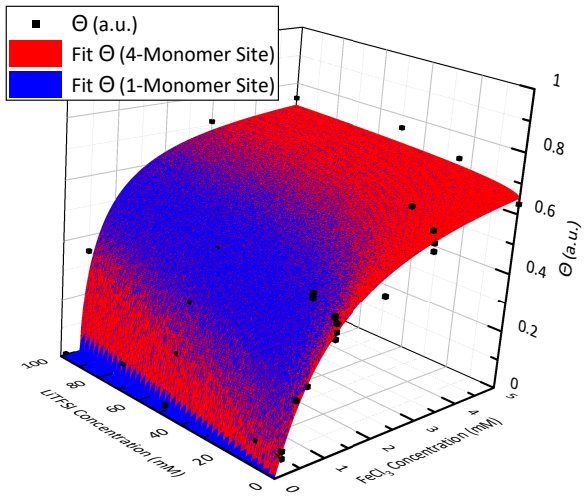

Figure C.14. Comparison of the Θ fit using one P3HT monomer site size and a four P3HT monomer site size.

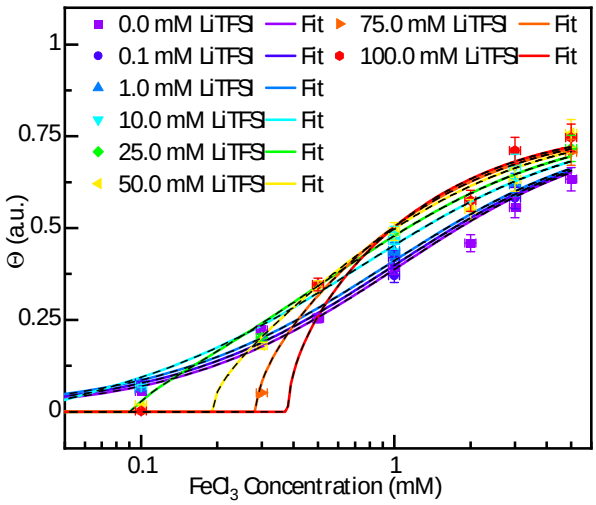

Figure C.15. Comparison of the Θ fit using one P3HT monomer site size (colored lines) and a four P3HT monomer site size (black dashed lines).

Table C.2. Θ fit parameters for P3HT film, defining site size as one P3HT monomer or four P3HT monomers.

Parameter	P3HT (one monomer site)	P3HT (four monomer site)
K_I (M^{-1})	971 ± 85	971 ± 85
ΔG_I° (eV)	-0.18 ± 0.01	-0.18 ± 0.01
K_{II} (M^{-1})	0.79 ± 0.16	0.2 ± 0.06
ΔG_{II}° (eV)	0.006 ± 0.007	0.04 ±0.01
C_t^0 (mM)	0.096	0.024
w (mole fraction water in LiTFSI)	0.0038	0.0038
Saturation (S)	0.79	0.79

C.10 Discussion of Θ: Is $\Theta \propto P1$ or $\propto \sum(P1, P2, P3)$?

In the manuscript, we estimate the fractional population of hole states using $\Theta = \frac{A_{P1}}{A_{P1}+A_N}$, where A_{P1} and A_N are the integrals of the P1 polaron peak and the sum of the neutral peaks. The P1 absorbance corresponds to energy transitions into the hole state formed within the polymer HOMO, while the P2 and P3 absorbances correspond to energy transitions of e^- into polymer LUMO states. We believe that using P2 and P3 absorption integrals in addition to P1 would overestimate the population of holes in the HOMO. This would make our analysis show higher hole populations than we believe to be physical. Since we only want to count the population of

holes on the polymer, we focus our analysis on P1.

For comparison, we've calculated $\Theta = \frac{\Sigma(A_{P1},A_{P2},A_{P3})}{\Sigma(A_{P1},A_{P2},A_{P3},A_N)}$ and fit with our isotherm model, (Figures C.16 and C.17). The fit parameters are presented in Table C.3. If we assume hole population is also related to P2 and P3 than extracted Θ from the UV-Vis-NIR increases by 5 to 50 %, with larger increases observed at lower doping concentrations. The extracted change in free energy from initial doping decreases by 0.02 eV to -0.2 eV while the change in free energy from exchanging anions remains constant at 0.04 eV. Since, including P2 and P3 in this estimation increases the max Θ, the saturated doping level increases up to 0.81.

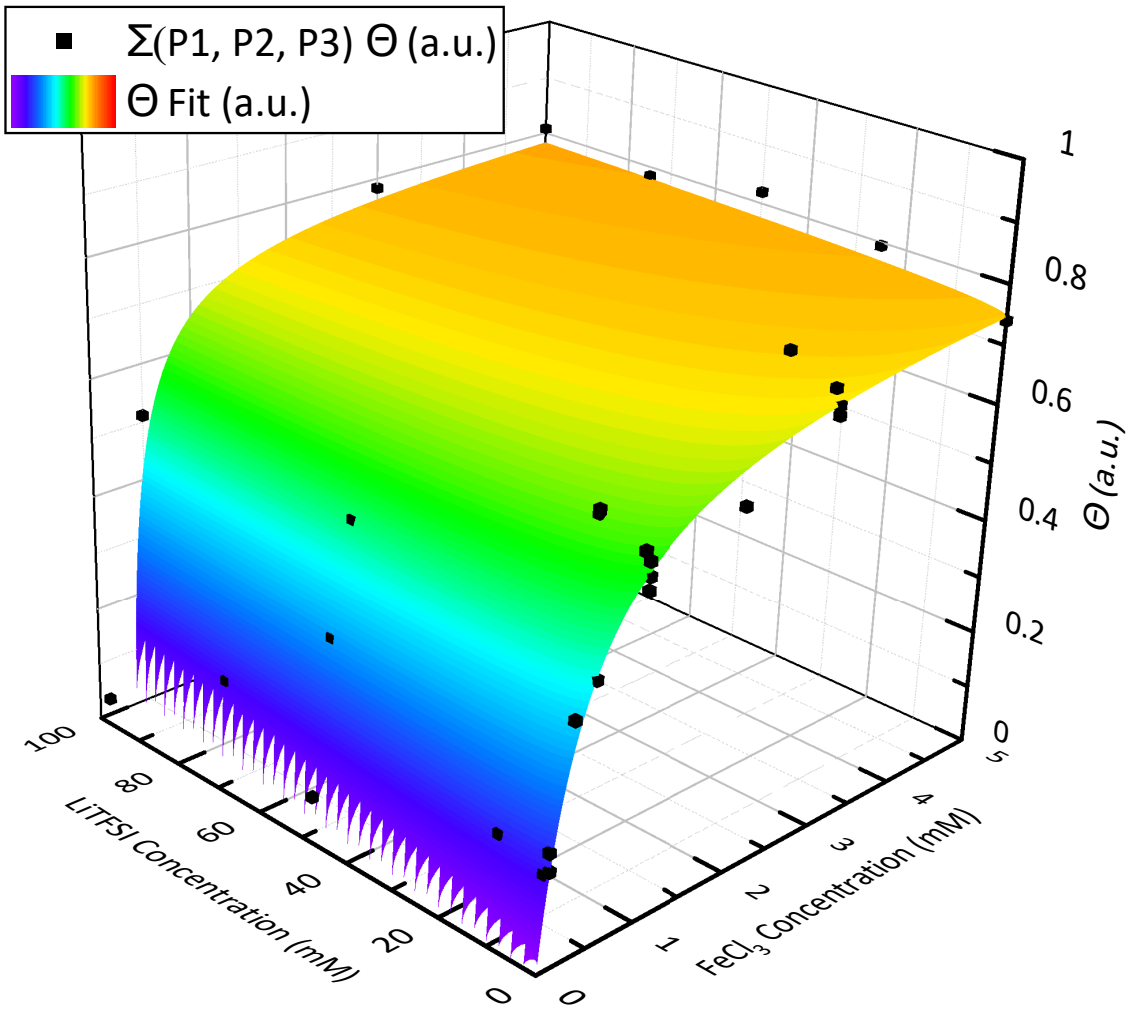

Figure C.16. 3D scatter plot of Θ calculated from UV-Vis-NIR of doped P3HT films with respect to prepared $FeCl_3$ and LiTFSI concentrations, assuming 1) the population of holes is related to the sum of the P1, P2, and P3 integrals and 2) cation site size corresponds to four P3HT monomers.

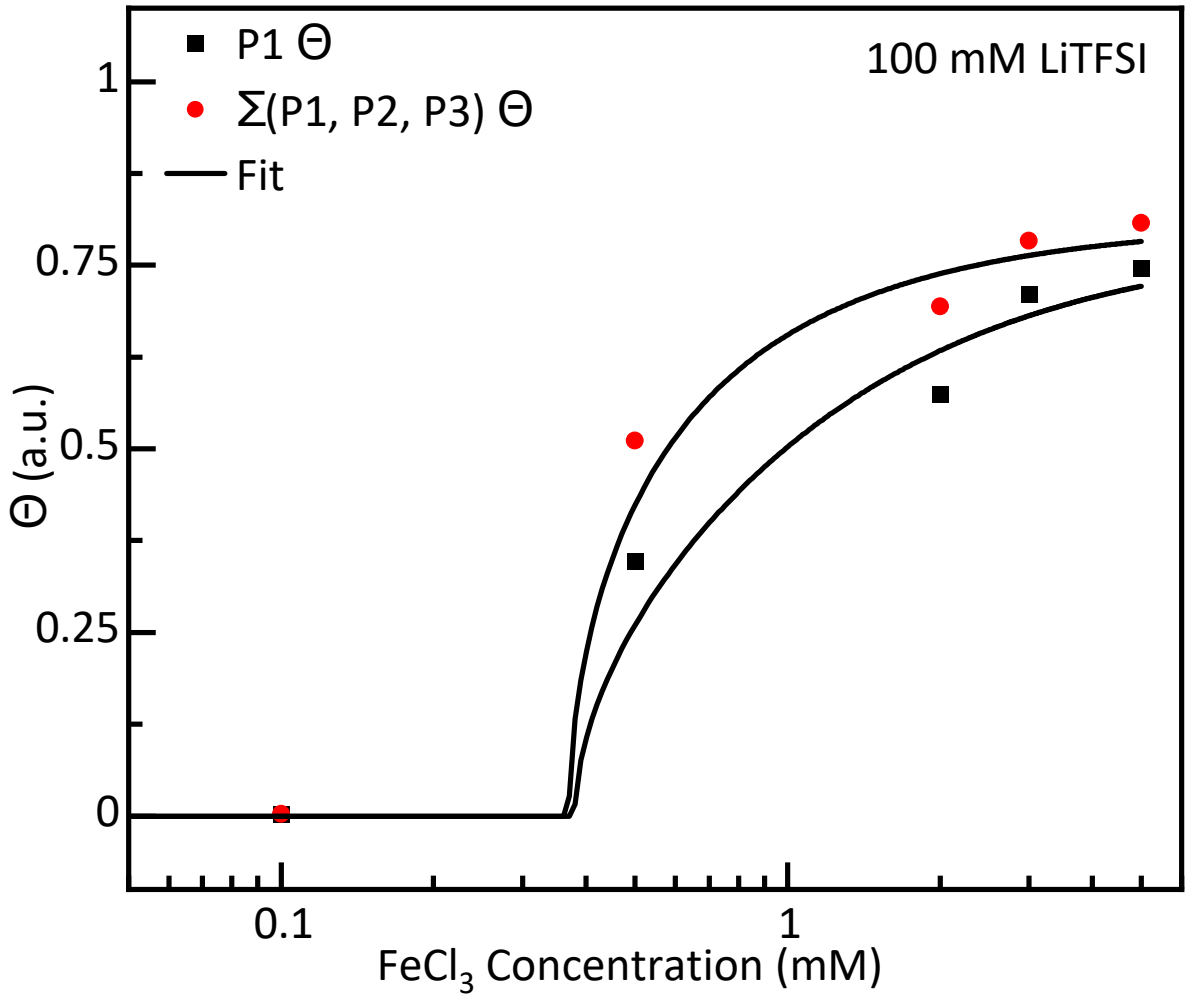

Figure C.17. 2D scatter plot of Θ calculated from UV-Vis-NIR of P3HT films with respect to prepared $FeCl_3$ (at 100 mM LiTFSI), assuming 1) the population of holes is related to the sum of the P1, P2, and P3 integrals and 2) cation site size corresponds to four P3HT monomers.

Table C.3. Comparison of Θ fit parameters for P3HT films, using either P1 or the sum of P1, P2, and P3 to define Θ.

Parameter	P3HT ($\Theta \propto P1$)	P3HT ($\Theta \propto \sum(P1, P2, P3)$)
K_I (M^{-1})	971 ± 85	2365 ± 200
ΔG_I° (eV)	-0.18 $\pm$ 0.01	-0.20 $\pm$ 0.01
K_{II} (M^{-1})	0.2 ± 0.06	0.23 ± 0.07
ΔG_{II}° (eV)	0.04 $\pm$0.007	0.04 ± 0.01
C_t^0 (mM)	0.024	0.024
w (mole fraction water in LiTFSI)	0.0038	0.0037
Saturation (S)	0.79	0.81

C.11 Anion Exchange Simulations

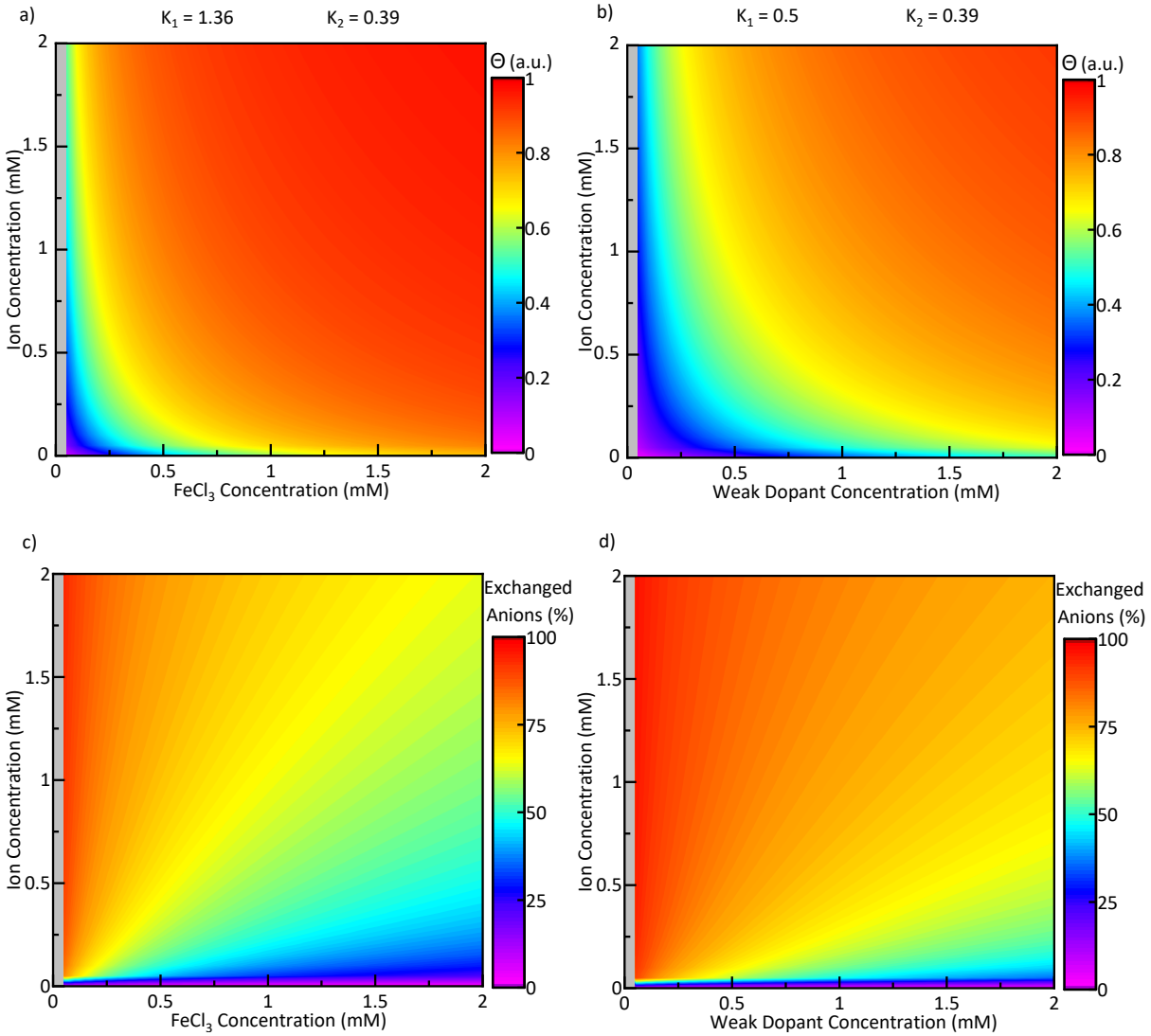

Figure C.18. a) Simulated Θ using the Anion Exchange Isotherm and c) corresponding percentage of doped polymer sites with exchanged anions for a P3HT film doped with a stronger dopant than $FeCl_3$ exchanged with an anion with a 40x larger K_2. b) Simulated Θ and d) corresponding percentage of doped polymer sites with exchanged anions for a polymer doped with a weaker dopant (K_1=0.5 mM^{-1}) and exchanged with an anion with a 40x larger K_2. Note: K_I and K_{II} are given in units of mM^{-1}

Figure C.18a shows the simulated fraction of doped sites over total sites (Θ) in a P3HT film sequentially doped with an even stronger molecular dopant (ie: K_I = 1360 M^{-1}) and an electrolyte with a ∼40 times greater anion exchange equilibrium constant than LiTFSI (ie: K_{II} = 390 M^{-1}), assuming the system has no water contamination and the same number of P3HT sites

($C_t^0 = 0.096$ mM) are available to dope. This demonstrates ~100% doping efficiency can be obtained at much lower dopant and ionic liquid concentrations by tuning the anion exchange rate ($\Theta = 0.99$ at 2 mM $FeCl_3$ and 2 mM ion concentration). Figure C.18c shows the corresponding percent of exchanged anions and demonstrates 63% of counter anions can be exchanged at 2 mM $FeCl_3$ and 2 mM ion concentrations.

Figure C.18b demonstrates the simulated Θ in a SP system sequentially doped with a weaker molecular dopant (K_I = 500 M^{-1}, ΔG = -0.16 eV) and the same stronger anion exchange process. This system is analogous to reducing the chemical potential for charge transfer between the polymer and dopant. Even with a weak polymer-dopant system, the doping efficiency approaches 100% at 2 mM dopant 2 mM ion concentrations ($\Theta = 0.98$). The corresponding percent of exchanged anions is shown in Figure C.18d demonstrates even greater anion exchange (75% at 2 mM dopant and 2 mM ion concentrations) is obtainable from a system with a weak molecular dopant and strong anion exchange.

C.12 Extra UV-Vis-NIR Tests

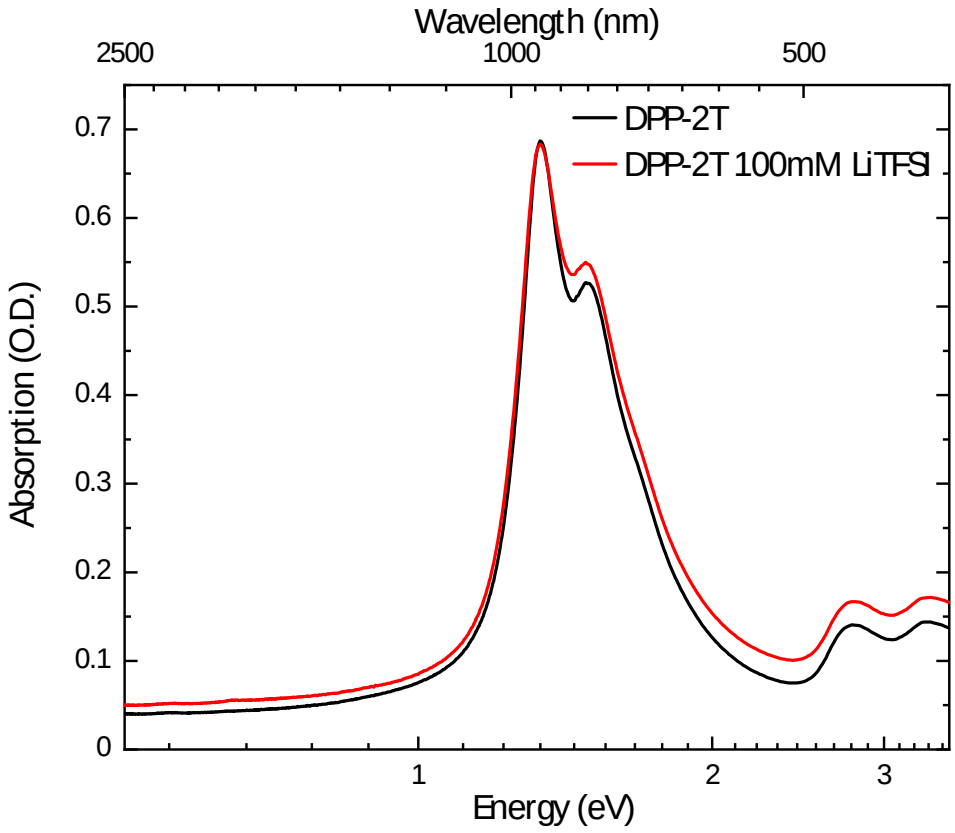

Figure C.19. UV-Vis-NIR spectra of PDPP-2T film, before and after soaking in 100 mM LiTFSI in nBA.

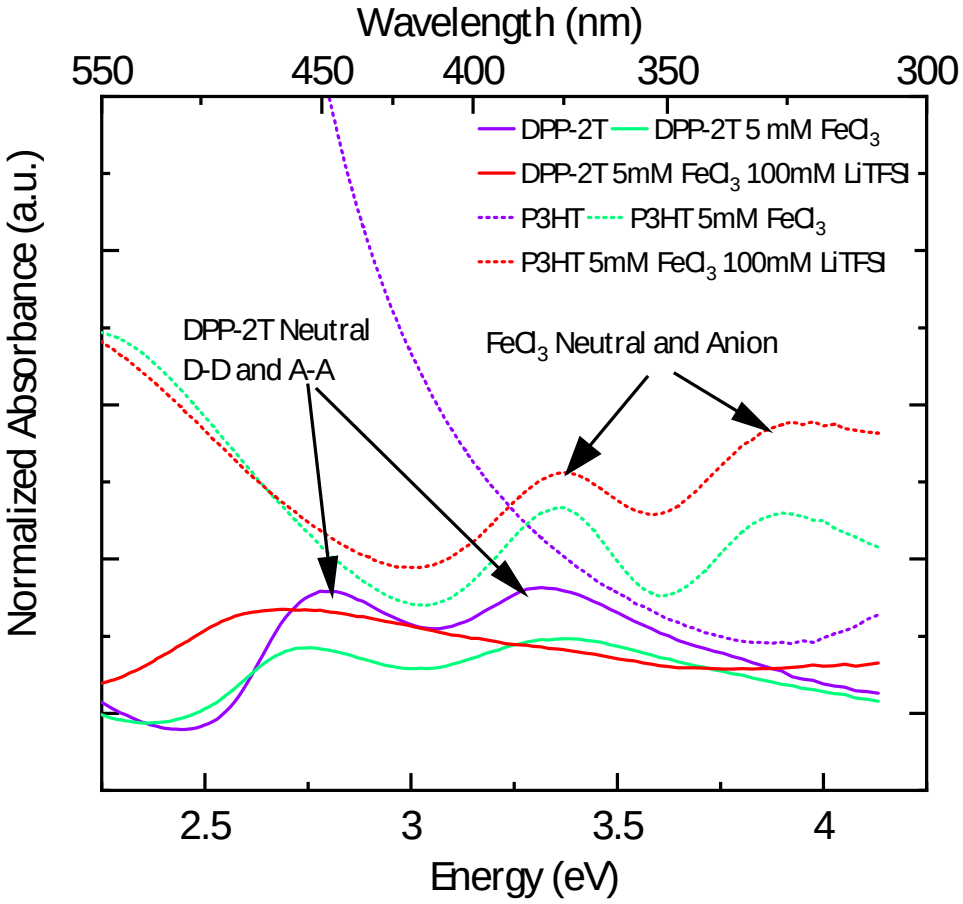

Figure C.20. High energy UV-Vis zoomed into $FeCl_3$ spectral peaks in doped P3HT films, and the absence of $FeCl_3$ peaks in doped PDPP-2T film.

C.13 Sheet Resistance IV Curves and Discussion of Conductivity Enhancements

Gosh et al. demonstrated increased hole delocalization in P3HT by increasing the distance between the hole and the dopant counter ion.[13] Although the spectral shifts associated with increased hole delocalization cannot be observed in our UV-Vis-NIR data due to limited spectral range of our detector, we suggest that the distance between the positive P3HT polaron (hole) and the anion may be increased by exchanging the $FeCl_3^-$ counter ion for the larger $TFSI^-$ anion, thereby increasing the population of unbound holes and in turn the macroscopic conductivity. The work of Aubry et al. describes the relationship between dopant anion size, location, and position of the polaron peak.[15] Future research is needed to address the effects of exchanged anion size on hole delocalization.

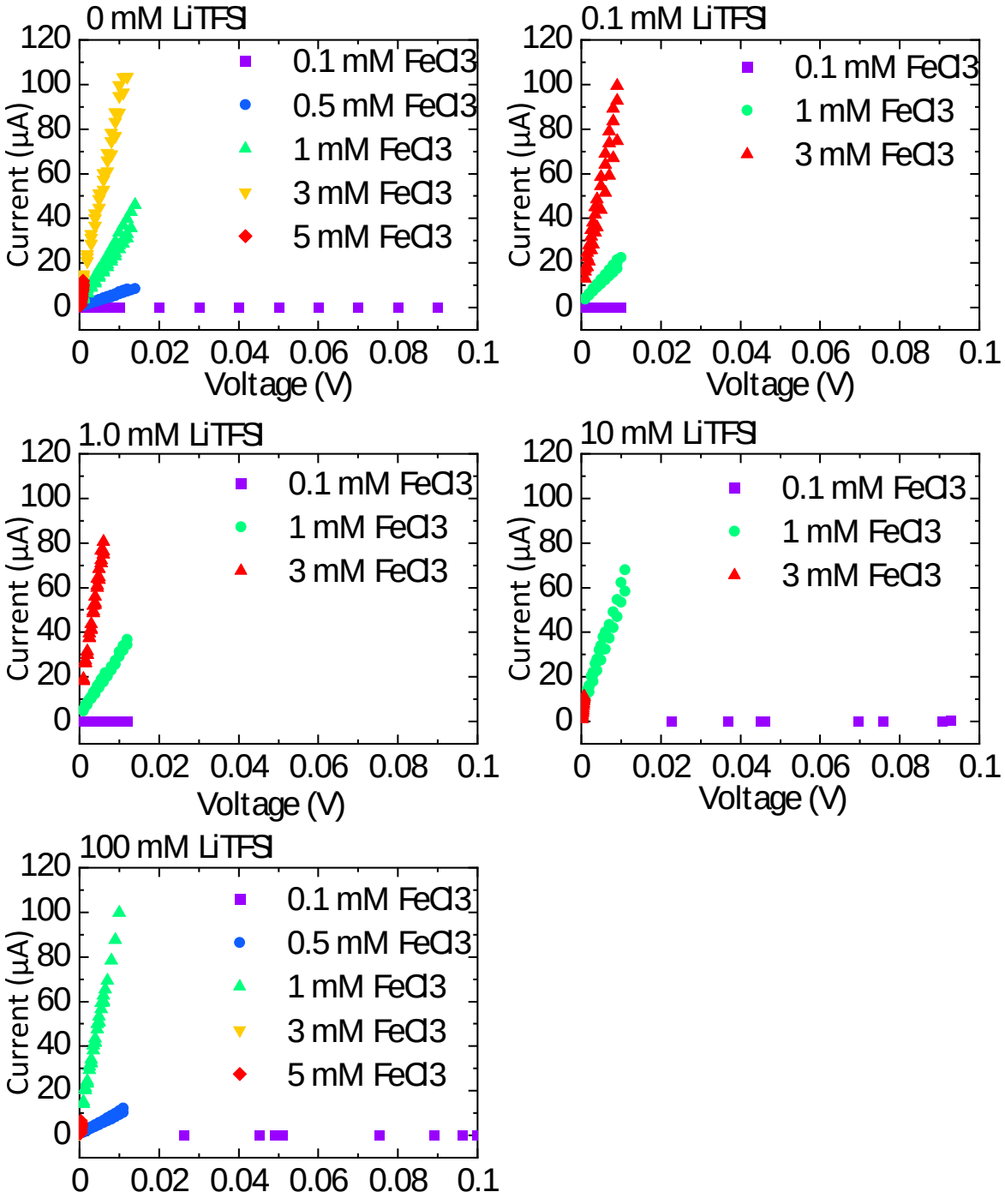

Figure C.21. IV curves from P3HT films doped with various $FeCl_3$ and LiTFSI concentrations

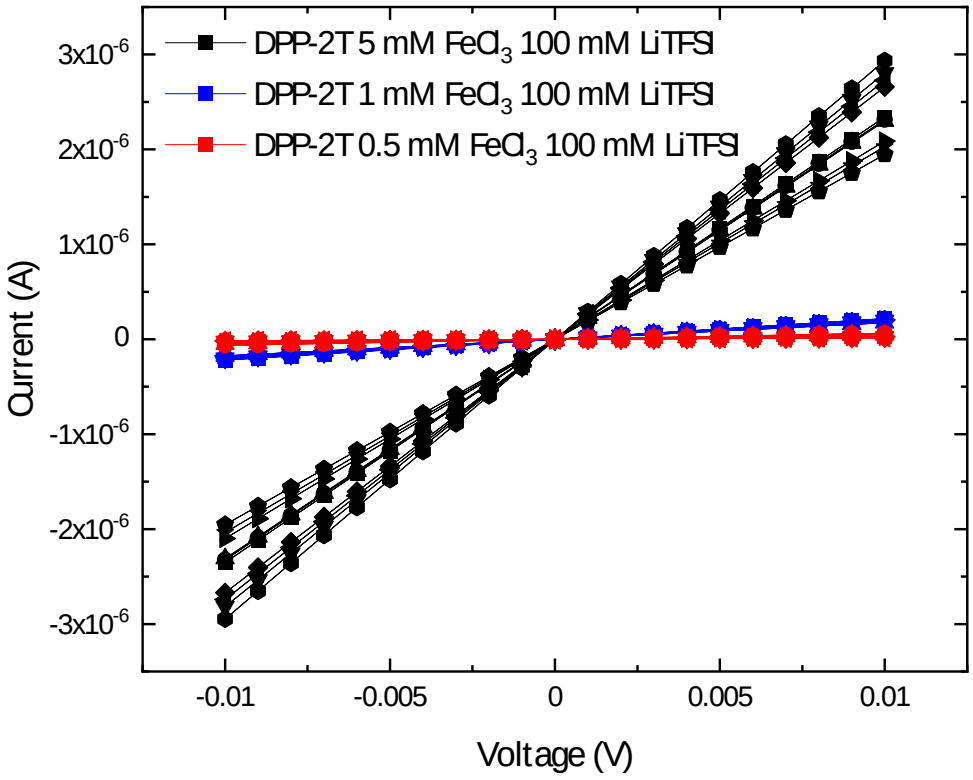

Figure C.22. IV curves from PDPP-2T films doped with 0.5, 1, and 5 mM $FeCl_3$ and 100 mM LiTFSI concentrations

C.14 Discussion of Carrier Density

Carrier density is directly proportional to the fraction of total polymer sites that possess a hole (Θ). To calculate the carrier density from Θ, we first estimate the minimum site size, which we define as the minimum number of monomer units that can hold a hole state. Two recent articles address this question directly by investigating the change in optical absorbance for doped oligothiophenes with increasing chain length. Density Functional Theory (DFT) simulations always predict a non-integer charge transfer state, which is not consistent with integer charge transfer observed in P3HT.[16] Measurement of co-deposited films show that integer charge transfer develops for chains with at least 10 thiophenes (10T), but for shorter oligomers only non-integer charge transfer states are detected.[17] We believe, however, that the hole volume along a polymer backbone is $<$ 10T. These measurements imply that a 10T section of a P3HT polymer is needed to host a hole state. Using a P3HT density of 1.1 g cm^{-3} and a site size of 10T, we estimate a maximum cite density of 3.3x10^{20}. Helpfully, Kang et al. measured a 3.3x10^{20} hole density in F4TCNQ doped PBTTT.[18] Their UV-vis spectrum clearly shows strong absorbance for neutral PBTTT, therefore less than $\sim$50% of the sites are doped. Since P3HT and PBTTT are electronically and chemically very similar, it is reasonable to consider the site density to be similar, thus the total site density of P3HT must be higher than 3.3x10^{20}.

For the PDPP-2T polymer, we assume that each monomer T-DPP-T is a single site. This assumption is justified by recent first principle simulations of alternating co-polymers.[19] Using a film density of 1.1 g/cm^3 we estimate a site density of 8.2x10^{20} for PDPP-2T. A 10% uncertainty in film density translates to a 10% uncertainty in cite density.

An assumption that a four thiophene (4T) section of P3HT is the minimum site size, yields an estimated 8.5x10^{20} holes/cm^3, nearly identical to that of PDPP-2T. For the remainder of this paper we assume a total site density of 8.5x10^{20} for P3HT and recognize that more accurate estimates of site density will improve our models predictive power.

The variable range hopping model (Equation C.27) was fit to the P3HT mobility data.[20, 21, 22]

$$\mu = \frac{\sigma_0}{e}\left(\frac{(T_0/T)^4 \, sin\,(\pi T/T_0)}{(2\alpha)^3 B_c}\right)^{T_0/T} p^{T_0/T-1} \tag{C.27}$$

The estimated PDPP-2T mobility increased from 0.009 to 0.117 $cm^2V^{-1}s^{-1}$ at 0.5 mM and 5 mM $FeCl_3$, respectively. These reported mobilities for PDPP-2T are lower than expected, since our conductivity measurements were made in the plane of the film, this may be explained by a predominantly face-on molecular packing.[23, 24] Additionally, our PDPP-2T sample has a relatively low molecular weight (M_w = 21.2 kDa, PDI = 4.5) and we expect higher mobilities can be obtained by increasing the polymer chain length.[25]

C.15 X-ray Photoelectron Spectroscopy

We performed x-ray photo-electron spectroscopy (XPS) on the PDPP-2T film sequentially doped with 5 mM $FeCl_3$ and 100 mM LiTFSI (Supporting Information Figure C.23) in an attempt to quantify Fe to F ratio in the film. The F 1s peak is clearly visible at 688.4 eV with FWHM of 1.78 eV while the expected Fe $2p_{3/2}$ peak at 711.3 eV is barely visible. Due to the low signal to noise ratio of iron, we are unable to determine the concentration ratio without considerable uncertainty. However, the absence of the Fe signal confirms that a significant fraction of $FeCl_3^-$ is exchanged with $TFSI^-$ and that our AED exchange model predicts the anion ratio within our ability to measure.

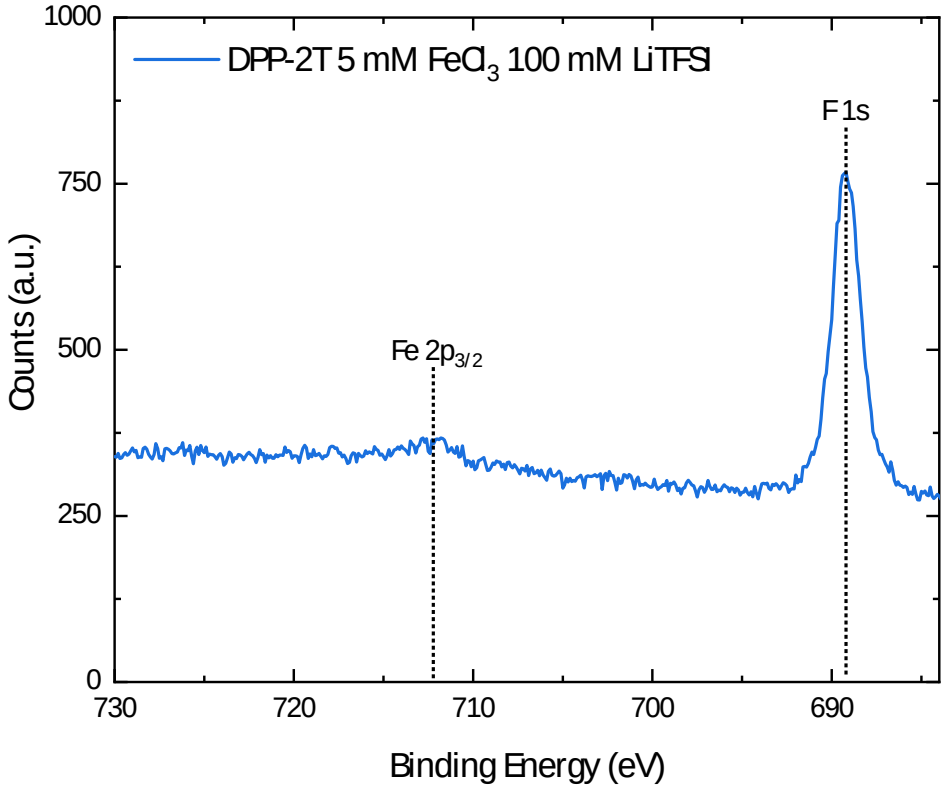

Figure C.23. X-ray photoelectron spectroscopy of PDPP-2T film doped with 5 mM $FeCl_3$ and 100 mM LiTFSI in the range of iron and fluorine

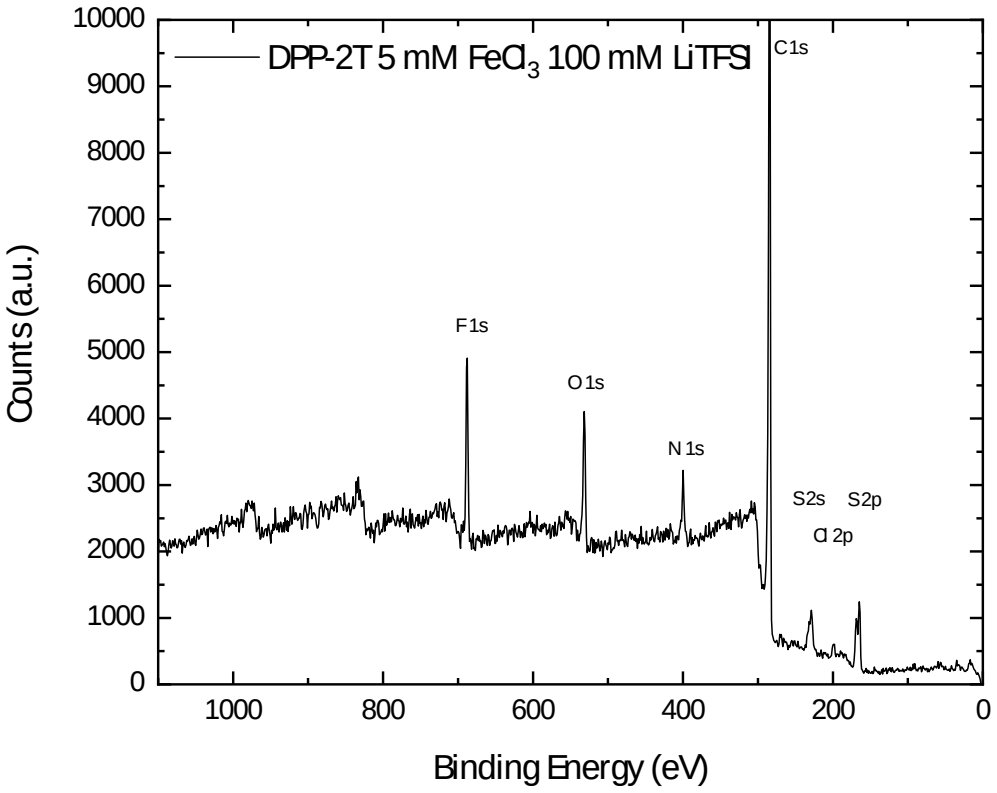

Figure C.24. X-ray photoelectron spectroscopy of PDPP-2T film doped with 5 mM $FeCl_3$ and 100 mM LiTFSI, full survey spectrum.

REFERENCES

[1] C. J. Mueller, E. Gann, C. R. McNeill, and M. Thelakkat, "Influence of fluorination in -extended backbone polydiketopyrrolopyrroles on charge carrier mobility and depth-dependent molecular alignment," *J. Mater. Chem. C*, vol. 3, pp. 8916–8925, 2015.

[2] F. Wang, K. Nakano, H. Segawa, and K. Tajima, "Phytol-derived alkyl side chains for -conjugated semiconducting polymers," *Chem. Mater.*, vol. 31, pp. 2097–2105, Mar. 2019.

[3] Y. Li, B. Sun, P. Sonar, and S. P. Singh, "Solution processable poly(2,5-dialkyl-2,5-dihydro-3,6-di-2-thienyl-pyrrolo[3,4-c]pyrrole-1,4-dione) for ambipolar organic thin film transistors," *Org. Electron.*, vol. 13, no. 9, pp. 1606 – 1613, 2012.

[4] K. Shiraishi and T. Yamamoto, "New -conjugated polymers constituted of dialkoxybenzodithiophene units: Synthesis and electronic properties," *Synth. Met.*, vol. 130, no. 2, pp. 139 – 147, 2002.

[5] C. Wang, D. T. Duong, K. Vandewal, J. Rivnay, and A. Salleo, "Optical measurement of doping efficiency in poly(3-hexylthiophene) solutions and thin films," *Phys. Rev. B*, vol. 91, p. 085205, Feb 2015.

[6] H. Bässler, "Charge transport in disordered organic photoconductors a monte carlo simulation study," *pss (b)*, vol. 175, no. 1, pp. 15–56, 1993.

[7] V. I. Arkhipov, P. Heremans, E. V. Emelianova, and H. Bässler, "Effect of doping on the density-of-states distribution and carrier hopping in disordered organic semiconductors," *Phys. Rev. B*, vol. 71, p. 045214, Jan 2005.

[8] S. Fratini, M. Nikolka, A. Salleo, G. Schweicher, and H. Sirringhaus, "Charge transport in high-mobility conjugated polymers and molecular semiconductors," *Nat. Mater.*, vol. 19, no. 5, pp. 491–502, 2020.

[9] P. Yee, D. T. Scholes, B. J. Schwartz, and S. H. Tolbert, "Dopant-induced ordering of amorphous regions in regiorandom p3ht," *J. Phys. Chem. Lett.*, vol. 10, pp. 4929–4934, Sept. 2019.

[10] J. Gao, B. W. Stein, A. K. Thomas, J. A. Garcia, J. Yang, M. L. Kirk, and J. K. Grey, "Enhanced charge transfer doping efficiency in j-aggregate poly(3-hexylthiophene) nanofibers," *J. Phys. Chem. C*, vol. 119, pp. 16396–16402, July 2015.

[11] I. E. Jacobs, E. W. Aasen, J. L. Oliveira, T. N. Fonseca, J. D. Roehling, J. Li, G. Zhang, M. P. Augustine, M. Mascal, and A. J. Moulé, "Comparison of solution-mixed and sequentially processed p3ht:f4tcnq films: Effect of doping-induced aggregation on film morphology," *J. Mater. Chem. C*, vol. 4, pp. 3454–3466, 2016.

[12] Y. Liu, "Is the free energy change of adsorption correctly calculated?," *J. Chem. Eng. Data*, vol. 54, pp. 1981–1985, July 2009.

[13] R. Ghosh, A. R. Chew, J. Onorato, V. Pakhnyuk, C. K. Luscombe, A. Salleo, and F. C. Spano, "Spectral signatures and spatial coherence of bound and unbound polarons in p3ht films: Theory versus experiment," *J. Phys. Chem. C*, vol. 122, no. 31, pp. 18048–18060, 2018.

[14] T. L. Murrey, K. Guo, J. T. Mulvey, O. A. Lee, C. Cendra, Z. I. Bedolla-Valdez, A. Salleo, J.-F. Moulin, K. Hong, and A. J. Moulé, "Additive solution deposition of multi-layered semiconducting polymer films for design of sophisticated device architectures," *J. Mater. Chem. C*, vol. 7, pp. 953–960, 2019.

[15] T. J. Aubry, J. C. Axtell, V. M. Basile, K. J. Winchell, J. R. Lindemuth, T. M. Porter, J.-Y. Liu, A. N. Alexandrova, C. P. Kubiak, S. H. Tolbert, A. M. Spokoyny, and B. J. Schwartz, "Dodecaborane-based dopants designed to shield anion electrostatics lead to increased carrier mobility in a doped conjugated polymer," *Adv. Mater.*, vol. 31, no. 11, p. 1805647, 2019.

[16] A. M. Valencia and C. Cocchi, "Electronic and optical properties of oligothiophene-f4tcnq charge-transfer complexes: The role of the donor conjugation length," *J. Phys. Chem. C*, vol. 123, pp. 9617–9623, Apr. 2019.

[17] J. T. Liu, H. Hase, S. Taylor, I. Salzmann, and P. Forgione, "Approaching the integer-

charge transfer regime in molecularly doped oligothiophenes by efficient decarboxylative cross-coupling," *Angew. Chem. Int. Ed.*, vol. 59, no. 18, pp. 7146–7153, 2020.

[18] K. Kang, S. Watanabe, K. Broch, A. Sepe, A. Brown, I. Nasrallah, M. Nikolka, Z. Fei, M. Heeney, D. Matsumoto, K. Marumoto, H. Tanaka, S.-i. Kuroda, and H. Sirringhaus, "2d coherent charge transport in highly orderedconducting polymers doped by solid state-diffusion," *Nat. Mater.*, vol. 15, no. 8, pp. 896–902, 2016.

[19] M. Balooch Qarai, X. Chang, and F. C. Spano, "Vibronic exciton model for low bandgap donoracceptor polymers," *J. Chem. Phys*, vol. 153, no. 24, p. 244901, 2020.

[20] C. Tanase, E. J. Meijer, P. W. M. Blom, and D. M. de Leeuw, "Unification of the hole transport in polymeric field-effect transistors and light-emitting diodes," *Phys. Rev. Lett.*, vol. 91, p. 216601, Nov 2003.

[21] W. F. Pasveer, J. Cottaar, C. Tanase, R. Coehoorn, P. A. Bobbert, P. W. M. Blom, D. M. de Leeuw, and M. A. J. Michels, "Unified description of charge-carrier mobilities in disordered semiconducting polymers," *Phys. Rev. Lett.*, vol. 94, p. 206601, May 2005.

[22] M. C. J. M. Vissenberg and M. Matters, "Theory of the field-effect mobility in amorphous organic transistors," *Phys. Rev. B*, vol. 57, pp. 12964–12967, May 1998.

[23] J. Rivnay, M. F. Toney, Y. Zheng, I. V. Kauvar, Z. Chen, V. Wagner, A. Facchetti, and A. Salleo, "Unconventional face-on texture and exceptional in-plane order of a high mobility n-type polymer," *Adv. Mater.*, vol. 22, no. 39, pp. 4359–4363, 2010.

[24] X. Zhang, L. J. Richter, D. M. DeLongchamp, R. J. Kline, M. R. Hammond, I. McCulloch, M. Heeney, R. S. Ashraf, J. N. Smith, T. D. Anthopoulos, B. Schroeder, Y. H. Geerts, D. A. Fischer, and M. F. Toney, "Molecular packing of high-mobility diketo pyrrolo-pyrrole polymer semiconductors with branched alkyl side chains," *J. Am. Chem. Soc.*, vol. 133, pp. 15073–15084, Sept. 2011.

[25] A. Gasperini, X. A. Jeanbourquin, and K. Sivula, "Effect of molecular weight in

diketopyrrolopyrrole-based polymers in transistor and photovoltaic applications," *J. Polym. Sci., Part B: Polym. Phys.*, vol. 54, no. 21, pp. 2245–2253, 2016.

Appendix D

Unfinished Work

D.1 Preamble

I've worked on several unpublished projects over the past 6 years. This chapter contains the ensemble of unpublished data and information obtained during my doctoral research. Some sections of this chapter will include data for future publications, while others contain learned information that will help future graduate students in Prof. Adam Moule's research group. This chapter will be ordered in chronological order with respect to my PhD timeline.

D.2 Small Angle Neutron Scattering of P3HT Nanofiber Dispersions

My first project in the Moulé group, was to fit a set of small angle neutron scattering (SANS) data (Figures D.1) that had been previously obtained by an older graduate student. The goal of this project was to study structure formation in solutions of P3HT and P3HT doped with F4TCNQ, as temperature was slowly cooled. Contrast was varied by changing the deuterium content in the surrounding solvent. The neutral P3HT solutions used a 3:1 deuterated toluene: deuterated octane solvent mixture. While the doped P3HT solutions were prepared with a 3:1 deuterated toluene: protonated octane solution.

D.2.1 Conclusions

Fits to the neutral P3HT solution SANS data is shown in Figure D.2. SANS shows an inflection in structure formation, above 40°C the polymer remains dissolved. At high temperatures the high Q SANS data was fit to a flexible-parallelepiped model. Fit parameters for the dissolved P3HT including, chain width, height and contour length is shown in Figure D.3 and Table D.1. The low Q data was fit to a power law to obtain the dimensionless fractal parameter (D_f). At 80°C, D_f of 2 corresponds to solvated gaussians chains, as the temperature cools to 60C, D_f of 3 demonstrates a coalescing of the polymer chains into a clustered network. As temperature is brought down to 40°C the P3HT chains aggregate into parallelepiped structures (Figure D.4), fit parameters are shown in Figure D.2.

To supplement the SANS data, I collected temperature dependent ultraviolet-visible (UVvis) data of P3HT solutions in both a cooling cycle (Figure D.5) and a heating cycle (Figure D.6). The cooling cycle demonstrates onset of fiber aggregation below 40°C, with aggregates be-

coming more J-like as temperature continues to drop to 20°C. The heating cycle demonstrates increased H-like aggregation as temperature increases from 20°C to 70°C. The dissolution onset at 40°C with complete dissolution achieved by 75°C.

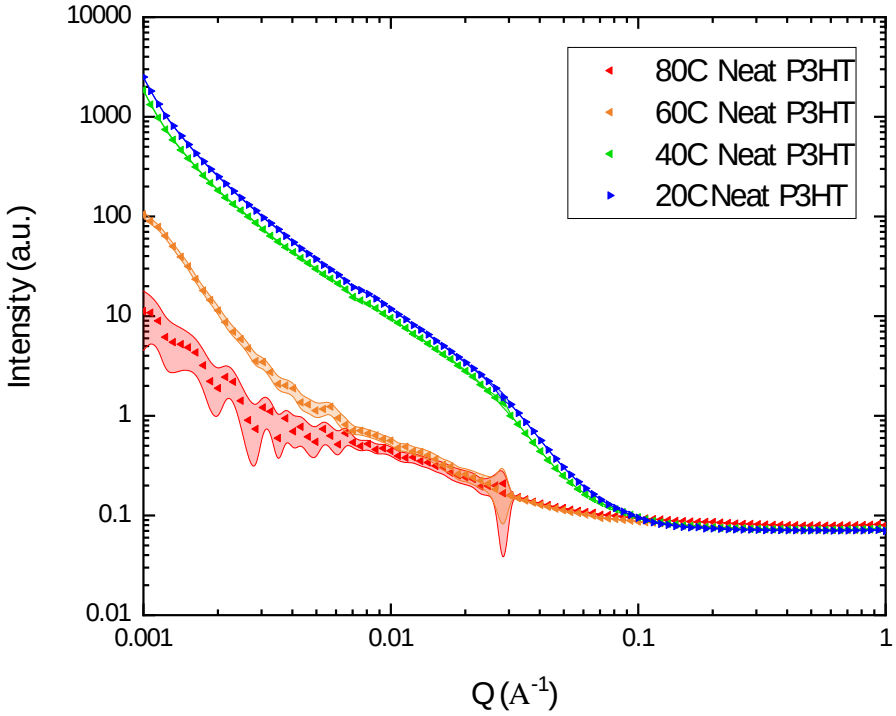

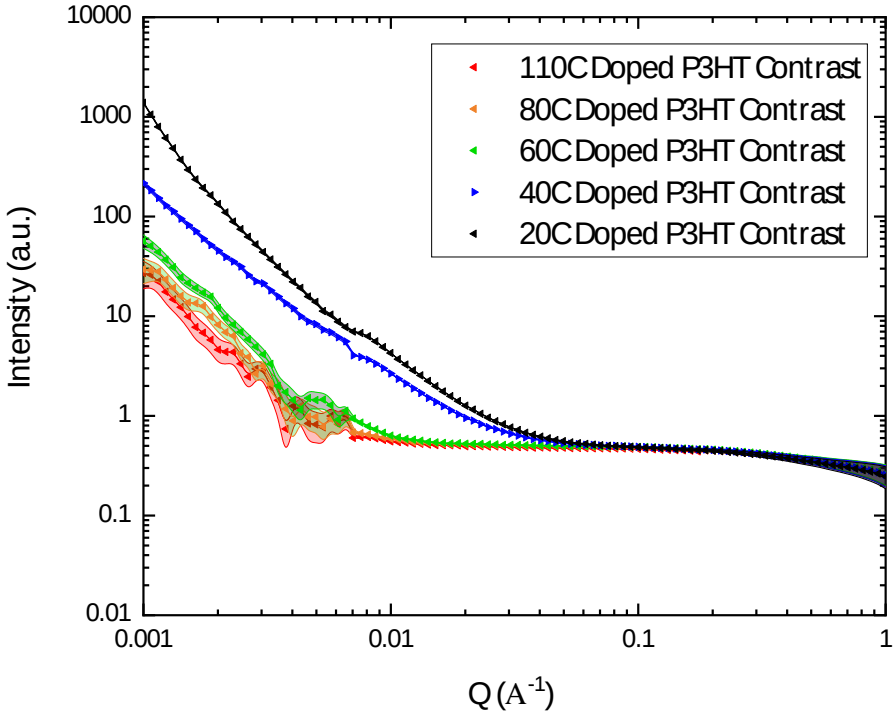

Figure D.1. Temperature dependent SANS data of neutral and doped P3HT solutions.

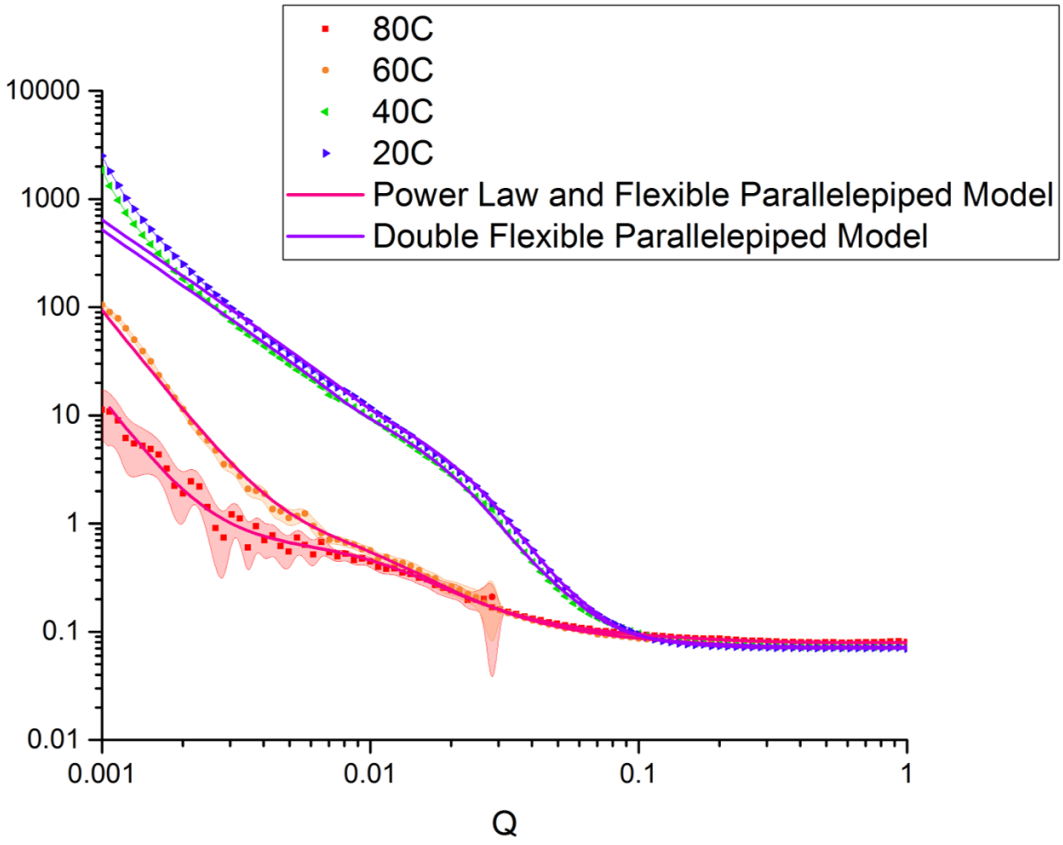

Figure D.2. Fits to the Neutral P3HT SANS data.

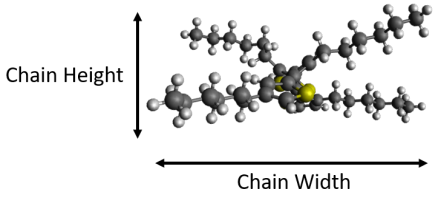

Figure D.3. Illustration of high temperature dissolved P3HT fit parameters.

Table D.1. Dissolved P3HT fit parameters. Showing the ensemble average chain width, height, contour length, and kuhn length. The dimensionless fractal parameter (D_f) fits to the low Q region of the SANS data.

T (°C)	Height (Å)	Width (Å)	Contour Length (Å)	Kuhn Length (Å)	D_f
80	7.5 ± 0.2	11.9 ± 0.4	872 ± 20	76 ± 1	2.2 ± 0.5
60	6.0 ± 0.1	19.1 ± 0.3	840 ± 10	88 ± 2	3.1 ± 0.1

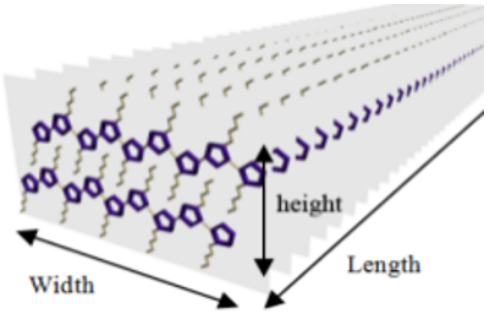

Figure D.4. Illustration of low temperature P3HT fiber fit parameters.

Table D.2. P3HT Fiber fit parameters. Showing the ensemble average fiber width, height, contour length, and kuhn length.

T (°C)	Height (Å)	Width (Å)	Contour Length (Å)	Kuhn Length (Å)
40	37.1 ± 0.1	185.4 ± 0.5	$8E^7 \pm 6E^7$	402 ± 3
20	46.8 ± 0.2	460.6 ± 0.6	$1E^6 \pm 6E^5$	354 ± 2

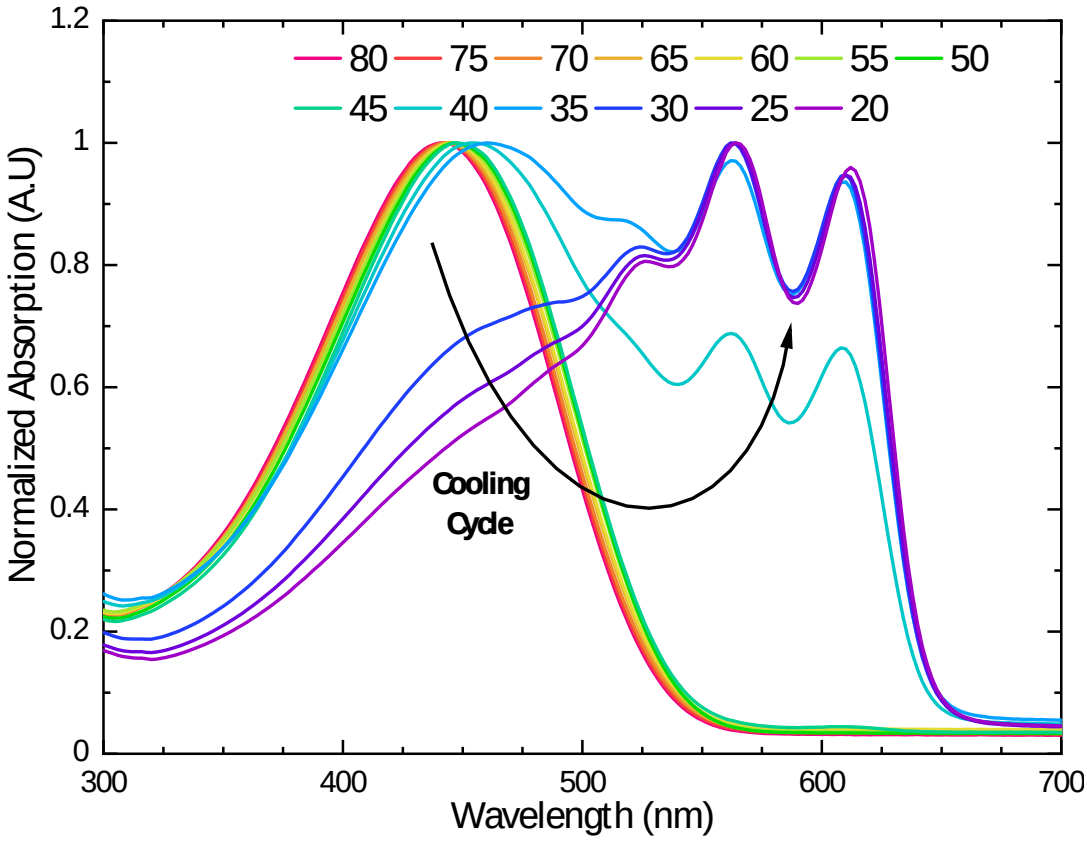

Figure D.5. Temperature dependence UV-vis of 2mg/mL P3HT in 3:1 tol:oct solution as the solution is cooled down at a 20C/hr ramp rate, with 30 min soaks at 60, 40, and 20C.

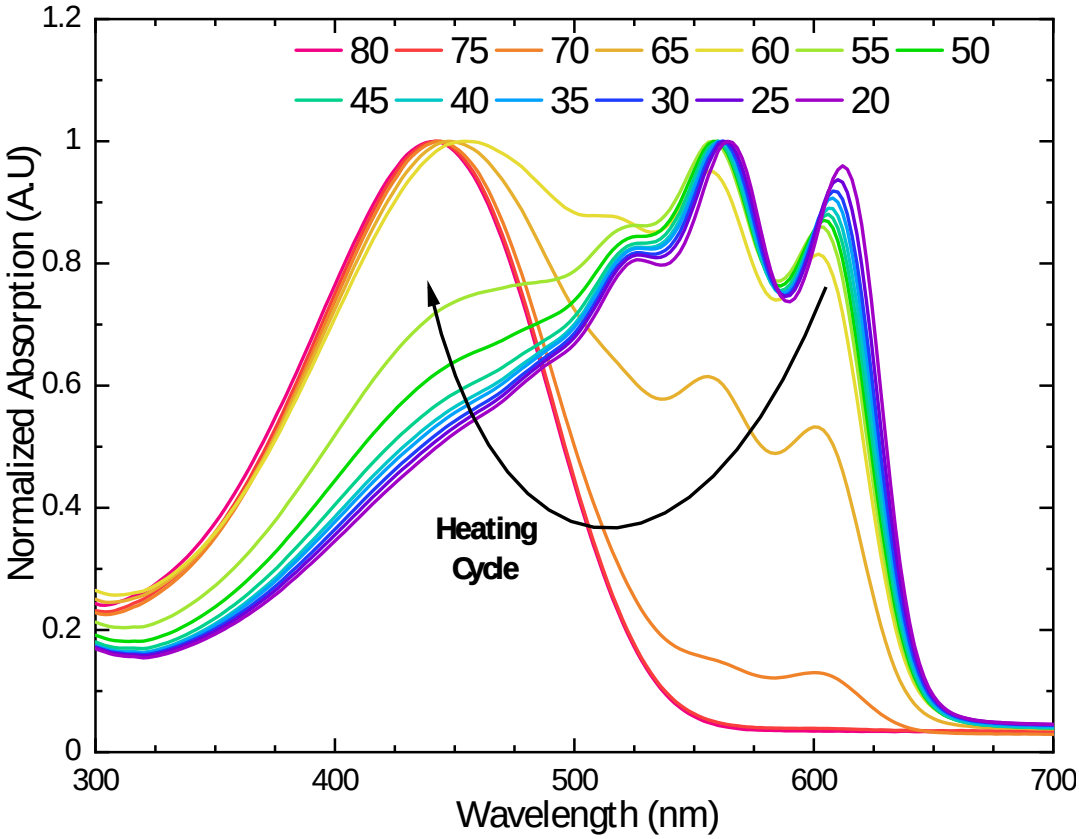

Figure D.6. Temperature dependence UV-vis of 2mg/mL P3HT in 3:1 tol:oct solution as the solution is heated up at a 20C/hr ramp rate, with 30 min soaks at 20, 40, and 60C.

I was unable to obtain useful fits for the doped P3HT SANS data due to the sample configuration (Figure D.1). The use of protonated octane in the solution preparation greatly increased incoherent scattering from the neutrons, effectively increasing the background noise floor of the measurement. This increased background floor prevented extraction of scattering dimensions below 20 nm length scales. Since the relevant characteristic length scales of the P3HT parallelepipeds are shorter than 20 nm, I was unable to obtain a quantitative comparison.

D.3 Grazing Incidence Small Angle Neutron Scattering

In 2017, I collected grazing incidence small angle neutron scattering (GISANS) data on a neat P3HT film and an F4TCNQ doped film, while they were exposed to a saturated deuterated chlorobenzene (dCB) vapor environment (Figures D.7 and D.8). This data was meant to supplement the neutron reflectometry data discussed in Chapter 1, by contributing in-plane solvent swollen domain size. However technical issues that occurred during data collection reduced my

confidence in the data quality and led me to leave it out of the publication.

The two distinct peaks in the Q_x=0 line cuts correspond to the incoming neutron beam (lower peak) and the specularly reflected beam off of the film surface. As expected the specularly reflected peak shifts to lower Q_z as wavelength is increased. I was expecting to analyze the scattering as a function of the Q_{xy} coordinate, however due to an unexpected beam line issue we were unable to collect data for a long enough period of time to increase signal to noise ratio. Additionally, the beam line was not prepared for this kind of measurement and the potential for instrumental artifacts is high.

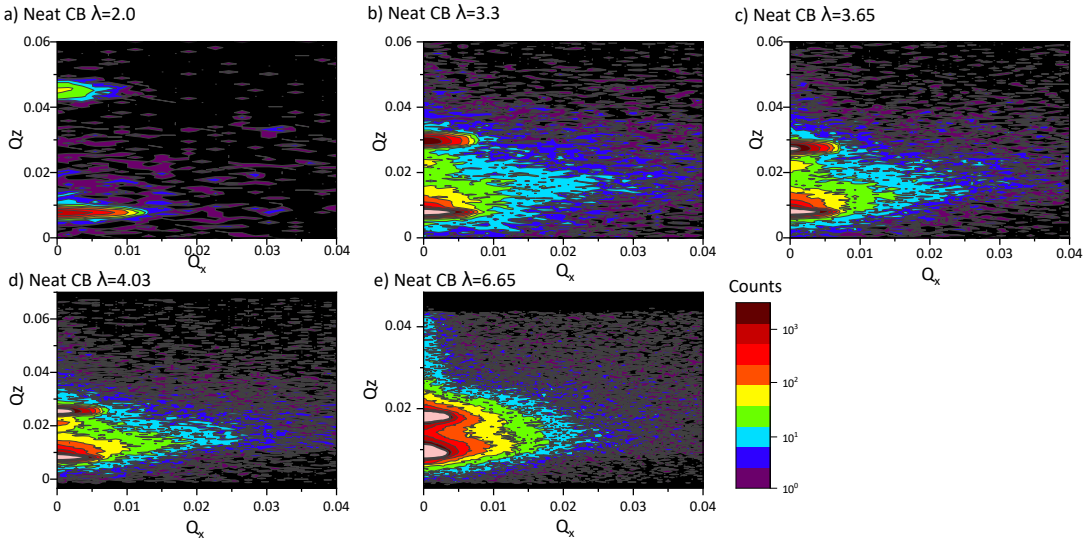

Figure D.7. GISANS data from a neat P3HT film swollen with dCB as a function of wavelength.

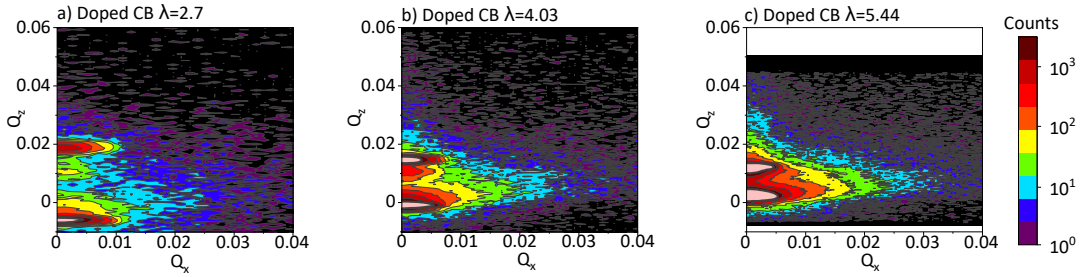

Figure D.8. GISANS data from an F4TCNQ doped P3HT film swollen with dCB as a function of wavelength.

D.4 Small Angle Neutron Scattering of P3HT:PEO Melts

This work was intended as a side project. The goal was to collect and analyze SANS data for our collaborator, Natalie Stingelin. The Stingelin group had demonstrated that when the conjugated polymer poly(-3-hexylthiophene) (P3HT) was blended with an insulating bulk polymer such as poly(ethylene oxide) (PEO) or poly(ethylene) (PE), it solidifies into a more planar conformation and undergos an order/disorder transition from microstructures dominated by H-like aggregation to J-like (Figure D.9).

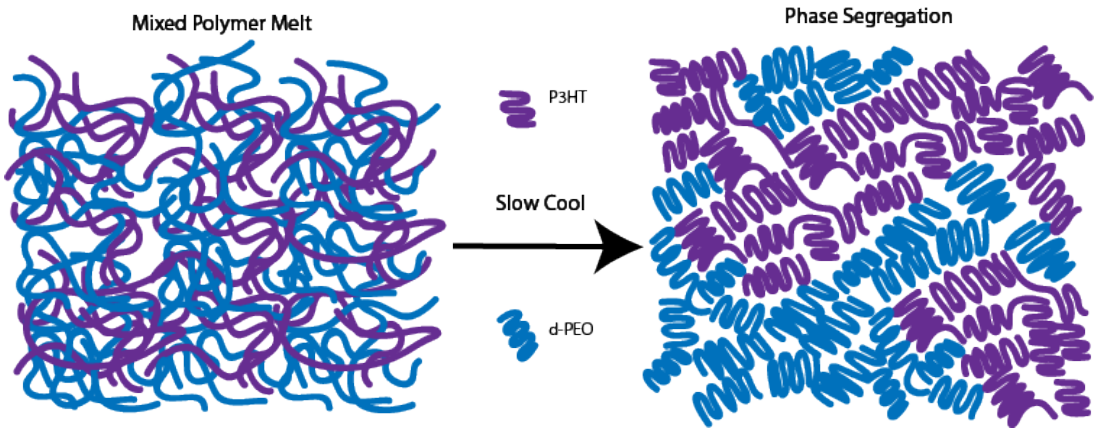

Figure D.9. Illustration of phase segregation upon cooling a mixed P3HT/PEO melt.

I collected SANS data at Oak Ridge National Lab. The sample was was a P3HT/PEO powder mixture, prepared by our collaborators at Basque University. The sample was loaded into the beamline and the temperature was slowly ramped up from 25°C to 150°C. The data and subsequent ellipsoidal form factor fits are shown in Figure D.10. An illustration of the extracted morphological parameters are shown in Figure D.12. There are no observed changes in the SANS data as a function of temperature. The sample was composed of P3HT ellipsoids with polar and equatorial radii $R_P \sim 37$ and $R_E \sim 5$ nm, respectively. The elliposoids were surrounded by a matrix of mixed PEO/P3HT domains. Extracted volume fraction of the ellipsoid domains and the volume fraction of P3HT in the mixed domain is shown in Figure D.13. In order to extract volume fractions I made the assumption that there was no water present in the sample. This is likely a poor assumption, since I visibly observed condensation in the sample vial. I vaccumed the sample overnight before loading into the SANS instrument, however PEO is highly miscible with water. Since there is no way to estimate the extent of the water con-

tamination there is likely a large systematic error in the volume fraction analysis. There is an observed shift in the P3HT lamellar stacking peak due to thermal expansion(Figure D.11). As the temperature was increased the P3HT lamellar spacing increased from 16.4 to 17.4$\AA$.

Since there are minimal structural changes observed in the SANS data, it is unlikely that our collaborators are going to continue this project.

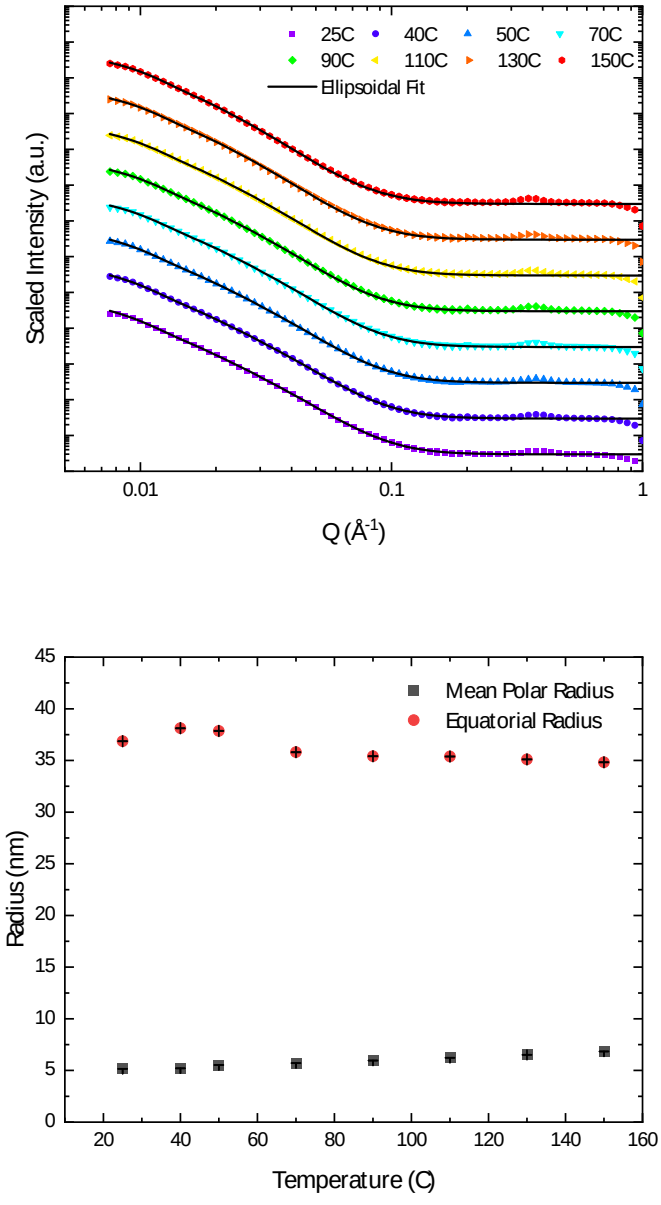

Figure D.10. (top) Temperature dependent SANS P3HT:PEO mixtures, fit with an ellipsoidal form factor. (bottom) Extracted ellipsoidal radii.

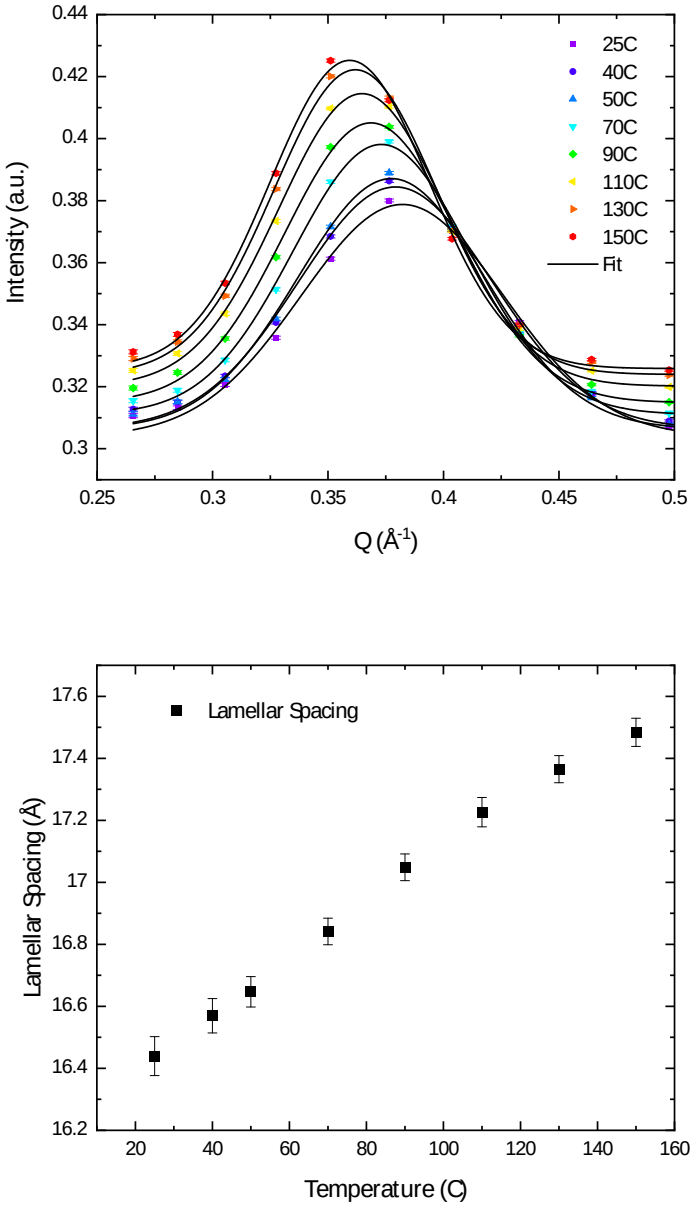

Figure D.11. (top)Temperature dependent SANS P3HT:PEO mixtures, fit the lamellar peak at high Q. (bottom) Extracted P3HT Lamellar Spacing.

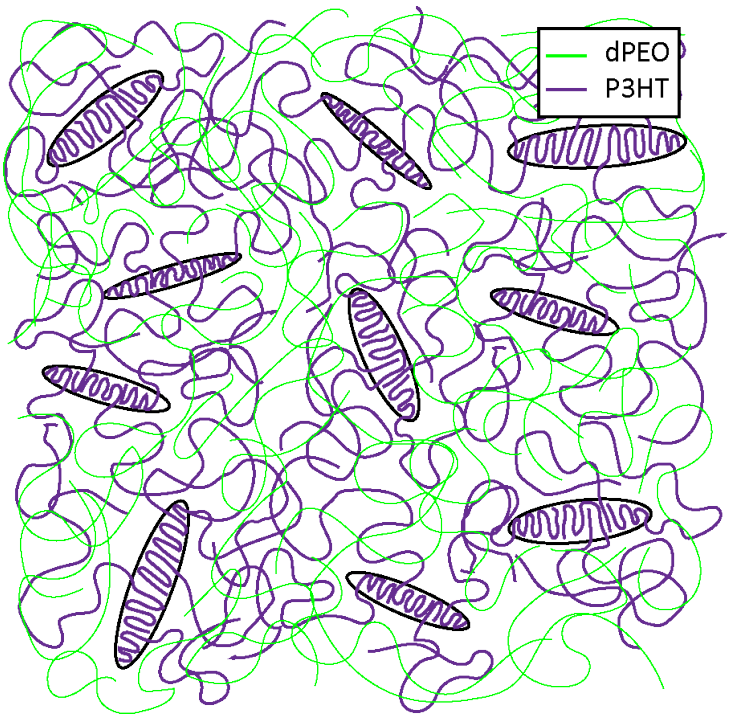

Figure D.12. Illustration morphology extracted from SANS. P3HT ellipsoids surrounded by a matrix of mixed P3HT/PEO domains.

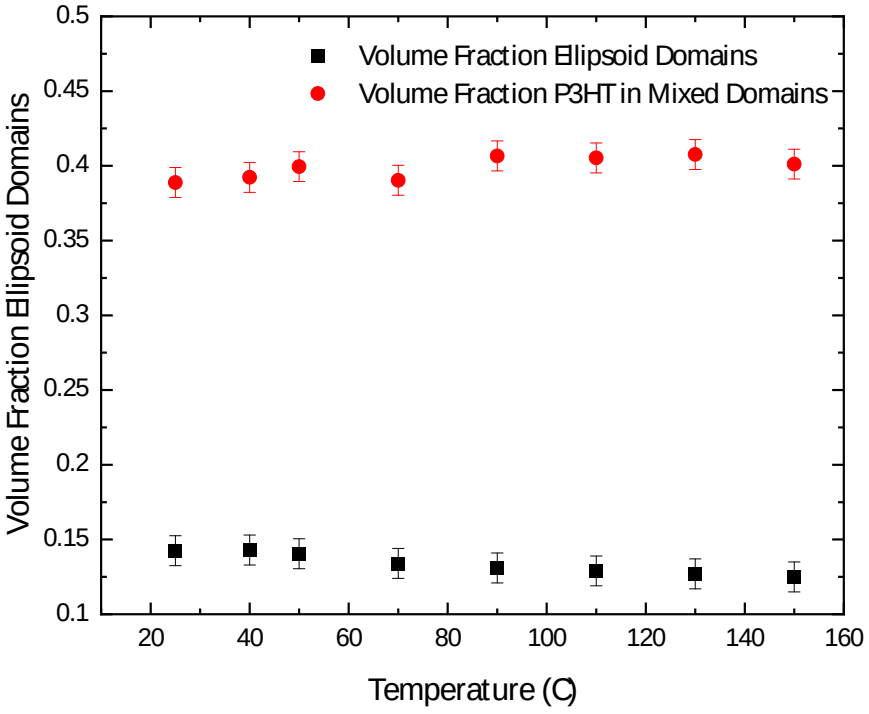

Figure D.13. Extracted volume fraction of pure P3HT ellipsoidal domains and the volume fraction of P3HT in the mixed P3HT:PEO matrix.

D.5 Fabrication of Blade Coater

In 2018-2019, I managed a team of German exchange students to design and fabricate a lab scale blade coater (Figure D.14).This involved providing guidance through the design process, acquiring and fabricating parts, and writing LabView software to control automated components. The purpose of building this equipment was to expand my groups solution deposition methods to one that is capable of depositing consistent micron thick films.

In the end, this blade coater is capable of depositing smooth polymer films with thicknesses on the order of 100s of nanometers to micrometers. Several instrument parameters can be tuned to adjust film thickness and quality. There are three manual knobs for controlling the height and angle of the coater blade. The substrate stage can be heated to a desired temperature to control solvent evaporation rate. The stage is mounted on a linear actuator. The acceleration, velocity, travel distance, and deceleration of the stage is controlled by a custom LabView program.

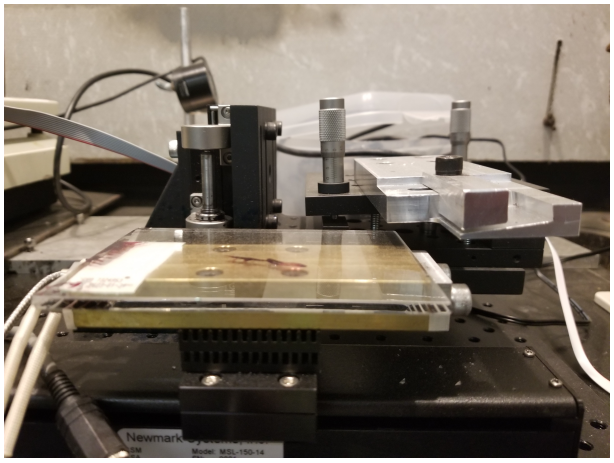

Figure D.14. Image of fabricated blade coater, including automatic linear stage actuator, and custom temperature controller.

D.6 Upscaling Photothermal Lithography

From 2017 to 2020, I worked on developing a projection photothermal pattering system. The goal was to fabricate a machine capable of photo-thermally patterning semiconducting polymer thin films with a smallest feature size of 1 μm and overall patterned area approaching 1 cm^2. The project included two iterations of machine design, with many component upgrades over the 3 year span. The result is a $\sim$\$75K Projection Photothermal Lithography Microscope (PPLM).

Photothermal patterning is a process where an image is projected onto a semiconducting polymer thin film while it is immersed in a solvent. The solvent quality must be such that the film doesn't dissolve at room temperature but will dissolve at a mildly elevated temperature (40-100°C). In the locations where the light is projected onto the film, photons are absorbed and create excitons. The excitons that relax to ground state through non-emissive processes results in local heating of the film. Once the local temperature surpasses the dissolution temperature (DT), the polymer dissolves, leaving behind a negative patterned image.

There are several experimental parameters that can be tuned to influence pattern feature size and sharpness, but it all comes down to controlling polymer dissolution rate. The miscibility between the polymer and solvent influences the DT. The DT must be low enough to be obtained by optical absorption, yet large enough so that mild macroscopic heating does not induce full film dissolution. I've determined that DT is easiest to control by tuning the composition of a binary solvent mixture (see subsection D.6.2). Minimizing polymer polydispersity is ideal for narrowing the dissolution temperature range. The wavelength, power, and exposure time of the laser influences the amount of energy absorbed into the film. If the absorption bandwidth of a given semiconducting polymer does not overlap the input laser wavelength, than no patterning will occur. Likewise, photon density must be high enough to create a local heating rate that surpasses the rate that heat diffuses into i) the solvent, ii) the neighboring polymer domains, and iii) the glass substrate.

The greatest challenge of PPLM is creating consistent patterns. It's not that this technique isn't capable of creating consistent patterns. However, there remain a few optical artifacts that need to be corrected in this system. I will discuss the details of the fabrication and suggested modifications in the subsection D.6.1. After fabricating the microscope, my plan was to systematically quantify the effects of laser power, exposure time, objective lens magnification, solvent quality, and photomask feature size on the pattern feature size/sharpness and overall patterned area. Unfortunately, the inability to obtain consistent patterns has limited my quantitative analysis.

In addition to fabricating the PPLM machine, I initiated several patterning related projects for a variety of organic electronic applications, including photovoltaics, optical gratings, nanowires,

electrodes, and transistors. I designed eighteen custom photomasks that should lead to several publications. I will discuss the photomasks and their potential projects in the subsection D.6.3.

D.6.1 Fabrication of Projection Photothermal Lithography Microscope

In order to prove the efficacy of the projection photothermal lithography concept, I constructed the prototype shown in Figure D.15a). This prototype consisted of a cheap 2.5W 445nm diode laser, a mirror to guide the laser, a photomask composed of a 1000 mesh TEM grid sandwiched between two glass slides, and a 10X microscope objective lens to project the image onto a semiconducting polymer film. All of the components were positioned manually. I guided a particularly talented undergraduate, Justin Mulvey, to obtain a series of patterned P3HT films using this prototype. This is the first demonstration of controlling depth and feature size of patterns obtained through projection photothermal lithography by varying laser exposure time and solvent quality. Figure D.17 presents AFM height images of patterned P3HT films with respect to exposure time, and mixing ratio of dichlorobenzene (DCB) and methyl-tetrahydrofuran (mTHF). Further discussion of the influence of solvent mixing ratio is located in subsection D.6.2.

There were a few technical challenges revealed during this prototyping process. First off, this design suffered from alignment issues. The scaffolding for positioning the optical components frequently moved. Also, it was particularly challenging to maintain orthogonal alignment of the optical components with respect to the laser beam. In addition to alignment issues, the output beam of 445nm laser diode had an oblong beam shape with an inhomogeneous optical density and resulted in large variations of pattern depth and sharpness over each individual exposure area. The projection photothermal lithography microscope was developed to overcome these technical challenges.

Figure D.15b) illustrates the individual components of the projection photothermal lithography microscope. Several components were upgraded to improve optical alignment and laser homogeneity. I upgraded the laser system to a 1-5W (1% stability) variable 405nm laser diode from CNI Laser. The beam is homogenized through a square beam optical fiber and additional equipment was added to remove optical speckle. The beam is output through a collimator to produce a corner to corner beam size of 14 mm with a beam divergence of 5 mrad at a 100 cm

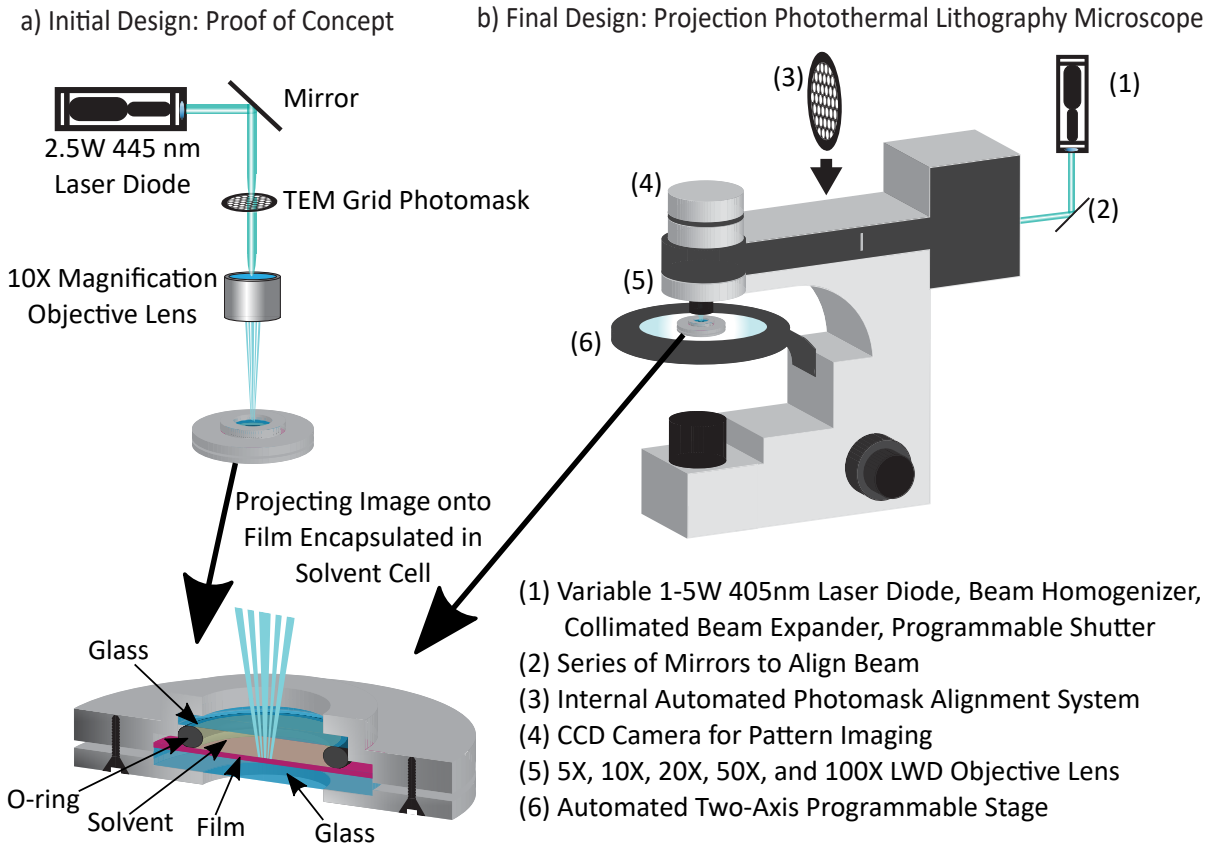

Figure D.15. Schematics of a) the first prototype of projection photothermal lithography setup and b) the final projection photothermal lithography microscope.

working distance. The beam passes through a NM-Laser high powered LSTXYW8 laser shutter with CX3000B shutter control board before being directed into the back of a Leica DM2700 microscope. Three mirrors are used to carefully position the beam path to remain orthogonal to optical components within the microscope. Three neutral density filters (OD 0.5, OD 2, OD 3) are installed inside microscope (They can be flipped in/out of the beam path). An internal iris was removed and replaced with a custom fabricated photomask insertion and alignment system. Photomasks can be exchanged through the side of the microscope. The photomask alignment system consists of mask holder mounted on a ball bearing track. The mask holder is attached to an electronic Actuonix linear actuator. Once the photomask is installed into the microscope, the actuator is electronically controlled to move the photomask into the image plane. Light from the laser travels through the photomask, out the microscope objective lens, and is projected onto the film surface. The film/solvent cell is mounted on a Marzhauser programmable stage. The

stage can be manually controlled via joy stick for initial positioning of the sample. I guided another undergraduate researcher, Daniel Tiffany-Appleton, to write a LabView program that synchronizes stage movements with the pulsing of the automatic shutter. The overall patterning area of a single exposure varies (0.1-1mm^2) depending on the objective lens magnification. The synchronization of stage and shutter movements automates multiple exposures and increases the overall patterning area to the stage dimensions ($\sim$10 cm^2). At this point the only thing limiting overall patterning area is the size/quality of the solvent cell. Although, this system greatly improved optical alignment and beam homogeneity the system needs a few more adjustments to improve consistency and repeatability of the pattern formation.

A new optical artifact was discovered using the PPLM, this will be refereed to as a 'ghost pattern'. These ghost patterns are a second set of pattern features that are slightly offset (1-3μm) from the main pattern and have a shallower pattern depth (Figure D.16). This artifact is likely caused by multiple reflections off of glass/air and glass/solvent interfaces in the solvent cell. This artifact should be fixed by redesigning the solvent cell so that both of the windows are always exactly parallel to each other and orthogonal to the laser beam. This is particularly challenging given the current constraints for minimizing the distance that the light travels through the solvent layer in the cell before reaching the semiconducting polymer film. I suggest building the next set of cells using a stiffer metal than aluminum ie: stainless steel.

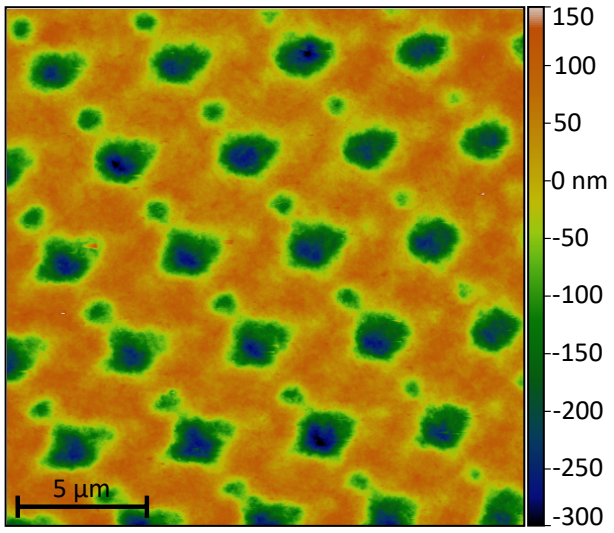

Figure D.16. AFM height image of ghost pattern artifact.

There are a few more equipment upgrades that will improve pattern consistency and repeatability. First, the linear actuator that moves the photomask into the image plane in the microscope has a poor tolerance and repeatability ($\pm$0.1 mm). Also, it is controlled on an analogue scale from 0 to 100% extension of the actuator. The current Actuonix PQ12 actuator was chosen due to budget constraints and because it fit within the limited space in the microscope. I suggest replacing this actuator with something that has memory of the exact position/extension of the actuator with a precision and repeatability of $\pm$0.01 mm. Next, it is clear that there is a variation in the image clarity across the projected photomask shadow on the polymer film. This is due to a minor misalignment of either the photomask or the solvent cell ($\pm < 5^{\circ}$), making either of them not perfectly orthogonal to the laser beam. This can be improved by fabricating a new photomask holder/solvent cell with higher precision parts. For upgrading the these components, I suggest using parts fabricated from a more rigid metal than aluminum. Finally, the current collimator creates laser beam that is not perfectly collimated (Divergence = 5 mrad). It is currently positioned 100cm from the image plane in the microscope (desired location of photomask). Since the beam continues to diverge after reaching this plane a significant portion of the light ($\sim$50%) doesn't reach the objective lens. This significantly reduces the photon flux incident on the semiconducting polymer film. This can be fixed by introducing new optics to correct the divergence.

D.6.2 Effects of Binary Solvent Quality on Photothermal Patterning

Polymer dissolution temperature (DT) can be controlled by tuning the mixing ratio of a binary solvent mixture. One of the solvents must be a poor solvent for the polymer, with a DT$>\sim$ 100°C, while the other solvent should have a polymer DT less than room temperature. As the concentration of the good solvent increases the DT decreases, approaching the DT of the pure solvent/polymer system.

Figure D.17 show AFM height images of P3HT patterns that were created using the preliminary optical set up. The exposure time was varied from 15 to 60s and a dichlorobenzene:methyltetrahydrofuran (DCB:mTHF) binary solvent mixture was adjusted from 0 to 20% DCB. DCB is a good solvent for P3HT and will fully dissolve the film at room temperature while mTHF is a poor solvent for P3HT. Pattern depth increases with increasing DCB content and longer

exposure times. I must mention that these AFM images were cherry picked from each patterned film. There were large variations in pattern depth and sharpness within each of the sample configurations due to the alignment issues discussed in the previous subsection.

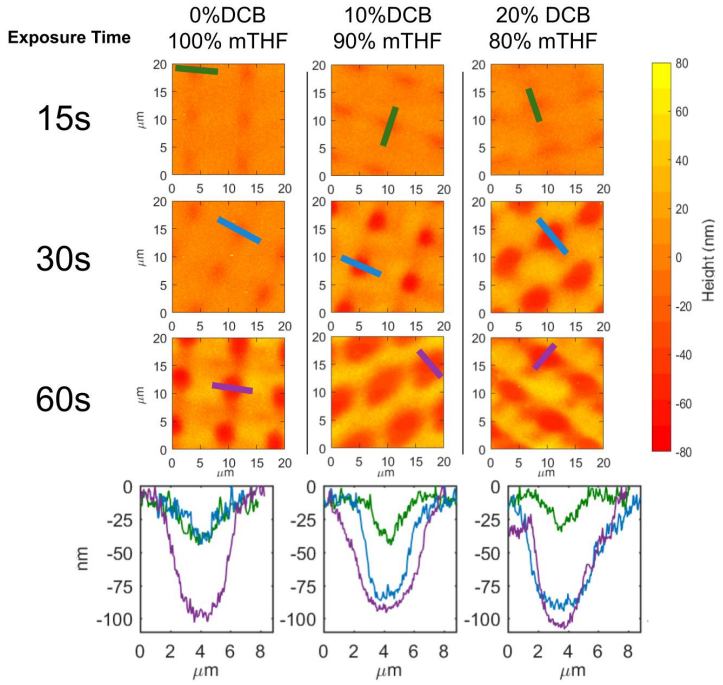

Figure D.17. AFM height images of P3HT films patterned with initial prototype equipment. Pattern depth is adjusted Solvent quality was tuned by the adjusting the mixing ratio THF and DCB. Three different exposure times

Figure D.18 demonstrates how P3HT dissolution temperature can be tuned between 35 - 85°C by controlling the mixing ratio of binary solvent mixture of chlorobenzene and cyclohexanone. Figure D.19, demonstrate AFM height images of P3HT film patterns obtained using the projection microscope with a 445nm laser diode and 20 second exposure times. The pattern quality is varied by changing the DCB:CHN binary mixing ratio from a) 20:80, b) 25:75, and c) 30:70. As the CB content increases the DT decreases, which increased the pattern feature size (from a given laser power/exposure time). Figure D.19d) and e) depict height cross sections from the 25:75 and 30:70 solvent ratios respectively. By increasing the DCB content from 25 to 30% the mean feature size increases from 1.6 to 2.7 μm, and the mean center-to-center distance between the features decreases from 8.56 to 7.62μm.

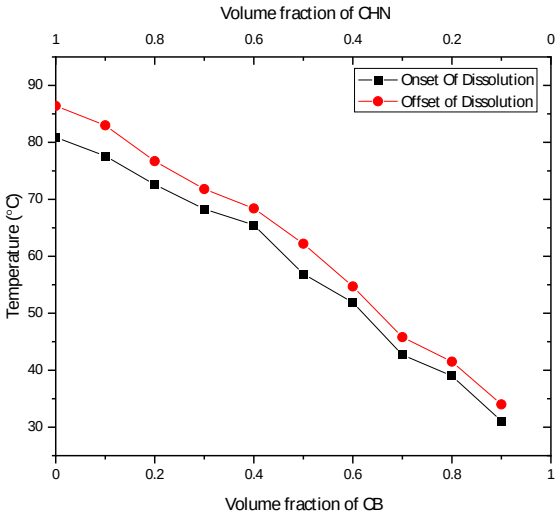

Figure D.18. Dissolution Temperature of P3HT film, immersed in a binary solvent mixture of chlorobenzene (CB) and cyclohexanone(CHN).

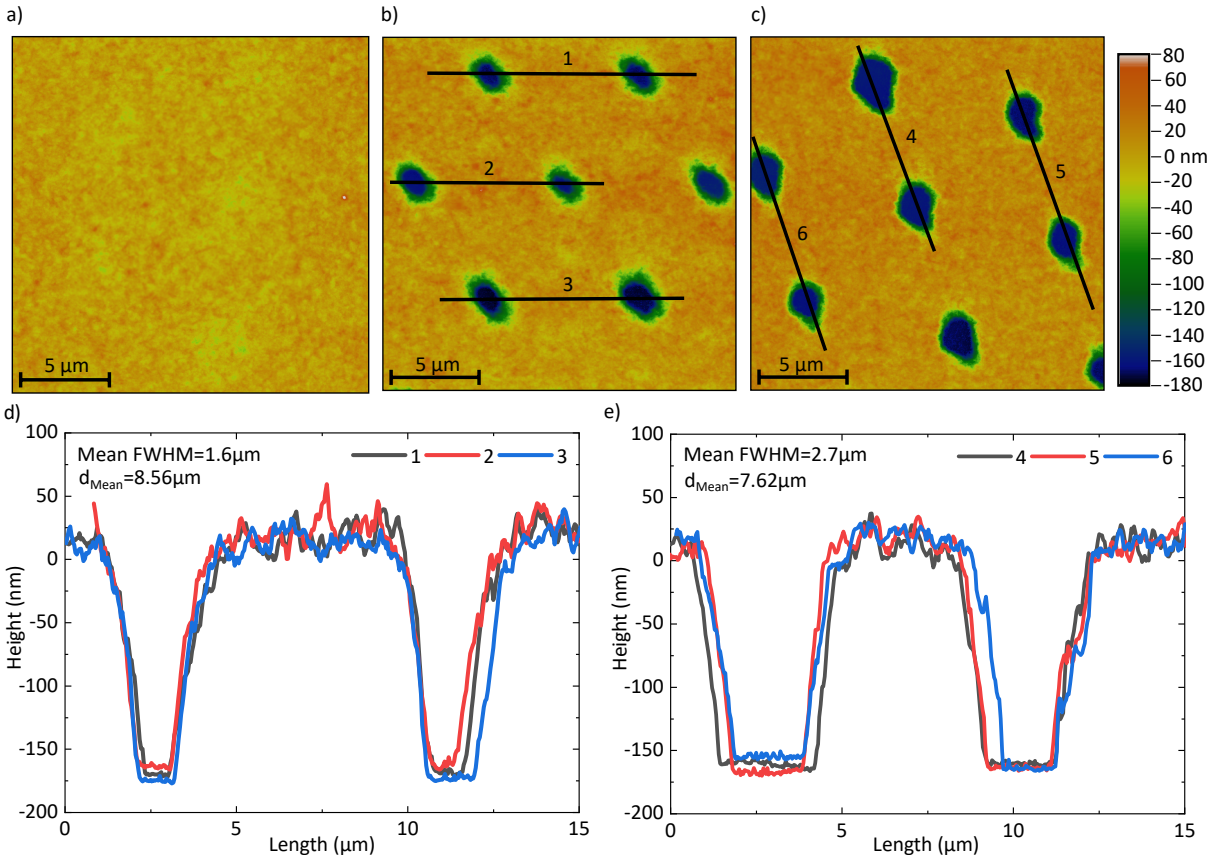

Figure D.19. AFM height images of patterned P3HT with DCB:CHN solvent ratios a) 20:80, b)25:75, c) 30:70. d) and e) depict AFM cross sections from the 25:75 and 30:70 ratio images respectively.

D.6.3 Photomask Designs

I pro-actively planned several pattern designs for a variety of application based publications. This section provides an overview of the designed patterns. Their prospective applications are listed in Table D.3. All of the photomasks were designed using Layout Editor and custom manufactured by photomask portal. Each photomask is a 1x1 inch 40 mil soda-lime substrate with chrome patterns deposited on one side. Optical images of the photomasks are depicted in Figures D.20 through D.37.

Table D.3. Description of designed photomasks.

Potential Applications	Description of Desired Pattern	Figures
Photovoltaics, Photodetectors	Hexagonal and square matrices of holes.	D.20, D.22, D.35 and D.36
Photovoltaics, Photodetectors	Hexagonal and square matrices of islands.	D.21 and D.23,
Transistors	Square matrix of square transistors.	D.24
Optical Gratings	Series of 1D patterns with a series of feature size and separations.	D.25, D.26, D.33, and D.34
Trident Transistor	Matrix of trident shaped transistor designed to increase transitors width/length ratio.	D.27
Doped Polymer Trident Transistor Electrodes	This is the negative image pattern of the trident transistor. Its purpose is to pattern doped semiconducting polymer electrodes.	D.28
Nanowires	1D linear patterns for polymer nanowires with a various nanowire widths and separations	D.29-D.32

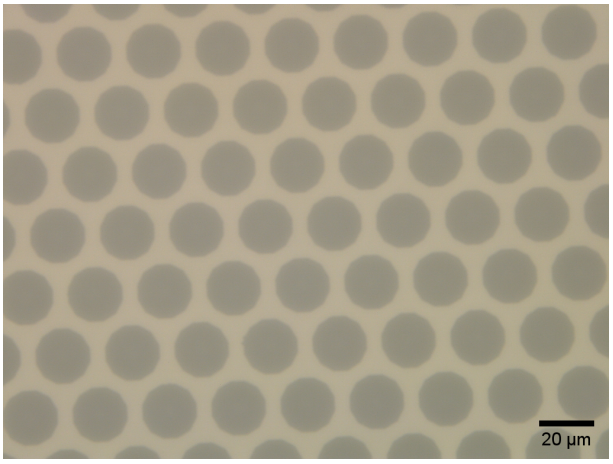

Figure D.20. Hexagonal Matrix of 20um holes, 5um separation.

Figure D.21. Hexagonal Matrix of 5um islands, 20um separation.

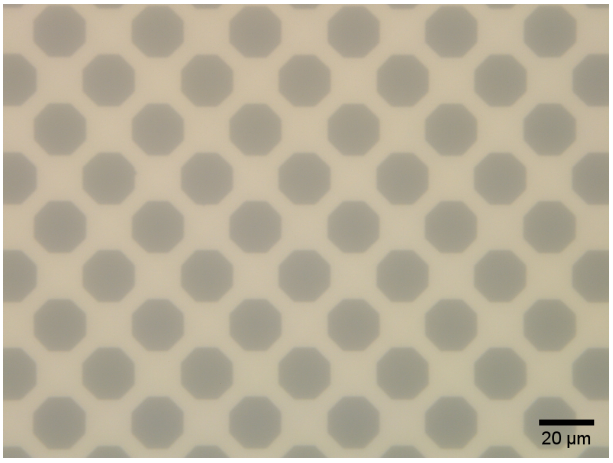

Figure D.22. Simple Cubic Matrix of 20um holes, 5um separation.

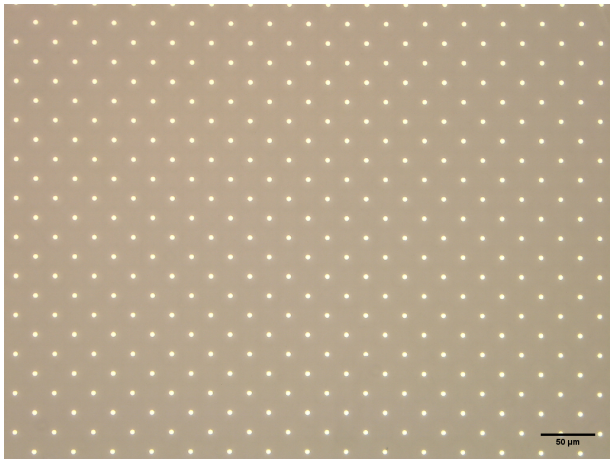

Figure D.23. Simple Cubic Matrix of 5um islands, 20um separation.

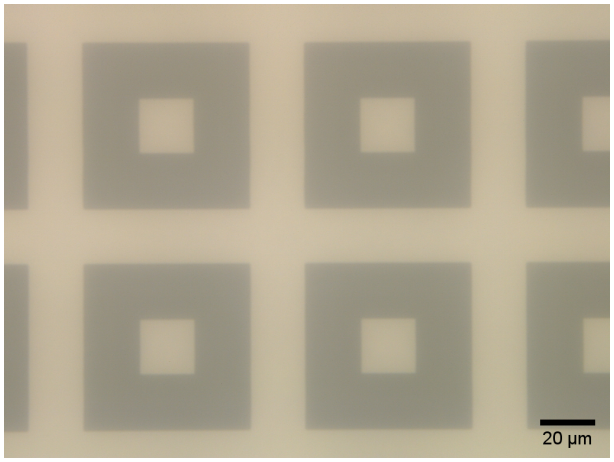

Figure D.24. Simple Cubic matrix of 20x20um transistors, 20 um edges, 20um separation.

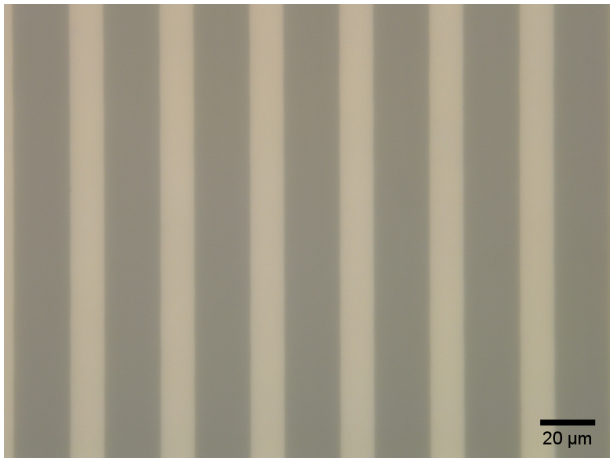

Figure D.25. Optical Grating 20um Slit, 12.5um spacing.

Figure D.26. Optical Grating 20um slit, 30um spacing.

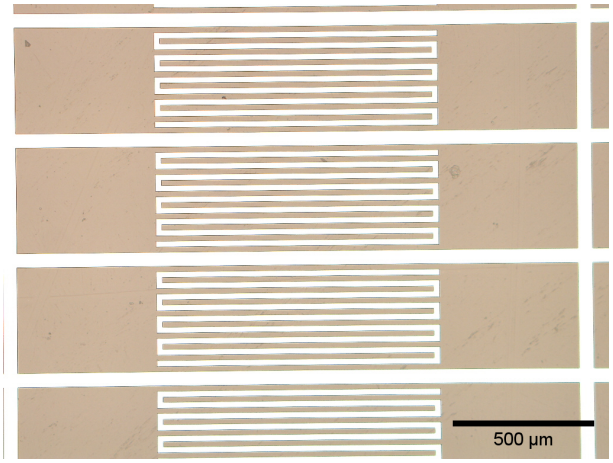

Figure D.27. Trident transistor 1000um channel width, 20um channel length.

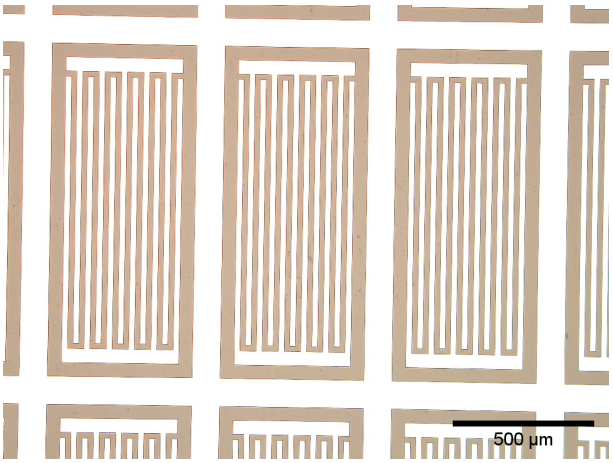

Figure D.28. Doped Electrode Trident Transistor: 20um transistor length, 10220um transistor width.

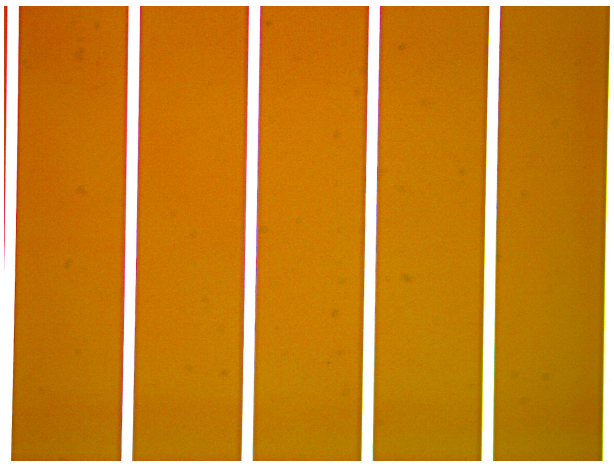

Figure D.29. Grating(nanowires): 200um slit, 20um spacing.

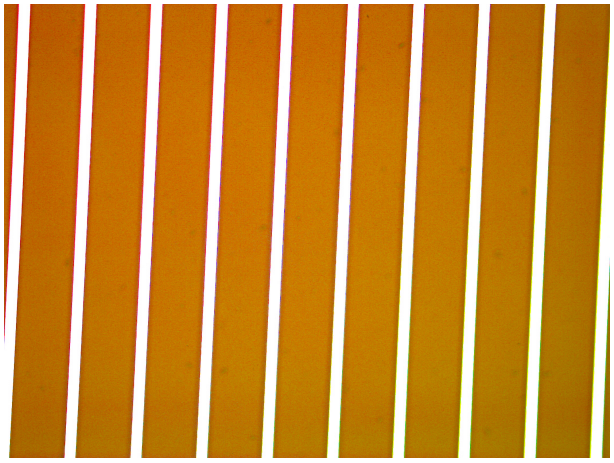

Figure D.30. Grating (nanowires): 100um slit, 20um spacing.

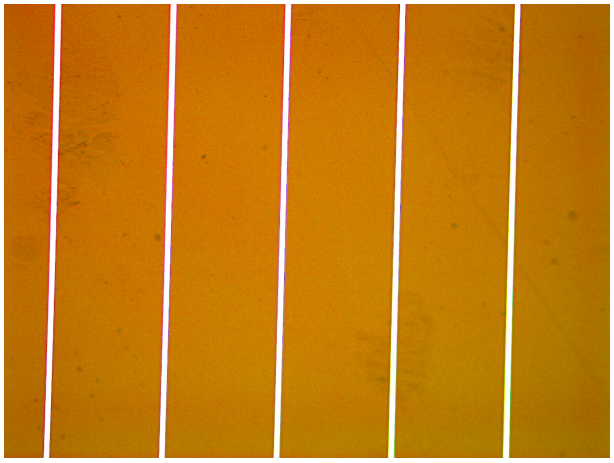

Figure D.31. Grating (nanowires): 200um slit, 10um spacing.

Figure D.32. Grating(nanowires): 100um slit, 10um spacing.

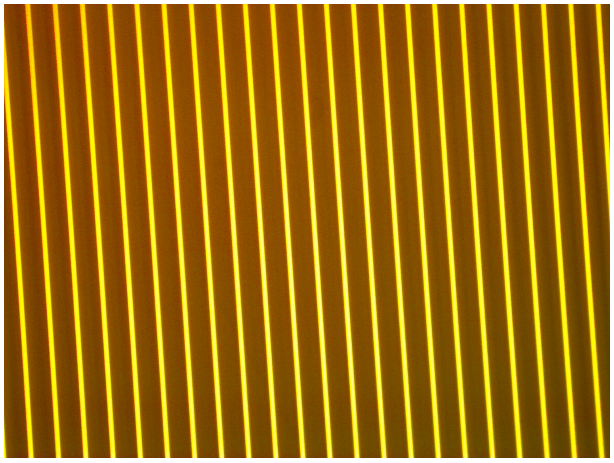

Figure D.33. Optical grating: 20um slit, 5um spacing.

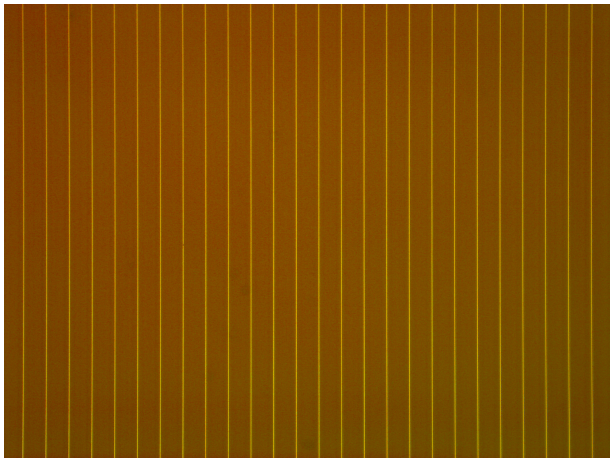

Figure D.34. Optical grating: 20um slit, 1um spacing.

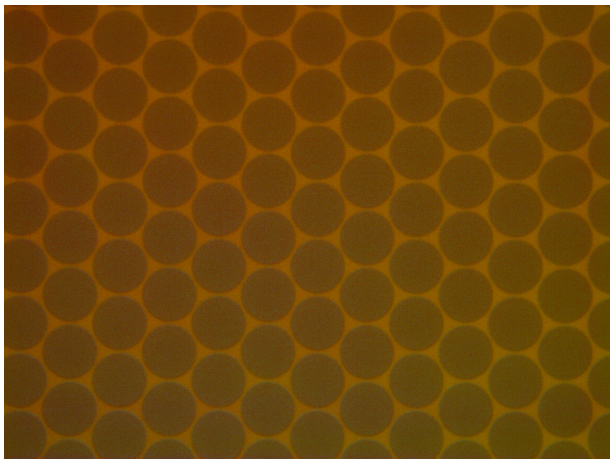

Figure D.35. Hexagonal matrix of 20um holes, 1um separation.

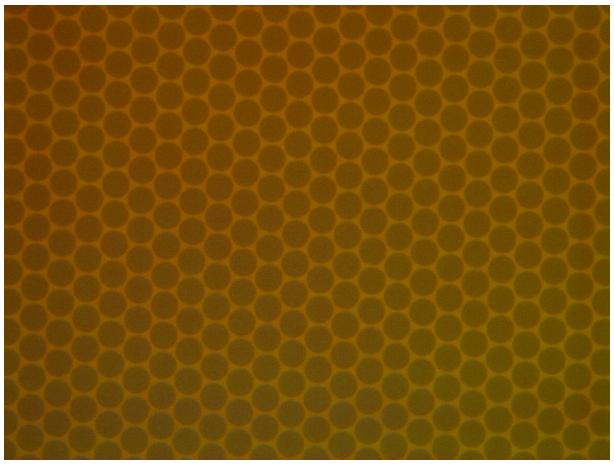

Figure D.36. Hexagonal matrix of 10um holes, 1um separation.

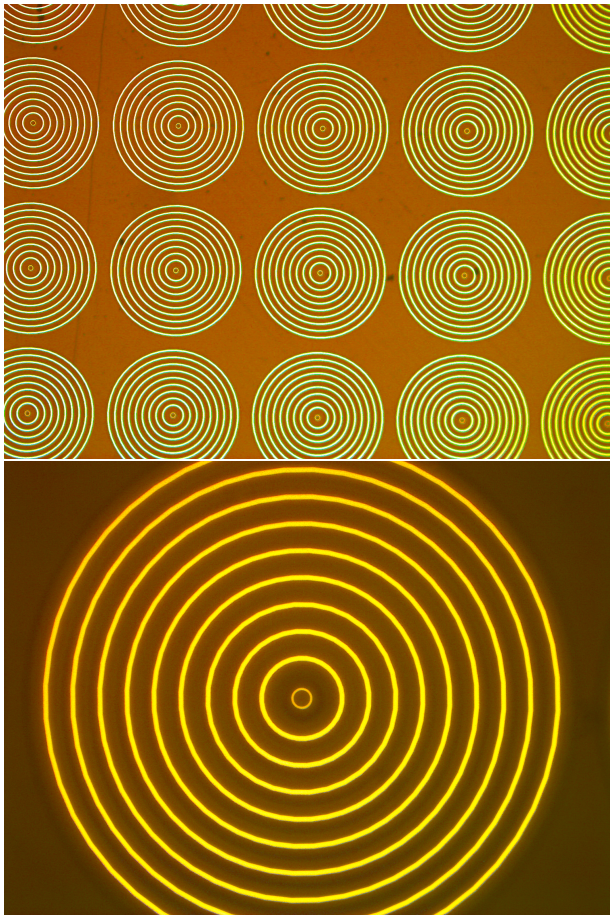

Figure D.37. Simple cubic matrix of targets, 20um diameter center transparent ring, 5um solid rings (10 total), 20um transparent separation, 50um spacing between targets.

D.6.4 Smallest Obtained Feature Size from Projection Photothermal Patterning

Figure D.38 demonstrates an AFM of the smallest obtained feature size using the projection microscope to photo-thermally pattern P3HT. This pattern was obtained using a 5W 405 nm laser and the photomask from Figure D.25, projected through a 100X magnification long working distance lens. The intent of this pattern was to create P3HT nanowires. After I obtained this pattern I designed the photomasks from Figures D.29-D.32, to increase the separation distance between the wires. This would enable our collaborator Prof. Dong Yu to more effectively measure nanowire conductivity.

This project was placed on hold after I started my internship at the National Renewable Energy Laboratory, in early 2020. After, the COVID-19 pandemic started the project has been suspended until further notice. This project still has great promise for creating networks of semiconducting polymer nanowires.

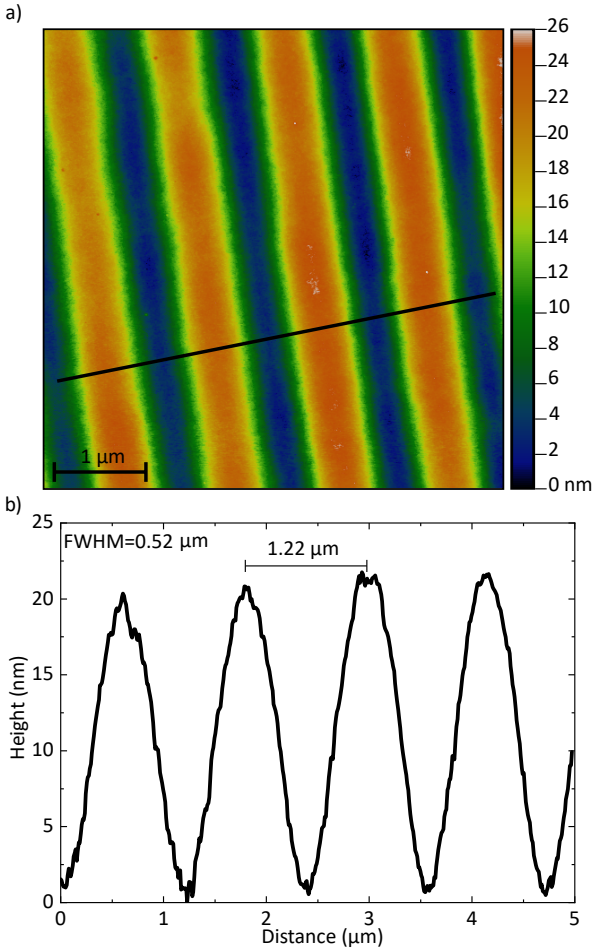

Figure D.38. Smallest achieved feature size. P3HT, 405nm 5W laser diode, new photomasks

D.7 Patterning P3HT/ITIC Bulk Heterojunction

In 2019, I worked with another particularly talented undergraduate, Alice Ferguson, on increasing photovoltaic efficiency in organic photovoltaics (OPVs) by patterning the back side of the film to increase light absorption. I attempted to create back patterned bulk heterojunction (BHJ) OPV using the donor P3HT and acceptor ITIC but ran into a miscibility challenge.

The process for creating a patterned OPV film is illustrated in Figure D.39a). First a 1000nm thick P3HT film is blade coated onto a substrate. Next the projection photothermal lithography microscope is used to pattern $\sim$700 nm deep pattern features into the film. After patterning, ITIC is spin coated onto the patterned surface and thermally annealed to drive ITIC diffusion into the P3HT layer. Figure D.39b) shows the final device goal architecture.

To test whether sequential deposition of ITIC onto a P3HT induced a bulk heterojunction

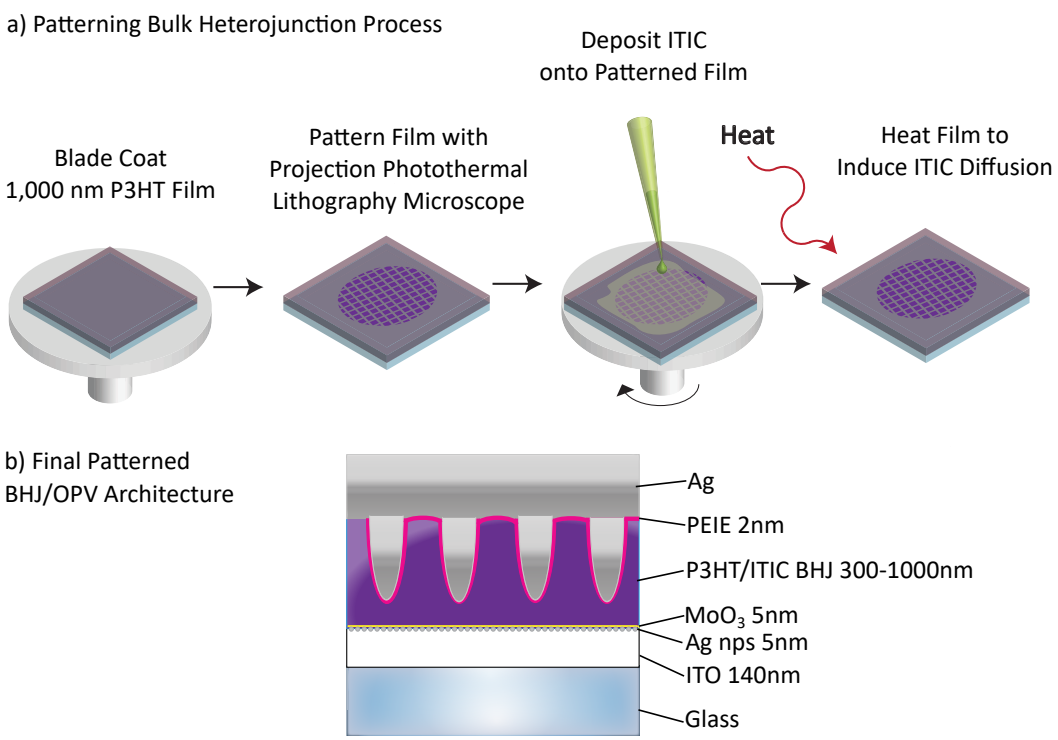

Figure D.39. a) Illustration of film deposition and patterning steps for creating a bulk heterojunction organic photovoltaic. b) Final desired OPV architecture.

vs bilayer architecture we performed fluorescence spectroscopy (Figure D.40). 1000 nm P3HT films were blade coated from 25mg/ml solution in 3:1 CF:CB, blade height 1mm from substrate surface and stage set to 40C. 20mg/ml ITIC solutions in methylene chloride (MC) were spun coat on top of the P3HT films at 1000 RPM for 60s then annealed in the glove box for 10m at 100C.

Fluorescence data was collected in reflection mode. The films were excited at 540nm from both the glass side of the film and the air side of the film. The fluorescence shows that the glass side of the film is P3HT rich and the air side is ITIC rich. P3HT exhibits a broadband fluorescence from 600nm to 725nm. P3HT fluorescence from the glass side of the sample quenches after ITIC is deposited, indicating some intercalation of ITIC all through the 1000 nm thick P3HT layer. After thermally annealing, P3HT fluorescence further reduces indicating increased ITIC diffusion into the P3HT domains. This reveals that a partial BHJ architecture forms with P3HT rich domains. When probed from the air side of the sample, only ITIC fluorescence is observed at 800nm, indicating the formation of a P3HT/ITIC bilayer. The pure

ITIC sample was excited at 650nm.

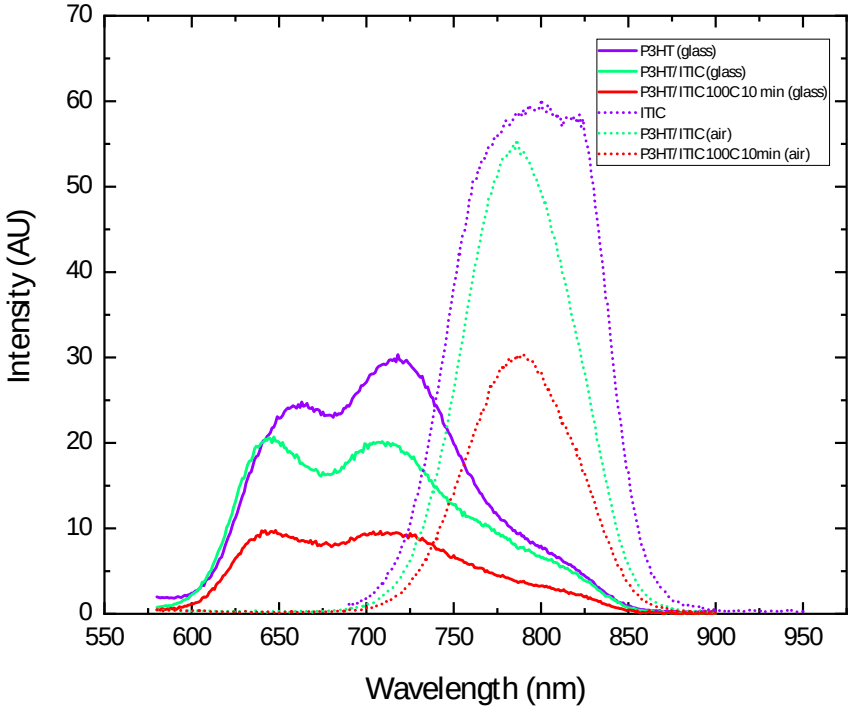

Figure D.40. Flourescence of 1000nm thick P3HT film, neat, with ITIC layer deposited ontop, and after thermally annealing at 100°C for 10 minutes. Measurements were made in reflection mode with light incident through both the glass interface (P3HT rich side), and the air interface (ITIC rich side).

We also tested P3HT fluorescence as a function of solvent exposure and thermal annealing (Figure D.41). P3HT fluorescence mildly quenches when exposed to MC indicating mild re-organization of the film morphology. However, more significant changes were observed in the P3HT/ITIC film confirming partial BHJ formation upon deposition of ITIC.

Figure D.42 shows UV-vis of ITIC with a broadband absorption from 550nm to ∼775nm. Absorption doesn't change when thermally annealing under nitrogen or ambient environments. I attempted to perform UV-vis of the 1000nm thick P3HT film, however the film thickness was too great to perform transmission measurements. Since the extinction coefficient of P3HT is large, all of the incident light within the absorption cross section was absorbed by the film. The transmitted photon flux was below the detection limit of our equipment. Figure D.43 shows

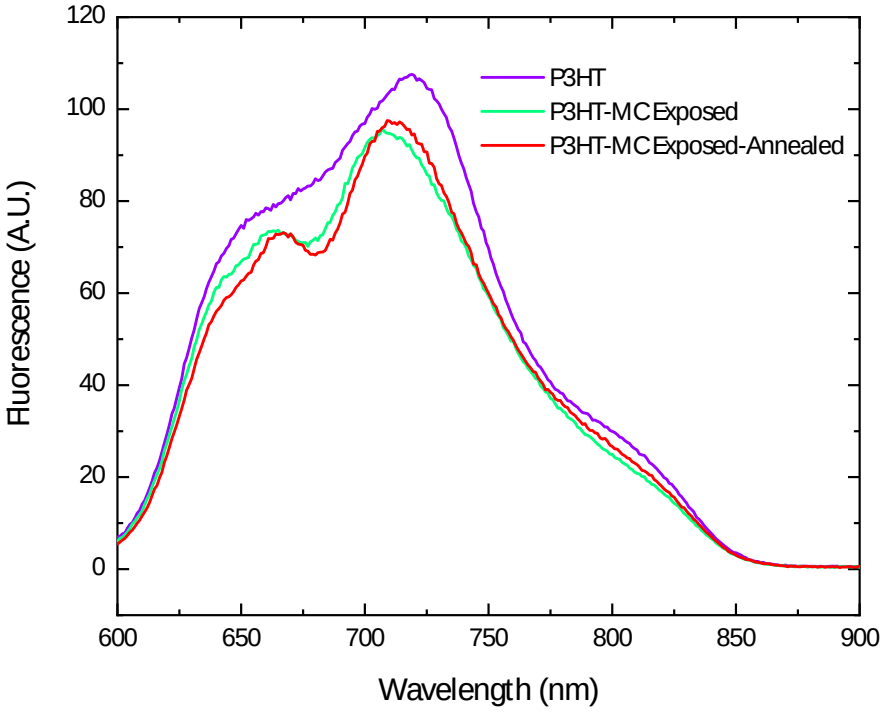

Figure D.41. Florescence of a 1000nm thick P3HT film, as deposited, exposed to MC, and thermally annealed.

UV-vis of a 500nm thick P3HT film with and without ITIC deposited onto. Again, a 500nm P3HT film is too thick; the low flux of the transmitted light at the P3HT absorption maximum is near the limit of the detection limit of the equipment (causing noise at ~500-550nm).

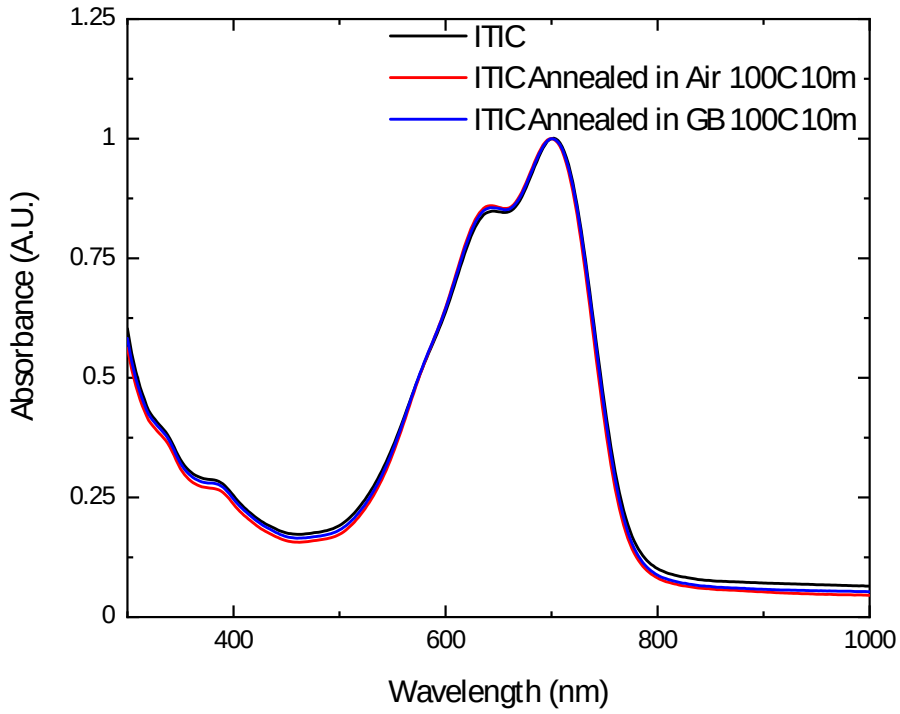

Figure D.42. UVvis of ITIC film, as deposited, annealed in glove box, or annealed in air.

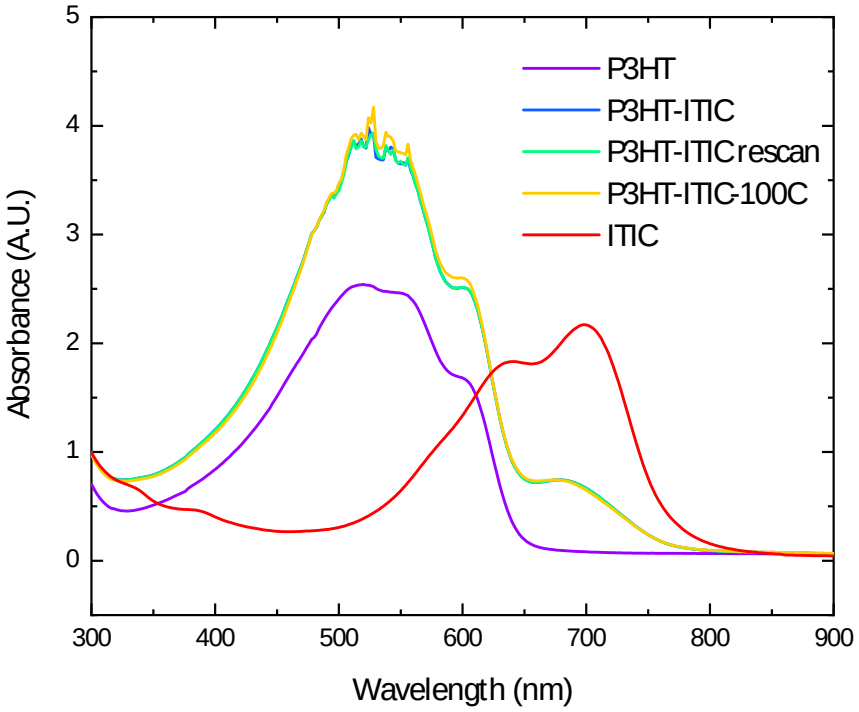

Figure D.43. UVvis of 500 nm blade coated P3HT film, with and without ITIC spun coat ontop. Note: film too thick for spectrometer range (see noise above 3.5 A.U.).

In August 2019, I collaborated with Artem Levinsky and Prof. Gitty Frey at Technion, Technical University of Israel, to collect cross-section scanning electron microscopy (SEM) images of patterned P3HT/ITIC films. There was one major constraint I overcame in order to complete these measurements. Projection photothermal lithography patterning is currently limited to patterning polymer films on a transparent substrate, while cross section SEM must be performed on a cleavable conducting substrate (extrinsic silicon). I developed the process illustrated in Figure D.45 to transfer a pre-patterned P3HT/ITIC/Ag film onto a n-type silicon substrate. First the P3HT film is blade coated onto a water soluble PEDOT:PSS film. The P3HT film is then patterned with the projection photothermal lithography microscope before spin coating ITIC onto the patterned film. AFM of the pattern before depositing ITIC is shown in Figure D.44. Next, silver (Ag) is deposited onto the film, and a $\sim$1nm hydrophobic surfactant, 1,2-ethanedithiol (EDT), is spin coated onto the silver layer. Ag is deposited onto the n-type silicon substrate and a $\sim$1nm layer of EDT is spin coated on top. The P3HT layer is carefully floated onto a water bath, allowing the PEDOT:PSS layer to dissolve. The silicon substrate is then carefully lowered onto the floating film. Once the film adheres to the substrate, it is lifted out of the bath. At Technion, Zinc was diffused into the polymer film using their atomic layer deposition (ALD) equipment. The zinc provides better contrast for the SEM imaging. Once the ALD was complete the film was manually cleaved for SEM. Figure D.46 shows an SEM image of the cleaved bilayer through an unpatterned section of the film. We found it particularly difficult to cleave the film directly through a set of pattern features. This images reveals the P3HT/ITIC bilayer formation. To get a better view of the patterns, we cut out a section of the film with a focus ion beam (FIB), the SEM cross-section of the patterned bilayer is shown in Figure D.47.

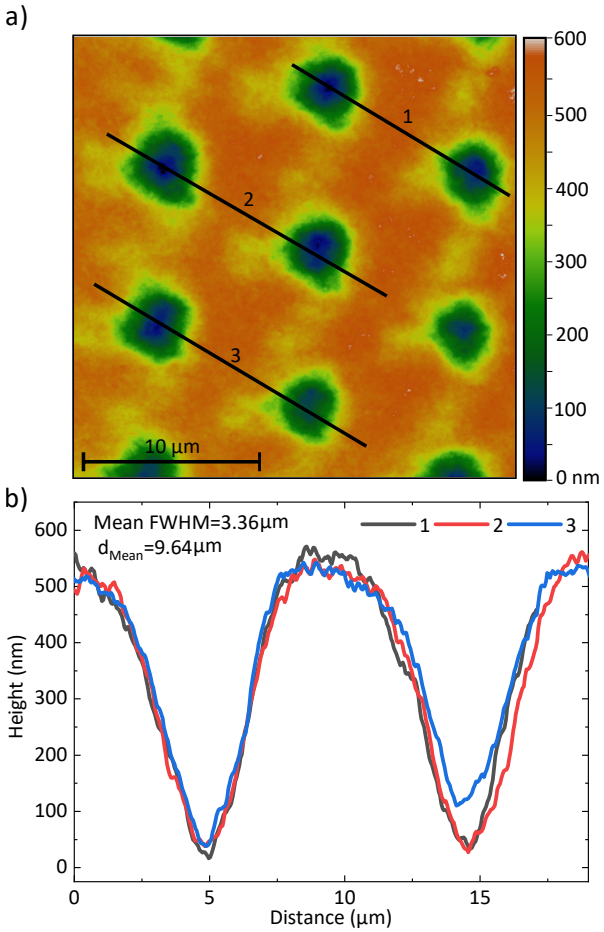

Figure D.44. AFM of Blade Coated 1000 nm thick P3HT film deposited from 3:1 CF:CB (blade height: 0.9mm, Acceleration: 200 $mms^{-}2$, Velocity: $30mms^{-1}$, Stage Temperature 40C). Patterned with 445nm laser (Photomask: hexagonal lattice of 20μm holes with 5μm separation) through 10x Objective Lens, five 5s pulses (2s wait between pulses)

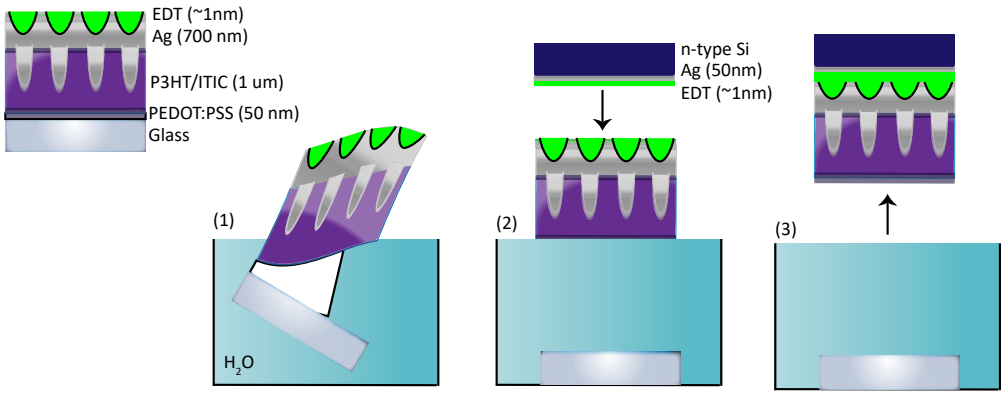

Figure D.45. Scheme for transferring patterned film from transparent substrate to silicon substrate to perform SEM.

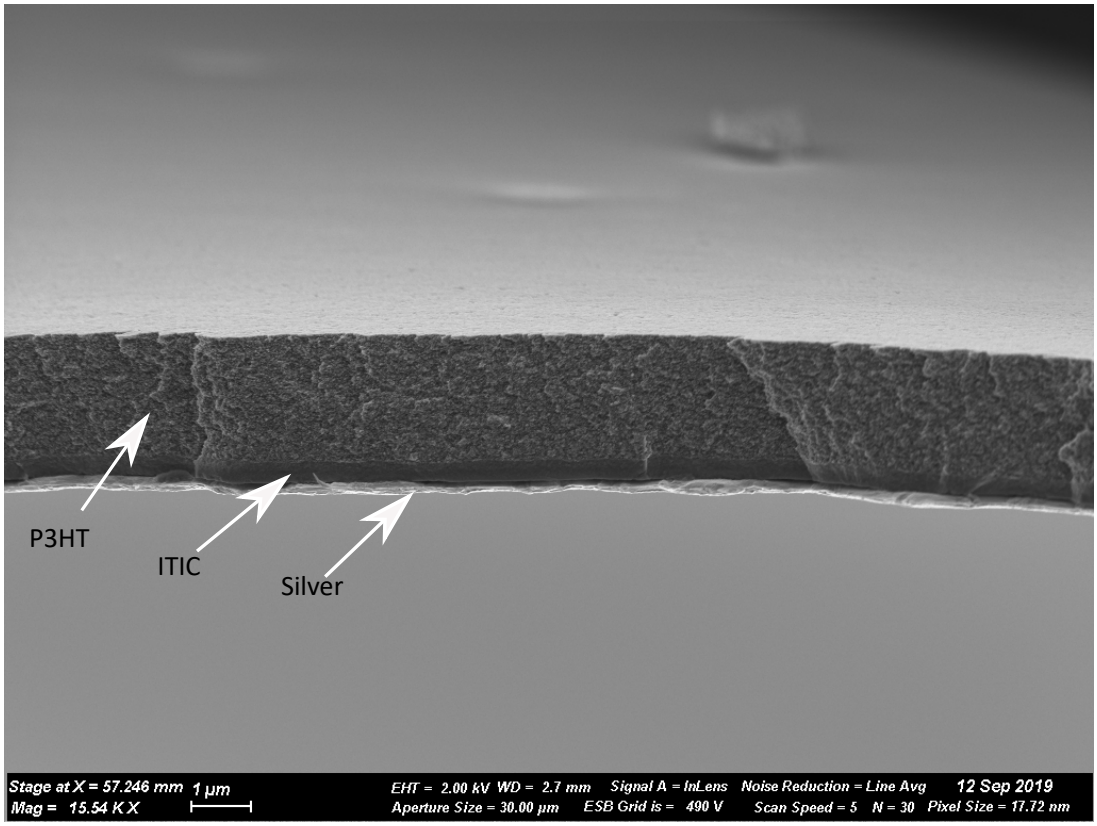

Figure D.46. Cross section SEM image of P3HT:ITIC bilayer after zinc ALD.

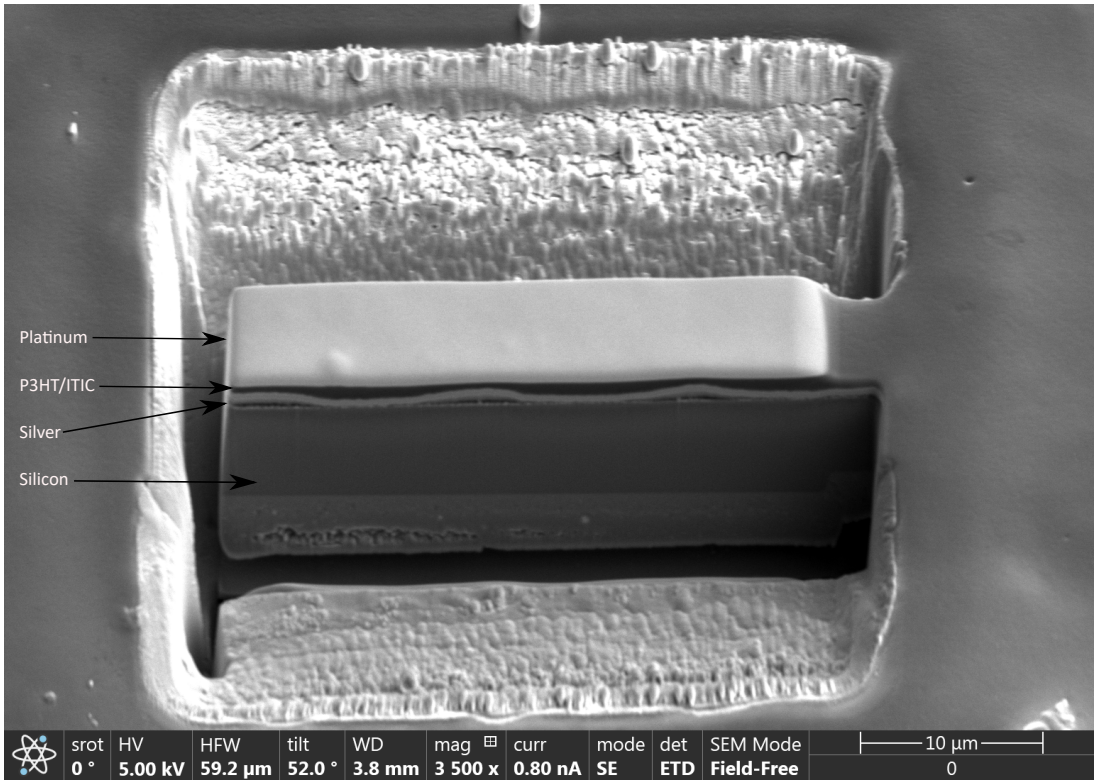

Figure D.47. SEM image of FIBed patterned P3HT:ITIC bilayer cross section.